

UNCLASSIFIED

SECURITY CLASSIFICATION OF THIS PAGE (When Data Entered)

JMC FILE COPY

AD-A196 122

REPORT DOCUMENTATION PAGE		READ INSTRUCTIONS BEFORE COMPLETING FORM
1. REPORT NUMBER AFIT/CI/NR 88-145	2. GOVT ACCESSION NO.	3. RECIPIENT'S CATALOG NUMBER
4. TITLE (and Subtitle) PRELIMINARY DEVELOPMENT OF A ROBOTIC LASER SYSTEM USED FOR OPHTHALMIC SURGERY		5. TYPE OF REPORT & PERIOD COVERED MS THESIS
6. AUTHOR(s) MICHAEL STEPHEN MARKOW		6. PERFORMING ORG. REPORT NUMBER
7. PERFORMING ORGANIZATION NAME AND ADDRESS AFIT STUDENT AT: UNIVERSITY OF TEXAS - AUSTIN		8. CONTRACT OR GRANT NUMBER(s)
9. CONTROLLING OFFICE NAME AND ADDRESS		10. PROGRAM ELEMENT PROJECT, TASK AREA & WORK UNIT NUMBERS
11. MONITORING AGENCY NAME & ADDRESS (if different from Controlling Office) AFIT/NR Wright-Patterson AFB OH 45433-6583		12. REPORT DATE 1988
		13. NUMBER OF PAGES 247
		14. SECURITY CLASS. (of this report) UNCLASSIFIED
		15. DECLASSIFICATION DOWNGRADING SCHEDULE
16. DISTRIBUTION STATEMENT (of this Report) DISTRIBUTED UNLIMITED: APPROVED FOR PUBLIC RELEASE		
17. DISTRIBUTION STATEMENT (of the abstract entered in Block 20, if different from Report) SAME AS REPORT		
18. SUPPLEMENTARY NOTES Approved for Public Release: IAW AFR 190-1 LYNN E. WOLAVER <i>Lynn Wolaver</i> 21 July 88 Dean for Research and Professional Development Air Force Institute of Technology Wright-Patterson AFB OH 45433-6583		
19. KEY WORDS (Continue on reverse side if necessary and identify by block number)		
20. ABSTRACT (Continue on reverse side if necessary and identify by block number) ATTACHED		

DTIC  
ELECTE  
AUG 03 1988  
S D  
AD

DD FORM 1 JAN 73 1473

EDITION OF 1 NOV 65 IS OBSOLETE

UNCLASSIFIED

SECURITY CLASSIFICATION OF THIS PAGE (When Data Entered)

**THE PRELIMINARY DEVELOPMENT OF  
A ROBOTIC LASER SYSTEM USED  
FOR OPHTHALMIC SURGERY**

Publication No. \_\_\_\_\_

Michael Stephen Markow, Ph.D.  
The University of Texas at Austin, 1987

Supervising Professor: Ashley J. Welch

→ This dissertation describes the experimental analysis and design of a second generation robotic laser system used for ophthalmic surgery. The goal of this research project is to develop an automated laser delivery and retinal observation system that is capable of placing multiple lesions of predetermined sizes into known locations in the retina. The goal of this dissertation is to show that from an economic, scientific, and engineering standpoint, the proposed design for this new system is feasible.

The first generation laser system is the slitlamp microscope with a laser delivery system, where the laser is controlled by the manual dexterity of the ophthalmologist. This new system is designed to augment the ophthalmologist, making the operator more efficient with less training. The system is intended to simplify the surgical process while improving accuracy, speed, and safety.

This task can be divided into three areas. The first is to completely develop an automated retinal observation system, which will allow the computer to observe all areas of the retina automatically. The second part of the task is to design a computer controlled pointing and tracking system for the laser, which will keep the laser positioned onto one spot on the retina during small movements of the eye. The third portion is to design and test a reflectance measuring system that monitors and controls the size of the lesion. All three parts must be integrated into one cohesive, economical system.

The work presented in this dissertation sets the groundwork for the project. A design is presented and justified. The areas of the design that are questionable from an engineering standpoint are investigated and analyzed. These areas include the tracking of the retina, placement of the lesions for diabetic retinopathy, and real time monitoring of the lesion growth.

Integrating the many ideas into a cohesive design and analyzing the feasibility of this design is the basis of this dissertation.



Accession For	
NTIS - COMAD	J 111
DTIC TAB	
Unannounced	
Justification	
By	
Distribution	
Availability Codes	
Dist	Availability Codes
A-1	

THE PRELIMINARY DEVELOPMENT OF  
A ROBOTIC LASER SYSTEM USED  
FOR OPHTHALMIC SURGERY

APPROVED BY

SUPERVISORY COMMITTEE:

Spauld  
B. F. Womack  
John A. Zuck  
John A. Zuck  
John A. Zuck  
John A. Zuck



**THE PRELIMINARY DEVELOPMENT OF  
A ROBOTIC LASER SYSTEM USED  
FOR OPHTHALMIC SURGERY**

Publication No. \_\_\_\_\_

Michael Stephen Markow, Ph.D.  
The University of Texas at Austin, 1987

Supervising Professor: Ashley J. Welch

This dissertation describes the experimental analysis and design of a second generation robotic laser system used for ophthalmic surgery. The goal of this research project is to develop an automated laser delivery and retinal observation system that is capable of placing multiple lesions of predetermined sizes into known locations in the retina. The goal of this dissertation is to show that from an economic, scientific, and engineering standpoint, the proposed design for this new system is feasible.

The first generation laser system is the slitlamp microscope with a laser delivery system, where the laser is controlled by the manual dexterity of the ophthalmologist. This new system is designed to augment the ophthalmologist, making the operator more efficient with less training. The system is intended to simplify the surgical process while improving accuracy, speed, and safety.

This task can be divided into three areas. The first is to completely develop an automated retinal observation system, which will allow the computer to observe all areas of the retina automatically. The second part of the task is to design a computer controlled pointing and tracking system for the laser, which will keep the laser positioned onto one spot on the retina during small movements of the eye. The third portion is to design and test a reflectance measuring system that monitors and controls the size of the lesion. All three parts must be integrated into one cohesive, economical system.

The work presented in this dissertation sets the groundwork for the project. A design is presented and justified. The areas of the design that are questionable from an engineering standpoint are investigated and analyzed. These areas include the tracking of the retina, placement of the lesions for diabetic retinopathy, and real time monitoring of the lesion growth.

Integrating the many ideas into a cohesive design and analyzing the feasibility of this design is the basis of this dissertation.

Copyright

by

Michael Stephen Markow

1987

*Dedicated to*

*My Parents*

*who took me to the first grade  
in 1962,*

*Radiana,*

*who is always there,*

*and*

*Abe, Josh, and Jenny,*

*may they surpass  
all my accomplishments.*

**THE PRELIMINARY DEVELOPMENT OF  
A ROBOTIC LASER SYSTEM USED  
FOR OPHTHALMIC SURGERY**

**BY**

**MICHAEL STEPHEN MARKOW, B.S.E.E., M.S.**

**DISSERTATION**

Presented to the Faculty of the Graduate School of  
The University of Texas at Austin  
in Partial Fulfillment  
of the Requirements  
for the Degree of

**DOCTOR OF PHILOSOPHY**

**THE UNIVERSITY OF TEXAS AT AUSTIN**

**December 1987**

## Acknowledgements

It is said that an individual surrounds himself with people he most wants to be like. To this, it was an honor to have been guided from day to day by Dr. A. J. Welch. He is a mentor that I will never forget. Dr. Grady Rylander has also provided me with his special kind of encouragement and inspiration, of which I will always be grateful. Thanks also goes to Dr. John Pearce for sharing with me a part of his diverse knowledge and to Dr. Baxter Womack for providing me with advice and a special friendship. I have also benefited from Dr. Tesar's industrial experience and Dr. John Valvano's computer knowledge. I sincerely appreciate the kind words from Arthur, Dixie, Jody, and Jane. Thanks to Helen for helping with the graphics.

This project was a joint effort of many individuals. Many of the ideas presented in this dissertation were formed during group discussions. These individuals include Dr. A. J. Welch, Dr. Grady Rylander, Dr. Wolfram Wienberg, Lyle Margulies, Youli Yang, Shahriar Gaffari, and Nandu Desai. We also had assistance from Dr. Fermin Tio and Dr. Brian Berger. We appreciate the help from Intel, Coherent, Cohu, and Olympus for providing us with the equipment.

I render thanks to Youli Yang, who has worked side by side with me during thick and thin. I am much obliged to the entire group of graduate students, whose camaraderie made this work enjoyable. I appreciate Marianna Clark's help, who

allowed me to use her routines for image processing. A warm round of applause should be given to those individuals who proofread the manuscript: my committee, Dina Markow, and Nick Markow. Not to be forgotten is the United States Air Force, who provided me with the time and money to do this research.

A warm thanks goes to my three children, Abe, Josh, and Jenny, who sacrificed their precious time with their dad so I could do my research, and a special thanks to Mom and Dad, who kept my wife and kids entertained during these last three years.

Last, but unquestionably the most important, my deepest and warmest gratitude must be given to my wife, Radiana. She read the manuscript, listened to my complaints, and patiently but intently urged me to finish. This work could not have been done without her. May I provide this special woman the strength in her future endeavors that she gave me in this endeavor.

Michael Stephen Markow

The University of Texas at Austin

August, 1987

## Table of Contents

Acknowledgements	v
Table of Contents	ix
Chapter 1 Introduction	1
1.1 The Research Goals for this Dissertation	1
1.2 The Goal of the Project	2
1.3 Overview of the Dissertation	3
1.4 Motivation	4
1.5 Milestones	6
1.6 Progress	7
1.7 Breadth of Project	7
1.8 Economic Implications	8
Chapter 2 Anatomy and Light Interactions of the Eye	9
2.1 Anatomy of the Eye	10
2.2 Tissue Optics and Damage	18
2.3 Optics of the Eye	29
2.4 Applications of Lasers in Ophthalmology	38
Chapter 3 Overview of the System	41
3.1 Overview	41



3.2 Functional Block Diagram	44
-3.3 Advanced Features	48
Chapter 4 The Retinal Tracker	51
4.1 Background	52
4.2 The Theory of Matching	53
4.2.1 Definitions	54
4.2.2 Mathematical Foundations	56
4.2.3 Matching Algorithm	60
4.2.4 Edge Detection	62
4.2.5 Clustering	64
4.2.6 Spring-Loaded Matching	65
4.2.7 Two-Stage and Coarse-Fine Window Matching	66
4.2.8 Growth Curves	67
4.2.9 Search Area	69
4.3 The Registration of Retinal Images	71
4.3.1 The Retinal Tracking Task	71
4.3.2 The Blood Vessel Template	74
4.3.3 Building the Template	82
4.3.4 Template Validation	83
4.3.5 The Search Area and Expansion	90
4.3.6 The User Interface	92
4.4 Results	94

4.5 Strengths and Weaknesses	95
-4.6 Conclusions	103
Chapter 5 Control of Lesion Size	105
5.1 Previous Work	105
5.2 Lesion Development	108
5.3 <i>In Vivo</i> Rabbit Liver Experiment	111
5.3.1 Experimental Procedure	111
5.3.2 Results and Discussion	115
5.4 Egg Yoke Experiment	119
5.5 <i>In Vitro</i> Beef Liver Experiment	120
5.6 Problems and Suggested Improvements	121
5.7 Lesion Control Criteria	125
5.8 Conclusion	127
Chapter 6 Retinal Image Processing	128
6.1 Introduction	128
6.2 Video Funduscopy	129
6.3 Retinal Image Analysis	130
6.3.1 Spatial Analysis	130
6.3.2 Temporal Analysis	132
6.3.3 Chromatic Analysis	133
6.4 The Detection and Treatment of Retinal Disorders	136
6.5 Diabetic Retinopathy - A Case Study	137

6.5.1	Diagnosis and Treatment of Diabetic Retinopathy	138
6.5.2	Detection of Retinal Blood Vessel	139
6.5.3	Detection of Retinal Blood Vessel	140
6.5.4	Selecting Lesion Locations	149
6.6	Conclusion	151
Chapter 7	Instrumentation	152
7.1	Introduction and Hardware Overview	152
7.2	The Fundus Camera	154
7.2.1	An Overview of Fundus Cameras	154
7.2.2	Imaging with the Fundus Camera	157
7.2.3	Illumination Source	159
7.2.4	Fixating Device	162
7.2.5	Pixel Separation	163
7.2.6	Fundus Camera Autoalignment	164
7.2.7	Stereoscopic Fundus Cameras	165
7.2.8	Mosaics	166
7.3	Video Cameras and Video Cassette Recorders	167
7.3.1	General Specifications	168
7.3.2	Chromatic Specifications	170
7.3.3	Temporal Specifications	171
7.3.4	Spatial Specifications	173
7.3.5	Video Camera for Retinal Observation	178

7.3.6 Video Camera for Lesion Monitoring	180
7.3.7 Video Cassette Recorders	181
7.4 Computer Hardware and Video Boards	183
7.4.1 Video Boards	183
7.4.2 The Computer	186
7.4.3 Quickening the Retinal Tracker	187
7.4.4 Decreasing Execution Time	188
7.4.5 The Optimum Video Rate	189
7.5 Computer Software	192
7.5.1 Master Computer Software Design	192
7.5.2 Tracking Computer Software Design	196
7.5.3 Lesion Computer Software Design	198
7.6 Laser Delivery System	200
7.7 Optics	205
7.7.1 Coaligning the Optical Systems	206
7.7.2 Focussing the Laser	210
7.8 System Costs	212
7.9 Safety	213
7.10 Conclusion	214
Chapter 8 Further Research	215
8.1 General	215
8.2 Light Interaction with Tissue	216

8.3 Retinal Tracking	216
8.4 Retinal Image Processing	217
8.5 Instrumentation	219
8.6 Optics	220
8.7 Mechanical	220
8.8 Software	221
Chapter 9 Summary of Major Accomplishments	222
Appendix 1 Algorithm to Identify a Closed Area	224
Appendix 2 Correlation Calculations	227
Appendix 3 Comparing the MTF's of a Video Camera,	231
Bibliography	233

## **Chapter 1 Introduction**

### **1.1 The Research Goals for this Dissertation**

The research goals for this dissertation are to analyze, design and demonstrate the feasibility of a second generation laser delivery system used for retinal surgery. This robotic laser must be capable of placing multiple lesions of predetermined sizes into known locations in the retina. This task can be divided into three areas. The first is to completely develop an automated retinal observation system, which will allow the computer to observe all areas of the retina automatically. The second part of the task is to design a computer controlled pointing and tracking system for the laser, which will keep the laser positioned onto one spot on the retina during small movements of the eye. The third portion is to design and test a reflectance measuring system that monitors and controls the size of the lesion. The theme of the research for this dissertation has been to design and integrate these three subsystems along with many other concepts and ideas into a cohesive, economical, and usable system.

Clinically adequate lesions are a function of laser burn duration, laser wavelength, and laser power density. Power density is often separated into laser power and laser spot size. These are controllable by the ophthalmologist or computer. The lesions are also a function of the optical, thermal, and damage properties of tissue, which are not controllable. The ophthalmologist's purpose is to coagulate the tissue in the proper

manner such that optimal therapeutic value is achieved. The controllable parameters are modified depending on both the noncontrollable parameters and the disease being treated. It is very important to note that this system is not concerned with determining the required damage, for this is the ophthalmologist's job, but merely to inflict the chosen damage once it is determined. The machine can possibly identify certain features in the retinal image that signify a possible disorder, but it cannot compare to the diagnostic abilities of an ophthalmologist. But, in some controlled situations, it should be possible for a machine to inflict damage with more precision and speed than an ophthalmologist.

Specifically, this dissertation accomplishes the following. First, a substantial amount of information pertinent to the system design is provided. Second, the proposed design is presented and examined. Third, an algorithm to perform retinal tracking is developed and analyzed. Fourth, blood vessels are identified in a retinal image and lesion locations for panretinal photocoagulation are selected. Fifth, laboratory experiments that examined and controlled lesion sizes are discussed.

## 1.2 The Goal of the Project

The goal of the project is to develop an automated laser delivery and retinal observation system that is capable of placing multiple lesions of predetermined sizes into known locations in the retina.

Desired specifications for this system are a system cost of about \$200K, a pointing accuracy of the laser on the retina of about 10  $\mu\text{m}$ , a 16 ms reaction time to patient movement, and an absolute final lesion width within 10% of the desired lesion

width. A prototype, if built today, would probably cost about \$250K. This prototype would also provide a pointing accuracy of the laser on the retina of about 70  $\mu\text{m}$ , a 50 ms reaction time to patient movement, and an absolute final lesion width within 30% of the desired lesion width. These specifications are only estimates: a prototype is required for more accurate estimates.

This system is designed to augment the ophthalmologist, making the operator more efficient with less training. The ophthalmologist would interact with the system to gather diagnostic information and thus determine the proper treatment for any disease. Present systems are archaic and their operation is similar to a video arcade game. The system is intended to simplify the surgical process while improving accuracy, speed, and safety.

### **1.3 Overview of the Dissertation**

The statement of purpose for this research is given above. This chapter also provides the introduction to this dissertation, discusses the motivation for this research, and reviews the breadth of the project. Chapter two discusses background information, including the anatomy and optics of the eye, laser interaction with tissue, and current applications of lasers in eye surgery. Chapter three presents an overview of the system. Chapters four, five, and six discuss three major areas of the project: the retinal tracker, control of the lesion size, and retinal image processing. Chapter seven details the instrumentation, and chapter eight lists areas for further research on this project. The last chapter provides the significance of this research. An unpublished addendum is included with this dissertation that contains the hardware



schematics for the 32 x 32 camera, and the listings for the tracking, lesion monitoring, and video board software.

#### 1.4 Motivation

This research is motivated by the impact lasers have had and will continue to have on ophthalmology. The use of lasers in eye surgery provides for a quick, noninvasive method for the treatment of many disorders on an outpatient basis. To treat the ocular fundus, a lesion is placed in the retina that will have some therapeutic value. Argon, krypton, and Nd:YAG lasers are the typically used lasers. In spite of the many advances in bioengineering over the past years, a rather antiquated method is still employed by the ophthalmologist in controlling the lesion's position and size. The patient's head is positioned in a chinrest with the forehead leaning against a headrest (Figure 1-1). The head is immobilized with a head strap. The patient fixates on a small light with one eye, thus stabilizing (to some degree) both eyes. The power, spot size, and exposure for the laser burn are dialed into the controls of the laser. The ophthalmologist views the patient's retina with a slitlamp microscope. Quite often a Goldman contact lens is used to optimize energy coupling into the eye, keep the eyelid open, protect the cornea, and give a stable view of the retina. Different areas of the retina are imaged by manipulating a joystick. A low power aiming beam in the center of view indicates the spot the laser will irradiate. The ophthalmologist focuses the image and laser by twisting the joystick. Focussing is achieved when the low power laser spot is minimal in diameter and the microscope is focussed onto the retina. The ophthalmologist presses a foot pedal to fire the laser. This opens the

shutter for the required time and creates a thermal lesion at the position of the focussing beam, provided the patient's eye or the ophthalmologist's hand does not move.

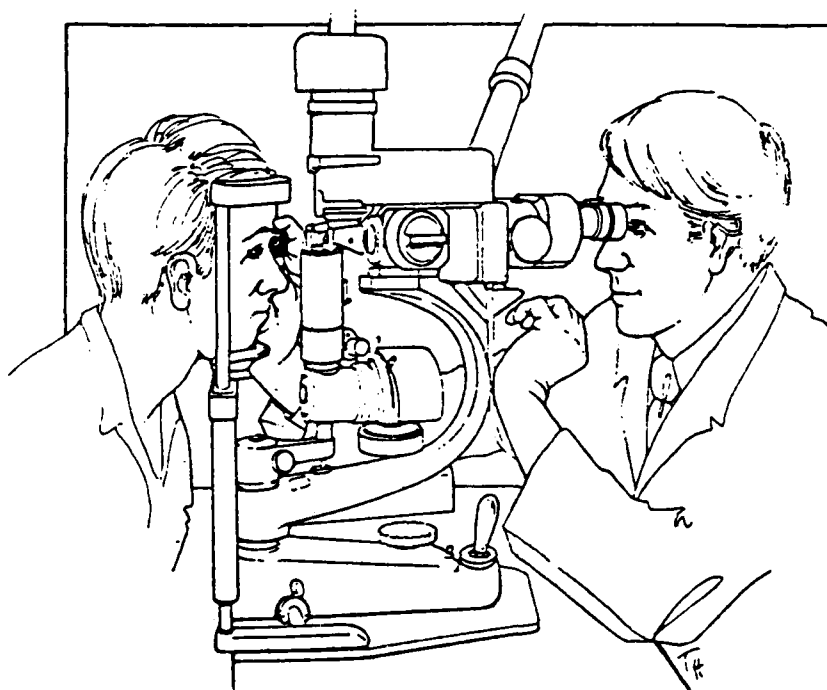


Figure 1-1 Slitlamp microscope with laser delivery system [1-1].

Using small doses initially, successive burns are made until the lesion visually appears to be of the desired size and depth. The laser is then redirected to other areas and burns are made using the power setting that was established in the first set of burns.

There are several drawbacks to the above procedure. First, the size of the lesion is judged by its appearance under the slitlamp microscope. Subjectively evaluating the lesion's size in this manner can lead to excessive irradiation, resulting

in hemorrhaging, or insufficient irradiation, resulting in minimal therapeutic value. Second, the ophthalmologist controls the laser's position with a joystick. Unless a retrobulbar anesthesia is administered, eye movement can result in accidental damage in undesired areas. Third, as many as 3000 burns need to be made in a single eye for some diseases, such as diabetic retinopathy. This procedure is usually performed in three one-hour sessions, a tedious job for the ophthalmologist and the patient. A robotic laser might be able to produce accurate lesion sizes at precise locations in only one-tenth the time.

Surprisingly, most errors made in both size and position of the lesion are not as serious as one might think. The lesion size can vary significantly and still provide the required results. However, as new applications and techniques are found for lasers in ophthalmology, more precision and ease of operation may be welcomed.

### 1.5 Milestones

The development of the research for the project can be outlined in three milestones. The first milestone will be to develop a system that accomplishes two tasks. The first task is to monitor the lesion in real time and turn the irradiating laser off when the lesion reaches the predetermined size (5 ms response time). The second task is to monitor the position of the laser on the retina and turn the laser off if the eye moves out of position (50 ms response time).

The second milestone will be to further develop the two tasks. The lesion monitoring in the first task must be extended to turn the laser off when the lesion is at a requested width and depth. The second task must be upgraded to adjust the laser's

position on the retina as the eye makes small movements. This will require the development of a system that views the retina and delivers this view to a computer. A computer controlled laser delivery system must also be built before this milestone can be reached.

The third milestone will be to completely develop the automated retinal observation system, which will allow the computer to observe all areas of the retina automatically. Many advanced features that might be included in this design are discussed in Chapter 3, "Overview of the System". Clinical evaluation of the system and FDA approval will also be done during this final stage. Liability issues must also be fully addressed. This third milestone might very likely be performed by a commercial company.

### **1.6 Progress**

This dissertation almost completes milestone one. A complete system has not been assembled but many of the subsystems have been analyzed. The second milestone can be accomplished with much of the equipment available here at UT Austin, which includes an Olympus fundus camera, Coherent laser delivery system, and two Intel computers. The preliminary design work is in progress for milestone three, but the system cannot be implemented until funding becomes available.

### **1.7 Breadth of Project**

This project spans a broad spectrum of areas. This is a bioengineering task, which requires a knowledge physiology. Some animal work must be performed to

complete the research on reflectance changes during lesion formation. The device will be used by ophthalmologist for work on patients; hence the user and patient interface must be properly designed. The use of lasers must be understood, to include the control aspects associated with laser positioning. This project includes optics of the eye, laser delivery optics, fundus camera optics, and tissue optics. Cameras must be interfaced to the fundus camera and the computer system. A significant amount of software must be written, which includes real time processing. Images must be analyzed for retinal feature extraction and real time tracking. The fundus camera will have to be servo driven. The entire system must be mechanically built and integrated into an aesthetic looking system that can be placed in a clinic. It must be reliable, economical, useful, and safe. And lastly, it must be marketed and sold.

### **1.8 Economic Implications**

This dissertation presents a preliminary design of a second generation laser system used for retinal surgery. This is not a final design for an actual system, but merely a suggested design from all the information and work that has been accumulated at this time. Further research is required before a final design can be established. To actually put a system like this into full production, a rather large, concerted effort by a company is required. This would involve many engineers (optics, electrical, computer, software, and mechanical), many technicians, many millions of dollars, and five to six years. A clinical study with the FDA approval is also required. The results of the research for this dissertation are intended to show that a system like this is economically and scientifically feasible.

## **Chapter 2 Anatomy and Light Interactions of the Eye**

This chapter provides diverse background information on the eye. Light is one of the few modalities that allows noninvasive access to the retina. The present uses of light in the eye can be divided into two categories. The first category is the application of light energy to an area of the eye to create therapeutic damage, either mechanical, thermal or photochemical. The second category is the application of light energy to an area of the retina such that reflections can be measured, and hence extract information. The former application started when Gerhard Meyer-Schwickerath in 1946 [2-35] used a carbon arc light source to create a lesion in the retina. This was later followed by Campbell's use of the laser to do the same in 1963 [2-50]. The retrieval of information from the fundus took hold with the invention of the ophthalmoscope in 1851 by Helmholtz [2-5] and the first fundus photograph by Jackman and Webb in 1886 [2-25].

The first section of this chapter will review the anatomy of the eye. Next, light interaction with tissue and tissue damage will be analyzed. The absorption, transmission, reflection, and scattering of light in tissue will be discussed. Tissue damage resulting from three mechanisms will be reviewed, concentrating on thermal damage. The next section will discuss optics of the eye and the last section will review applications of lasers in ophthalmology.

## 2.1 Anatomy of the Eye

This section will discuss the anatomy and light interaction of the eye. A schematic view of the normal eye is shown in Figure 2-1. Light enters the eye through the cornea, passes through the pupil, and is focused by the lens onto the retina. The cornea and lens are the refracting structures, developing approximately 60 D (D stands for diopter, which is the reciprocal of the focal length). The lens can change its shape, and hence allows the system to focus over a wide range of distances (accommodation). The pupil is an aperture formed by the iris and can change diameters with changing light environments. The aqueous and vitreous humor are clear fluids that fill the interior of the eye and help maintain the intraocular pressure. Most of the laser procedures are performed on abnormal eyes with variable opacities of the lens (cataract), aqueous humor (hyphema), or vitreous humor (vitreous hemorrhage).

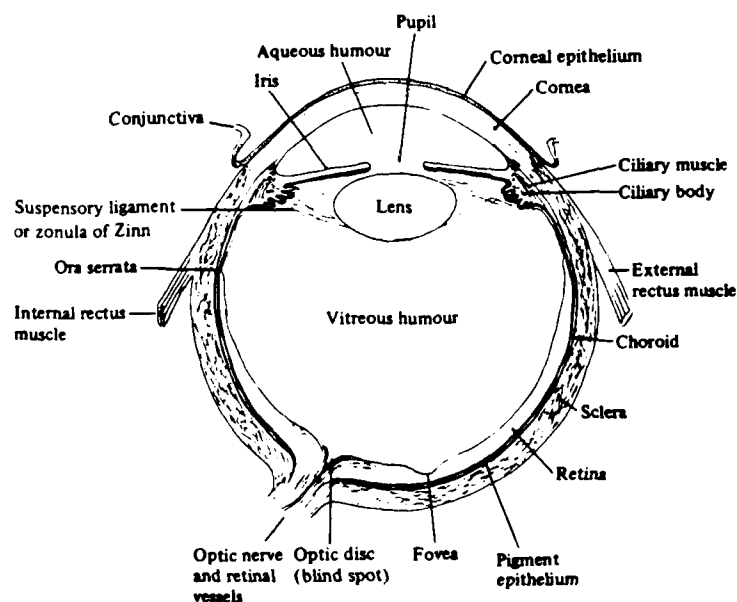


Figure 2-1 Diagram of the human eye [2-2].

The posterior portion of the eye is composed of several layers. A histological section through this area is shown in Figure 2-2. The internal limiting membrane (top of the figure) is the inner surface of the retina. The retina extends to the retinal pigment epithelium (listed as just the pigment epithelium in Figure 2-2). Light enters the tissue from the top of the picture and proceeds through all the inner layers of the retina relatively unimpeded. The actual detecting mechanisms for light, the outer segments of the rods and cones, are located in the tissue between the connecting cilium and the retinal pigment epithelium (only about 1% of the total light directed onto the retina is absorbed here). The other layers of the retina (between the internal limiting membrane and the connecting cilium) are visual preprocessing nerves cells. The layer of nerves under the internal limiting membrane is called the nerve fiber layer (not labeled in Figure 2-2), and can be seen as small striations in a fundus image. The retinal pigment epithelium absorbs most of the light that bypasses the detectors, thus dampening reflected images (about 50 % of the total light directed onto the retina is absorbed here while the remaining light is absorbed in the choroid). This layer contains melanin granules, an extremely high absorbing pigment. Since the retinal pigment epithelium is extremely absorbent, it is generally the first layer of the eye to succumb to thermal damage under laser irradiation. The next two layers are the choriocapillaris and the choroid, which are very vascular tissue and provide the circulation to the distal (outer) one-third of the retina. These areas are the most highly metabolic areas of the body. Lastly, the sclera (which is not shown but resides below the choroid in the Figure 2-2) is the protective tough outer coat of the eye. It's important to note that intraocular pressure and the metabolism of the retina-choroid are



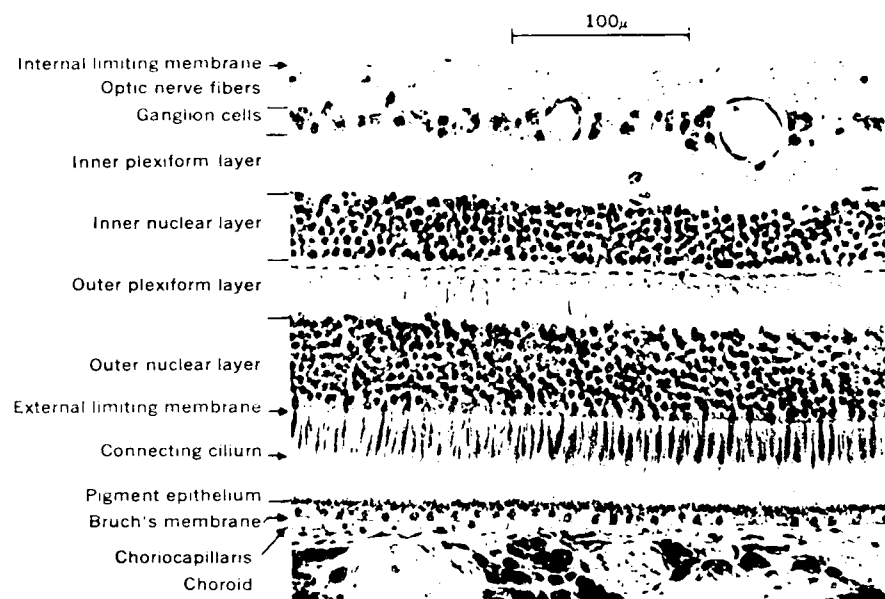


Figure 2-2 A photomicrograph of peripheral retina of macaque monkey, with major structures and layers labeled [2-9].

the only mechanisms holding the retina against the retinal pigment epithelium. If the normal pressure relationships are lost, the retina will collapse and fall inward toward the center of the eye.

If one were to peer into the eye through the pupil, the major features of the retina would become visible (Figure 2-3). The retina extends at least  $200^\circ$  around the nodal point of the eye (angular measurements will be defined below). The image in Figure 2-3 only shows about  $30^\circ$  of the retina. The most striking landmark is the optic disk, which is a white circular area measuring about 1.5 mm. This is the point of the retina where the optic nerve exits to the brain. Also emanating from this area are the retinal blood vessels, which nourish the interior two-thirds of the retina. These arteries and veins are visible and can be seen to meander over the entire surface of retina. It's interesting to note that the optic disk is a natural blind spot because it is void of rods and cones.

A short distance distal (away from the nose) to the optic disk is the fovea. Most of the human acute vision takes place in this small sensitive area. Central vision is contained in a cone of only one degree, whereas the entire visual field encompasses over  $180^\circ$ . The fovea, which is only  $1500\text{ }\mu\text{m}$  in diameter, contains a large number of densely packed red and green cones and is primarily used for photopic (day) vision. A single laser burn in this area can reduce an individual's vision from 20-20 to 20-400. The fovea is located in a region called the macula, which is approximately  $5000\text{ }\mu\text{m}$  in diameter and also subserves acute vision. This area has a yellow hue from the xanthophyll pigment contained in the inner and outer plexiform layers of the retina (Figure 2-2). The huge area outside the macula is called the periphery, and provides for peripheral and scotopic (night) vision.

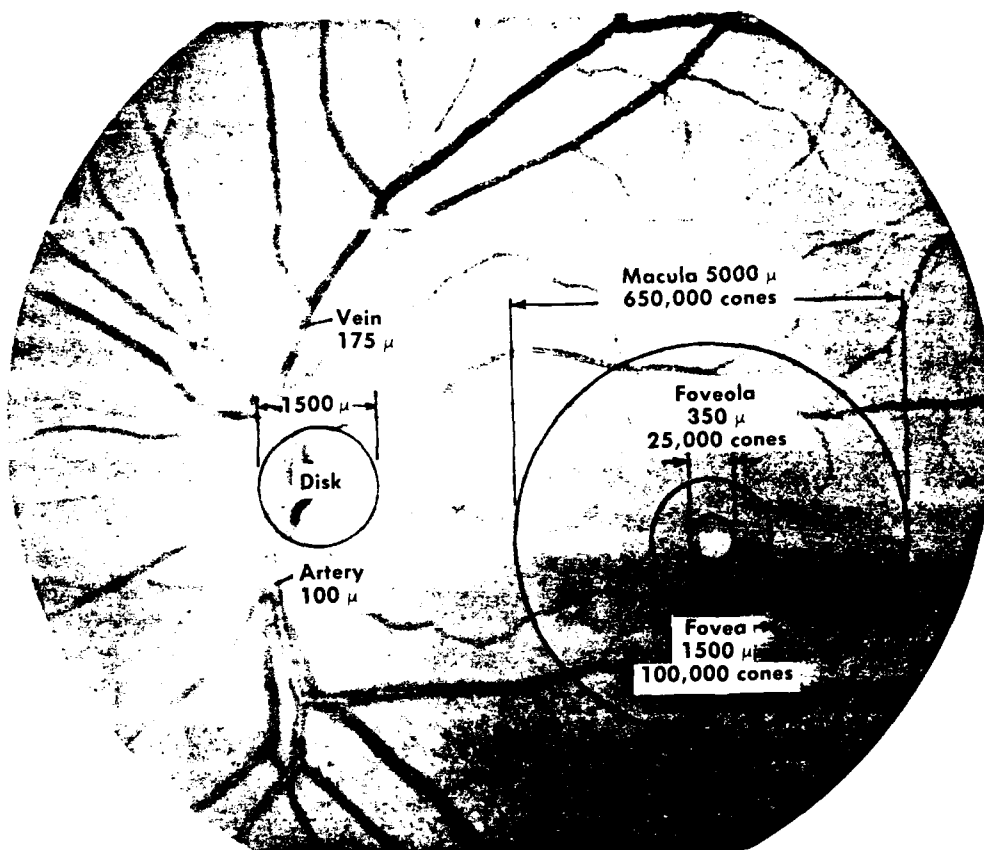


Figure 2-3 Posterior pole of the left retina [2-36].

The pupil is the eye's aperture. Its diameter shrinks in bright light and enlarges in dim light. When viewing the retina with an ophthalmoscope, the size of the pupil makes a significant difference in the quality and field of view of the image. When the pupil is larger, it's easier to see into the eye and more illumination can enter the eye for a brighter image. (Mydriasis is the dilating of the pupil with a drug to allow better viewing of the fundus.) The pupil can dilate up to 9 mm in some individuals. Acquiring a good retinal image and performing laser surgery on those individuals with poor mydriasis can be difficult. While performing a clinical test on a fundus camera, Ducrey [2-16] recorded the maximum dilatation of each patient. The results are shown in Table 2-1.

Maximum Pupil Size	Percent of Individuals
2 mm	0.5 %
3 mm	3 %
4 mm	7 %
5 mm	12 %
6 mm	27 %
7 mm	27 %
8 mm	20 %
9 mm	4 %

Table 2-1 Number of individuals (in percent) and their maximum dilation [2-16].

Commonly, references to retinal distances are made in angles rather than distance. As shown in Figure 2-4, the radial angle subtends from the optical axis of the eye outward to a point on the retina, with the nodal point as the apex of the angle.

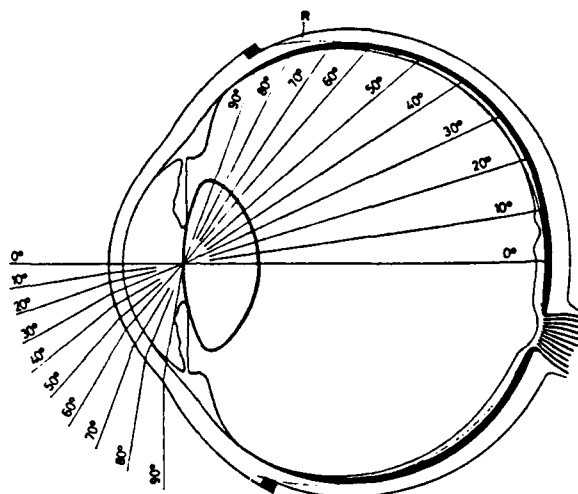


Figure 2-4 Cutaway view of the eye showing the radial angles [2-29].

An image of the retina is shown in Figure 2-5. This image was taken with a equator-plus camera developed by Pomerantzeff [2-39]. A grid has been superimposed onto the picture which maps the retina into a spherical coordinate system. In this picture, the radial angle varies between  $0^\circ$  and  $80^\circ$  and the tangential angle varies a full  $360^\circ$ . The equator of the eye (which divides the globe of the eye into its anterior and posterior halves) is located at a radial angle of about  $66^\circ$  [2-16]. The equator is not at  $90^\circ$  because the angles subtend from the nodal point of the eye. For the human eye, one second of arc at a radial angle of  $0^\circ$  is equal to  $4.9 \mu\text{m}$  on the retina [2-2]. Drasdo [2-15] used a schematic eye and calculated the distance to be  $4.6 \mu\text{m}$ . Drasdo also calculated that, at a radial angle of  $100^\circ$ , one radial minute of arc is equal to  $1.8 \mu\text{m}$  and one tangential minute of arc is equal to  $3.0 \mu\text{m}$ . Thus the retinal area per solid angle at a radial angle of  $100^\circ$  is 5 times less than at a radial angle of  $0^\circ$ .

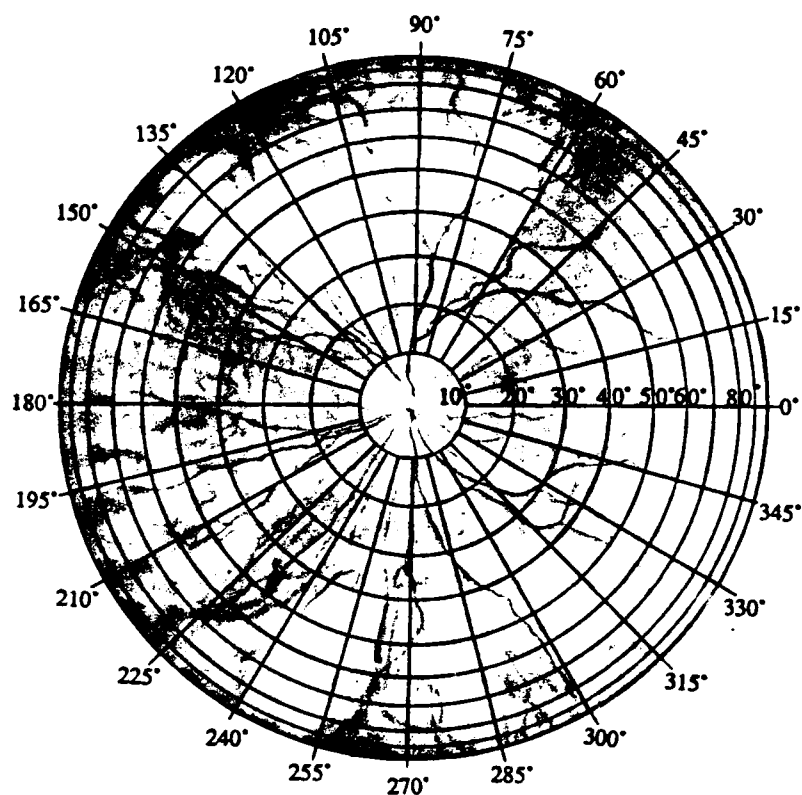


Figure 2-5 A grid superimposed on a picture of the fundus [2-15]. Locations on the retina are generally referred to by angle, not distance. The picture was taken using an Equator-plus camera [2-39]. One minute of a degree near the posterior pole is equal to approximately 5  $\mu\text{m}$ .

This is important when calculating absolute retinal image sizes in the peripheral retina.

The head and eyes are positioned, subconsciously, so that the object on which the eyes want to fixate is focused onto the fovea. Eye movements are classified into categories of several types. The first is saccadic eye movement, which is a very quick, voluntary movement that positions the eye to a target of interest in space [2-27]. These movements are ballistic, in that once they have started they are difficult to change in flight. The angular velocity and acceleration of these movements can exceed  $600^\circ/\text{sec}$  and  $40,000^\circ/\text{sec}^2$ , respectively [2-17]. Another type of eye movement is smooth pursuit, which keeps the eye on a target once it has been located. These movements include small (5-15 minutes of arc), unconscious slow drifts with quick corrective jerks. Smooth pursuit movements are required because the visual system does not have a DC response and the retinal image must continually move. The last source of eye movement to be mentioned here are small oscillations at a frequency of 50 Hz and amplitudes of only 1 minute of arc. These are considered residual noise, or the mechanical inability of the eye muscles to keep the eye completely motionless [2-2]. Aside from the eye, it is interesting to note that the head has a maximum angular velocity and acceleration of  $200^\circ/\text{sec}$  and  $10,000^\circ/\text{sec}^2$ , respectively [2-3 and 2-41]. If both head and eyes move together, the visual system's ability to acquire and track a target is admirable.

## 2.2 Tissue Optics and Damage

This section provides the background information on light interaction with tissue. Both laser and nonlaser irradiation will be discussed. A laser provides elec-

tromagnetic energy that is, within reason, collimated, monochromatic, spatially and temporally coherent, and highly radiant. That is, the energy propagates in only one direction and of only one frequency, the phase at all points on a given plane perpendicular to the beam's direction of travel will be constant, the phase of all these points will not change with time, and the laser energy can have a very high fluence, or energy density. Because of these properties, laser energy can be predicted and managed far better than electromagnetic energy which does not have these properties.

When the light interacts with tissue, the optics of the tissue dictates the light's dispersion in the tissue. Light energy incident on tissue is either reflected, absorbed, scattered, or transmitted, as shown in Figure 2-6(a). The tissue properties associated with these quantities are the reflection coefficient, absorption coefficient, scattering coefficient, and transmission coefficient. Scattering also follows a phase function (Figure 2-6(b)), which dictates the direction the light scatters. These five parameters can be used to describe light energy interacting with tissue except at boundaries. Diffuse reflections, which can be likened to scattered light at the surface, can be accounted for in the boundary conditions.

Tissues that resemble refracting structures, such as the human cornea and lens, have very high transmission coefficients and very low absorption and scattering coefficients in the visible band (i.e. it's transparent to the human eye). The refraction, reflection, and diffraction associated with these tissues can be analyzed using geometric optics.



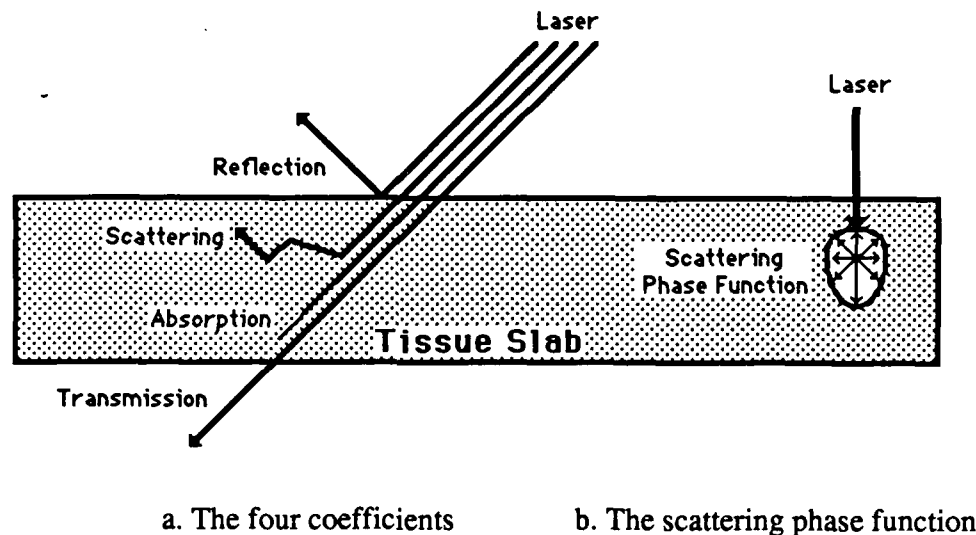


Figure 2-6 Optical Properties of Tissue

Reflection, scattering, and transmission are responsible for the light distribution in the tissue, while absorption refers to the energy that is converted from electromagnetic to thermal energy in the tissue. These five parameters have been calculated for a few tissues; if the parameters are known, the amount of input thermal energy at all points in the tissue can be calculated.

As light enters the tissue, it is usually absorbed and scattered in an exponential fashion with depth, as can be shown in a slight modification of Beer's law [2-49]:

$$E(z) = E_0 e^{-\gamma z} \quad (2-1)$$

where

$$\gamma = \kappa + \sigma$$

and

$E(z)$  : irradiance of light as a function of  $z$  ( $\text{W}/\text{cm}^2$ )

$E_0$  : irradiance of light at the surface where  $z=0$  ( $\text{W}/\text{cm}^2$ )

$\gamma$  : attenuation coefficient ( $1/\text{cm}$ )

$\kappa$  : absorption coefficient ( $1/\text{cm}$ )

$\sigma$  : scattering coefficient ( $1/\text{cm}$ )

$z$  : depth ( $\text{cm}$ )

The spatial shape of the rate of energy deposition ( $\text{W}/\text{cm}^3$ ) created by the laser irradiance ( $\text{W}/\text{cm}^2$ ) is often called the source term, since it dictates where and when the energy will be added. The source term is given by [2-49]:

$$S(r, z) = \kappa E(r, z) \quad (2-2)$$

where

$S(r, z)$  : source term or heat deposition at point  $(r, z)$  ( $\text{W}/\text{cm}^3$ )

$E(r, z)$  : irradiance of light as a function of  $r$  and  $z$  ( $\text{W}/\text{cm}^2$ )

$\kappa$  : absorption coefficient ( $1/\text{cm}$ )

$r$  and  $z$  : radial and axial distance ( $\text{cm}$ )

Generally, the next step is to define the degree of damage caused by the energy. There are three types of radiation insults in the spectral range of 400-1400 nm : mechanical, thermal, and photochemical [2-21]. Each of these will be discussed.

Mechanical damage can be divided into two categories, plasma forming and nonplasma forming. If the exposure duration is between  $10^{-9}$  to  $10^{-12}$  seconds and the applied irradiance is in the mega to terawatt per  $\text{cm}^2$ , then a plasma is formed

within the tissue with temperatures inside the plasma greater than 10,000 °C [2-31]. Generally, either Q-switched or mode-locked Nd:YAG lasers are used to create this type of disturbance. The irradiance is so high that electrons are stripped away from molecules and ions are formed. The resulting damage is caused by the ionization, the rapidly expanding plasma, and the latent stress in the tissue.

The second category of mechanical damage is associated with irradiances below that for plasma formation but above that for uniform thermal heating. The standard ophthalmological lasers (such as continuous wave Argon or low power Q-switched lasers) can cause this type of damage. In this mechanism, rapid heating generally occurs in the melanin granules. The resulting damage is caused by tissue fracture from bulk tissue displacement, acoustic wave vaporization, and electric field damage to cellular membranes [2-31]. During ophthalmic laser surgery these appear as small explosions and are the attempt to create lesions at too high a laser power in too short a period of time [2-42].

As just discussed, the first form of damage is mechanical. The second form of damage is the denaturation of protein when the tissue is subject to a temperature rise over a time period. The thermodynamic properties of tissue explain this form of damage quite well. As the light energy is absorbed, it is converted into thermal energy. The thermal energy then moves throughout the tissue by either conduction, convection, or radiation. In the fundus, conduction generally overwhelms convection and radiation. The general form of the heat conduction equation in cylindrical coordinates is [2-49]:

$$\rho c \frac{\partial T}{\partial t} = \frac{k \partial T}{\partial r^2} + \frac{k \partial T}{r \partial r} + \frac{k \partial^2 T}{\partial z^2} + S \quad (2-3)$$

where

$T(r,z,t)$  : temperature at point  $(r, z)$  at time  $t$  ( $^{\circ}\text{C}$ )

$t$  : time (s)

$k$  : thermal conductivity ( $\text{W}/\text{cm}^{\circ}\text{C}$ )

$\rho$  : density ( $\text{g}/\text{cm}^3$ )

$c$  : specific heat ( $\text{J}/\text{g}^{\circ}\text{C}$ )

$r$  and  $z$  : radial and axial distance (cm)

$S(r,z,t)$  : heat source at point  $(r, z)$  at time  $t$  ( $\text{W}/\text{cm}^3$ )

The tissue properties are the thermal conductivity, specific heat, and density. The heat source was discussed above. This assumes a cylindrical coordinate system with the light propagating down the  $z$  (axial) axis.

Once the temperature in the tissue is known at a given point and during all times, the thermal damage can be calculated. The damage integral of Henriques [2-23], using Arrhenius' reaction rate equation, suggests that the damage is dependent on the time that the tissue is elevated to some temperature. The damage integral is :

$$\Omega(r, z) = A \int_{t_i}^{t_f} \exp(-E/RT) dt \quad (2-4)$$

where

$t_{i,f}$  : initial and final time that damage is to be accessed (sec)

$r$  and  $z$  : radial and axial distance (cm)

$T$  : temperature (K)

$A$  : pre-exponential factor (1/sec)

$E$  : activation energy for the reaction (J/mol)

$R$  : universal gas constant ( $R = 8.3143$ ) (J/mol-K)

$\Omega(r, z)$  : damage integral

For a uniform, single protein media,  $\Omega=1$  corresponds to a denaturation of 63% of the molecules at the point in the tissue where the integral is computed [2-23]. Welch obtained experimental values for  $A$  and  $E$  for the fundus of the eye, which are [2-48]:

$$A = 1.3 \times 10^{99} \text{ (1/sec)}$$

$$E = 627,600 \text{ (J/mol)}$$

These numbers can vary dramatically with different tissue. Agah *et al.* [2-1] found the following values for collagen denaturization in arterial tissue:

$$A = 4.2 \times 10^{25} \text{ (1/sec)}$$

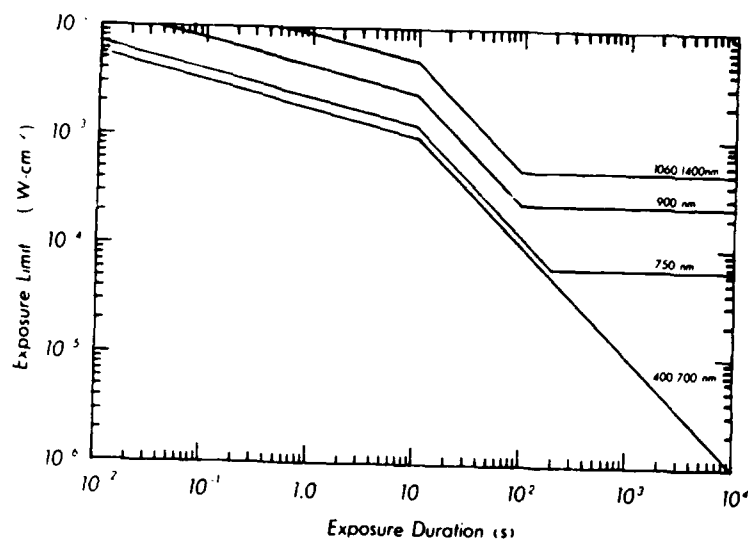
$$E = 180,000 \text{ (J/mol)}$$

These equations rely heavily on the optical and thermal properties of tissue. Unlike the constants for many materials, biological tissues tend to be much less uniform resulting in a greater variability of its constants. Absorption coefficients can

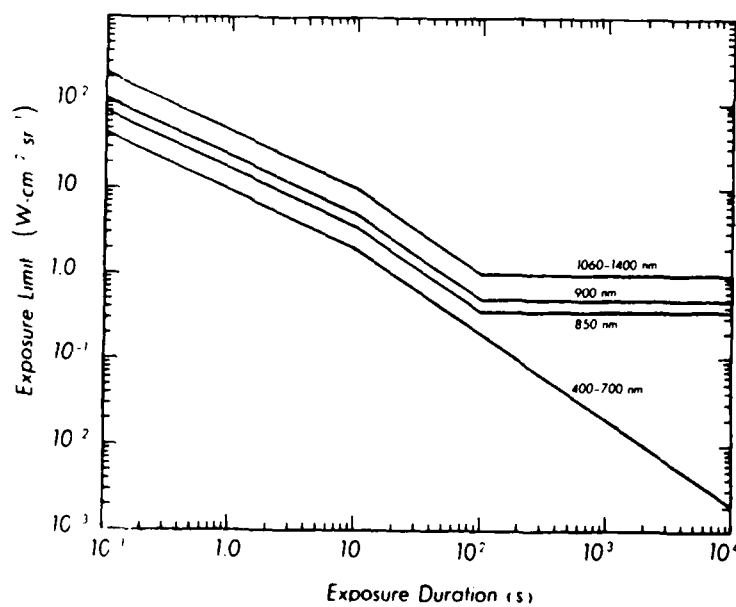
vary by a factor of 6 in the retinal pigment epithelium of the eye from person to person [2-47]. Also, a complete knowledge of the source term is required. In the irradiation of the retina with a laser, the optical parameters of the eye may also be estimates; hence the spot size of the laser may not be precisely known. Thus the predicted damage values can vary significantly from the actual damage in a clinical environment. In a controlled experimental environment where retinal image size is known, Welch and Polhamus [2-48] showed that measured temperatures and visible damage compared favorable with mathematical models.

During the late 1960's and early 1970's extensive research was performed to develop a comprehensive set of exposure limits for the eye and skin to laser irradiation [2-44]. This work culminated in the laser safety guidelines, ANSI Standard 136.1, for the eye. The graph relating irradiance to exposure duration for direct viewing of a laser is shown in Figure 2-7(a) [2-43]. As expected from the Arrhenius equation, there is a time dependency. There is also a wavelength dependency at longer exposure durations, which follows the wavelength dependency of the absorption coefficient in the retinal pigment epithelium and choroid. These guidelines are designed to provide a safety margin of 10 for protection against accidental laser exposure [2-14].

Let's take an example of how these guidelines might be applied in the use of a small HeNe laser (100  $\mu$ W) used in the eye for illumination a small area or for pointing of an invisible laser. If the diameter of the retinal image is 3.6 mm, and for this simple example assume that the laser has a uniform radiant energy over its spot size, then the irradiance is equal to:



(a)



(b)

Figure 2-7 (a) Exposure limits for viewing a direct CW laser source. (b) Exposure limits for viewing an extended source or diffuse CW laser source [2-43].

$$\frac{\text{Laser Power}}{\text{Area Laser Irradiates}} = \frac{0.0001}{\pi \left( \frac{0.36}{2} \right)^2} \approx 10^{-3} \text{ W/cm}^2 \quad (2-5)$$

From Figure 2-7(a), the maximum permissible retinal exposure would be 10 seconds.

A second graph from the ANSI standards is shown in Figure 2-7(b) [2-43]. This graph is used with extended sources, where the spot size of the irradiation directed toward the eye is larger than the pupil of the eye. This type of illumination might be a diffuse lamp. Notice the vertical axis is radiance and has the terms of  $\text{W/cm}^2\text{-sr}$ . Delori showed that the observation illumination on a Zeiss fundus camera on its highest setting exceeds the Maximum Permissible Exposure after only 3.3 minutes of exposure. He found that the Topcon fundus camera also exceeds the Maximum Permissible Exposure after only 1.7 minutes on its highest setting [2-14].

An interesting question is, "At what laser irradiance and exposure does the laser tissue damage turn from thermal damage into nonplasma mechanical damage?" The separation of the region between clinical blanching (thermal lesion) and the region of hemorrhaging (nonplasma mechanical damage) is shown in the graph in Figure 2-8. This graph was developed by examining 200 lesions in 13 chinchilla grey rabbit eyes [2-6]. Notice that as the exposure time decreases, the safety margin between a well formed thermal lesion and mechanical damage decreases. Both regions merge at an exposure time of about 10 ms, which implies that below 10 ms it is difficult to cause thermal damage without some mechanical damage and hemorrhage.



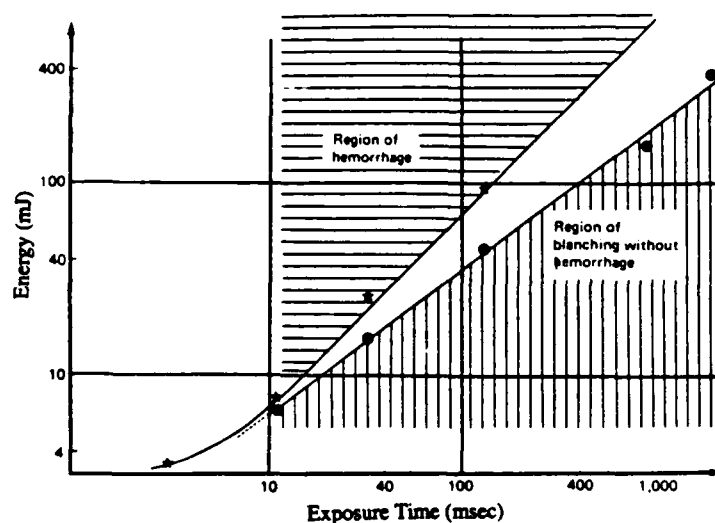


Figure 2-8 The separation of two regions; the region of clinical blanching and the region of hemorrhages, depending upon the exposure time. Both regions merge at an exposure time of about 10 ms [2-6].

Aside from the mechanical and thermal damage, a third form of damage is concerned mainly with the retina and is called an actinic effect. The damage occurs at a wavelengths around 400-550 nm and temperatures too low to cause thermal damage. The photochemical nature of this damage is unknown [2-21]. In several experiments with monkeys and rabbits, Lawwill [2-28] used a four point criteria to judge damage by actinic effects. They were indirect ophthalmoscopic examination, dark adaptation function of flash ERG (electroretinogram), light and electron microscopic examinations. Damage was of the form of a compromised retinal pigment epithelium and disrupted outer segments with an associated reduction in the ERG measurement. One of their major findings was that the damage potential at 457.9 nm is more than 10

times that at 590 nm. They also found that the potency of laser light is less than two times that of a broad-band incoherent source. When roughly comparing their data to a human undergoing observation with an old slitlamp microscope, they imply that the light supplied by this instrument is one half of the threshold for damage for a 15 minute continuous exposure.

### 2.3 Optics of the Eye

This section will first present the chromatic properties of the eye. The geometrical optics of the eye will be explained next, followed by a discussion of the minimal retinal image.

The chromatic properties of the eye vary across the visible band of light. The frequencies that the four detectors in the eye are sensitive to are shown in Figure 2-9 [2-2]. The three of concern are the blue (420 nm), the green (530 nm), and the red (560 nm). Others researchers have placed the maxima of these action spectra at 443 nm, 535 nm, and 570 nm, respectively [2-27]. These are the frequencies which enable an ophthalmologist to distinguish color features while viewing a patient's retina. It would seem logical that the three cones would define the three colors. This is not the case and there are several theories that attempt to explain why not. These will not be discussed here. But, to clarify color, Table 2-2 list each color and its approximate wavelength. Notice that the color red is actually centered around 600 nm. Thus, the red cone is more of a yellow-green cone with some sensitivity in the red band.

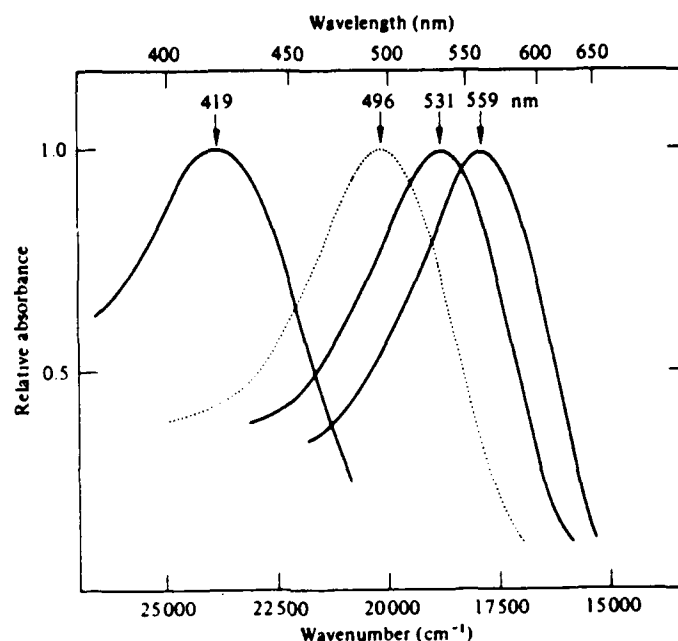


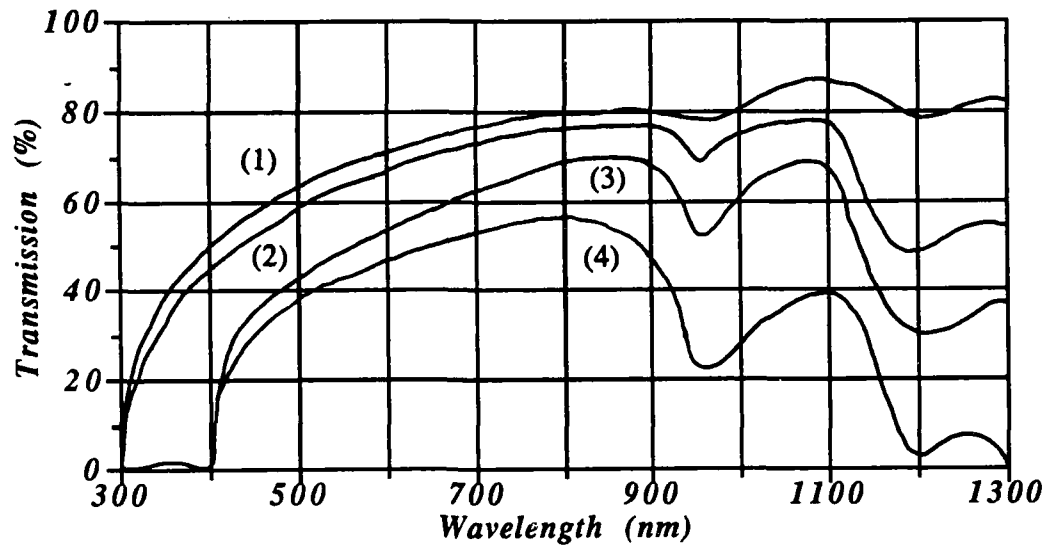
Figure 2-9 The absorbance spectra of the four photopigments of the normal human retina. The dotted line refers to the spectra of the rods. The quantity labeled relative absorbance is normalized and thus is independent of the actual concentration of cones in the eye. The sensitivity of the blue spectra (419 nm) is actually at least an order of magnitude less than the green (531 nm) and red (559) (which are about equal) [2-2].

Color	Wavelength (nm)
Violet	390-455
Blue	455-492
Green	492-577
Yellow	577-597
Orange	597-622
Red	622-780

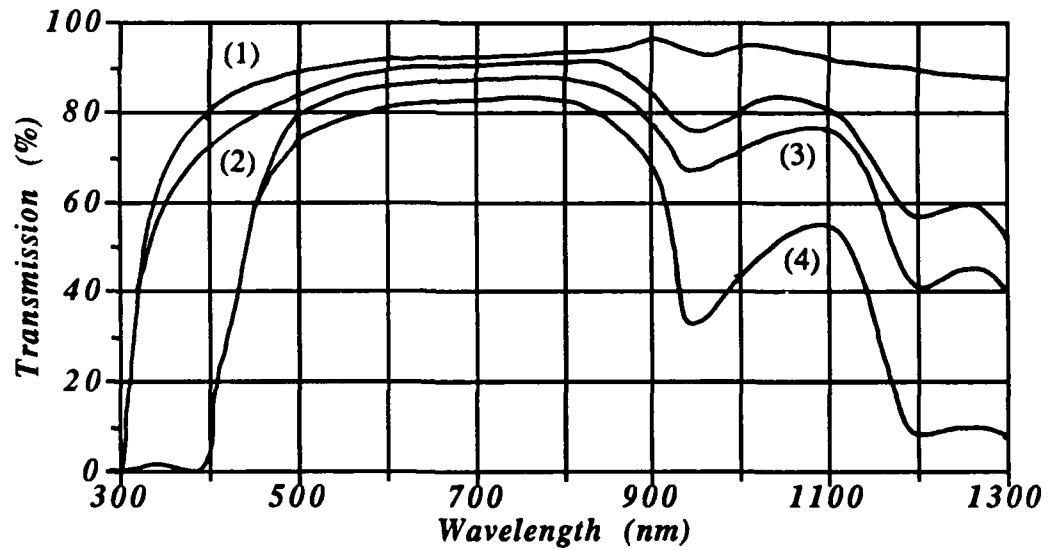
Table 2-2 Approximate vacuum wavelengths of the colors in the visible band [2-22].

Since these wavelengths must reach the retina, it's interesting to note the percent transmission of visible light through the anterior segment of the eye. The graph in Figure 2-10(a) shows the percent of direct light incident on the cornea that reaches the retina [2-7]. If forward scattering is incorporated to measure total light transmission, the percent transmission increases substantially (Figure 2-10(b) [2-7]). For the direct light calculations, Boettner measured the quantity of energy entering a detector at an acceptance angle of only  $1^\circ$ , while an acceptance angle of  $170^\circ$  was used for the total light transmission. The first graph is used to understand the amount of useful energy that is returned in a reflected image of the retina. The second graph is used to calculate the total amount of light energy reaching the fundus, such as for damage calculations.

Once the light has been transmitted to the retina, it's important to know what percent of the light is reflected back. This is shown in Figure 2-11 [2-19]. This energy is collected by the cameras to formulate images of the fundus. Since blood vessel detection is important, the attenuation coefficient for reduced hemoglobin (curve 2) and oxygenated hemoglobin (curve 3) is shown in Figure 2-12 [2-32]. The maxima for reduced hemoglobin occurs at 555 nm and the two maxima for oxygenated hemoglobin occur at 542 nm and 577 nm. The concept is to find the wavelength of the light that has a maximum reflection off the retina and maximum absorption by the blood vessels or vice versa. This produces the best contrast. From the two figures, a wavelength of about 550 nm is the best. This would allow the fundus camera to illuminate with only 550 nm light and get the best signal for the amount of input energy



(a)



(b)

Figure 2-10 Cumulative direct (a) and total (b) transmission spectra of the pre-retinal media. 1: transmission of cornea; 2: cornea + aqueous humor; 3: cornea + aqueous humor + lens; 4: cornea + aqueous humor + lens + vitreous. The curves are based on the light absorbed by the media together with losses by reflection and scattering. The curves in (a) do not include forward scattering, while the curves in (b) do include forward scattering [2-7].

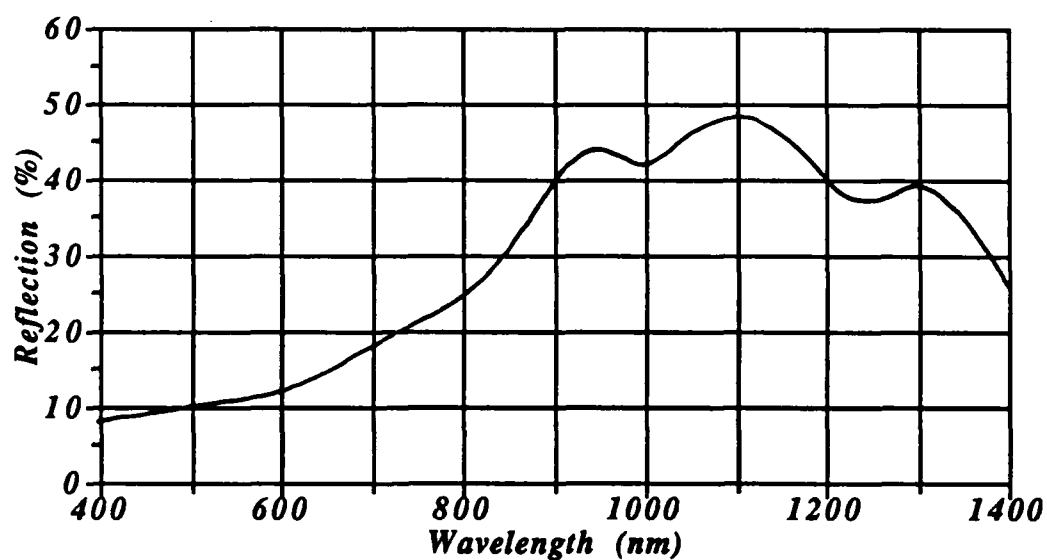


Figure 2-11 The percent reflection from the retinal pigment epithelium and choroid of a human eye [2-19].

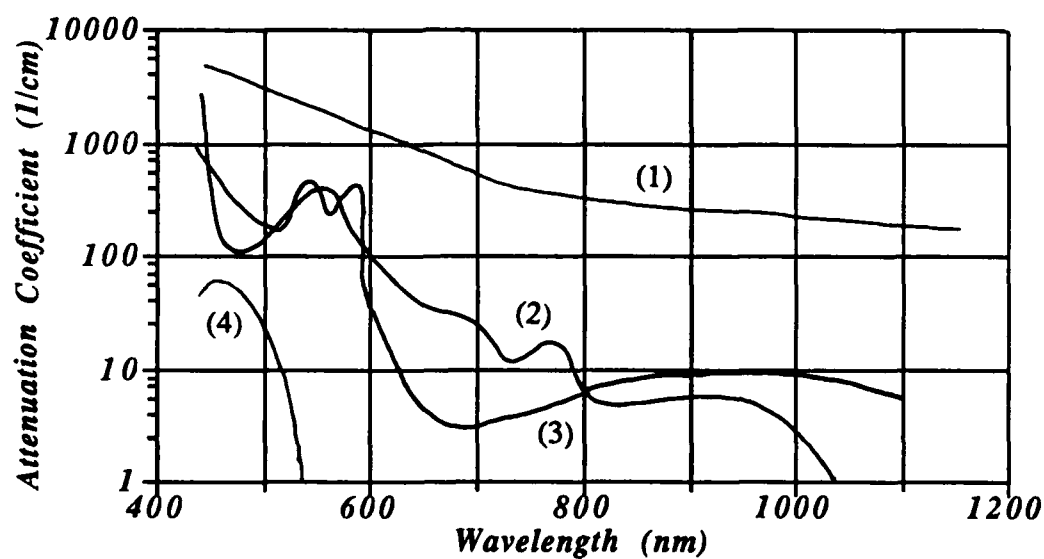


Figure 2-12 Attenuation coefficient for 1: melanin; 2: reduced hemoglobin; 3: oxygenated hemoglobin; 4: macular xanthophyll [2-32].

(which should always be kept to a minimum). This subject will be discussed more in Chapter 6, "Retinal Image Processing".

Another area where the chromatic characteristics of tissue are important is in the fundus. The two other curves in Figure 2-12 relate the attenuation coefficient for melanin (curve 1) and macular xanthophyll (curve 4), while the absorption in the human retinal pigment epithelium and choroid is shown in Figure 2-13 [2-19]. Since the melanin is the main absorber in the retinal pigment epithelium, it would seem appropriate that the melanin curve and the curve in Figure 2-13 tend to decrease with increasing wavelength. For lasers in the shorter visible wavelengths, such as Argon green at 514.5 nm, the absorption is very high and damage occurs quickly during laser surgery. The damage is centralized around the boundary of the retinal pigment epithelium and the choriocapillaris [2-32]. At longer wavelengths, such as Krypton red at 647 nm, a substantial amount of laser energy would pass through the retinal pigment epithelium and would be absorbed into deeper areas of the choroid or even transmitted through to the sclera. Curve 4 in Figure 2-12 would seem to indicate that, when irradiating the macula as opposed to nonmacular areas with an Argon green laser, there should be more damage in the inner and outer plexiform layers of the retina. Further discussions in this area will be given in Chapter 5, "Control of Lesion Size".

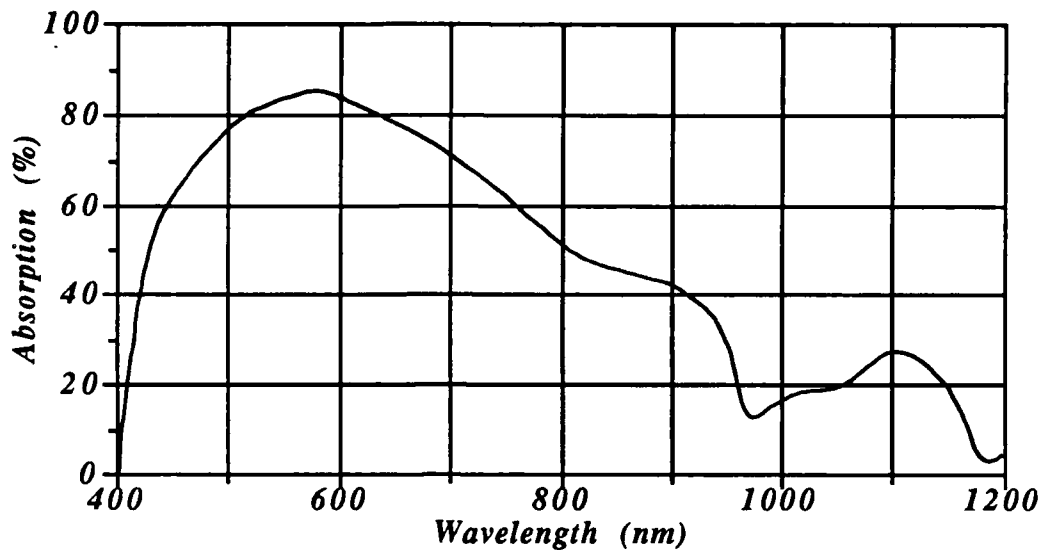


Figure 2-13 The total absorption in human retinal pigment epithelium and choroid for light incident on the cornea [2-19].

An important question in dealing with the eye is, "What is the retinal image size of a laser or an object that the eye is focused on?" An optical schematic of the eye is shown in Figure 2-13. There are four surfaces that refract light, the front and back surfaces of the cornea, and the front and back surfaces of the lens. Unlike many optics that are completely surrounded by air, the cornea is surrounded by air on its outer surface and aqueous humor on its inner surface. Because of this change in the index of refraction, the use of nodal points and principle planes are required in the optical calculations of the eye. There are six cardinal reference points of the average human eye, as shown in Figure 2-14. The six points are the anterior ( $F_a$ ) and posterior ( $F_p$ ) focal points, the two principle planes ( $H, H'$ ) or points ( $P, P'$ ), and the two



nodal points ( $N, N'$ ). All calculations can be done with these six points. For instance, to calculate the retinal image size of an object, the following equation can be used:

$$\frac{\text{Image size}}{\text{Object size}} = \frac{\text{Distance of image to } N'}{\text{Distance of object to } N} \quad (2-6)$$

If the dimensions are used from Figure 2-14, and if the object size and distance from cornea is known, the image size can be calculated as follows:

$$\text{Image size} = \frac{17 \text{ mm} * \text{Object size}}{\text{Object distance from cornea} + 17 \text{ mm}} \quad (2-7)$$

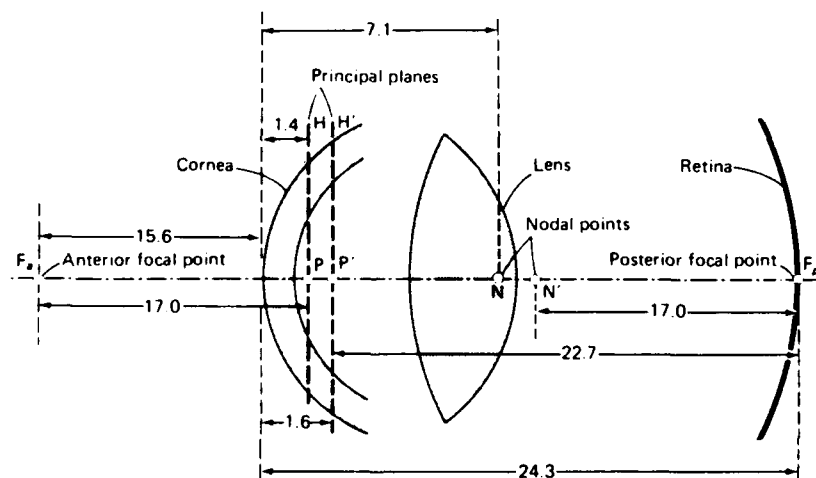


Figure 2-14 Dimensions of the six cardinal reference points of the average human eye. Dimensions are in millimeter. The six points are the anterior ( $F_a$ ) and posterior ( $F_p$ ) focal points, the two principle planes ( $H, H'$ ) or points ( $P, P'$ ), and the two nodal points ( $N, N'$ ) [2-27 and 2-37].

This equation is not applicable in the calculations of laser retinal image sizes because lasers have collimated light and always focus to a point. The standard technique for creating different spot sizes on the retina is to defocus the laser with a defocussing lens (i.e. focus the laser at a point behind or in front of the retina). Spot size calculations are a function of the power of the defocussing lens, the divergence angle of the laser, and the optics of the eye.

Four caveats should be mentioned. First, the dimensions shown in Figure 2-14 are averaged values. Obviously, from the number of individuals that wear corrective eyeglasses, the dimensions may not be accurate. Second, the eye can accommodate to focus at different distances. For a ten year old child, the accommodation can change the power of the eye by 11 D. Third, the equations are derived for vision on the optical axis of the eye. A substantial error exists in the periphery because of the nonlinear projections as shown in Figure 2-5. Fourth, these equations do not account for the many other aberrations associated with optics, such as astigmatism, chromatic aberration, spherical aberration, diffraction, and coma.

But, all is not lost. Takata [2-46] and Polhamus [2-38] have developed extensive equations that accurately predict laser retinal image sizes if all the parameters of the eye are known. Optometers measure the required correction for an eye so that the eye can focus parallel rays onto the retina when the eye is relaxed. Automatic optometers are accurate to within 0.10 D [2-13]. If the axial length of the eye is known (distance from the outer surface of the cornea to the retina along the optical axis), then an accurate retinal image size can be calculated. This distance can be measured with laser range finding or ultrasound (see Chapter 7, "Instrumentation").

One common question is, "What is the minimum retinal spot size that can be produced with a laser?". This equates to the modulation transfer function of the eye. If the laser's energy is colinear before it enters the eye, and if the laser is directed down the optical axis of the eye, the smallest spot size that can be produced with a pupil size of 2.0 mm is about 3 minutes of arc, or 15  $\mu\text{m}$  [2-11]. This measurement is the width of the base of the optical line spread function and is very close to the diffraction limits of the eye [2-11]. The line spread deteriorates to about 50  $\mu\text{m}$  at a radial angle of 30° [2-26]. At angles larger than 30° aberrations become substantial. Astigmatism can cause 10 to 15 D of error at 30° [2-10], and it increases with the square of the tangent of the oblique angle [2-29]. Some of the astigmatism can be corrected with astigmatic correction devices [2-10].

#### 2.4 Applications of Lasers in Ophthalmology

The laser's use in medicine has grown steadily in the past 20 years and is continuing to expand. Areas of applications include ophthalmology, cardiovascular, chest medicine, dermatology, gastroenterology, gynecology, neurosurgery, otolaryngology, urology and photodynamic therapy. Depending on the disease, different lasers, energy densities and burn durations are used to produce some required effect. Because the laser can reach portions of the eye noninvasively, ophthalmology was the first areas to use lasers extensively. Some of these applications follow.

Coagulation of the fundus is performed by applying heat with the laser to a small area of the fundus. The tissue denatures and forms scar tissue. When properly done, this process can have therapeutic value. For example, retinal detachment is the separating of the neural retina from the retinal pigment epithelium. This problem re-

sults from vitreous traction, retinal tear, or numerous other traumas to the eye. Vision will be lost if treatment is not provided to prevent or delimit retinal detachment. The scar tissue formed by coagulation welds the retina to the retinal pigment epithelium and prevents further separation.

Heat can also be applied to blood vessels, resulting in the coagulation of the tissue and blood. If the vessel is hemorrhaging, coagulation will seal the leak and prevent further loss of blood. Blood from a bleeding vessel in the eye may cloud the vitreous humor and obscure vision. Macular degeneration is a common disease that exhibits hemorrhaging under the retina and can be treated with photocoagulation.

Diabetic retinopathy is a serious disease exhibited by some diabetics. The blood vessels in the eye proliferate along the surface of the retina and into the vitreous cavity. This may result in retinal detachment and vessel hemorrhaging. The laser can treat both problems. This disease also produces metabolic changes within the eye, which can be treated by using panretinal photocoagulation. This technique inserts a large number of lesion into the periphery of the retina which improves the metabolic situation in the remaining central retina by destroying the ischemic peripheral retina. Generally, the desired lesion width is 500  $\mu\text{m}$  spaced approximately one-half burn widths apart. Some ophthalmologist will want 200  $\mu\text{m}$  lesion sizes posteriorly to allow for a better fit between blood vessels, while others will want a 1000  $\mu\text{m}$  lesion size anteriorly to hasten the procedure [2-45]. All areas of the retina except the macula and optic disk are irradiated. Large blood vessels are also not irradiated to avoid occluding the vessel. Approximately 1200 to 1600 burns are placed in the retina, but as many as 7500 lesions per eye have been reported [2-8]. Barr [2-4] measured the total retinal area of ten autopsy eyes and found it to be 1050  $\text{mm}^2$ . He calculated that

the maximum number of 500  $\mu\text{m}$  burns that can be used to treat the extramacular retina is 5500. These calculations assumed that the burns were continuous and overlapping, a situation that Barr [2-4] said was difficult to achieve clinically. The number of treatment sessions vary, but generally two to three sittings are used to complete the surgery.

Another serious disease is an intraocular malignant tumor. The application of heat to the tumor will slow or stop the cancerous growth in conjunction with hematoporphyrin-derivative. In lieu of treatment, enucleation of the eye is normally the result [2-12].

Lasers can also be used in the anterior segment of the eye. The pressure caused by glaucoma can be reduced by means of an iridectomy between the anterior and posterior chamber, or a perforation in the trabecular meshwork of Schlemm's canal.

This chapter has provided a basic understanding of the eye and how light interacts with the eye. Applications of lasers in ophthalmology have also been discussed.

## Chapter 3 Overview of the System

This chapter presents an overview of the most recent proposed design of a second generation robotic laser system used for ophthalmic surgery. This design is under development at the University of Texas at Austin. The first generation laser system is the slitlamp microscope with a laser delivery system, where the laser is controlled by the manual dexterity of the operator. All of the standard engineering trade-offs have been used in the development of the design, to include making it economical, feasible, user-friendly and reliable. An overview of the proposed target system will be given first, followed by a detailed explanation of the functional block diagram for the system. This section will conclude with a discussion of the advanced features of an ideal system.

### 3.1 Overview

This section presents an overview of the proposed system. The system is based on a fundus camera, not a slitlamp microscope. Since a wide image of the retina is required, a fundus camera capable of delivering a field of view of at least 50° should be used. The patient lies down on a comfortable couch as opposed to sitting on a stool, as shown in Figure 3-1. This method is used in Europe and has found some use in the USA [3-2]. The patient's head rests on the couch and is stabilized

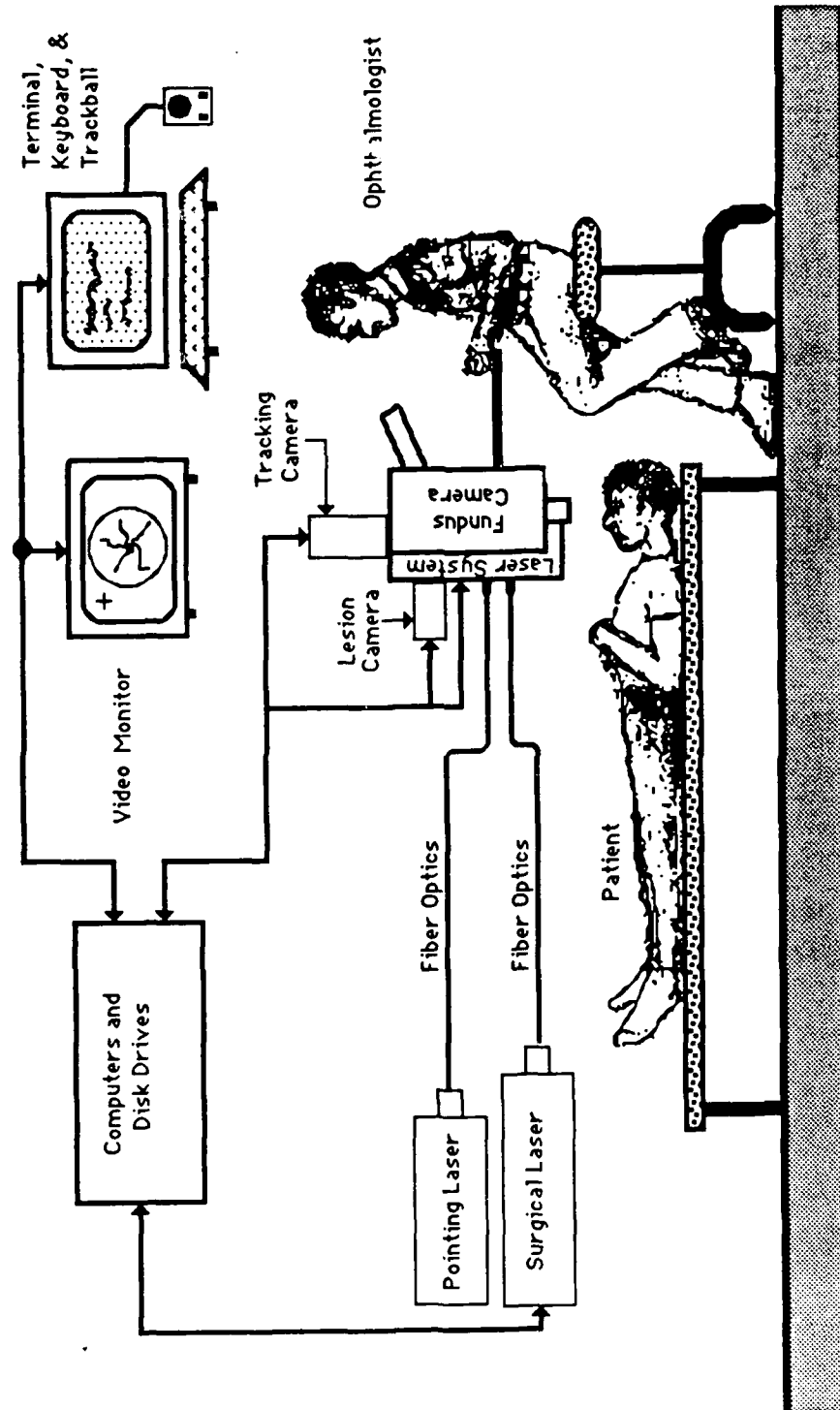


Figure 3-1 A system overview of a robotic laser used for eye surgery.

with three cushions on three sides of the head (left, right, and top). In the supine position, the head is more stable and the patient more comfortable. Retrobulbar anesthesia is not used but eye drops for pupil dilation are required. A contact lens (which is required with a slitlamp for retinal viewing) is not required for the fundus camera.

The fundus camera is moved into position. A fixating source is located in front of the fellow eye (the eye not being observed). This fixating source is actually a small plate with about 30 lights mounted in a circular pattern with only one light on at any one time. The patient focuses on this point. Fixation not only stabilizes the accommodation of the eye, but also prevents the operative eye from wandering because the operative eye and the fellow eye move conjugately. The computer can switch to any one of these lights thus enabling the computer to change the patient's eye position. *This alternate fixation strategy allows the computer a view of all areas of the retina automatically without operator assistance.*

The ophthalmologist or technician initializes the computer and then focuses the fundus camera on the pupil by physically moving the camera with a joystick. A cursor must be centered on the pupil. The camera is then focussed downward onto the retina. The operator adjusts the working distance, which is the distance from the fundus camera objective to the surface of the cornea, by sharpening the image of a bar on the bottom of the image. The system is adjusted so that the optic disk is in the center of the image when the center light of the fixating disk is lit. A tracking camera images the retina and feeds this information to a TV monitor and a computer. The computer now takes over all focussing and retinal imaging.



If this were an initial examination, a technician would perform the initial screening. If needed, a fluorescence angiogram would be done. The computer would scan the entire retina within 15 minutes and allow the patient to rest or go home. The pictures would then be processed to build a mosaic of the entire retina. The processing would also detect blood vessels, the optic disk, the fovea, and any abnormal features that the computer is capable of detecting (see Chapter 6, "Retinal Image Processing"). The results are then examined by the ophthalmologist.

If retinal surgery is needed, a second session is required. The ophthalmologist interfaces to the system with the computer screen and the TV monitor. A trackball enables the ophthalmologist to either pinpoint each spot that requires irradiation or an area that may need many burns. A magnification system enables the ophthalmologist to view any area of the retina with one of three magnification levels (50°, 30°, 10°). The computer queries the operator for lesion position, size, and depth. The ophthalmologist may modify, update, and display all lesion information. When complete, the computer begins to insert lesions in the patient's eye. The ophthalmologist may request that the lesions be placed into the retina one at a time, several at once, or all at once. This allows the ophthalmologist to observe the computer's actions and modify the placement of future lesions. A magnified view of the lesion can also be displayed on the monitor.

### 3.2 Functional Block Diagram

A functional block diagram of the proposed system is shown in Figure 3-2. The eye on the left of the figure is viewed by both the fundus camera and the laser delivery system. Presently, laser delivery systems are only interfaced with slitlamps.

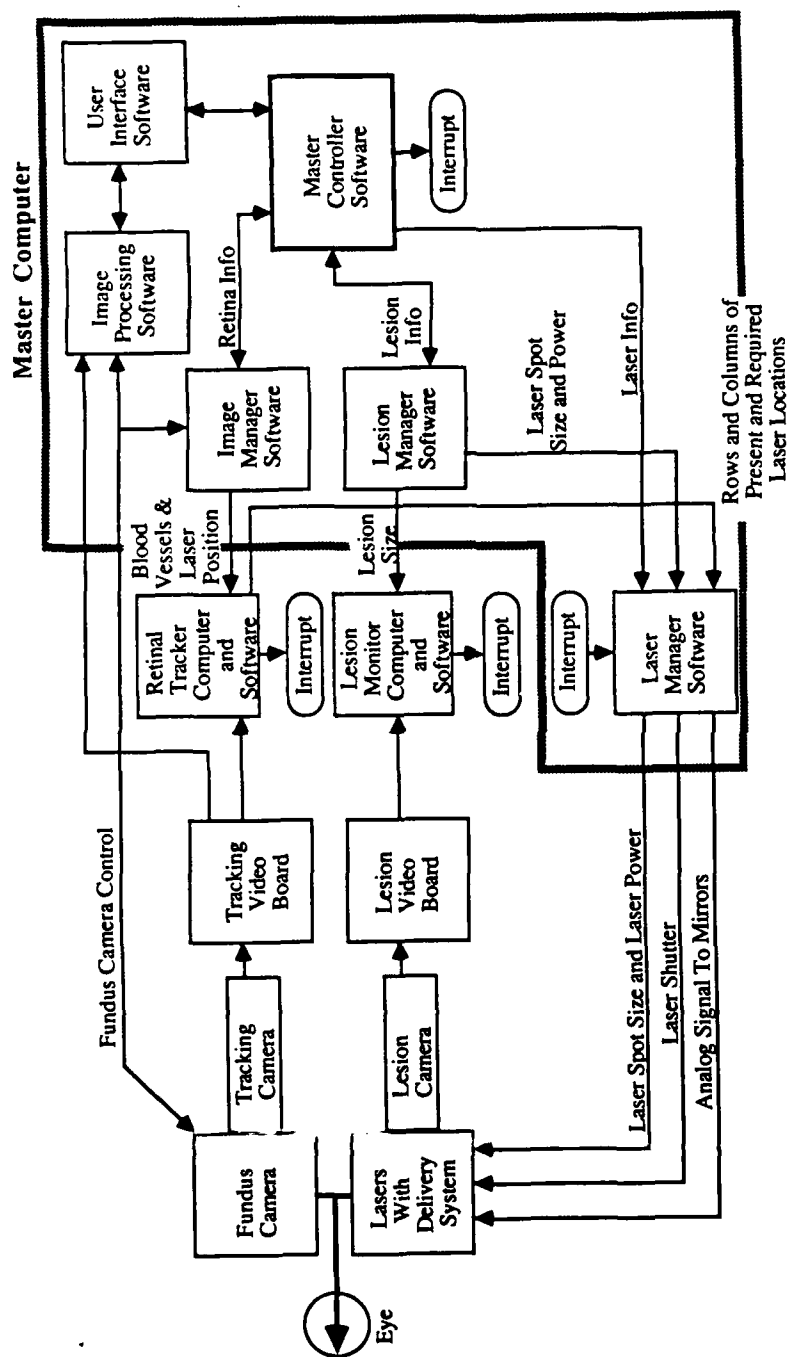


Figure 3-2 The functional block diagram of a robotic laser used for eye surgery.

A fundus camera has been chosen in the proposed design instead of a slitlamp microscope because of the superior retinal image and the wide field of view that the fundus camera produces. Excellent imaging is required if tracking is to be performed by a computer. This reason alone outweighs the disadvantages of its bulkiness, added expense, and monocular viewing.

At the present time, all retinal surgery requires the application of a contact lens. The advantages of using a contact lens are better coupling of the laser, the dampening of eye movement, and the elimination of eye blinks. The advantages of not using a contact lens are ease of operation and patient comfort. The tendency of the proposed design is to avoid the application of a contact lens if possible.

The fundus camera contains the tracking camera which views large areas ( $50^\circ$ ,  $30^\circ$ ,  $10^\circ$ ) of the fundus. The laser delivery system contains the lasers and the lesion video camera, which are coaligned and view the same small area (about  $1^\circ$ ). Sophisticated optics must be built to integrate all these systems.

The tracking camera views the retina through the fundus camera using just the field illumination. This image is passed to a video digitizing board (Tracking Video Board in Figure 3-2) in the computer and then is displayed on the video monitor. The Retinal Tracker Software has real time access to this digitized data through dual port memory, which is formatted as 512 by 512 pixels with 256 gray levels running at 30 frames per second in the standard RS-170 interlaced format.

The position of the pointing laser and the surgical laser are controlled by the Laser Delivery System via the Laser Manager Software. The operator controls the laser with the joystick. The User Interface Software accepts this input and passes these to the Laser Manager Software, which adjusts the lasers accordingly. The lesion

camera, formatted as 32 by 32 pixels with 256 gray levels running at 420 frames per second, monitors the same area as the lasers. The output of this lesion camera is fed to another video digitizing board (Lesion Video Board in Figure 3-2) in the computer, where the data is monitored in real time by the Lesion Monitor Software to measure the lesion growth.

There will be at least three computers within the system. The tracking computer performs the retinal tracking, the lesion computer performs the lesion monitoring, and the master computer acts as the boss and absorbs all other tasks.

The tracking computer runs just the Retinal Tracker Software. Its job is to take the initial blood vessel and required laser position information from the master computer, track the retina as it moves, and update the laser delivery software with updated coordinates. If a loss of lock occurs, it must interrupt the master signifying a loss of lock.

The lesion computer runs just the Lesion Monitoring Software. The lesion computer's job is to take the desired size of the lesion from the master computer, monitor the growth of the lesion, and interrupt the master when the lesion reaches the desired size. This computer also contains the interval timer which monitors the total time the laser has been on. If the laser has been on for too long a duration for a particular size lesion, the lesion computer will interrupt the master computer whether or not the lesion is at the right size.

The master computer handles the user interface, performs the image, lesion, and laser management, and absorbs all other miscellaneous tasks. The User Interface Software involves showing the right image to the operator, controlling the trackball, and interrupting the system if the operator wants the laser turned off immediately.

The Image Processing Software performs the image analysis of the retina, detects all blood vessels and other abnormalities, and builds the data base of all the images and blood vessels from all the areas of the retina. This package also builds the lesion data base. The position of lesions are derived either from the ophthalmologist with the trackball or through computer calculations. The Image Managing Software's task is to keep the correct image in view and feed the Retinal Tracking Software the proper coordinates. The Lesion Manager Software maintains the data base of all the lesions, to include size and position. The Laser Manager Software controls the laser. It contains the interrupt service routine that closes the laser's shutter when an interrupt occurs.

### **3.3 Advanced Features**

This section will describe advanced features that could be added to the system once a prototype has been tested.

A prime addition to the system might be the use of acousto-optical cells to perform the fine image matching operation [3-1]. The cells correlate the analog data directly from the video camera, bypassing the digitizing process and computers. These devices could greatly improve the spatial accuracy and time response of the tracking system and reduce tracking errors.

For the system to automatically view any area of the retina, the computer must be able to maneuver and focus the camera. As the patient moves his/her eye, the camera has to be slightly repositioned to realign the system with the pupil (moving the entire head is also an alternative). The camera movement will require 3 dimensions of translational movement and two dimensions of tilting movement (with respect to the patient's optical axis). The alignment is minimized by pivoting the cam-

era around the pupil. Motorizing the system will also aid the operator in maneuvering the bulky camera. Focussing might be performed automatically by either using infrared detectors or edge detection in the retinal image.

The computer could perform the initial alignment of the patient with the camera. The patient's head must always be positioned within the three cushions. Starting with the fundus camera about 50 cm above the patient, the computer can peer through the fundus camera with the video camera and locate the outline of the head and neck, then the eyes, and then the pupils. The fundus camera will then be centered over the pupil of the operative eye at the working distance of the camera. Ultrasound (similar to what is used in the new 35 mm autofocus cameras) could be used for accurate distance measurements. The camera then focuses onto the retina.

The laser's power, spot size, and shutter must be controlled by the computer. If the computer is to control the absolute spot size of the laser, it must know the absolute size of the features on the retina. Using an optometer to measure eye correction and laser range finding or ultrasound to measure the axial length of the eye, the computer can then make these calculations.

The field illumination of the retina might also be controlled by the computer. Control of the intensity of the field lamp and feedback with a light meter will help the computer allow minimal yet sufficient field illumination to view the fundus. The light can also be interrupted when not needed.

The Zeiss fundus camera has an astigmatism control to correct the astigmatism error encountered during viewing of the periphery. This device has been shown to considerably sharpen pictures of the peripheral retina. The computer could manage these two controls (angle and magnitude) to sharpen the images.

Another advanced feature is the idea of applying this system to laser surgery on the anterior portion of the eye. A robotic system would be especially adept in doing radial keratotomy.

Complete retina analysis systems have just recently surfaced and appear to be very popular and beneficial. These systems also include permanent laser disk storage systems for file archival. Since the computer can view all areas of the retina automatically, computer generated mosaics would be a logical next step.

Since most clinics could not afford to buy this laser delivery system and another fundus camera for retinal photography, this system must perform all the functions of a normal fundus camera. This might include a 35 mm camera (most fundus cameras have this), a Polaroid camera (many fundus cameras have this), stereo viewing (Zeiss has a little flip mirror so that two pictures can be taken with different orientations), binocular viewfinder (Kowa systems have this option), ID and date stamping (most have this option), fluorescein angiography filters (all cameras have this), and blink detection systems (similar to the CR4-45NM Canon system).

A power line monitor would be required in a system where the computer has control over a laser in the eye. Any power fault must result in the immediate closure of the shutter. One last feature could be a talking fundus camera, which allows the operator to hear the critical parameters without monitoring the displays. This is not an original idea; the Canon CF-60U already has such system.

## Chapter 4 The Retinal Tracker

This chapter will discuss the retinal tracker. The retinal tracker's responsibilities are to track the retina and the laser's position, and then provide the laser delivery system with the present and required laser position's coordinates. The tracker must also interrupt the Master Controller if it loses track of the retina.

Two critical parameters in the design of the tracker are its expense and complexity. With an unlimited budget, trackers are already available for this task. Even so, these trackers are quite sophisticated and would present a problem in realistically manufacturing these devices for common use in an ophthalmologist's offices. Because the target cost for the entire robotic system is \$200K, the tracker's cost must be minimized. Since the system already uses a personal computer, a video digitizing board, a video camera, and a fundus camera to view the retina, it would be very advantageous to also use these to track the retina. The goal for the research in this area is to show the extent that tracking can be performed using only this equipment.

Background data on past and present retinal trackers will be presented first. The theory of registration will then be discussed followed by a proposed method to track the retina. The results of the tracking routine will then be shown. Finally, the strength and weaknesses of the tracker will be listed.



#### 4.1 Background

One of the first applications of a video camera to track the retina was discussed by Carl Berkley at the Workshop on Television Ophthalmology in 1965 [4-27]. He mentioned that the retinal image could be held steady by fixing on a portion of the retinal image and deriving a feedback signal. Kelly and Crane analyzed the fundus tracker problem in 1968 [4-18]. They proposed using a circular scanning technique instead of the normal X-Y scanning technique. They showed how picture registration could be performed with just a single scan around the optic disc (one complete circle). The signal to noise ratio required for this scheme was a problem that they never fully addressed. They never built a complete fundus tracker because the means to accomplish registration in real time was not available.

Crane continued this work with Cornsweet and Steele [4-7, 4-8 and 4-9], and designed a three-dimensional eyetracker. This device uses two purkinje-images (the reflected images from the surfaces of the cornea and lens) to track the anterior part of the eye. Timberlake and Crane [4-31] used this device to develop a stabilized laser for photocoagulation of the retina. Once the laser is positioned by the operator, this system monitors small movements of the anterior surface of the eye and adjusts two mirrors such that the laser remains aimed at one location on the retina. This device has an accuracy of one minute of arc [4-32] and has a time response of 1 millisecond [4-10]. This system has been shown to track the retina quite well in a controlled, experimental setting [4-28]. It is not ideal for the proposed system discussed in this dissertation for several reasons. The tracker just by itself (without the laser delivery system) cost \$60,000. It is optically quite complicated and would present a problem in realistically manufacturing and maintaining these devices for common use in an

ophthalmologist's offices. It also does not provide an image of the retina which is required for laser positioning by the computer.

Other systems are available that track the anterior segment of the eye using either infrared detectors reflecting off the limbus [4-5] or a video camera viewing the pupil [4-17]. Because the eye's movement includes some translation (it is not strictly rotational), tracking the anterior part of the eye does not necessarily track the posterior part of the eye [4-1 and 4-26].

The picture registration problem is being extensively researched [4-2, 4-3, 4-4, 4-6, 4-11, 4-12, 4-14, 4-15, 4-19, 4-20, 4-22, 4-23, 4-29, 4-30, 4-33 and 4-34]. Real time registration at video rates is a problem of wide interest. Some companies claim to have developed extremely fast systems that register pictures at video rates if the contrast between target and background is greater than 40% [4-16]. Other researchers are developing less expensive hardware to aid the microprocessor in its number crunching [4-13 and 4-21]. These systems will most likely lead to an inexpensive, commercial product that could be used in the robotic laser project discussed in this dissertation.

## **4.2 The Theory of Matching**

Picture registration, otherwise known as matching, is the alignment of similar images in two or more pictures. The two pictures are generally misregistered by rotation, scaling, and translation. Other problems, such as nonlinear distortions, often exist. When computer time is abundant, the pictures can eventually be registered, usually with an excellent success rate. But if the matching must be performed in a limited time, such as during a real time task, the registration task becomes difficult if

not impossible. Many methods are available to either decrease the error rate or decrease the computation time. Even though the proposed algorithm only matches translation, a discussion of rotation and scaling will be included since the proposed algorithm can be extended to incorporate these dimensions.

#### 4.2.1 Definitions

Picture registration, in its simplest form, is comparable to overlaying two transparencies of the same picture such that similar images coincide. Registration and matching have the same meaning. It's important to note that matching must include the use of a reference picture. The reference picture is the source of most (if not all) the information required for the matching. This process can also be considered as a transformation of a point in one coordinate space to a point in another coordinate space. Generally, a subset of the reference picture (called a window or a template) is compared against all positions in the picture to be matched. The position that yields the closest similarity between the window and picture is the proposed match.

Picture matching can be performed using optics, analog computers, or digital computers. This chapter will only discuss registration on a digital computer since this is the manner that most registration is performed today. Before the registration begins, the pictures will be filtered, sampled and digitized. The pictures will then be in the form of a two dimensional array of pixels (picture elements), each pixel represented by a digital word, each word being 8 bits long. The magnitude of these words correspond to the gray level, or intensity, at a particular point in the picture.

Misregistration of two images can take many forms. The three most common problems are rotation, scaling, and translation, often called RST mismatch. Rotation

is the angular twisting of one picture with respect to the other. Scaling is the magnification of one picture with respect to the other. Scaling and magnification have the same meaning. Translation is the displacement of the two pictures in the horizontal and/or vertical directions.

This discussion is mainly concerned with RST mismatches. Registration of pictures with these problems are somewhat manageable. However, more complicated problems occur frequently. For example, images may be fuzzy because of defocussing, or distorted because of different camera views. Significant distortion exist in retinal views near the eye's equator, where the aberrations of the lens and cornea create severe distortions. Luckily, the distortions in this particular case are repeatable.

The registration system can be characterized by its probability of error and its computation time. The error will be:

$$\text{Probability of Error} = \frac{\text{number of incorrect matches}}{\text{total matches attempted}} \quad (4-1)$$

The criteria for the registration system used in the proposed design discussed in this dissertation is to minimize the probability of error while minimizing computation time. Generally, decreasing the probability of error will result in an increase in computation time, and vice versa. This trade-off is application dependent and becomes critical in a real time task. In the particular task of tracking the retina for the proposed design, there is not sufficient computer time to ensure a zero probability of error. But, what's more important than a zero probability of error is the guarantee that the tracker knows when it has lost track. The laser can then be shut down without incident.

### 4.2.2 Mathematical Foundations

This section will give an overview of the mathematics required for an understanding of the matching algorithms. A detailed discussion is provided in the references [4-24 and 4-25].

The following definitions [4-6] for window, search area, and subimage will be used in this chapter. An array  $S$ , the search area, will be the picture to be matched (Figure 4-1). This will be an  $L \times L$  array with each element in the array representing a pixel, and each pixel will have  $K$  gray levels, i.e.

$$\begin{aligned} 0 \leq S(i, j) \leq K-1 \\ 1 \leq i, j \leq L \end{aligned} \quad (4-2)$$

Often  $L$  will equal 512 and  $K$  will equal 256.

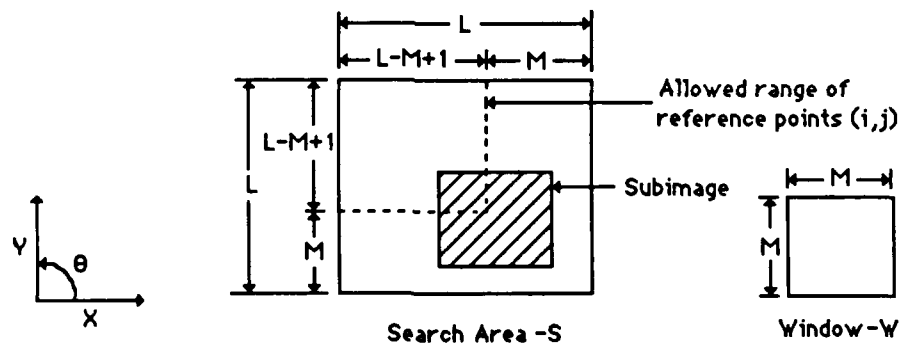


Figure 4-1 Search Space [4-6].

A second  $M \times M$  array,  $W$ , is the window. The window is always smaller than the search area ( $M < L$ ) and is a subset of the reference picture. Remember that the reference picture and the search area are two distinct pictures. Identifying the size and position of the window will be discussed at a later time. The window has the same gray levels as the search area; i.e.,

$$\begin{aligned} 0 \leq W(l, m) \leq K-1 \\ 1 \leq l, m \leq M \end{aligned} \quad (4-3)$$

A notation for  $M \times M$  subimages is:

$$\begin{aligned} S_M^{i,j}(l, m) &= S(i+l-1, j+m-1) \\ \text{where } 1 \leq l, m \leq M \\ 1 \leq i, j &\leq L - M + 1 \end{aligned} \quad (4-4)$$

Each subimage is referenced by its upper left corner coordinates  $(i, j)$ . Thus,  $S_M^{i,j}(l, m)$  is a subimage in the search area that the window is positioned over.

There are many methods for comparing the degree of match or mismatch between two pictures. Three common techniques are shown in Table 4-1. The absolute value of the difference is similar to the squared error except the squared operation has been replaced by the absolute value, which is easier to perform on the computer. The comparison of the subimages that results in the smallest  $D(i, j)$  is the best match. The cross correlation with the largest  $R(i, j)$  is the best match. The correlation process

Table 4-1 Similarity Equations

1. Absolute value of the difference

$$D(i,j) = \sum_{l=1}^M \sum_{m=1}^M |W(l,m) - S_M^{i,j}(l,m)| \quad (4-5)$$

2. Cross-correlation

$$R(i,j) = \sum_{l=1}^M \sum_{m=1}^M W(l,m) S_M^{i,j}(l,m) \quad (4-6)$$

3. Correlation Coefficient

$$\rho(i,j) = \frac{\left( M^2 \sum_{l=1}^M \sum_{m=1}^M W(l,m) S_M^{i,j}(l,m) \right) - \left( \sum_{l=1}^M \sum_{m=1}^M W(l,m) \right) \left( \sum_{l=1}^M \sum_{m=1}^M S_M^{i,j}(l,m) \right)}{\sqrt{\left( \left( M^2 \sum_{l=1}^M \sum_{m=1}^M W(l,m)^2 \right) - \left( \sum_{l=1}^M \sum_{m=1}^M W(l,m) \right)^2 \right) \left( \left( M^2 \sum_{l=1}^M \sum_{m=1}^M S_M^{i,j}(l,m)^2 \right) - \left( \sum_{l=1}^M \sum_{m=1}^M S_M^{i,j}(l,m) \right)^2 \right)}} \quad (4-7)$$

where  $1 \leq i, j \leq L - M + 1$

can also be done using Fast Fourier Transform techniques, which reduces the computer's calculation time [4-3]. The correlation coefficient is a computationally extensive algorithm but produces very good results. The correlation coefficient  $\rho(i,j)$  will vary from -1 to +1, with -1 representing a negative correlation, 0 representing no correlation, and +1 representing the best correlation.

The images can also be preprocessed before the similarity routine is applied, which will either decrease the total computation time or the probability of error. Two of these pre-processors are the binary reduction routine and the gradient routine.

In the binary reduction routine, each pixel of  $W(l, m)$  and  $S_M^{i,j}(l, m)$  can only take on a value of 1 or 0 determined by thresholding each pixel by the median (or average) of the image. This is often called a black and white picture. The multiplication or addition in the similarity measures then becomes a simple exclusive-nor function as shown in Table 4-2. When a pixel in the window  $W(l,m)$  agrees with a pixel in the reference picture  $S_M^{i,j}(l, m)$ , the output will be a "1"; otherwise the output is "0".

$W(l,m)$	$S_M^{i,j}(l, m)$	$W(l,m) \ominus S_M^{i,j}(l, m)$
0	0	1
0	1	0
1	0	0
1	1	1

Table 4-2 Exclusive-Nor Truth Table

The gradient is a popular method of preprocessing and emphasizes the edges in the image. The equation is



$$|\nabla S_M(i,j)| = \sqrt{(S_M(i+1,j) - S_M(i-1,j))^2 + (S_M(i,j+1) - S_M(i,j-1))^2} \quad (4-8)$$

These similarity and preprocessing routines can be combined to register two images. It is extremely difficult to theoretically predict which equations will do the best job with the minimal amount of computation time. The algorithm to perform registration will be discussed next along with some experimental results by Svedlow comparing the different methods.

#### 4.2.3 Matching Algorithm

The algorithm for an RST correlation is as follows. For the translation correlation, the window must be shifted in the X and Y direction, performing a correlation at each shifted position. Care must be exercised to keep the window inside the search area. For rotation, the window will be rotated by some angle  $\emptyset$  before the comparison. For scale, the window will be expanded or shrunk by some M before the comparison. For rotation and scale, the window will have to be extrapolated between pixel points (resampled) such that the window's pixels directly overlay the pixels of the picture to be matched. To find the angle  $\emptyset$  that produces the best match, many guesses must be tried. Accordingly, to find the best magnification M that produces the best match, many guesses for M must be tried. Notice that  $\emptyset$  could be any angle between  $0^\circ$  and  $360^\circ$ , and M could be less than, equal to, or greater than one. The range and resolution of these guesses is difficult to estimate and application dependent.

Assume the picture size is 500 x 500 and the window size is 50 x 50. For a comparison such as translation, there will be  $(500 - 50 + 1)^2 \approx 200,000$  subimages to match the window against. This assumes the translation resolution is no smaller than the distance between two pixels and the window always fully overlaps the picture. If the rotation is constrained to  $\pm 30^\circ$  with the desired resolution of  $0.5^\circ$ , then 120 angles must be attempted. If the scale can vary from 0.7 to 1.3 with a resolution of 0.01, then 60 magnification factors must be attempted. Thus, there will have to be  $60 \times 120 \times (500 - 50 + 1)^2$  comparisons, with each of these comparing  $50^2$  sets of pixels. This is equal to about 3.66 trillion sets of pixels. Probably most of the rotations and magnifications will require resampling. Obviously, each degree of freedom complicates the algorithm by orders of magnitude.

If only translation is considered, some interesting questions are "What is the best similarity measure?", "What is the best preprocessing algorithm?", and "How long would it take to execute on a personal computer?". Svedlow [4-30] used each of the above described algorithms on LANDSAT images. His results are presented in Table 4-3. The percent of acceptable registration is shown for each of the combinations of preprocessing and similarity measure. The number in parenthesis shows the time (each unit equals 200 milliseconds) that a 80286 microprocessor would require to accomplish one comparison of a window (50 x 50) against its subimage using the selected method. For a 500 x 500 image, 450 x 450 comparisons must be made. Thus, for the best method, which is the correlation coefficient with a preprocessing operation of the magnitude of gradient, it would take a 80286 microprocessor about 175 minutes to accomplish the full correlation (translation only). Even the quickest method takes about 7 minutes.

SIMILARITY OPERATION	PREPROCESSING OPERATION			
	Original Imagery	Magnitude of Gradient	Threshold at Median	Threshold the Magnitude of Gradient
Correlation Coefficient	90% (16)	100% (26)	65% (10)	90% (20)
Correlation Function	38% (5)	74% (15)	55% (5)	87% (15)
Sum of Absolute Value of Differences	69% (1)	92% (11)	62% (5)	87% (15)

Table 4-3 Percent of acceptable registration attempts using satellite photos of farming land. The number in parentheses shows the normalized computer time to accomplish one comparison of the registration using a 50 by 50 pixel window. One time unit equals approximately 200 ms [4-30].

Obviously, these routines are time consuming and do not lend themselves to real time applications. The next portion of this chapter will discuss other methods to register two images, especially aimed at reducing the computation time.

#### 4.2.4 Edge Detection

Andrus, Campbell, and Jayroe [4-2] discuss a routine called binary boundary maps. Using an algorithm similar to a combination of the gradient routine and the binary reduction algorithm, the picture and window are compressed into a black and white picture with the "1" 's showing up at boundaries and "0" 's everywhere else. An

example of what a binary boundary map might look like for the retina with its associated blood vessels is shown in Figure 4-2.

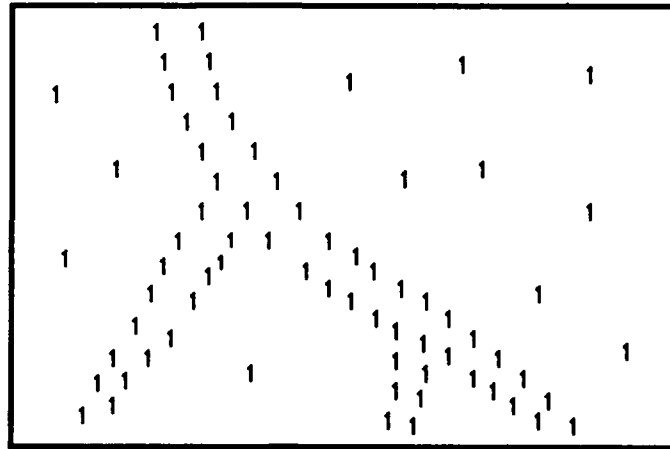


Figure 4-2 Binary boundary map.

Notice that the boundary of the blood vessel is outlined. The data can be further reduced by only considering the linked set of "1" 's (the "1" 's that adjoin one another). These would represent a true boundary. It is suggested that miscellaneous points that do not occur along a continuous line can be discarded. These points would not represent a boundary. Comparisons are then made by only comparing the boundaries of the window with the boundaries of the picture to be matched. The matching routine searches out the positions of the "1" 's in the window (which can be calculated prior to the matching loop), and then looks for "1" 's at the corresponding location in the picture to be matched. The comparison with the most corresponding "1" 's is the projected match. The routine can be extended to search for corresponding "0" 's in both the window and the picture.

The Andrus, *et al.* [4-2] believe that their routine works better than others when the boundaries of the pictures to be matched remain unchanged but the intensities or colors have changed. For example, this type of problem is seen in pictures of the earth during crop rotation and changes of season, when the boundaries of the fields have not changed but their color has. From this discussion, it appears that using edges is a powerful technique in image registration. As a matter of fact, it could be argued that all the information in an image is derived from a combination of edges.

#### 4.2.5 Clustering

Clustering is often called "symbolic" matching, referring to the matching of segments as opposed to the matching of points. There are two concepts that lead to understanding of this method. First, windows do not have to be constrained to a block of pixels. *If an aircraft is to be located in a picture, then an airplane shaped window* might be more appropriate. This would exclude extraneous background data that would only hinder the match. Second, windows need not include every pixel within its boundaries. This concept was introduced in binary boundary maps, where only the "1" 's were matched.

Stockman, Kopstein, and Benett [4-29] discuss this technique for RST transformation. They propose a complicated scheme that joins (or vectors) one prominent landmark in the window to another (done by humans, not by machines). The algorithm then attempts to match these patterns or clusters to the picture to be matched. An example is the detection of two airplanes on the ground. The airplanes might have a background of white concrete, green grass, or a combination of both; this would obscure edge detection. Using clustering, the prominent points on the aircraft will be

vectored together. The tip of the nose, the tips of the wings, and the tips of the horizontal stabilizer could be vectored between planes and vectored together on each plane. The registration system then attempts to look for these patterns in the picture to be matched. The authors augment their analytic work with excellent examples. This technique, depending on the application, could be quicker (fewer pixels in the window) and more accurate (eliminate miscellaneous data in the window). The problem is locating the window, which most likely requires human intervention.

#### 4.2.6 Spring-Loaded Matching

When the picture to be matched is stretched or warped, spring-loaded matching can be employed. This technique is discussed in numerous references [4-11, 4-12 and 4-22]. Two or more windows are located in the registration picture. The separation (or distance) between each window is calculated. These windows are then connected together using "springs". This "elastic harness" is then used as a stretchable window to perform the matching. The amount of stretch or compression of each spring is monitored. The calculations for the comparisons are complicated. These calculations find the optimum match using the degree of match in each window with its respective subimage and the degree of stretch or compression in each spring.

An example will illustrate how a human face can be located in a picture. For simplicity, assume the human's face is looking directly at the camera. The prominent features of the face are the hair, two eyes, nose, mouth, left side of face, and right side of face. Since humans differ substantially, a single window might not work. If seven windows are used, one for each feature of the face, and they are connected with nine springs as shown in Figure 4-3, then the elastic harness is ready for use. The obvious

difficulty that the algorithm will have is working with seven windows and nine springs.

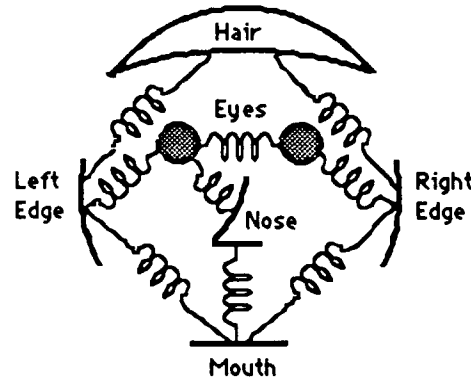


Figure 4-3 Schematic representation of the face with components and their linkages [4-12].

A similar method called "Rubber-Mask" is discussed by Widrow [4-34]. This method employs a rubber window, where, once a match is established, the window is slightly stretched to fine tune the match. Excellent examples, especially with chromosomes, are presented in the references.

#### 4.2.7 Two-Stage and Coarse-Fine Window Matching

Two interesting approaches to windowing is the two-stage window matching and a coarse-fine window matching, both by Rosenfeld and Vanderbrug [4-23 and 4-33]. For the first method, a small subwindow is compared against all positions of the picture to be matched. For all comparisons that result in a value below some threshold (i.e. indicates that there might be a match), the full size window is then used

to repeat that particular comparison. Only these repeated full size window comparisons are used to determine the projected match. Thus only a small number of comparisons are required with the larger window.

A similar system is used for their second method. The window and the picture to be matched are divided into a grid system. An average value is found for each block in the grid, and these averaged values are used for coarse (reduced resolution) comparisons. Those comparisons that result in values below a threshold are repeated using the original window (full resolution window).

The above two approaches use Equation 4-5, the absolute value of the difference, as the indicator for the degree of similarity between the picture to be matched and the window. Goshtasby, Gage, and Bartholic [4-15] have used a similar approach for two stage window matching, except they use Equation 4-6, the correlation method, as the similarity measure. They analytically derive a method to calculate the threshold value for the smaller window and provide experimental data to support their calculations.

#### 4.2.8 Growth Curves

This speedup technique uses the rather clever idea of terminating the comparison process of a subimage if it appears that the pixels that have been compared show excessive mismatch. For example, assume that the absolute value of the difference (Equation 4-5) is used as the comparison process. A plot can be made of the summation, starting with the first pixel to be matched and continuing to the last pixel to be matched. The curve will monotonically grow as a function of the mismatch between the window and the picture. If the difference is great (the pictures do not match), the



growth will be quicker than if the difference is small (the pictures might match). This plot is called the cumulative mismatch curve or a growth curve. An example of three curves is shown in Figure 4-4. The curve with the slowest rise per pixel is showing the best match (plot C). An example of a criteria for a mismatch might be the exceeding of a threshold before 35 pixels have been compared.

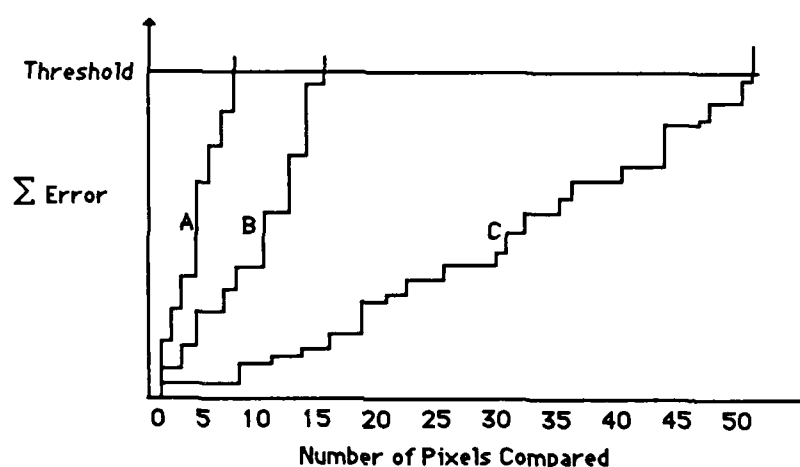


Figure 4-4 Growth Curves for three comparisons [4-6 and 4-19]

Once a comparison exceeds the threshold, the matching terminates immediately, thus saving computation time. This matching position is also declared a mismatch. Only those comparisons not exceeding threshold are sorted to find the proposed match. Calculating the threshold value is difficult and very application dependent. Reference [4-6] provides suggestions for calculating this threshold.

An unwanted side effect of this method is the introduction of a stochastic execution time. Because the termination of computation is determined from the image,

some images might require more computer time while others might require less computer time. In real time matching where the routine must be done by a certain time, the expected computation time and the available time for computation must be carefully managed.

#### 4.2.9 Search Area

A frequent matching application is the real time registration of a frame by frame sequence of pictures of a slightly changing scene. All matching techniques mentioned above can be used, but the time to match must be less than the time between successive images. An important consideration is the distance the tracked object is capable of moving from one frame to the next. Depending on the spatial and temporal resolution, the maximum distance an object can move between frames might be limited. Thus, once the window has been matched to the picture, the successive searches only need to be made a limited distance from the previous match.

An example of a retina tracker will illustrate this technique. As mentioned in Chapter 2, "Anatomy and Light Interaction of the Eye - Anatomy of the Eye", the eyeball can move up to 600°/sec and the approximate posterior nodal distance is 16.7 mm. Since the arc length is just the radius multiplied by the angle in radians, the surface of the retina can move approximately

$$2 \pi \left( \frac{600^\circ/\text{sec}}{360^\circ} \right) (16.7 \text{ mm}) \approx 175 \frac{\text{mm}}{\text{sec}} \quad (4-9)$$

If the temporal sampling is the standard video rate of 60 fields per second (every 0.017 sec), a point on the retina will move

$$\left(175 \frac{\text{mm}}{\text{sec}}\right) \left(0.017 \frac{\text{sec}}{\text{field}}\right) = 3 \frac{\text{mm}}{\text{field}} \quad (4-10)$$

If a 256 x 256 pixel sensor is imaging a 12.8 x 12.8 mm area, the spatial resolution is approximately

$$12.8 \text{ mm} / 256 \text{ pixels} = 0.05 \frac{\text{mm}}{\text{pixel}} \quad (4-11)$$

The number of pixels the image on the retina will move in one frame is thus

$$3 \frac{\text{mm}}{\text{field}} / 0.05 \frac{\text{mm}}{\text{pixel}} = 60 \frac{\text{pixels}}{\text{field}} \quad (4-12)$$

Once the tracker has locked onto the blood vessel, subsequent matches need only search 60 pixels in all directions. For a window size of 50 x 50 pixels and a picture size of 256 x 256 pixels, this reduces the search time by one-eleventh.

The circular window can be further reduced by using an ellipse instead of a circle for the window shape because the eye tends to move more left and right than up and down.

Now that a background has been established, the next section will proceed to develop the best tracking algorithm for the proposed system.

### 4.3 The Registration of Retinal Images

The general theory can extend only so far before the application dependent images have to be examined. This section will first examine the retinal tracking task. Next, the makeup of the template that is used to identify the location of a blood vessel cross sections will be explained. It will be shown how the computer develops this template from a preliminary reference image of the retina. Once this template has been developed, the computer then examines the sequence of moving images, where it must locate the exact position that corresponds to the prechosen template. The template validation will then be discussed, followed by an explanation of the search area, the expansion, and finally the user interface. The section following this one will provide the results of the actual tracking. The routine described will be limited to matching just translation since the eye does not seem to rotate significantly.

#### 4.3.1 The Retinal Tracking Task

In the retinal tracking case, the images to be matched are those of the retina. These pictures are imaged at a rate of 60 frames per second with a spatial resolution of 512 x 256 pixels (the image size and frame rate is dictated by the standard RS-170 specification: see Chapter 7, "Instrumentation - General Specifications" for an explanation of the RS-170 specification). In most all clear images of the retina, blood vessels are predominate. Two 29 x 16 pixel digitized subimages of the retina are shown in Figures 4-5 and 4-6. These subimages depict a blood vessel and a bifurcation of a blood vessel. These images behave well under the similarity routines shown in Table 4-1. A cross correlation using the absolute value of the difference of one row with all

	Columns															
	1	2	3	4	5	6	7	8	9	10	11	12	13	14	15	16
1	161	159	159	159	159	162	162	164	164	160	152	139	137	141	144	152
2	166	165	165	160	163	165	163	162	159	154	151	145	143	147	159	153
3	168	168	167	165	160	159	160	159	157	154	147	143	143	146	153	154
4	168	171	168	168	165	163	162	156	149	148	139	137	144	151	170	172
5	166	167	170	166	164	165	159	156	151	144	144	142	143	151	159	163
6	170	169	169	166	163	166	159	154	150	146	145	148	155	165	168	168
7	167	167	168	166	166	167	164	160	152	147	144	142	144	153	157	159
8	167	168	170	166	167	163	156	149	141	137	140	149	151	168	167	163
9	167	167	167	165	166	166	162	159	149	147	147	147	153	159	163	168
10	169	167	163	161	159	159	159	151	151	149	148	148	150	154	157	157
11	174	174	172	167	164	163	159	159	145	145	145	150	155	161	164	164
12	169	168	164	164	165	162	156	143	135	138	146	155	159	158	154	154
13	169	169	168	168	168	163	154	145	141	141	147	159	166	168	166	163
14	168	165	165	166	163	162	154	143	140	142	143	151	155	155	156	159
15	168	168	165	165	163	163	151	146	141	142	146	157	161	164	164	162
16	173	173	172	170	168	163	161	141	137	137	141	146	149	151	152	158
17	169	167	163	161	159	159	158	154	152	151	145	150	150	157	159	161
18	171	170	168	163	162	159	153	146	143	148	152	154	154	155	154	156
19	162	165	164	161	153	143	141	141	143	150	151	166	162	165	163	163
20	168	169	167	163	164	162	155	143	139	143	152	163	167	166	163	160
21	164	166	166	160	152	141	138	136	136	140	147	157	165	166	164	165
22	156	156	157	157	155	152	149	144	141	144	151	155	160	160	160	160
23	158	158	160	161	157	151	144	139	142	145	153	162	161	162	161	160
24	163	162	162	161	158	158	153	150	150	151	155	157	159	162	163	161
25	163	163	163	163	161	154	146	142	142	145	150	155	161	162	159	159
26	165	162	160	157	155	150	145	145	141	145	151	154	159	161	161	159
27	168	168	164	160	152	148	144	143	144	141	155	159	159	159	158	157
28	162	163	161	156	145	140	140	142	149	152	149	149	153	157	157	156
29	166	166	166	160	149	137	135	137	147	155	163	160	159	160	159	159

Figure 4-5 Subimage of a 512 x 512 image of the retina depicting a blood vessel (Bold numbers below 150).

		Columns															
		1	2	3	4	5	6	7	8	9	10	11	12	13	14	15	16
Rows	1	31	133	134	138	143	143	143	145	145	143	144	141	137	138	138	138
	2	26	129	135	141	149	149	148	150	148	147	148	148	149	150	150	152
	3	36	137	140	141	141	141	141	141	141	141	139	138	140	140	143	142
	4	33	132	132	136	140	142	145	145	145	150	148	149	147	147	151	149
	5	35	132	135	138	138	141	143	142	143	143	143	146	144	145	148	145
	6	29	130	135	141	143	143	143	143	144	142	146	150	152	152	150	149
	7	135	134	136	136	136	138	140	141	143	142	144	144	142	144	144	146
	8	32	132	132	134	136	137	141	142	142	145	143	143	144	144	145	147
	9	135	133	133	135	140	142	142	141	138	137	140	140	145	146	148	150
	10	141	138	132	128	127	129	134	137	142	142	145	146	146	149	149	146
	11	147	142	137	137	137	142	147	143	137	137	137	141	143	145	151	151
	12	152	145	135	129	132	132	137	136	146	143	146	146	145	145	147	147
	13	149	144	138	135	131	130	133	137	140	140	140	143	143	142	145	144
	14	155	151	144	138	133	133	134	136	137	137	140	144	147	147	149	149
	15	154	148	142	134	130	131	131	131	135	136	139	143	143	147	147	145
	16	155	150	137	130	125	124	125	127	132	135	135	137	138	138	142	147
	17	152	149	145	137	134	131	131	132	132	132	135	138	137	135	141	142
	18	155	152	146	139	136	131	129	129	129	135	135	135	134	134	137	136
	19	151	150	145	143	139	136	136	132	131	131	131	131	131	133	134	137
	20	159	155	147	125	126	126	124	121	121	121	124	128	131	134	140	141
	21	162	159	148	137	126	122	124	123	123	123	126	128	132	136	138	143
	22	157	153	147	135	134	126	126	128	130	133	136	137	138	140	145	152
	23	162	159	156	146	131	124	123	123	124	132	139	143	145	144	147	151
	24	166	163	159	150	140	132	128	128	128	131	136	140	143	146	147	152
	25	159	156	151	140	132	127	126	126	129	135	141	146	146	149	154	151
	26	165	163	160	151	134	118	114	118	124	139	151	159	159	154	155	154
	27	161	157	155	152	146	139	136	136	137	147	155	158	156	157	157	155
	28	165	164	160	152	135	124	124	127	135	148	159	159	155	154	154	154
	29	159	156	153	149	145	140	137	136	136	146	153	160	162	164	166	162

Figure 4-6 Subimage of a 512 x 512 image of the retina depicting a blood vessel bifurcation (Bold numbers below 140).

other rows in the image of a 512 x 512 picture is presented in Figure 4-7. It is clear that the row matched with itself is the best match (row 250) and the other rows become more uncorrelated as the row moves away from that point. Since this similarity routine and others are computationally exorbitant, they cannot be used in the real time tracker of the proposed design without added hardware. If hardware were available at a reasonable cost, such as a vector processing board or an optical correlator, the above type of correlation would be quite satisfactory. The following algorithm uses only a personal computer and video digitizing board. The software is burdened with the task of monitoring the 7.8 Mbytes of data per second to keep track of certain distinguishing landmarks (i.e. blood vessels).

#### 4.3.2 The Blood Vessel Template

This subsection will discuss the template and the building of the template from the reference picture. Since there exist excellent edges (blood vessels) in most images of the retina, it would seem prudent to examine the detection of blood vessels using edge detection algorithms. The template suggested by a binary boundary map is still too computational extensive for a small personal computer. But clustering brings forth the idea of using a template to detect the two edges of a blood vessel.

The template used in this routine is shown in Figure 4-8. The large box is the window as defined in "Mathematical Foundations" above. Two smaller subwindows, or subtemplates, exist inside the larger window. Filter width corresponds to the width of a preselected blood vessel in a reference picture (see "Building the Template" below). One template is used to identify a horizontal blood vessel and the other is used to identify a vertical blood vessel. Each of the small shadowed boxes within

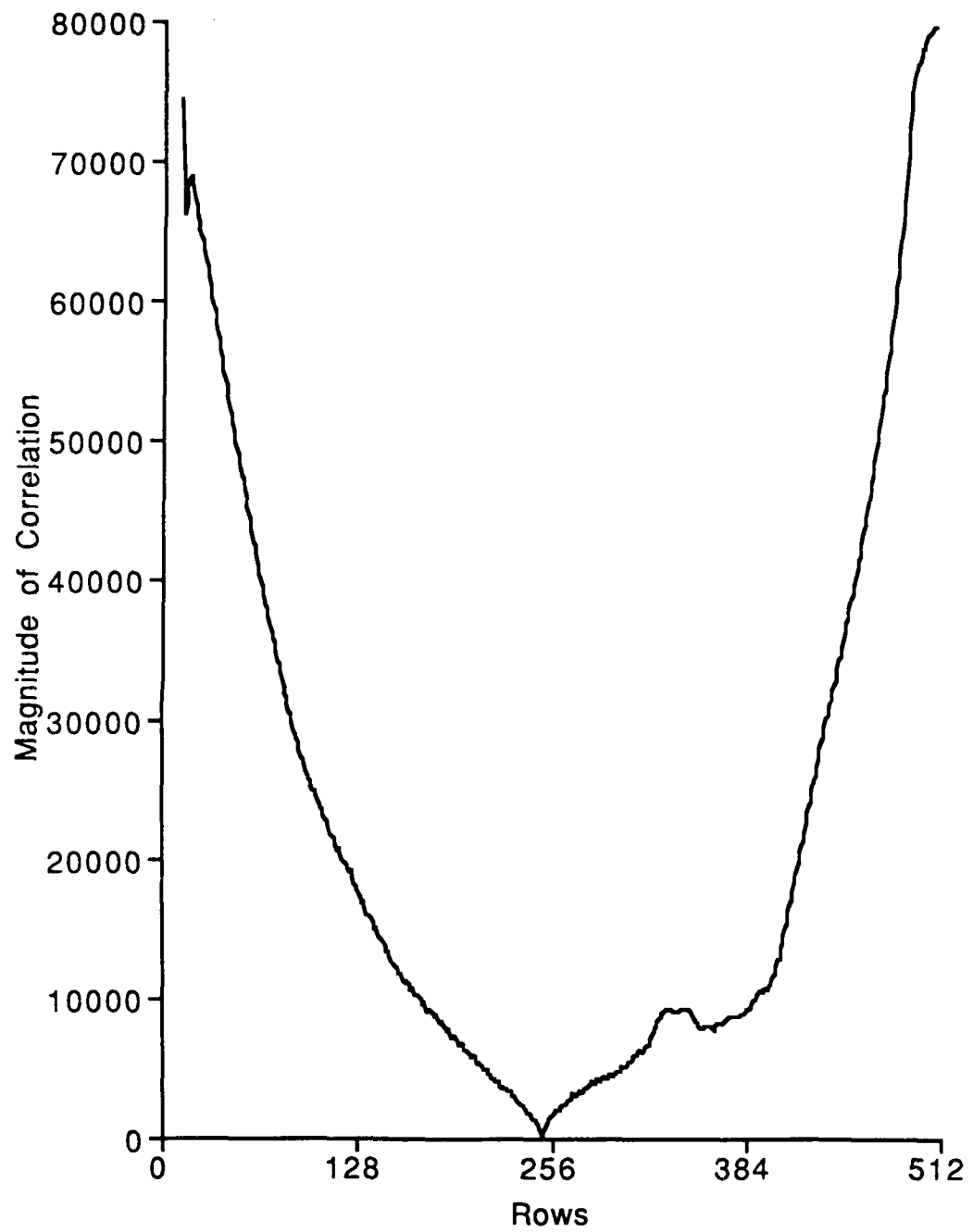


Figure 4-7 Correlation of row 250 with all other rows using the absolute value of the difference similarity measure.



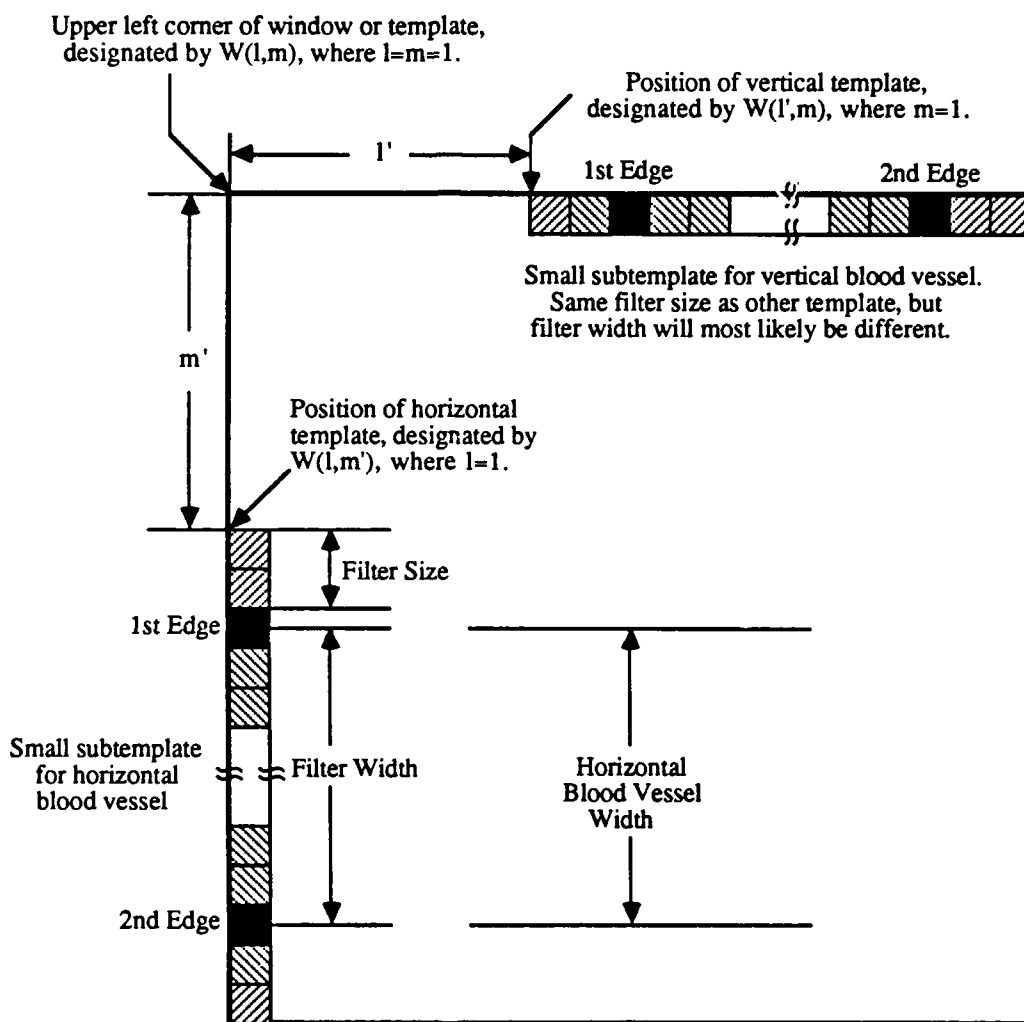


Figure 4-8 The window which contains two templates used to identify two blood vessels, one vertical and one horizontal. Each small shadowed box represents a pixel.

these subtemplates are pixels. The black boxes are also pixels and would correspond to an edge of a blood vessel. To understand how the template identifies a blood vessel refer to Figure 4-9. The array is a subset of an image, with each number specifying a gray level at that pixel. In the standard notation, this image would be designated  $S_M^{i,j}(l,m)$ , where  $i, j$  would be the coordinates in the image over which a window would be positioned. A blood vessel can be distinguished by the bold-faced numbers. The box centered over the blood vessel would correspond to the top right subtemplate in Figure 4-8. The other subtemplate is not shown. To identify the blood vessel, the first edge (refer to Figure 4-8) is detected by first adding the value of the two pixels from the interior of the blood vessel near the edge, which are 138 and 136 in Figure 4-9. Next, the two pixels from the outside of the blood vessel near the first edge are added together, which are 160 and 152 in Figure 4-9. The first sum is then subtracted from the second sum. If an edge exists down the center (the edge would be located at the pixel whose value is 143 in Figure 4-9 and would be the black box in Figure 4-8), then the calculations will result in a large number. The second edge is detected likewise, by adding 136 and 140, and subtracting this from the sum of 157 and 165. The magnitude of the blood vessel's correlation is the combination of the two sides. If a blood vessel's two edges line up with the template (the two edges fall under the two pixels represented by black boxes), then the correlation will be a large number. Anything else will result in a smaller number. Thus for this algorithm, large numbers represent the best fits. The filter size of the template is the number of pixels used per blood vessel divided by four and the width of the template is the inner distance from edge to edge (Figure 4-8). More will be said about the filter size later. The width of the filter corresponds to the width of the preselected blood vessel. If a thicker or

	Columns															
	1	2	3	4	5	6	7	8	9	10	11	12	13	14	15	16
1	161	159	159	159	159	162	162	164	164	160	152	139	137	141	144	152
2	166	165	165	160	163	165	163	162	159	154	151	145	143	147	149	153
3	168	168	167	165	160	159	160	159	157	154	147	143	143	146	153	154
4	168	171	168	168	165	163	162	156	149	145	139	137	144	156	170	172
5	166	167	170	166	164	165	159	156	151	144	144	142	143	151	159	163
6	170	169	169	166	163	166	159	154	150	146	145	148	155	165	168	168
7	167	167	168	166	166	167	164	160	152	147	144	142	144	153	157	159
8	167	168	170	166	167	163	156	149	141	137	140	149	161	168	167	163
9	167	167	167	165	166	166	162	159	149	147	147	147	153	159	163	168
10	169	167	163	161	159	159	159	154	151	149	148	148	150	154	157	157
11	174	174	172	167	164	163	159	149	145	145	145	150	155	161	164	164
12	169	168	164	164	165	162	156	143	135	138	146	155	159	158	154	154
13	169	169	168	168	168	163	154	145	141	141	147	159	166	168	166	163
14	168	165	165	166	163	162	154	143	140	142	143	151	155	155	156	159
15	168	168	165	165	163	163	159	146	141	142	146	157	161	164	164	162
16	173	173	172	170	168	163	151	141	137	137	141	146	149	151	152	158
17	169	167	163	161	159	159	158	154	152	151	149	150	150	157	159	161
18	171	170	168	163	162	159	153	146	143	148	152	154	154	155	154	156
19	162	165	164	161	153	143	141	141	143	150	161	166	162	165	163	163
20	168	169	167	163	164	162	155	143	139	143	152	163	167	166	163	160
21	164	166	166	160	152	143	138	136	136	140	147	157	165	166	164	165
22	156	156	157	157	155	152	149	144	141	144	151	155	160	160	160	160
23	158	158	160	161	157	151	144	139	142	145	153	162	161	162	161	160
24	163	162	162	161	158	158	153	150	150	151	155	157	159	162	163	161
25	163	163	163	163	161	154	146	142	142	145	150	155	161	162	159	159
26	165	162	160	157	155	150	145	145	141	145	151	154	159	161	161	159
27	168	168	164	160	152	148	144	143	144	148	155	159	159	159	158	157
28	162	163	161	156	145	140	140	142	149	152	149	149	153	157	157	156
29	166	166	166	160	149	137	135	137	147	155	163	160	159	160	159	159

Figure 4-9 Subimage of a 512 x 512 image of the retina depicting the blood vessel template used to identify a blood vessel.

thinner vessel is tested, the left template would produce a large number but the value of the right template would be small. In Figure 4-9, the filter size is two and the width is five.

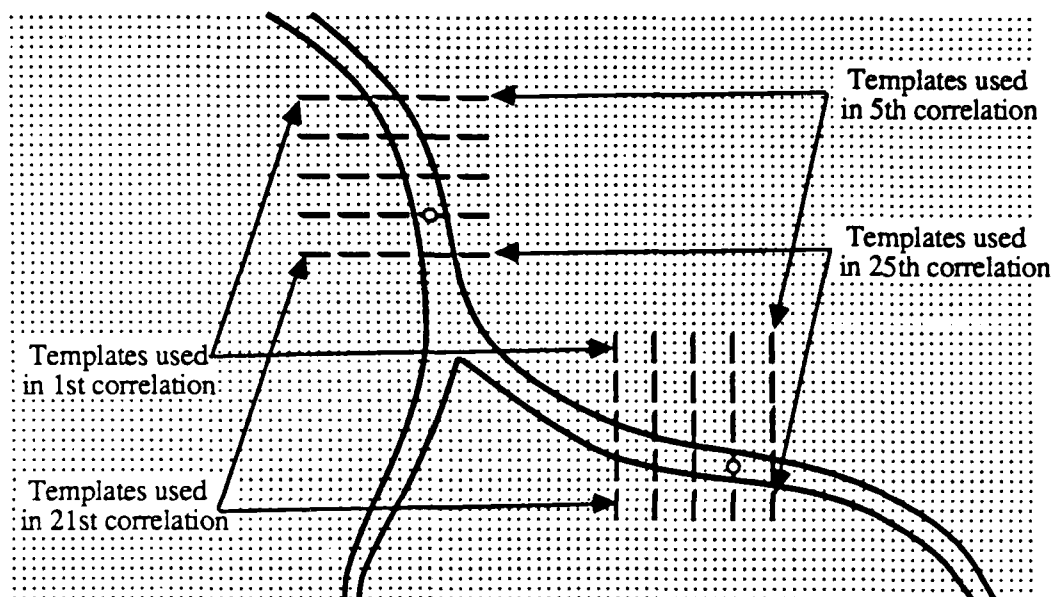
If the actual location of the vessel is not known, then the template is shifted around. (As will be discussed shortly, the locations of the vessels were known at some previous time: the template must be built somehow.) When the template is located directly over the two edges of the blood vessel, the correlation will be at a maximum and thus pinpoint the location of the blood vessel. Obviously, this template will yield a fairly good correlation along the entire length of the vessel. Thus one template will only fix one dimension. The matrix in Figure 4-10 shows the template values calculated at different shifted positions for the template in Figure 4-9. The position of the template in Figure 4-9 is given as the left most pixel. Thus, row 21 and column 4 correspond to the template's position as shown in Figure 4-9. The template value of -33 in row 13 and column 1 in Figure 4-10 corresponds to the template shifted 3 left and 8 up. Notice the high numbers in Figure 4-10 along the contour of the blood vessel, from bottom left to top right.

Using a "spring-loaded matching" idea, two (or more) templates are used at fixed distances, one (or more) for a horizontal blood vessel and one (or more) for a vertical blood vessel. The template is shifted to different positions, and a correlation (total correlation is the combination of the first template's correlation added to the second template's correlation) is calculated at each position. A correlation array is generated, where the position of the maximum number in the array will correspond to the best match. This is the position where the two templates overlay their respective blood vessels.

	1	2	3	4	5	6	7
13	-33	-5	36	80	91	63	15
14	-27	-7	26	56	67	51	21
15	-31	-10	24	58	76	64	25
16	-32	0	37	67	75	56	29
17	2	0	0	5	19	31	32
18	-5	18	36	43	41	31	1
19	22	62	84	67	28	-8	-31
20	-25	7	46	77	79	49	-4
21	13	50	77	84	67	31	30
22	-16	8	34	49	47	30	3
23	-10	25	60	71	52	16	-17
24	-4	6	24	31	31	23	5
25	-11	18	47	65	59	29	-5
26	6	23	41	49	43	35	1
27	24	48	59	51	28	3	-19
28	45	58	44	20	3	-5	-8
29	53	92	93	74	3	-34	-47

Figure 4-10 Shifted template values that correspond to the template in Figure 4-9. The template position is given as the left most pixel. The template shown in Figure 4-9 is located at row 21, column 4.

The shifting of a template with two subtemplates, represented by a horizontal line for the vertical blood vessel template and a vertical line for the horizontal blood vessel template, is depicted in Figure 4-11. The template is shifted in a 5 x 5 pattern. Notice that the shifting distance is not restricted to one pixel separation; in this example, the template is positioned over every fourth pixel. This is called the expansion. The search area would be defined as the total area over which the search is being performed, and would be 20 x 20 pixels in Figure 4-11. The size of the correlation array is still 5 x 5. In Figure 4-11, the position corresponding to the template



### Legend

- A pixel
- | Edge template for a horizontal blood vessel (will be longer than shown).
- Edge template for a vertical blood vessel (will be longer than shown).
- ⊕ The best match considering both horizontal and vertical templates.

Figure 4-11 The area searched by two templates in a 5 x 5 search pattern. In the first correlation, the two templates are positioned in the top left corner of each matrix. The routine then performs a correlation at each position in the matrix, from left to right, top to bottom. The last known location of the blood vessel was at the center of the matrix. In this example, the blood vessel shifted one row down and one column to the right. The 19th correlation would produce the best match.

would be one row down and one column to the right from the center of the search area. The next search area will then be centered around this point.

#### 4.3.3 Building the Template

This routine assumes that the image of the retina is available before the tracking starts (the same image that will be tracked) and there is sufficient time that the image can then be exhaustively searched for the best template. The routine searches the inner area of the picture (the inside 412 x 412 pixels of a 512 x 512 array) for the best edges. Each pixel location in each row is checked for the existence of the first edge of a vertical blood vessel. The same type of subtemplate as explained above is used to identify the blood vessels. If an edge exists at a particular pixel location (that is if the template exceeds some threshold), then all widths from 2 to 9 are checked for the sister edge. If the best of these sister edges exceed some threshold, then that blood vessel (defined by its location, width, and magnitude of the correlation) is inserted into an ordered table. After each row and each pixel location is exhaustively checked, the best vertical blood vessels will reside on the top of the ordered table. Next, the horizontal blood vessels are found by examining every pixel location in every column. Another ordered table is generated to identify the best horizontal blood vessels.

The entire search for all the vessels takes about 30 seconds. The best locations are shown on the monitor, one at a time, to the operator. The operator chooses those blood vessels to be used for the tracking. This routine also insures that the best locations are at least 10 rows or columns apart, so that all the best locations will not

be from a small area. Once the two (or more) subtemplates are chosen, the computer formulates the large template which is used in the real time tracking algorithm.

#### 4.3.4 Template Validation

An interesting and necessary question is, "How good is the template idea?". The table in Figure 4-12 depicts the correlation values at different shifted positions (correlation array). That is, the template for the blood vessels is centered at row and column equal to (0, 0). At this center point, the template should show a maximum since the template is directly located over the blood vessels that it is designed to find. The template is then shifted a row and a column in all directions, and the correlation is calculated for each position. Each entry in the table designates a shifted position and its corresponding magnitude of the template correlation at that point. As expected, the magnitude of the correlation drops off as the template is shifted away from its ideal location. Actually, a 60 x 60 pixel search area was used, but only the center 21 x 15 pixels is shown in the table. The top 10 intensities for the larger area are listed along with the largest intensity not located near the real point. This intensity represents the largest possible false positive, especially if it exceeds the correlation of the proper match. Most of these false positives reside outside the 21 x 15 array (somewhere else in the 60 x 60 array) shown in Figure 4-12. The results for two blood vessels with a filter width of two are shown in Figure 4-12. The results for four blood vessels (two horizontal and two vertical) with a filter width of four are depicted in Figure 4-13, and the results of six blood vessels (three horizontal and three vertical) with filter width of six are shown in Figure 4-14. In Figure 4-12, the ratio of largest possible false positive to the true match is 83%, and the hill around the true



		Columns														
		-7	-6	-5	-4	-3	-2	-1	0	1	2	3	4	5	6	7
R o w s	-10	-22	-32	-52	-67	-80	-71	-41	-6	23	50	52	49	46	51	36
	-9	-57	-68	-69	-55	-48	-34	-17	11	32	52	47	39	35	32	16
	-8	-49	-61	-68	-58	-59	-47	-23	23	54	71	58	43	31	15	0
	-7	-46	-54	-54	-47	-47	-35	-6	33	58	68	58	44	25	1	-7
	-6	-56	-56	-45	-31	-12	6	16	31	49	66	71	61	50	20	2
	-5	-45	-49	-42	-42	-31	-3	30	57	74	87	82	65	43	20	14
	-4	-32	-31	-20	-14	-2	12	31	47	62	77	78	73	57	45	36
	-3	-33	-29	-12	-1	12	25	45	59	66	66	50	52	36	30	20
	-2	-62	-52	-24	-5	20	48	82	99	94	76	53	37	19	17	12
	-1	-58	-28	-2	20	47	69	88	87	77	58	48	27	7	5	-6
	0	-48	-41	-33	-12	25	69	114	120	91	48	29	8	4	-2	-7
	1	-65	-50	-23	13	47	84	115	107	81	52	35	4	-7	-14	-11
	2	-33	-29	-17	7	33	76	110	114	91	60	29	-5	-16	-12	8
	3	-32	-22	1	26	47	87	102	88	61	29	12	-6	-16	-13	0
	4	-23	-6	21	42	62	92	91	72	54	28	9	-10	-26	-18	-7
	5	-11	10	33	62	90	99	72	40	16	-4	-18	-24	-19	-7	1
	6	-9	19	49	74	93	90	64	39	13	-7	-24	-27	-12	-1	5
	7	31	55	72	76	68	56	41	15	-18	-32	-36	-25	-8	-5	-8
	8	22	44	70	85	76	52	32	9	-17	-29	-34	-30	-28	-26	-17
	9	31	55	80	84	67	39	11	-24	-44	-44	-34	-25	-27	-23	-21
	10	52	77	89	76	50	22	-2	-28	-38	-41	-31	-28	-42	-33	-28

Top 10 intensities in  
a 60 x 60 pixel area

120  
115  
114  
114  
110  
107  
102  
100  
99  
99

The largest intensity not  
located inside the above table.

100

Figure 4-12 The correlation at different shifted position for a template of two blood vessels and a filter size of two. Location (0,0) is the position where the templates are all centered on their respective blood vessel. The table in the bottom left are the top ten intensities in the 60 x 60 area, where the 21 x 15 array is the center portion of this larger area. Also shown is the largest intensity located somewhere in the 60 x 60 area but not located in the 21 x 15 central array. This number represents the largest false positive.

		Columns														
		-7	-6	-5	-4	-3	-2	-1	0	1	2	3	4	5	6	7
R o w	-10	-145	-158	-185	-212	-238	-240	-189	-103	22	136	203	226	196	156	93
	-9	-125	-187	-260	-294	-329	-286	-171	-34	121	230	260	255	206	162	94
	-8	-213	-262	-298	-263	-245	-181	-76	48	168	257	274	256	205	145	74
	-7	-158	-224	-280	-272	-264	-194	-85	85	231	318	320	255	176	97	39
	-6	-120	-171	-220	-198	-173	-102	0	145	254	322	308	254	184	93	25
	-5	-164	-169	-160	-113	-68	-3	56	154	233	286	292	271	232	150	83
	-4	-111	-141	-154	-154	-115	-18	89	209	300	335	304	276	226	148	99
	-3	-124	-111	-95	-77	-16	71	169	254	303	307	267	232	181	122	88
	-2	-152	-107	-53	-23	53	142	216	265	285	253	208	190	134	96	69
	-1	-229	-175	-113	-56	54	159	276	336	347	307	257	194	126	84	55
	0	-294	-234	-151	-43	113	262	399	449	421	327	240	133	38	-9	-30
s	1	-251	-221	-168	-78	51	199	332	375	355	269	195	99	44	19	28
	2	-274	-249	-175	-58	79	223	344	366	330	257	185	76	27	-2	4
	3	-242	-211	-147	-44	75	208	318	350	317	249	165	56	13	13	45
	4	-154	-143	-93	-14	79	182	238	246	218	157	92	30	11	30	72
	5	-140	-101	-28	59	137	223	266	262	231	171	70	4	-11	13	72
	6	-68	-9	73	147	196	227	205	146	87	29	-38	-60	-26	26	75
	7	-58	6	101	188	235	240	187	112	27	-46	-103	-103	-54	4	54
	8	59	121	181	209	202	164	90	6	-71	-123	-138	-108	-49	7	48
	9	27	83	143	188	187	141	87	20	-49	-83	-99	-87	-76	-52	-37
	10	34	75	127	172	156	93	24	-72	-158	-190	-189	-142	-106	-74	-40

Top 10 intensities in  
a 60 x 60 pixel area

449  
421  
399  
375  
366  
355  
350  
347  
344  
336

The largest intensity not  
located inside the above table.

280

Figure 4-13 The correlation at different shifted position for a template of four blood vessels and a filter size of four. Location (0,0) is the position where the templates are all centered on their respective blood vessel. The table in the bottom left are the top ten intensities in the 60 x 60 area, where the 21 x 15 array is the center portion of this larger area. Also shown is the largest intensity located somewhere in the 60 x 60 area but not located in the 21 x 15 central array. This number represents the largest false positive.

		Columns														
		-7	-6	-5	-4	-3	-2	-1	0	1	2	3	4	5	6	7
R o w s	-10	-451	-487	-524	-503	-453	-351	-194	-4	201	384	470	440	384	284	152
	-9	-575	-629	-678	-632	-567	-421	-216	39	286	472	547	510	436	323	191
	-8	-683	-725	-741	-637	-511	-319	-82	199	439	621	652	593	489	343	201
	-7	-596	-661	-678	-567	-444	-237	18	305	537	686	696	629	522	375	240
	-6	-563	-605	-598	-474	-334	-120	156	446	652	785	768	705	567	382	225
	-5	-677	-641	-544	-346	-133	133	394	633	776	830	772	692	564	403	258
	-4	-563	-555	-487	-350	-146	133	416	675	831	883	827	758	608	437	294
	-3	-523	-456	-336	-170	63	324	563	740	827	829	753	670	538	410	283
	-2	-479	-390	-227	-43	202	442	656	775	793	722	609	510	370	265	169
	-1	-530	-415	-235	-39	223	484	743	865	873	792	676	539	356	218	112
	0	-587	-430	-197	79	411	729	991	1065	1001	825	626	403	178	19	-70
	1	-447	-330	-143	72	334	586	801	851	793	630	467	266	97	7	-35
	2	-449	-354	-175	57	340	606	821	866	776	600	433	211	42	-33	-64
	3	-341	-240	-78	130	370	591	737	737	633	461	284	76	-57	-108	-84
	4	-266	-185	-49	134	316	493	605	575	465	300	133	-51	-136	-151	-99
	5	-216	-108	31	195	353	507	575	498	365	198	25	-152	-210	-192	-121
	6	-116	-16	128	268	393	480	453	328	164	-29	-201	-328	-326	-239	-120
	7	-117	-11	118	239	334	371	320	204	50	-114	-265	-362	-351	-275	-177
	8	-57	47	192	303	348	338	237	76	-95	-234	-343	-389	-337	-253	-151
	9	-87	7	138	249	287	288	203	55	-89	-216	-321	-363	-371	-336	-276
	10	-50	32	145	224	243	191	54	-120	-273	-386	-442	-422	-377	-288	-189

Top 10 intensities in  
a 60 x 60 pixel area

1065  
1001  
991  
883  
873  
866  
865  
851  
831  
830

The largest intensity not  
located inside the above table.

501

Figure 4-14 The correlation at different shifted position for a template of six blood vessels and a filter size of six. Location (0,0) is the position where the templates are all centered on their respective blood vessel. The table in the bottom left are the top ten intensities in the 60 x 60 area, where the 21 x 15 array is the center portion of this larger area. Also shown is the largest intensity located somewhere in the 60 x 60 area but not located in the 21 x 15 central array. This number represents the largest false positive.

match is relatively small (a negative number is only 4 pixels away from the true match). But in Figure 4-14, the ratio is only 47% and the hill is somewhat larger. It appears more blood vessels and larger filter sizes produce better results.

This data is somewhat qualitative and does not clearly indicate the probability of a false positive. Nor is it clear that using many blood vessels with large filter sizes is better than using few blood vessels with smaller filter size. The three histograms of the tabular data (the entire 60 x 60 array) in Figure 4-15 relates the magnitude of the correlation with the number of occurrences of that magnitude. Four blood vessels were used, and the three histograms depict a filter size of two, four, and six. These plots are an unnormalized sample probability density function. Notice the surprising results: the filter size does not appear to make a large difference in the probability of a false positive. If it did, the waist of the density function would shrink as the filter size increased. Not shown but calculated was the same type of histogram with two blood vessels and six. The same conclusion was reached. But, the three histograms in Figure 4-16 correspond to a fixed filter of four and the number of blood vessels was varied between two and six. These histograms clearly show that the more blood vessels used in the template, the less likely a false positive will occur (the waist of the density function shrinks). Not shown are the histograms for filter sizes of two and six. The results are the same. The important conclusion is that instead of using two blood vessels at a filter size of six, it is much better to use six blood vessels at a filter size of two.

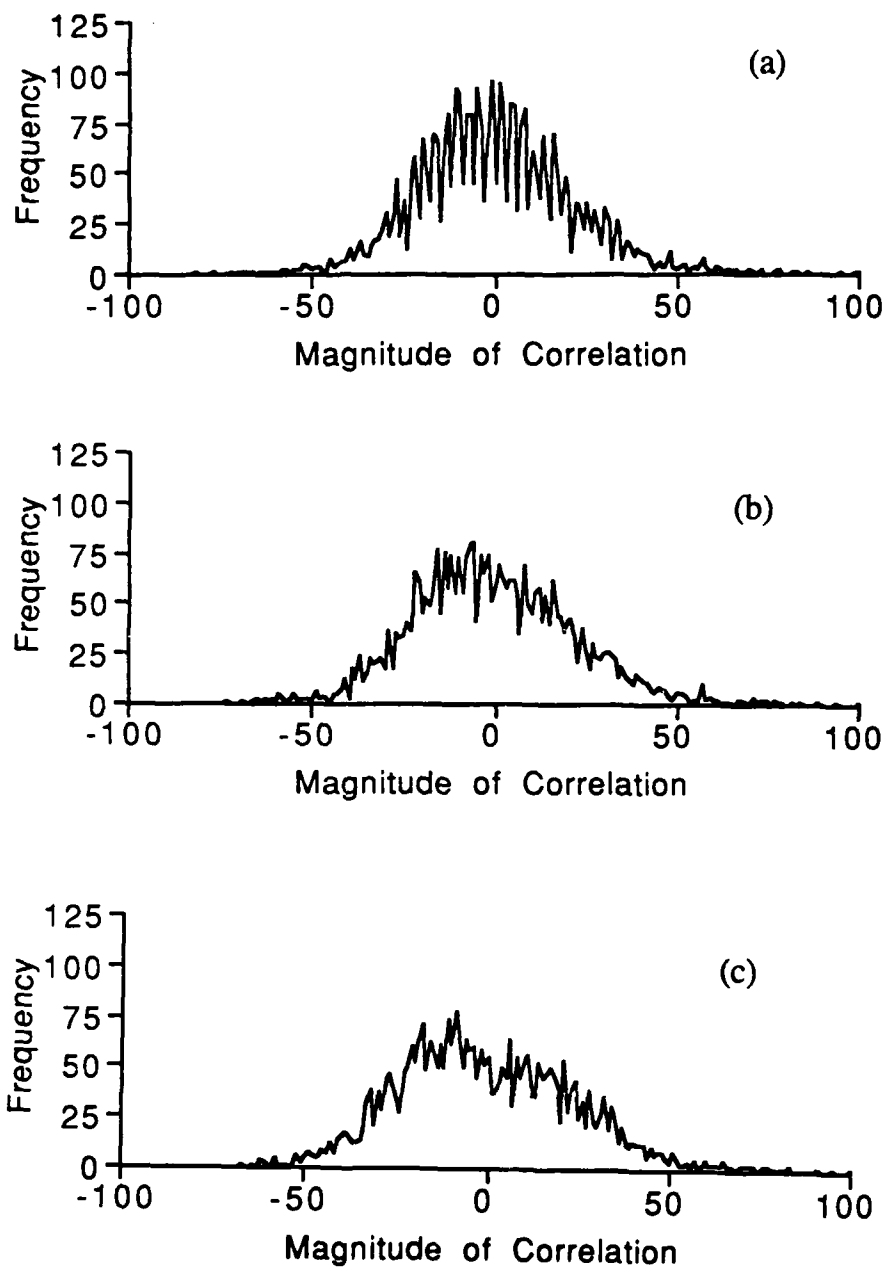


Figure 4-15 Histogram relating the magnitude of the blood vessel correlation with the frequency that the magnitude occurred. The number of blood vessels is four. (a) Filter size of 2. (b) Filter size of 4. (c) Filter size of 6.

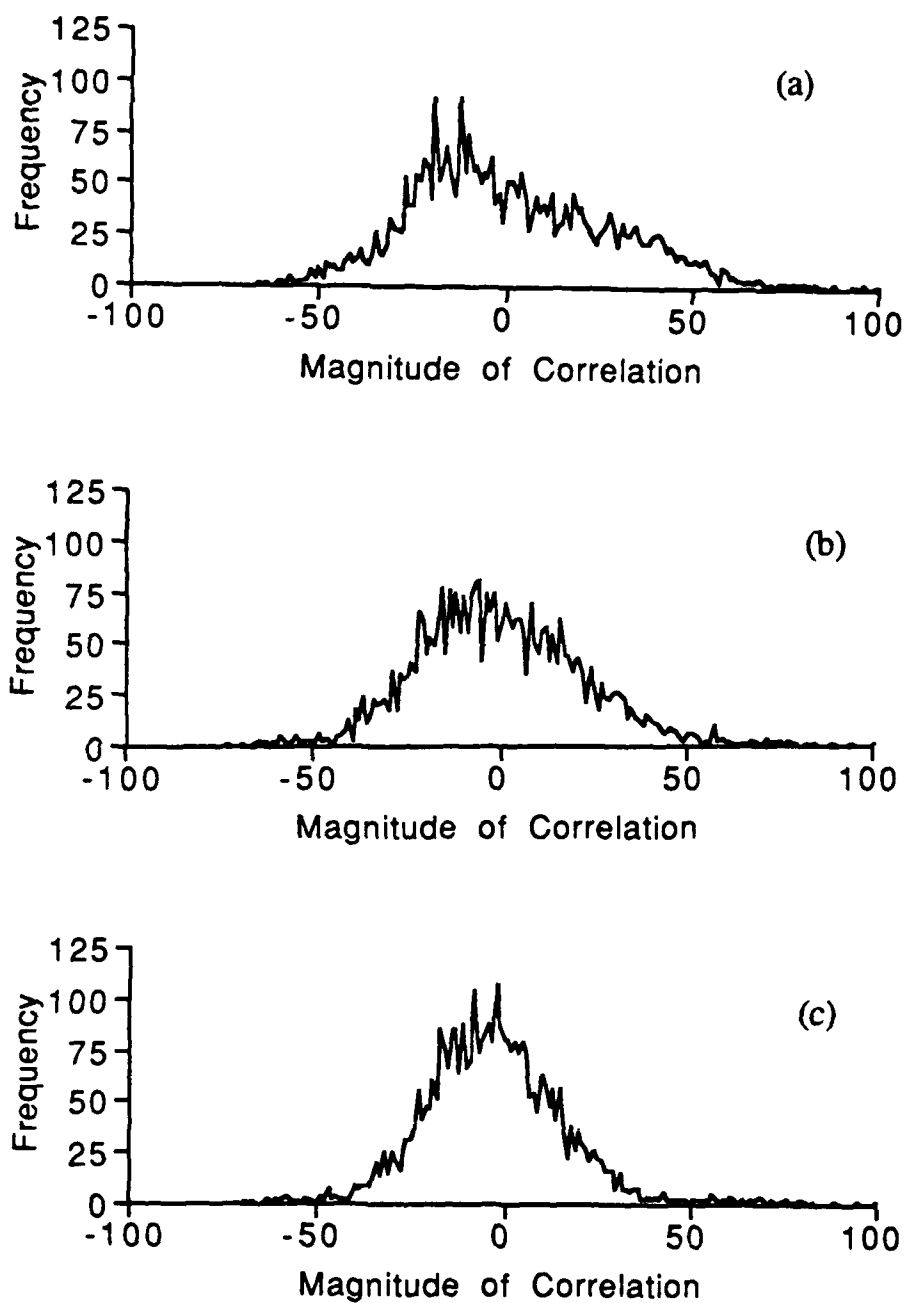
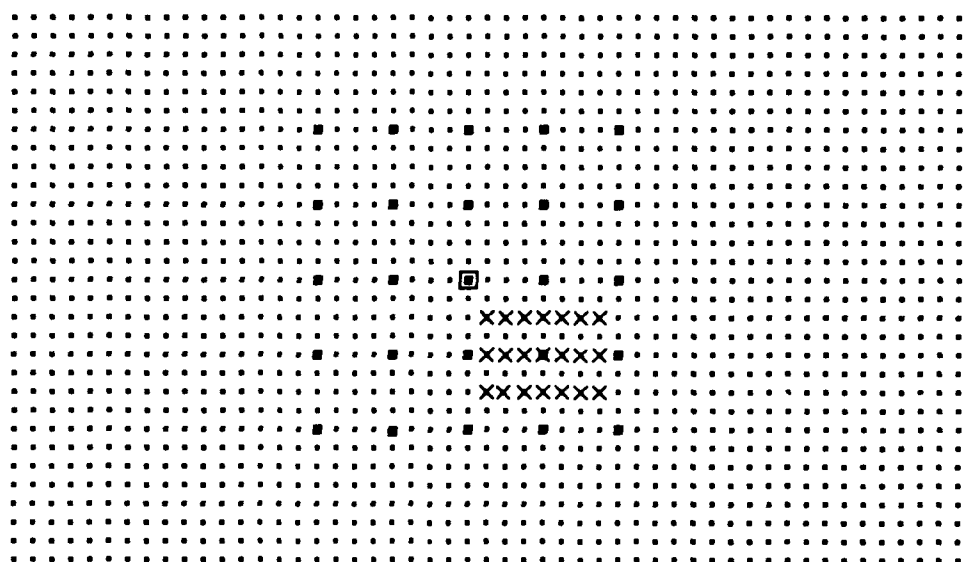


Figure 4-16 Histogram relating the magnitude of the blood vessel correlation with the frequency that the magnitude occurred. The filter size is four. (a) Two blood vessels. (b) Four blood vessels. (c) Six blood vessels.

#### 4.3.5 The Search Area and Expansion

The last consideration in the design of the tracker was the size and expansion of the search area. Recalling the coarse and fine window matching discussed earlier, the tracker can search a larger area if it first searches a coarse area by skipping several rows and columns. It then performs a fine search around the pixel of the best coarse match. The search area can thus be made larger and hence the tracker can maintain lock on faster moving objects. The size of the search area is defined as the number of correlations performed in the X and Y direction, while the expansion is defined as the number of rows or columns skipped in the coarse search area. The size of the expansion, which must be small enough to avoid skipping over the real match, can be determined from the tables in Figures 4-12, 4-13, and 4-14. The rule is that all the correlations within an expansion size window around the true match must be larger than the nearest false positive. (This can be eased to some degree by performing a fine search on the two or three best coarse matches, but at a cost of more computation time.) As seen in Figure 4-14, all the correlations in a 4 x 4 pixel area centered around the true match are above the highest false positive. Thus, this example would suggest that the expansion could be four.

The search area is constrained by either the speed of the tracked object or the largest search area the computer can calculate in the permitted time. The Intel computer system running an 8086 microprocessor was severely limited by the latter. The search area used in the tracker is shown in Figure 4-17. Its size is 5 x 5 with an expansion of four. The fine tune expansion window is also shown. The legend explains the symbols. In Figure 4-17, the center pixel was the best match from the last field. The coarse search area is centered around this pixel. The coarse algorithm then



### Legend

- A pixel.
- ◻ The pixel with the previous fields highest fine correlation, thus the pivot point for this fields coarse correlation.
- A pixel where a coarse correlation is centered.
- ✕ The pixel with this fields highest coarse correlation, thus the pivot point for this fields fine correlation.
- ✕ A pixel where a fine correlation is centered.

Figure 4-17 Coarse and fine search area for a search area of five and an expansion of 4. The fine search area includes all the area within the confines of the 4 x 4 coarse search area. Since an odd/even interlace pattern is used, every other row cannot be read during any particular field.



found that one row down and one column to the right was the best coarse match. The fine tune search area is then defined to be all the pixels within a 4 x 4 pixel area centered on this best match. Notice for the particular case where the RS-170 standard is used, the odd/even interlace only permits the reading of every other row (see Chapter 7, "Instrumentation - General Specifications").

The coarse/fine search area works exceedingly well. The lower graph in Figure 4-18 shows the magnitude of the best coarse correlations and the upper graph shows the magnitude of the best fine correlation. Each solid triangle in the lower graph represents the best coarse correlation within a 5 x 5 search area for that particular registration. The empty triangles in the upper graph represents the best fine tune match around this coarse correlation.

To speed this routine even further, the growth curve was also implemented. During the calculation of each edge of each blood vessel at any given shifted position, each edge is compared against a threshold. If any edge fails to exceed this threshold, the calculations for that position are terminated and that position is considered a poor match. (Notice that the similarity routine proposed in this chapter results in a large number for a poor match, not a small number as discussed under "Growth Curves" above) This threshold is tricky to calculate, and is dependent on the precalculated correlation. Nonetheless, even zero proved to shorten the computation time.

#### 4.3.6 The User Interface

To put things in perspective, the step by step procedure for using the routine will be given. The computer asks the operator for the number of blood vessels (always even), the size of the search area (always odd), the expansion, and the target

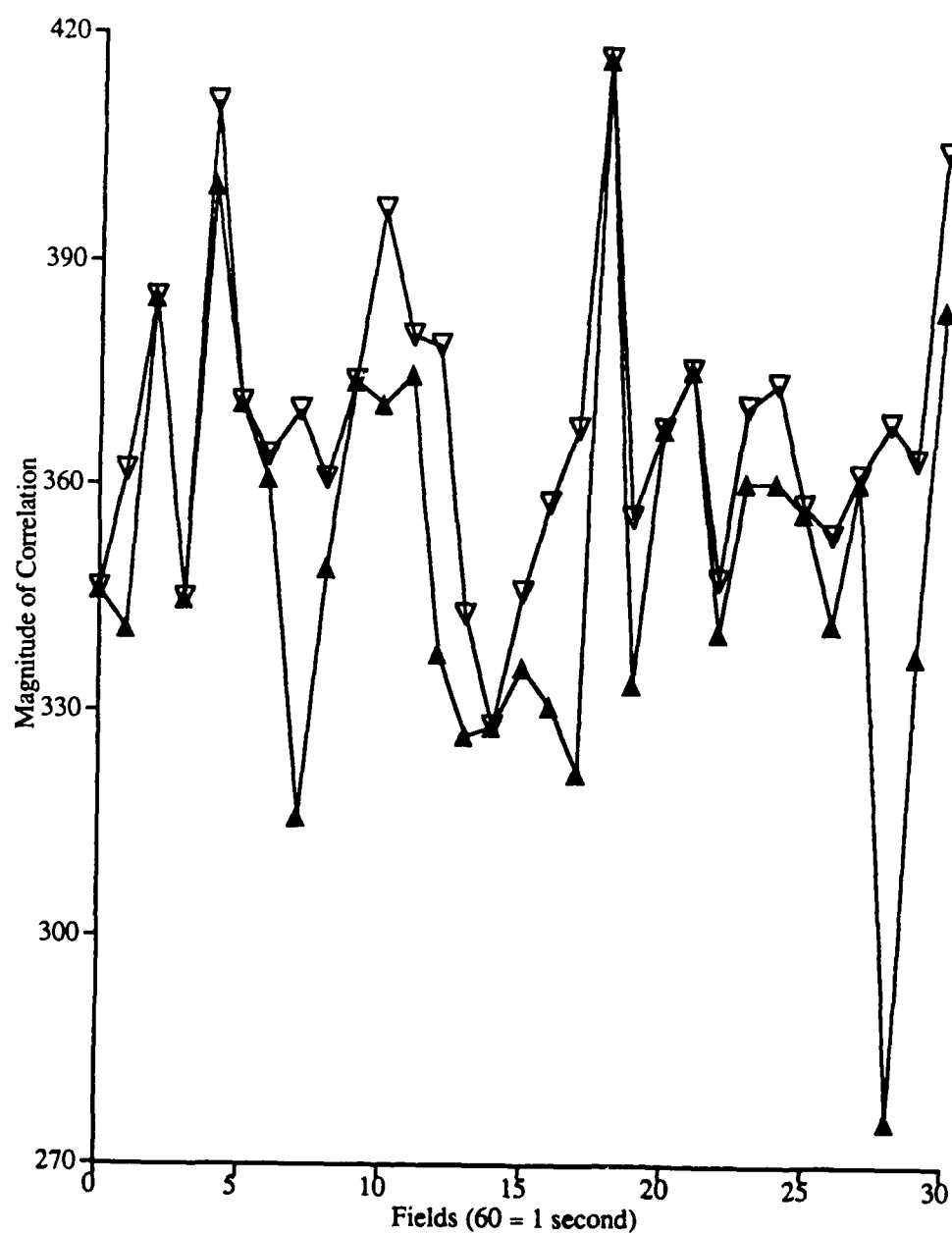


Figure 4-18 Magnitude of the coarse correlation (lower plot) and the magnitude of the fine correlation (upper plot) during a 1/2 second period of tracking.

row and column. The target row and column are mock coordinates for the lasers position. The video system is then put in a continuous mode, with the video board digitizing the images in real time. When the operator is ready, he/she hits the return key on the keyboard and the computer freezes the next frame in the video buffer. Within 30 seconds, the best blood vessels are then found and shown to the operator one vessel at a time. Bars are drawn on the video monitor across the blood vessel. The operator chooses to either use that vessel or continue to look for another vessel further into the ordered table. When the required number of vessels have been chosen, the computer waits to start the tracking. The operator hits the return key and the computer searches for the best correlation at the last known location of the blood vessels. The outputs of the tracker are two analog signals, one for the row direction and one for the column direction. These are the analog equivalents of the updated target row and column, and will be used to direct the servo mirrors for the laser. In the test routines, the coarse and fine correlations were also saved along with the updated digital target coordinates.

#### 4.4 Results

The tracker routine was tested on video taped images of a photograph of the retina. These video images were made using a Cohu SIT camera attached to a Zeiss fundus camera focused onto the photograph of the retina, the latter moving in a smooth circling fashion at different frequencies. This image has about equal quality to an image of a normal retina using the same cameras. Real retinal images were not used in the tracking algorithm because the Zeiss fundus camera does not have the

proper optical interface to the SIT camera. This yields images with a very narrow field of view.

To insure that the tracker initially locks onto the retina, the retinal image had to be approximately at the same position in its rotational travel when the routine calculated the best blood vessels. This could only be done on the slower moving images. On the faster circling routines, the tracker would aimlessly wander during the first second before the retina circled around and came within the acquisition range of tracker. The tracker sometimes had to be restarted several times before a lock was established. Four blood vessels were used with an expansion of four and a search area of  $5 \times 5$ .

The output of the tracker for the retina circling at 0 Hz,  $1/3$  Hz,  $1\ 1/2$  Hz, and 5 Hz is depicted in Figures 4-19 thru 4-22, respectively. For each frequency, the target row, target column, and fine correlation is shown. The initial coordinates of the target row and column was equal to (200, 200). At higher frequencies, the tracker consistently failed to establish lock.

#### **4.5 Strengths and Weaknesses**

This section will discuss the strengths and weaknesses of the system. Suggestions and improvements which will enhance the tracker's performance will also be given.

The algorithm for tracking is very efficient. If six blood vessels are used at a filter size of two, then only 48 memory fetches to the video board are made during one correlation instead of 256,000. All computations are additions and subtractions,

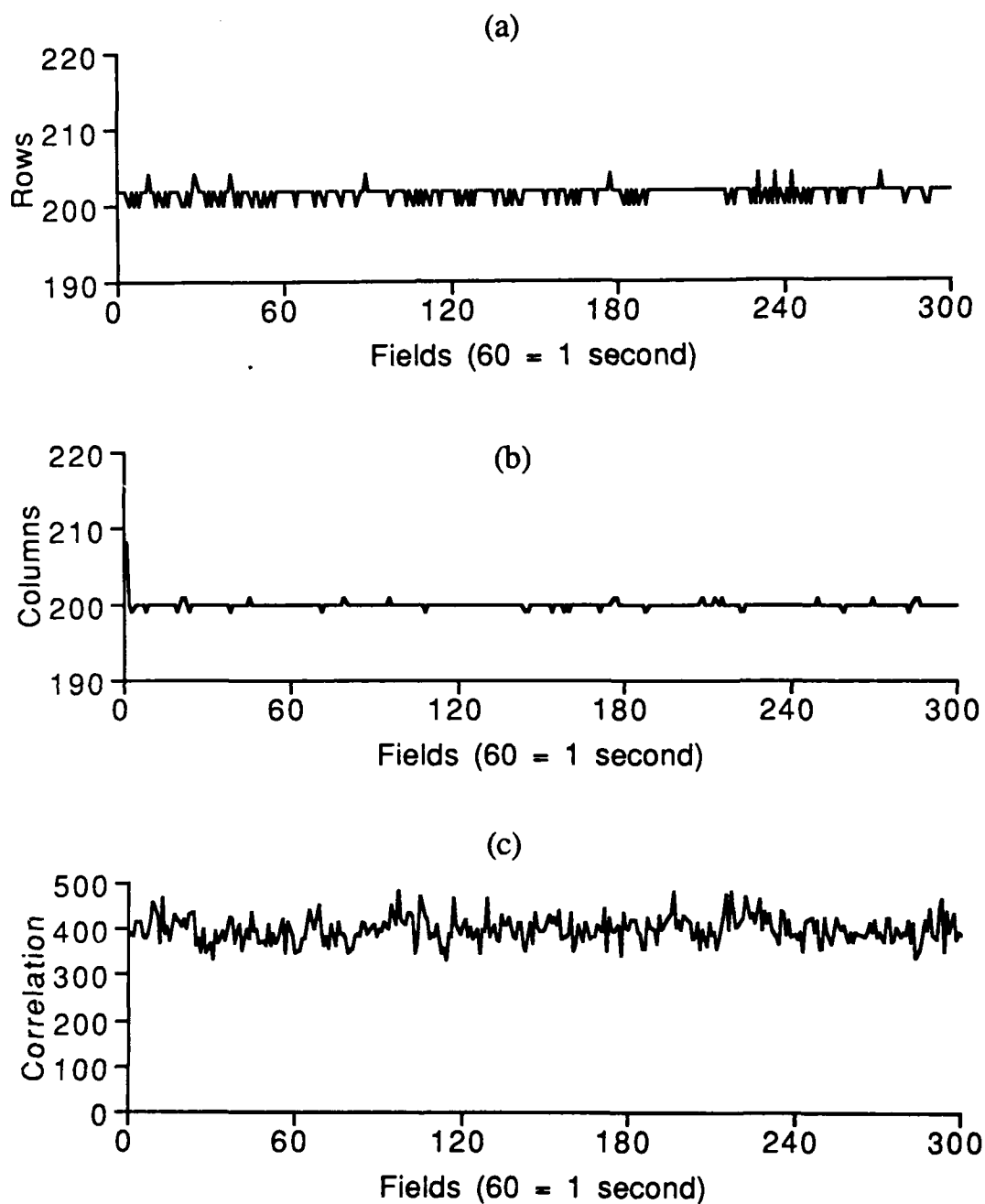


Figure 4-19 The output of the tracker while tracking a stationary photograph of the retina. (a) Row output when the initial target location was 200. (b) Column output when the initial target location was 200. (c) The fine correlation. The precalculated correlation was 514, larger than the real time calculations.

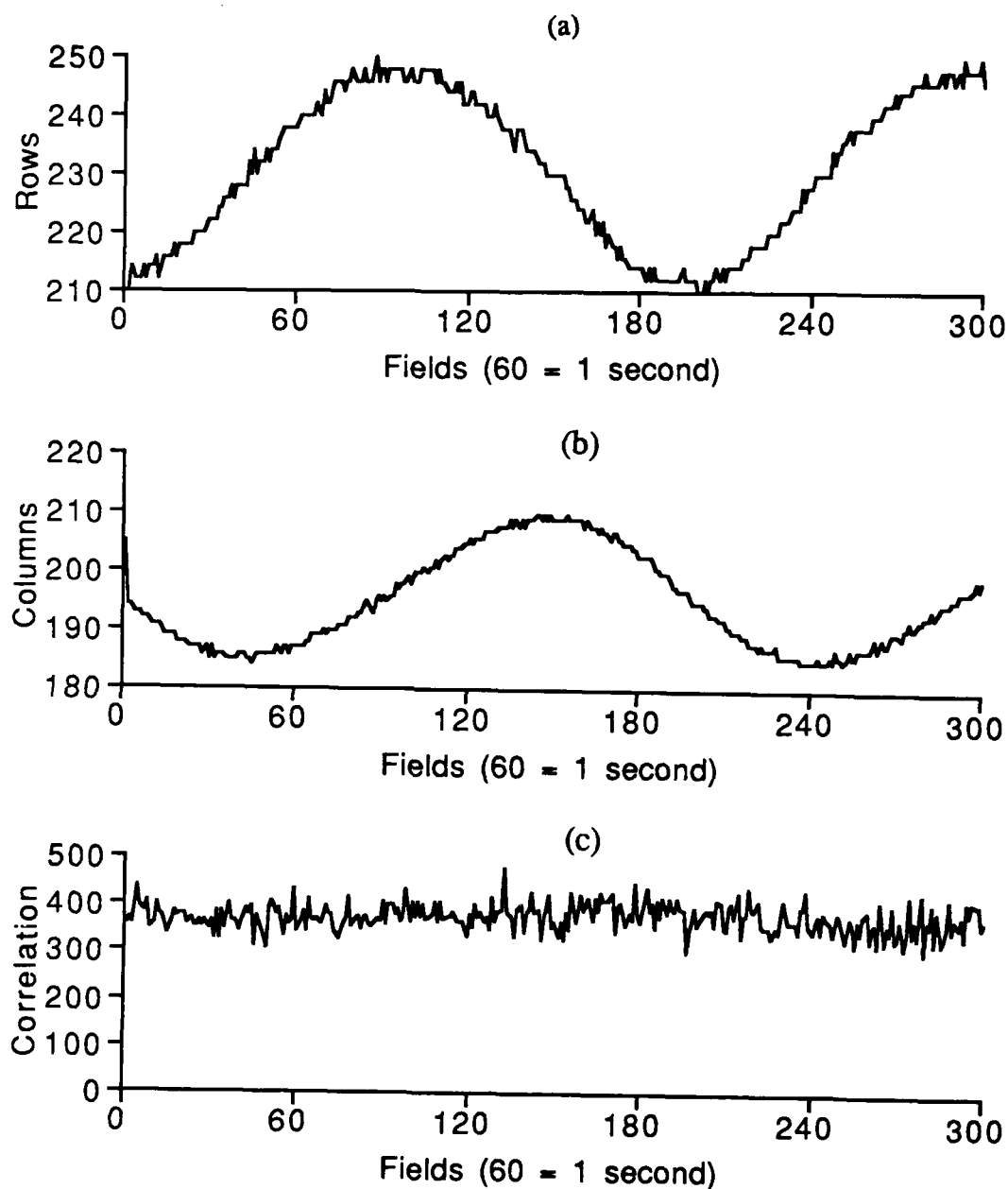


Figure 4-20 The output of the tracker while tracking a photograph of the retina circling at approximately 1/3 Hz. (a) Row output when the initial target location was 200. (b) Column output when the initial target location was 200. (c) The fine correlation. The precalculated correlation was 473, larger than the real time calculations.

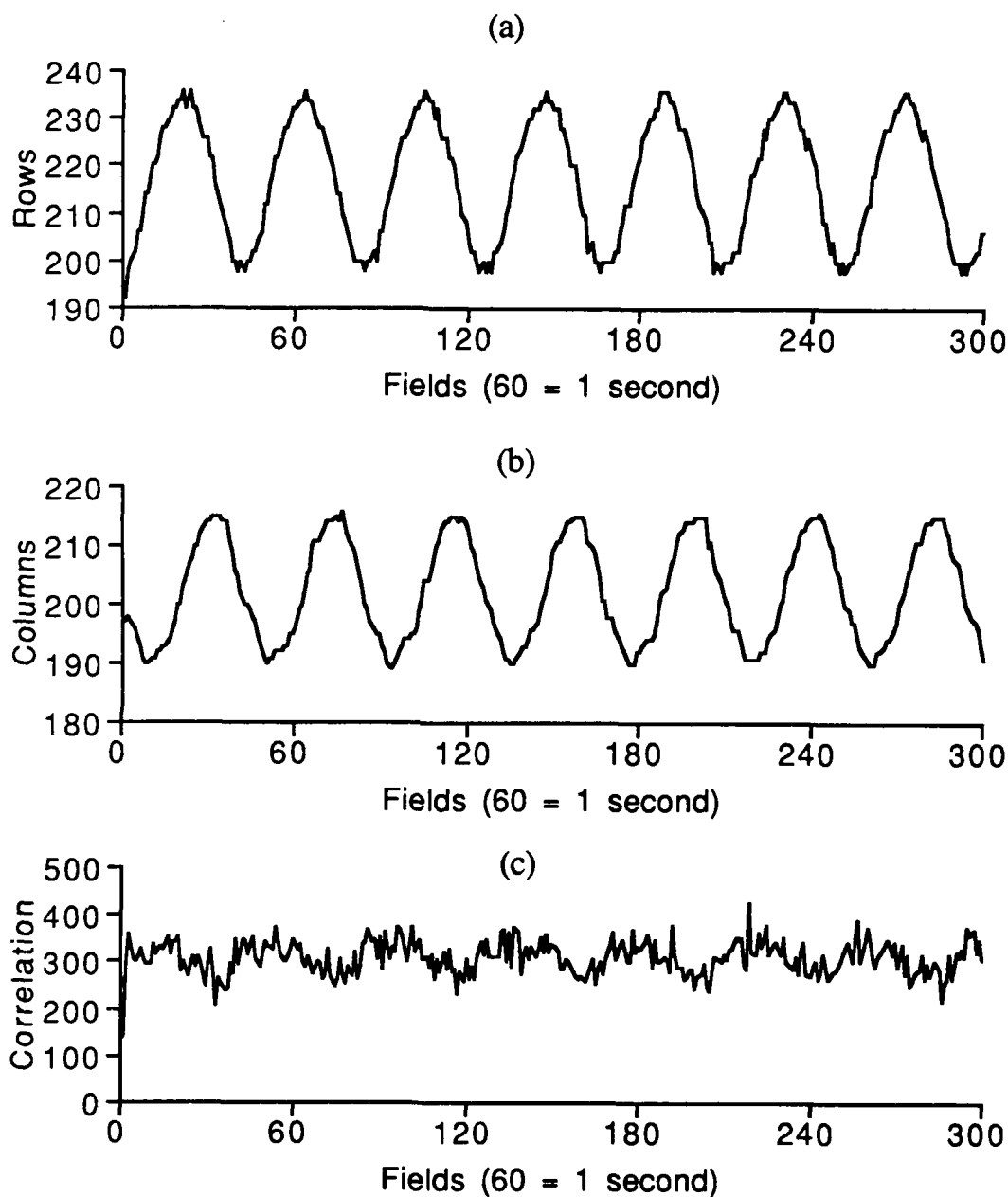


Figure 4-21 The output of the tracker while tracking a photograph of the retina circling at approximately  $1\frac{1}{2}$  Hz. (a) Row output when the initial target location was 200. (b) Column output when the initial target location was 200. (c) The fine correlation. The precalculated correlation was 437, larger than the real time calculations.

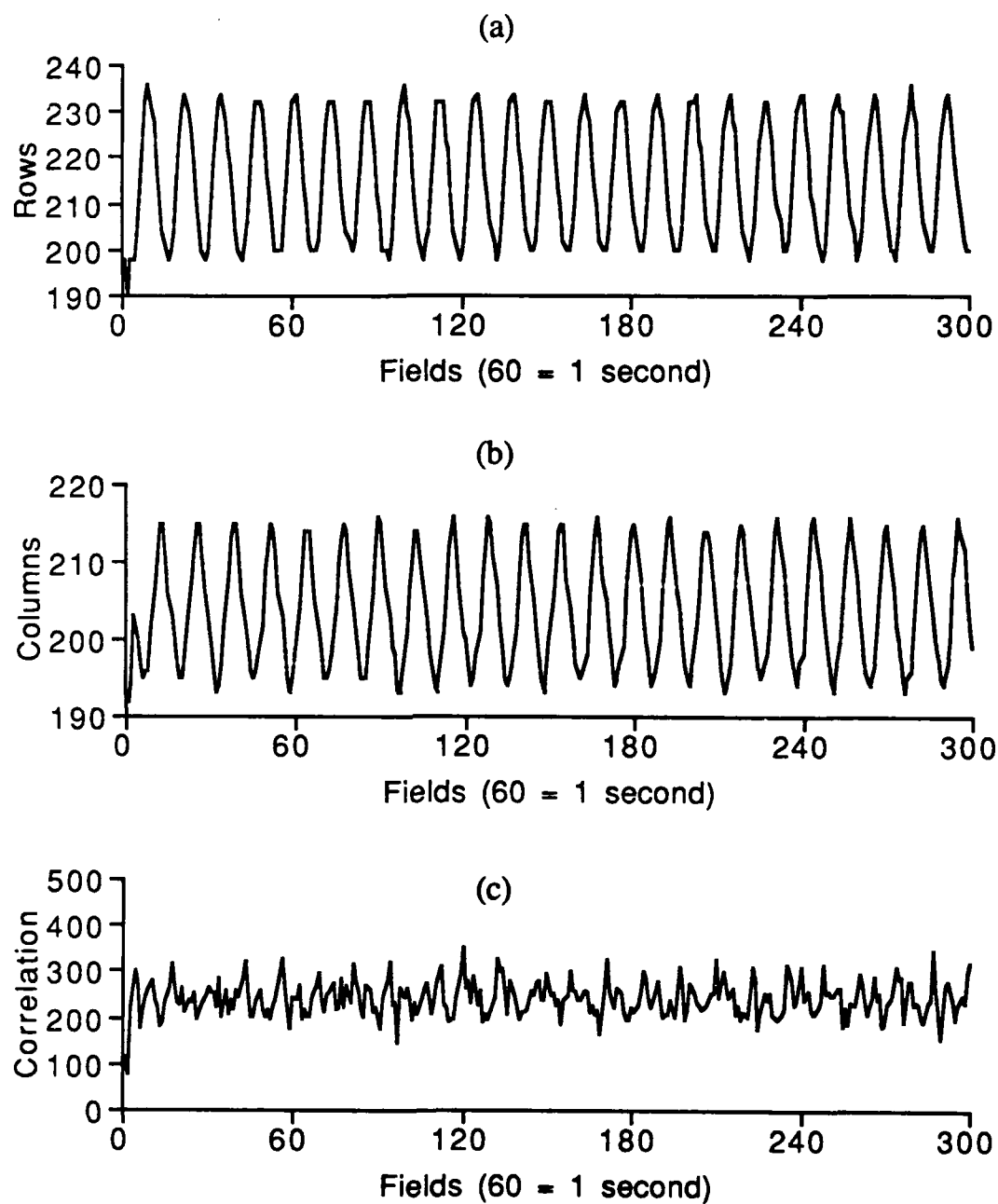


Figure 4-22 The output of the tracker while tracking a photograph of the retina circling at approximately 5 Hz. (a) Row output when the initial target location was 200. (b) Column output when the initial target location was 200. (c) The fine correlation. The precalculated correlation was 386, larger than the real time calculations.



no multiplication or division is used. The only shortening of the algorithm that has been suggested is to use only one edge of the blood vessel instead of two.

Caution must be exercised in the noise immunity of the system. One reason that two edges of the blood vessel instead of one is to increase noise immunity. The tracker might be less likely to follow spurious lines injected by the VCR, camera, or digitizing board. The correlation calculated from each edge in the algorithm might also be clamped such that it can only add a small portion to the total correlation. Thus one large edge will not be an automatic match.

The initial routine that identifies and delivers the best horizontal and vertical blood vessels to the real time tracking routine should be modified to insure that the vessels are indeed horizontal or vertical. Just because a blood vessel performs well with the horizontal templates does not prove that the vessel is horizontal. For example, assume that a very prominent blood vessel is at a  $45^\circ$  angle with respect to the horizontal axis. The edge templates might identify this vessel as both a good horizontal and vertical vessel because it performs well under the template scheme. If this vessel were used in the tracking routine, the tracker would meander up and down the vessel. Only one dimension is fixed. As shown in Figure 4-12, a skewed pattern develops if the vessels are not truly perpendicular. Large positive numbers surround the line formed from the bottom left to the top right of the array. When this data was taken, blood vessels were chosen that were not truly vertical and truly horizontal (even though they were at least within  $\pm 15^\circ$ ). To solve this problem, the initial identification routine must search up and down the vessel to confirm the vessel is indeed of the correct orientation. This routine should also insure that a chosen blood vessel is not one of the paired (and parallel) artery and vein combinations that are common in

the larger blood vessels of the retina (in Figure 2-3 the artery and vein that extends upward from the optic disk are parallel). This could provide the system with a significant false positive.

A significant problem is the smearing of the image by the video camera. This creates two problems. If the image is moving when a freeze frame is taken (to perform the initial calculations for the template), then a poor template will be generated. Secondly, the tracker calculates very poor correlations on images that are smeared, especially since it is looking for edges. Shuttered video cameras will be discussed in Chapter 7, "Instrumentation - Temporal Specifications".

The 8086 microprocessor is slow. The search area used was  $5 \times 5$  with an expansion of four. This equates to a total pixel search area of  $20 \times 20$ . But Equation 12 requires a  $60 \times 60$  pixel search area to maintain lock on a rapidly moving saccade. *The computer needs to be at least nine times faster.* Enhanced instrumentation, to include the computer, the digitizing board, and the video cameras, will be discussed in Chapter 7, "Instrumentation".

The best fine correlations are not equal to the precalculated correlation. Remember that the precalculated correlation was performed on a still video image while the fine correlations are performed on the real time images. This is depicted in Figures 4-19(c). The precalculated correlation was 514, but the real time correlations averaged about 400. And this was on a retinal image that was not moving. This problem is most serious because the computer does not know if it is locked; a critical requirement for the system. If the tracker losses lock, it must turn the laser off. This researcher attributes most of the problem to the noise from the VCR and camera,

which are also discussed in Chapter 7, "Instrumentation - Video Cameras and Video Cassette Recorders".

This same problem also surfaced in all attempts to have the tracker initially acquire the target in some graceful manner: by looking at some location for a match but not move until the correlation reached the precalculated correlation. This failed miserably and the tracker aimlessly wander until the circling retina moved within its acquisition range. In the real system, the tracker will have to the perform just this task. The patient will look into the fundus camera and the tracker will then take a snap shot of the retina. The patient will relax or go home. After the computer performs its template calculations, the patient will again look into the fundus camera. The tracker must wait for the patient's eye to move to the same position as it was during the snap shot, and then it will start tracking. This scenario is quite realistic and with the proper fixating device, the patient's eye will quickly be in the correct position.

The optic disk was not used as a feature to be tracked because not all the images of the retina will have the optic disk in view. Only blood vessels were used. But, for precision surgery around the macula where the optic disk will be in view, this researcher would highly suggest using the optic disk since it provides excellent contrast.

Only translation was addressed. Other problem areas might be scale changes, rotation, and nonlinear aberrations. If the fundus camera is properly focussed and adjusted, the scale changes (such as 50°, 35°, and 20° field of view) are programmable by the operator and can be fed to the tracking routine. The eye does not seem to rotate significantly. But, if there were small rotational changes, the slope of a

blood vessel would provide an excellent detector. The same type of blood vessel templates used in the tracker could be used, but only two positions on one smooth vessel need to be monitored for rotation. The algorithm discussed under Algorithms would not be implemented because of its computational expense.

The nonlinear aberrations tend to be a more serious problem. A significant aberration exists when viewing the periphery of the eye. An advantage is that the aberrations are somewhat repeatable, in that the identical image will be produced if the same field of view and the same area of the retina is viewed. They are also somewhat predictable in that the distortions grow worse as a more peripheral area of the retina is viewed. The problem, though, is that when the tracker is following the peripheral retina and the eye moves slightly, the template distances might have to be modified to maintain optimum tracking. The spring-loaded matching technique used in the template becomes very useful because the distances between blood vessel templates can be modified to accommodate the aberrations.

#### 4.6 Conclusions

The intention of the research in this chapter was not to build the actual tracking routine for the proposed system, but to show the extent that a personal computer with a digitizing board can track the retina. This research demonstrated that the system is capable of performing rudimentary tracking on a photograph of a retina undergoing smooth circular motions. This chapter and Chapter 7, "Instrumentation", lists many suggestions that will improve the tracker's performance. With these improvements, this researcher is convinced that a tracker can be built from a personal computer and digitizing board that will track the retina of a normal eye during small sac-

cadet, and close the laser's shutter during large saccades. All of these can be performed faster than the reaction time of a human operator. This researcher is not convinced that the accuracy (both spatial and temporal) will be satisfactory for precision surgery near the macula.

## Chapter 5 Control of Lesion Size

The goal of this subsystem is to place lesions of predetermined sizes into the retina. The premise of the system is that the change in reflection (the whitening) of the lesion relates to lesion's width and depth. An overview of the work done by other researchers will be provided first. Background information concerning lesion development problems and variables will be given next. Three experiments and their results will be discussed, one experiment that Youli Yang and this researcher performed on an *in vivo* rabbit liver, another experiment that Youli Yang performed on egg yoke, and a third that this researcher did on an *in vitro* beef liver. Suggested improvements on the experimental procedure will be given, and some suggested control criteria will be reviewed. The last section will be the conclusion.

### 5.1 Previous Work

There have only been a few groups of researchers who have worked on the problem of using reflectance as a criteria to control lesion size. Weinberg *et al.* from Germany measured the total reflectance from a developing retinal lesion using a single photomultiplier tube [5-10]. They concluded that for weak lesions, "through automatic control measuring reflection changes it becomes possible to produce reliably uniform lesions independently of optic and absorptive conditions" [5-10]. For more

prominent lesions, their conclusions were less optimistic, stating that, "the reflection rise does not yet provide for a method to reliably predict and control the coagulation effects from the initial phase of the reflection change" [5-11]. Quantitatively, their results are shown in Figure 5-1. The graph in Figure 5-1(a) shows that the lesion width as observed microscopically agrees well with the width as measured histologically. On the other hand, the graph in Figure 5-1(b) provides a quantitative measure on how the total reflection changes vary with microscopic measured areas. Notice that for an area of  $0.5 \mu\text{m}^2$  the reflection measurements vary from about 2 to 7. This is a substantial variation and would not be accurate enough for a computer to control lesion size. Based upon computer simulations, Weinberg *et al.* also suggested that the total reflectance measurements should actually be related to the total volume. Unfortunately, their histological data did not provide volume information so that they could not relate the total reflectance measurements to histological volume.

A second group of researchers venturing into this problem was Pomerantzeff *et al.* [5-8 and 5-9]. Their assumption was, "that this technique (Weinberg *et al.*) would be more efficient if the right amount of energy to be transferred to the tissue were determined before the irradiation" [5-9]. Their idea was to monitor the reflections from the fundus and estimate the absorbance of the retina at that point. The actual coagulating laser was used in the measurement. They measured the reflections from a test location on the retina and used this as a calibration on which to compare all other locations. Once a lesion was placed in the retina of the desired size (using ophthalmic evaluation), the energy used to create each successive lesion was increased or decreased in accordance with the comparison of the reflectance data from

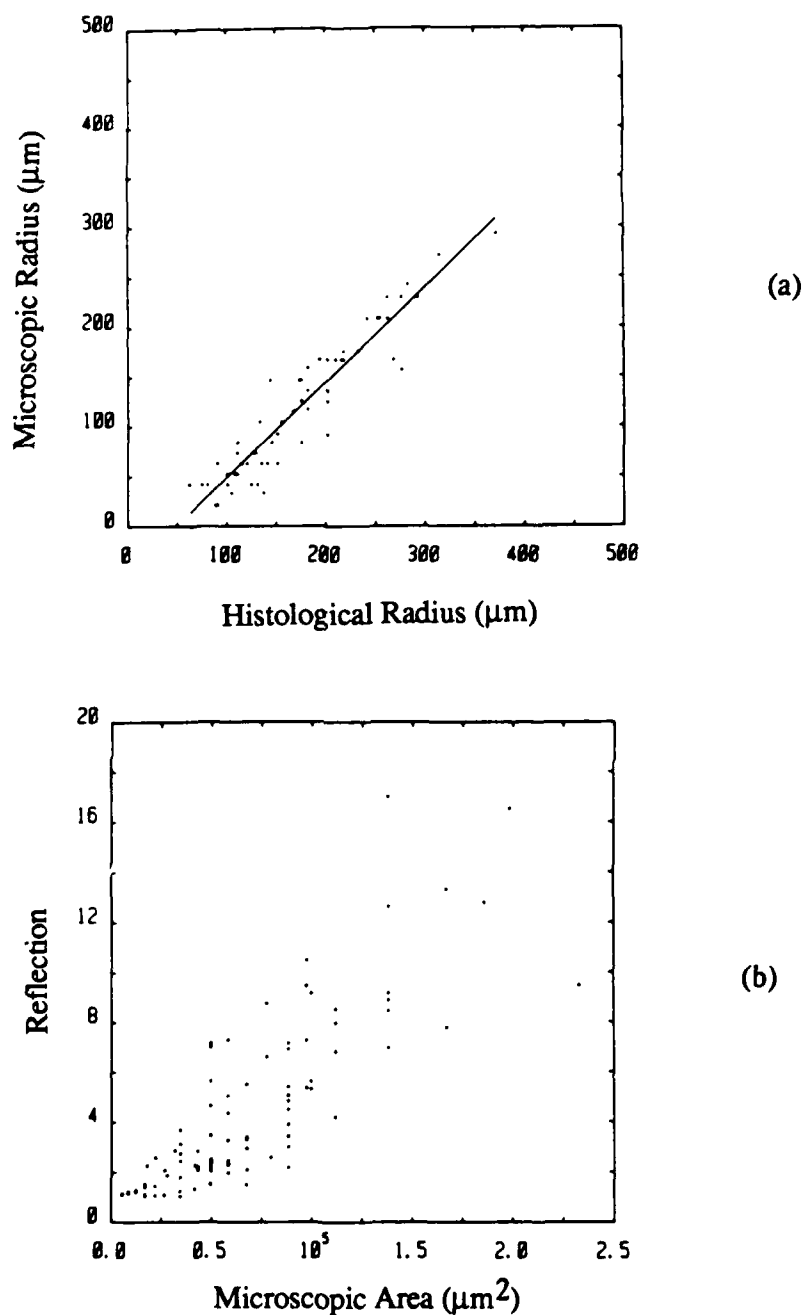


Figure 5-1 Correlation of the different measurements of the degree of damage. (a) Microscopic radius versus histological radius. (b) The reflection increase as a function of the microscopic area. The axis labeled Reflection is equal to the measured reflection increase minus the background, and then divided by the background [5-11].



the new location and the calibration location. This technique might be very useful. Unfortunately, no quantitative results were provided.

Mordon *et al.* [5-6] have analyzed lesion size as a function of several thermal parameters calculated in real time. They placed several lesions in stomach tissue and monitored the lesion development using a thermal camera. Their most successful parameter used to control lesion size was the integral of the 58° coagulation isotherm width as a function of time. They found that this measurement correlated with surface necrosis diameter with a correlation coefficient of 0.98.

## 5.2 Lesion Development

This section discusses the variables associated with lesion development. There are numerous therapeutic benefits derived by irradiating an area of the fundus. The techniques required to create the optimum effects in the tissue in all the different situations is poorly understood. This dissertation will not provide a detailed account of the diverse opinions and findings of the many researchers and ophthalmologists working in this area (Mainster's paper [5-4] provides a brief review). But, to better understand the problems, the approach to retinal surgery will be given followed by examples illustrating the many variables associated with retinal surgery.

1. The disease must be properly diagnosed.
2. If the disease can be treated by laser surgery, then the desired effects must be determined. These desired effects include the severity of the damage (a mild coagulating burn or a charring), the volume of the lesion (width and

depth), and the desired location of the damage (the depth into the fundus, the location on the retina, and the location with respect to other features).

3. The third step is to inflict the desired damage with a laser by varying the five laser parameters (wavelength, duration, spot size, power, and beam profile).
4. The last step involves the physiological reaction of the body to the damage with respect to the disease.

The complexity of this task can be appreciated by considering some of the variables along with some examples.

- a.) Different areas and layers of the retina contain different structures which have varying optical and thermal properties. As was shown in Chapter 2 (Chapter 2, "Anatomy and Light Interaction of the Eye - Tissue Optics and Damage"), even the same structures in different parts of the retina can have varying optical and thermal properties. For example, the macula contains xanthophyll pigment in the inner and outer plexiform layers. If a blue laser (the pigment absorbs blue light, see Figure 2-12) is used for coagulation in this area, the energy will be absorbed into the inner retina, producing neurosensory damage [5-4]. To reach deeper structures in the macula, blue light should not be used (this is why Krypton red has been suggested for the control of subretinal neovascularization in macular disease [5-13]).
- b.) Intraocular scattering (which increases with the patient's age) can expose normal retina adjacent to the treatment site. Scattering increases with decreasing wavelength; Argon blue light light scatters 25% more than Argon green and 300% more

than Krypton red light [5-2]. Thus, lesions could be larger than expected and the required laser energy must be increased in a highly scattering media.

- c.) The laser spot size on the retina is critical in determining the fluence (energy density) of the laser. An incorrect spot size can double or quadruple the desired power, resulting in hemorrhaging or mechanical damage [5-7]. The ophthalmologist does not have an accurate quantitative method to control and measure the retinal spot size (see Chapter 2, "Anatomy and Light Interaction of the Eye - Optics of the Eye", Chapter 7, "Instrumentation - Imaging with the Fundus Camera", and Chapter 7, "Instrumentation - Optics").
- d.) The optical properties of the tissue can actually change during lesion formation [5-3]. Once the lesion starts to turn white, it tends to reflect the energy and prevent the laser from penetrating to deeper levels. This concept is very important in the attempts to re-treat an area once a lesion has already been formed. Re-treatment to attain a deeper burn probably only serves to make the lesion wider, not deeper [5-4].
- e.) The laser duration for most ophthalmic burns is about 100 ms. This duration is considered optimal because shorter durations (with higher powers) leads to mechanical damage and hemorrhage (see Figure 2-8), but longer durations (and lower powers) permit patient reactions to the laser light (and hence eye movement). If a retinal tracker can be developed to account for patient movement, longer duration burns might prove to have some therapeutic value by gently heating the tissue and allowing for heat conduction away from the treatment site.
- f.) Patient pain can affect the manner by which lesions are produced. Krypton laser energy has been shown to give more pain than argon [5-1].

- g.) One of the more important variables for the applications discussed in this dissertation is the appearance of the lesion. Generally, inner retinal lesions (those produced by an Argon laser) tend to be more prominent than deeper, more extensive lesions (as produced with Krypton laser ) [5-5].
- h.) Individual tissues react differently to damage. Treatment follow up is always done and additional surgery is sometimes needed. Because damage cannot be exactly controlled, it's difficult to analyze the tissues reactions to differing levels of damage.

The point to emphasize in this section is the inability of the surgeon to quantitatively insert lesions of a desired width and depth.

### **5.3 *In Vivo* Rabbit Liver Experiment**

In an attempt to understand the spatial and temporal whitening of lesions during lesion formation, a series of lesions were produced in four *in vivo* rabbit livers. The lesion formations in liver tissue and retinal tissue are different. But, lesion formation in liver tissue can lead to an understanding in the reflection changes of protein and also serve to verify the equipment design. The rabbit liver is more accessible than the retina, and histology is less expensive. This section will provide the experimental procedure, the results, and discussion of this experiment.

#### **5.3.1 Experimental Procedure**

The experimental setup is shown in Figure 5-2. The rabbit was placed on a table which was tilted at an angle of about 50° toward the cameras and laser. An incision about 10 cm long was made from the sternum down the midline. The liver

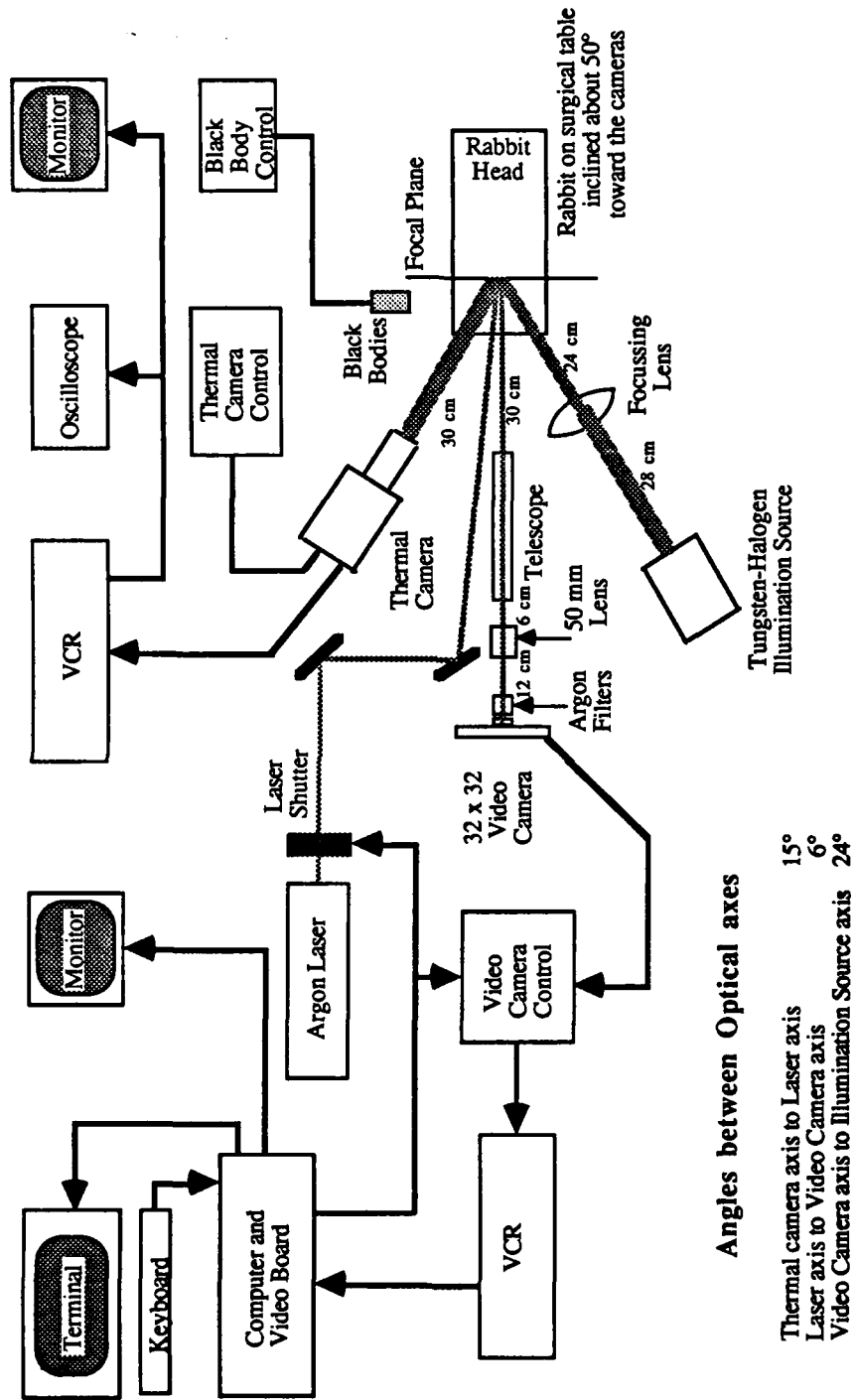


Figure 5-2 Experimental setup.

was isolated and made accessible by gentle pulling the liver from its position underneath the rib cage. It was kept in this position with sponges. The sponges were moistened with normal saline solution kept at 37° C. The surface of the liver was periodically moistened and was always moistened before an irradiations. The rabbits were euthanized 9 1/2 hours after the initial insult to the liver. The livers were removed from the animal and fixed in buffered formalin solution.

The tungsten-halogen source was focussed onto the target area, resulting in a very bright light. The 32 x 32 pixel camera also imaged the target tissue. This camera's video rate was 420 frames per seconds and the pixel separation on the retinal image was 320  $\mu\text{m}$ . The video data was recorded on a VCR's slowest speed.

A laser with a power of 2.5 watts and a spot size of 3.3 mm ( $1/e^2$ ) was also directed onto the target area. A computer controlled the shutter which in turn controlled the laser irradiation on the liver. The laser's duration was varied from 0.2 seconds to 0.9 seconds. A small needle secured to the end of a metal rod pinpointed the focal plane. This needle could be seen in the video image.

A thermal camera imaged the same target area. This camera had a pixel separation at the imaging plane of 23.75  $\mu\text{m}$ . Two black bodies were periodically inserted into the image to calibrate the camera. These black bodies were approximately 50° C and 100° C. The video output of this camera was monitored on an oscilloscope to insure the thermal data did not saturate (it was insured at the beginning of the experiment that a lesion created with the 0.9 second duration did not saturate. Unfortunately, some of the larger lesions throughout the rest of the experiment saturated anyway). The thermal data was recorded on the VCR's slowest speed.

Over 80 lesions were placed in the four livers. The exposure times varied from 200 ms to 1070 ms. Because the gain on the video camera was changed between the second and third rabbit (the initial gain appeared too low), the lesions were split into two data sets. Many lesions were not used because they were situated on a fold on the liver, the histologic data were incomplete or the lesion was asymmetric. The first data set was left with 19 lesions and the second data set was left with 29 lesions.

The microscopic widths of the lesions were measured under a microscope. The lesions were then histologically examined (both measurements were made by a Pathologist). At least three slices were examined from each lesion, and the slice with the largest width and depth was identified. The depth, width, and sectional area was measured from the identified slice. The sectional area was measured using a Summagraphic digitizing pad and the Sigma-scan program from Jandel Scientific.

The lesion's shape resembled a bowl. Three zones could be distinguished from the histological stains. In the very center of the lesion or bowl was the dilapidated zone, which consisted of dead tissue that was mechanically torn and separated. Around this area was a second shell called the denaturation zone, which consisted of dead, but intact liver cells. The third zone formed the bowl shape of the lesion and is the inflammatory or hemorrhagic zone. This inflamed area was distinguishable by the presence of inflammatory cells or neutrophils. The criteria used to calculate the extent of the histological damage was the outer most edge of the inflammatory zone.

The video data was processed to derive a plot of time versus width and a plot of time versus center intensity. A very careful measurement of the final width was

calculated by subtracting a background frame from the frame that contained the final lesion. This was called the visual width.

The thermal data was processed to derive a plot of time versus temperature at spatial points on the lesion (from the center of the lesion to the edge every 0.25 mm). This data was further processed to calculate the width where  $\Omega = 1$  (see Chapter 2, "Anatomy and Light Interaction of the Eye - Tissue Optics and Damage"). Because the activation coefficient of  $10^{98}$  resulted in very large lesion widths, widths derived with an activation coefficient of  $10^{95}$  and  $10^{93}$  were also calculated. The activation coefficient of  $10^{95}$  derived the widths that correlated the best with the microscopic and visual widths. Consequently, the data used in "Results and Discussion" refers to the widths derived using this coefficient. The axis that the thermal width was taken across (horizontal direction with respect to the table) corresponded to the axis that the visual width was taken across (caution must be exercised because the video data frame for the 32 x 32 camera is rotated 90°).

### 5.3.2 Results and Discussion

The results were disappointing. No matter how the data was compared and contrasted from the different sources, a strong correlation could not be found. The second data set provided better results because of the increased gain in the video camera. Only this data set is used for the following discussion. The linear correlation coefficient associated with different data sets is shown in Table 5-1. The four widths are shown plotted against one another in Figure 5-3.



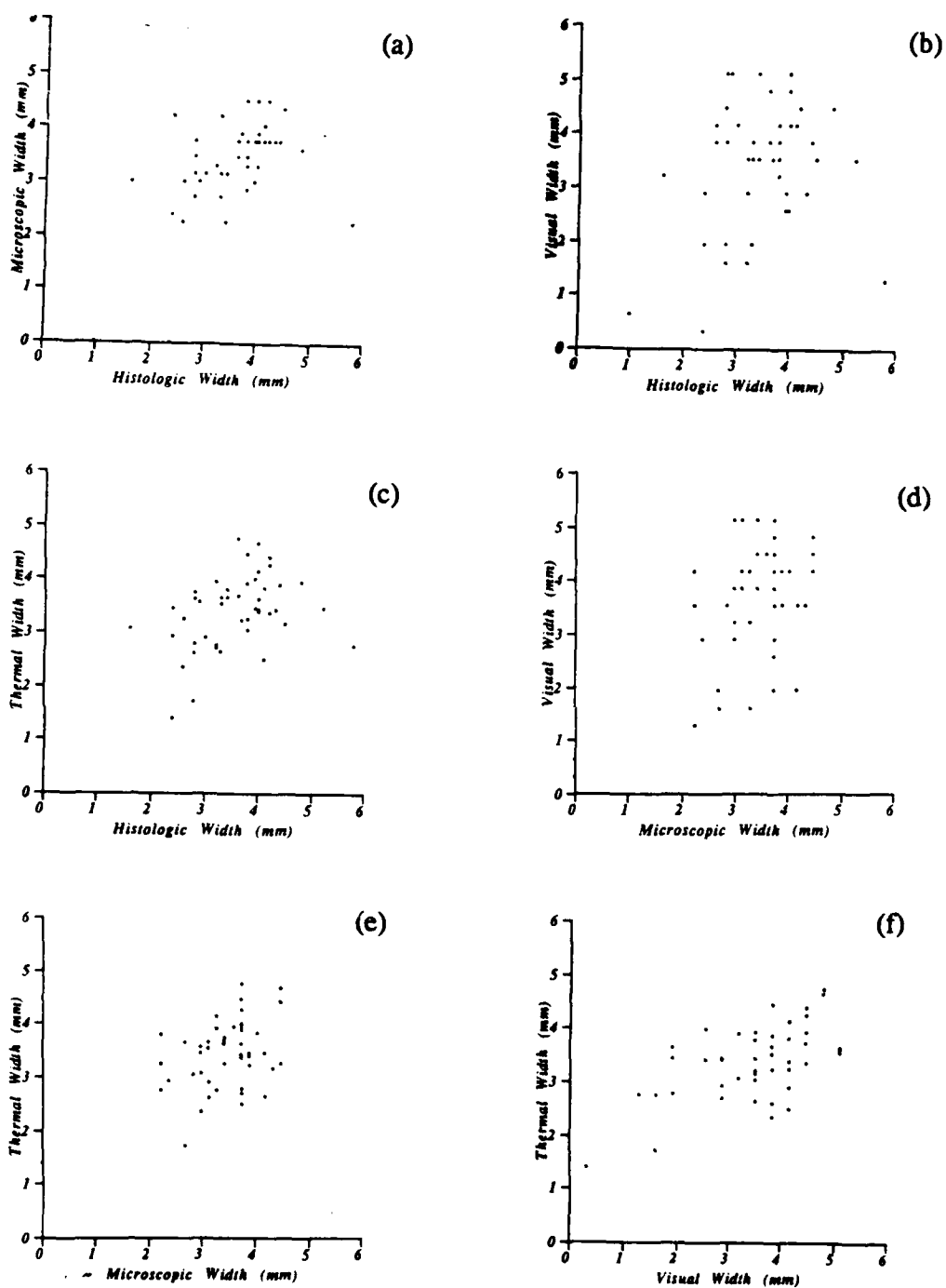


Figure 5-3 The histological, microscopic, visual, and thermal widths plotted against one another. The correlation coefficient is given in Table 5-2.

Data Sets Correlated	Correlation Coefficient
1. histologic width <u>versus</u> microscopic width	0.56
2. histologic width <u>versus</u> visual width	0.28
3. histologic width <u>versus</u> thermal width	0.56
4. microscopic width <u>versus</u> visual width	0.78
5. microscopic width <u>versus</u> thermal width	0.79
6. visual width <u>versus</u> thermal width	0.77
7. visual width <u>versus</u> center intensity	0.90
8. histologic depth <u>versus</u> center intensity	0.25

Table 5-1 The linear correlation coefficients for different data sets in the *in vivo* rabbit experiments.

The main goal during the data reduction was to compare the four widths (Figure 5-3) and explain why the correlations were not 1.00. The irregularities associated with each width will now be discussed.

Histologic data is notoriously prone to error because the tissue must be sliced at just the right point to attain the maximum width and depth. Generally, many slices are taken and all the slices are examined, a procedure that can get quite expensive. For the lesion in the rabbit liver, only three cuts were made. The histologic widths are further flawed because they were not necessarily cut on the same axis (or in the same directions) as any of the other widths (microscopic, visual, and thermal). The lesions were not symmetric because the visual widths were measured in two directions (width and height) and found to be 0.7 mm higher than wide (on the average). Thus a rather considerable error is introduced by this oversight. The inaccuracies of the histological depths and the measured sectional area are similar to the widths because they

are all measured from the same slice. These irregularities explain why the histologic data is in such poor correlation with all the other data sets.

The microscopic widths were also not measured on the same axis as the other widths. The second problem with this measurement is the judgement call on behalf of the evaluator. Other problems are the shrinkage due to the fixating agent (although it should be uniform), the handling of the tissue during the irradiation, removal and measurement, and the possible changes of the liver within the 9 1/2 hours before the animal was euthanized.

The visual data is probably the most accurate. It was processed very carefully to derive both width and height dimensions. The errors associated with the processing include a 60 Hz noise problem and the unnecessary addition of noise to the video data because the VCR's slowest speed was used.

The thermal widths were inaccurate for several reasons. First, the black bodies were not in view in the image at all times. Second, and probably most important, the background temperature of the livers before irradiation was extremely high. For one particular lesion, the liver was at 57° C before the irradiation. Third, an AC coupling problem in the video board required the data to be offset during the processing. This is just one more step that adds error to the signal (see Chapter 7, "Instrumentation - Video Cassette Recorder"). Fourth, the data was recorded using the VCR's slowest speed, which unnecessarily added noise. Fifth, the calculations for damage did not use the entire temperature curve because only 5 seconds of data was stored. The temperature curves stretched out to 6 to 7 seconds.

#### 5.4 Egg Yoke Experiment

Yang [5-12] used the same experimental setup to create lesions in egg yoke. Her experiment was aimed at verifying the experimental setup and understanding the whitening of protein during laser irradiation. The laser power was 2.5 watts, the spot size was 3.3 mm, and the laser durations varied from 4.5 seconds to 17 seconds. Her data is tabulated in Table 5-2. Microscopic data was measured using a microscope and visual data was measured with the video camera.

Data Sets Correlated	Correlation Coefficient
1. microscopic width <u>versus</u> visual width	0.77
2. microscopic depth <u>versus</u> central reflectance	0.89
3. microscopic volume <u>versus</u> total reflectance	0.96
4. microscopic width <u>versus</u> microscopic depth	0.96
5. visual width <u>versus</u> central reflectance	0.71
6. total reflectance <u>versus</u> central reflectance	0.94
7. total reflectance <u>versus</u> visual width	0.65

Table 5-2 The correlation coefficient for several data sets from lesion in egg yoke [5-12].

Notice the strong relationship between microscopic depth and central reflectance (which is the change in intensity of the detector imaging the center of the lesions). This data lends support to the hypothesis that the reflectance at a location relates to the depth of the lesion at that location. Also notice the strong correlation between the microscopic volume and total reflectance, but the poor correlation between the microscopic volume and visual width, which substantiates Weinberg's data discussed in "Previous Work" above. This data also provides some confidence that the system is working well. The poor correlation between visual width and micro-

scopic width is unexpected and can probable be attributed to the method of background subtraction and 60 Hz noise (the background subtraction is discussed under "Lesion Control Criteria" and the 60 Hz noise is discussed under "Problems and Suggested Improvements").

### 5.5 *In Vitro* Beef Liver Experiment

The same setup was used in this experiment as in the *in vivo* rabbit experiment. An *in vitro* beef liver purchased at the grocery store was used as the target tissue. The computer was programmed to open the shutter, monitor the width of the developing lesion, and close the shutter when the width reached 8 pixels (2.56 mm). This routine always monitored column 19 (chosen by the operator by examining a lesion burn). The threshold that each pixel in the column was compared against was 50 gray levels. If a pixel exceeded the threshold, then the width of the lesion was assumed to be one pixel larger. This threshold was chosen by the operator by examining a lesion burn. The value represented about 8 gray levels over the noise of the detectors. Background data was not subtracted from the data before the threshold was applied.

A total of 33 lesions were attempted. Two of the lesions were stopped by the computer prematurely (the shutter was not open for more than 16 ms). These false triggers were probably caused by the detectors sensing the laser's plasma light (discussed under "Problems and Suggested Improvements"). After the lesions were create in the liver, the tissue was placed in buffered formalin solution.

The minimum and maximum microscopic width of each lesion was measured and averaged to derive one width measurement for each lesion. All of these were then

averaged for all the lesions. The average width of all these lesions was 2.77 mm and the standard deviation was 0.343 mm (notice the standard deviation is equal to the discrete distance of one pixel). The duration of the burns varied from 533 ms to 1100 ms.

The conclusion from this experiment is that the system was very successful in controlling the microscopic widths of the lesions. The standard deviation was only 13% of the average width and the average width was within 8% of the desired width. The difference in the desired and actual lesion widths is probably caused by the lesion's slight growth after the laser is turned off (discussed in "Lesion Control Criteria"). These good results were attained in spite of the system problems, discussed under "Problems and Suggested Improvements".

## 5.6 Problems and Suggested Improvements

Some of problems and suggested improvements with the experimental setup and procedure follow:

1. The rabbit liver must be immobilized, kept perpendicular to the laser irradiation, and always in the focal plane of the two cameras. This is not a trivial problem to overcome because the liver is tucked underneath the rib cage and requires a gentle yet firm handling to properly isolate it and make it accessible. In the *in vivo* rabbit experiment, all three problems introduced error.
2. There is some question as to the length of time the rabbit should survive following the insults on the liver. The question that is associated with this question is, "How does the damage directly after the laser insult compare with damage hours, days and weeks later?" Granted this is another interesting item to research, but in

these experiments another independent variable should be avoided. It is also suggested that the animals should not live very long after the lesions are created in the liver.

3. Investigate the best method of fixing the tissue: either immersing the liver in buffered formalin solution, injecting gluteraldehyde into the circulation system of the rabbit, or freezing the liver quickly. Insure that the lesions are spaced adequately so that the pathologist can make the cut in the proper direction. Insure that each lesion is marked as to the direction that the cuts should be made. The idea is to calculate the histologic, microscopic, visual, and thermal widths in the same direction on a particular lesion. The microscopic measurements should be done before they are sent to the pathologist. Insure that the pathologist makes ample cuts to get the maximum widths and depths. Each lesion should also be photographed with a 35 mm camera using a close up lens directly after the lesion is formed. The photographs must be taken so that accurate widths can be measured from the picture.

4. The animal's temperature must be measured and controlled. This includes both the animal's rectal temperature and the liver's surface. The surface temperature of the liver is difficult to control for several reasons. First, it's exposed. Second, it's drying and needs to be moistened. Third, the illuminating lights are focussing a lot of energy onto the liver. Fourth, it's being irradiated with a laser. All of these need to be taken into account so that the thermal data is accurate and damage does not occur before the laser irradiation. The liver's surface temperature should also be recorded with the thermal camera at least during the previous minute before irradiation. Insure that the moisturizing water is at the same temperature as the liver and that it is constantly applied (maybe with a drip mechanism). In the *in vivo* rabbit experiment, the surface

temperature of the rabbit's liver was about 52 ° C, with some as high as 57°. There is an excellent possibility that damage occurred before the laser ever irradiated the area. At the very least, the tissue was "primed" by this elevated temperature. Damage calculations yield  $\Omega = 0.51$  if the liver is maintained at 57° C for 50 seconds (see Chapter 2, "Anatomy and Light Interaction of the Eye - Tissue Optics and Damage").

5. The thermal camera measurement must be taken with care. The difficulty with the thermal camera measurements is that these are absolute and not relative measurements. The black bodies must be placed in the image on the same row as the developing lesion. The temperature of the black bodies must be recorded at the time of the laser irradiation. Insure that the room temperature is recorded frequently. Insure that the specular reflections from illuminating light are not oriented toward the thermal camera. Insure that the thermal data is not saturating by monitoring the thermal video signal with an oscilloscope. Always record on the VCR's fastest speed and insure the recording heads are cleaned periodically. In processing the thermal data, insure the VCR heads are again cleaned and the DC offset problem is corrected on the video digitizing board (see Chapter 8, "Instrumentation - Video Cassette Recorder"). When stripping data from the VCR during data processing, choose the center of each lesion as accurately as possible. The lesion's center generally does not maintain its position from lesion to lesion.

6. The 32 x 32 detector system has its own set of problems. Insure that the camera is fully warmed before using it (turn it on 2 hours before use). Find a cooler source of illumination other than tungsten, such as a semiconductor laser (see Chapter 8, "Instrumentation - Video Camera used for Lesion Monitoring"). The tungsten lamp significantly heated the rabbit and liver. The light being fed to the camera must be



filtered to exclude all energy except the illumination source. In many of the lesions, the video camera detected an immediate increase in reflection even though the laser energy light was filtered extensively (five filters were used, each with an attenuation of  $10^{-5}$  at 514 nm). The light seeping through the filters was probably plasma light from the laser tube. Insure that the overhead fluorescent lights are turned off during the entire procedure. The camera is experiencing a slight 60 Hz noise problem, which could be caused by the overhead fluorescent lights, ground loops, or poor shielding. The 60 Hz noise is seen in the video data as a sinusoid moving slowing down the image. The noise was sufficient to swamp the signal from the lesion growth when the total reflectance was calculated (all  $32 \times 32$  pixels are added). When processing the data, each lesion must be examined individually to find its center pixel. The width calculation requires that the background be subtracted. Do not use an average background. Instead, use a pixel by pixel background (i.e. store each of the 1024 pixels values before the lesion formation and subtract this frame from the frame used to calculate the lesion's width).

7. When the computer performs real time lesion control, insure that the video signal from the camera is fed directly to the computer and VCR simultaneously. In the *in vitro* beef liver experiment, the signal to the computer came from the output of the VCR. This induces unnecessary noise and a time delay onto the signal.

8. Insure that the laser's intensity profile is symmetric (height versus width) by using the edge technique measurement. Also insure that the laser's profile is gaussian.

### 5.7 Lesion Control Criteria

At this point, the best method of determining the lesion size is to monitor the width of the lesion in real time. Monitoring one column is sufficient if the lesion is symmetric. The computer must periodically insure that the column it is monitoring is the center of the lesion. It should be possible to optically align the laser and video camera such that the lesion always appears centered at the same location in the video image (even though the system used in this experiment appeared to drift somewhat). A background reading must be taken within 5 seconds prior to the irradiation. The background reading is not an averaged reading but consist of each pixel in the column (if the column is unknown or might change, then several or all the columns must be stored as background readings). The variation in the background over the field of view of the camera is too great to use an average value.

The computer knows the pixel separation of the camera at the image plane. For this experiment, 3 pixels equaled a millimeter. The operator selects the desired width of the lesion. During the irradiation, the computer reads the 32 pixels in one column in each frame in real time. Each pixel's background is subtracted from its corresponding pixel in this input column. The computer compares each of the 32 pixels against a threshold. The threshold is generally about 5 to 8 gray levels. (When a pixel's gray level versus time is plotted, there is an envelope of noise associated with the plot. A threshold slightly above this envelope was chosen, which is about 5 to 8 gray levels. Notice that after the background is subtracted, the pixel should be hovering around a gray level of 0, and thus an increase of 5 to 8 implies that this pixel is imaging a point on the developing lesion.) The computer waits until the required number of pixels in the 32 pixel column exceeds the threshold. For example, if 3

pixels equal a millimeter and if the operator desired a 4 mm lesion, the computer would wait until 12 pixels exceed the threshold. The laser shutter would then be turned off.

Because the lesion tends to grow slightly after the laser is turned off, the computer program could predict this extra growth and turn the laser off prematurely. The actual lesion widths in the *in vitro* beef liver experiment, which were slightly larger than the desired width, might benefit from prediction.

Monitoring the absolute depth of the lesion is a difficult problem. The hypothesis that needs to be demonstrated is that the reflections at a location on the lesion corresponds to the depth of the lesion at that location. If this hypothesis were correct, an exponential relationship between intensity and depth might be expected because of a Beer's law absorption. That is, a change in whitening near the surface should be more visible (the reflections are not absorbed in the tissue) than a change in the whitening deeper into the tissue (the incident beam and its reflections are absorbed in the tissue). Many other factors are most likely involved, such as multiscattering, but are difficult to analyze. The data from the rabbit experiments did not show a strong correlation between the histological depth and the center intensity, either linear or exponential. Yang's [5-12] data with egg yoke showed a 0.89 linear correlation between microscopic depth and center intensity. The graph appears to show an exponential curve.

Total reflectance is most likely an indicator of lesion width and depth. But, the difficulty with using either central or total intensity to control the lesion size is one of the problems that Pomerantzeff *et al.* had encountered. How can absolute measurement be derived from the data? In other words, if the detector reads a change in

central intensity of 60 gray levels from the reflecting light, how deep in millimeters is the lesion at that point? The same problem occurs with total reflectance. The system would require an absolute calibration, which is very difficult to achieve in equipment used in a clinical environment on a varied population of patients.

Other criteria might also relate to lesion size. These include the time rate of change in either the total reflectance, width, or depth.

### 5.8 Conclusion

The data on the *in vivo* rabbit liver was inconclusive because of experimental procedure and equipment problems. A highlight of this chapter was the success of the video camera in controlling lesions in the *in vitro* beef liver. The standard deviation of the resulting widths for 31 lesions was 13%. The average of the resulting widths was only 8% larger than the desired width. Yang's egg yoke data supported the hypothesis that the intensity at a location is related to the depth of the lesion at that location. Her data also showed the strong correlation between the microscopic volume and total reflectance, but the poor correlation between the microscopic volume and visual width, which substantiates Weinberg's data. Many suggestions have been made which can only improve the quality of the data in future experiments. It would appear that there is an excellent chance that the width of the lesions can be quantitatively controlled and the depth can at least be qualitatively and possibly quantitatively controlled.

## Chapter 6 Retinal Image Processing

### 6.1 Introduction

This chapter will discuss the retinal image processing system. Video images of the eye can provide quantitative measurements of many aspects of the fundus. The data can be processed to detect features that are buried under the spatial, temporal and chromatic contents of each image.

The goal of this system, when used with a robotic laser, will be given first. Next, an overview of video funduscopy will be provided. Retinal image analysis, which can be divided into spatial, temporal and chromatic studies, will be reviewed. This will be followed by a discussion on the prospects of using computer vision in the automatic detection and treatment of retinal disorders. A case study on diabetic retinopathy will demonstrate the complexity of this task, but show that the computer can identify retinal blood vessels and select lesion locations for panretinal photocoagulation.

There are many pathologies of the retina that can be treated with laser irradiation. These pathologies require many methods of lesion placement. When used in conjunction with a robotic laser, the goal of the retinal image processing system is to identify and locate the pathology, and then select the specific area(s) where the lesion(s) must be placed to properly treat the pathology. Lesion size must also be

specified. The locations and desired lesion sizes are then passed to the tracker and laser delivery system.

This goal, though simply stated, is a monumental artificial intelligence task. Ophthalmologists and researchers are still in the primitive stage of developing rigid guidelines for the detection and treatment of retinal disorders. Once these guidelines are somewhat established for the human operator, maybe they can be used by a computer to detect and treat retinal disorders.

## **6.2 Video Funduscopy**

Video funduscopy is the imaging of the fundus using a video camera. In 1950 Harold Ridley used an orthicon tube camera to view the fundus [6-23]. The camera was quite bulky (about 2 feet long) and was mounted about 3 feet above the supine patient. Since the fundus camera had not been developed, one of his difficulties was the corneal reflex (reflections from the cornea). His problems also included insufficient light sensitivity of the camera and bulky equipment. Nonetheless, the blood vessels that exit from the optic disk were distinguishable in his images.

Potts continued this work in 1958 and experimented with spectral video imaging [6-21 and 6-28]. A workshop on television ophthalmoscopy in 1965 examined the idea of using the video camera in ophthalmology. They concluded that "the development of television ophthalmoscopy would require extensive research in several disciplines and would necessitate collaborative effort" [6-25]. In 1973 Van Heuven and Schaffer designed an image intensifier for their camera and performed video fluoroscopy, which is the video imaging during fluorescein angiography (discussed below) [6-29].

The retinal image processing systems started to evolve in the late 1970's [6-22]. The breakthrough that allowed these systems to become commercially feasible occurred in the early 1980's when both the light intensified cameras and the video digitizing boards became commercially available. Several companies are now marketing commercially available systems [6-4, 6-13, 6-14, 6-18, and 6-19]. These imaging systems are capable of performing a host of processing tasks, such as fluorescein angiogram evaluation, contrast enhancement, edge sharpening, optic disk measurements and image correlations.

### 6.3 Retinal Image Analysis

The analysis of the retinal images can be divided into three categories: spatial, temporal, and chromatic [6-6]. These categories are dependent and can be collectively used to analyze an image. Each of these will now be discussed.

#### 6.3.1 Spatial Analysis

Spatial studies analyze the static morphologic features of the fundus. These features are visible in a video image and include the optic disk, blood vessels, hemorrhages, exudates and the retinal nerve layer. Different algorithms and combinations of algorithms are geared toward detecting specific features and aspects of the fundus.

Two important characteristics of the optic disk are pallor and cupping. According to Schwartz [6-17], pallor is associated with the area of maximum contrast or the area lacking small blood vessels. Cupping is the depression of the optic disk surface. In normal eyes these coincide, but in patients with glaucoma the area of cupping is greater than the area of pallor. The quantitative measuring of the pallor and

cupping of the optic disk can lead to an early diagnosis of glaucoma. Nagin and Schwartz state that, "evaluation of these signs has been mostly subjective and differs considerable from observer to observer" [6-17]. They and other researchers have developed algorithms that identify the optic disk in the digitized image and measure these two parameters [6-1 and 6-5]. These methods involve either histogram analysis or boundary tracking. Nagin and Schwartz also state that, "there is a potential for an extremely high degree of sensitivity in detecting small changes in high resolution digital imagery".

The retinal nerve fiber layer is another feature that can be detected with computerized enhancements. Defects in the nerve fiber layer are an indicator of optic nerve disorders. This layer appears as striations, or parallel lines, in a video image. Defects in this layer appear as dark grooves with diminished striations and brightness [6-20]. These fibers are often buried in the other features and artifacts of the retina. Peli *et al.* [6-20] used histogram modification, extremum sharpening, directional oriented spatial frequency filters, and adaptive image enhancement to detect this layer. Their filters were divided into those that enhance features of the normal nerve retinal fiber and those that enhance features of the abnormal nerve fiber layer.

The identification of blood vessels is another important task for the image processing system. Akita and Kuga identified blood vessels by first using a local line detection algorithm, and then labeling and combining the lines to make a skeleton of the retinal vascular system [6-1]. They located the boundaries of the blood vessels and were successful in detecting hemorrhages and exudates. Exudates are deposits from leaking blood vessels and are indicative of several disorders of the retina. Their



results appear to be very effective but they mentioned that a statistical data base needs to be developed to get better coefficients for their algorithm.

Several investigators are examining the fundus and the iris during fluorescein angiography with a video camera [6-12 and 6-27]. This is called video fluoroscopy. Fluorescein angiography involves injecting a fluorescent dye into the patient's cardiovascular system and monitoring the dye with a video camera or time-lapse photography as it circulates throughout the body. The blood vessel become very distinct during fluoroscopy and leaks in the vasculature are easily detected. Tamura *et al.* [6-27] measured the areas of fluorescein leaks.

Stereo imaging of the eye is done routinely with slitlamp microscopes but only sparingly with fundus cameras [6-8]. An image processing system by IPS [6-14] provides depth profiles from the stereo pairs of a camera mounted on a slitlamp microscope. Many other researchers [6-9 and 6-16] have also examined stereo matching algorithms.

### 6.3.2 Temporal Analysis

Temporal studies analyze more than one video image and weaves the time dependency into the calculations. This type of analysis is by far the most difficult to perform from an instrumentation viewpoint. Applications in this area generally involve the circulation system, such as fluoroscopy.

Greene and Thomas successfully measured the blood flow in the retinal circulation system during fluoroscopy [6-11]. They used specialized gating hardware to monitor specific pixels in the video image. Fluoroscopy is also useful to evaluate

retinal artery and vein occlusions, neovascularization, hemorrhages, vascularized tumors, or vascular leaks [6-6].

Temporal studies can also be used to approximate the retinal artery blood pressure and pulse transmission from the heart to the retina [6-6].

### 6.3.3 Chromatic Analysis

Chromatic studies involve the analysis of an image when viewed in monochromatic light. As discussed in Chapter 2, the properties of the eye are dependent on the wavelength of light. Thus each structure in the fundus is sensitive to varying wavelengths, and this fact can be exploited by using the proper wavelength of light to view different structures. Three images of the retina in red, green, and blue illumination are shown in Figure 6-1 [6-3]. Behrendt and Wilson developed Table 6-1, which summarizes the features of the fundus that are visible in different spectral regions [6-2]. Notice in Figure 6-1(B) that the vasculature in green light is very distinct, as expected from the discussion in Chapter 2 and from Table 6-1. Also notice the lack of arteries in Figure 6-1(A) and the nerve fiber layer in Figure 6-1(C). This also agrees with Table 6-1.

A host of researchers have examined this area, starting with Vogt in 1921 [6-30]. The images that Peli *et al.* used in their examination of the nerve fiber layer were taken with green interference, red-free filters [6-20]. But Manor *et al.* found that green light at 540 nm provided better images than the red-free filters when examining the nerve fiber layer [6-15]. It's not the intent of this section to fully review this area, but only to make the point that chromatic analysis is extremely useful.

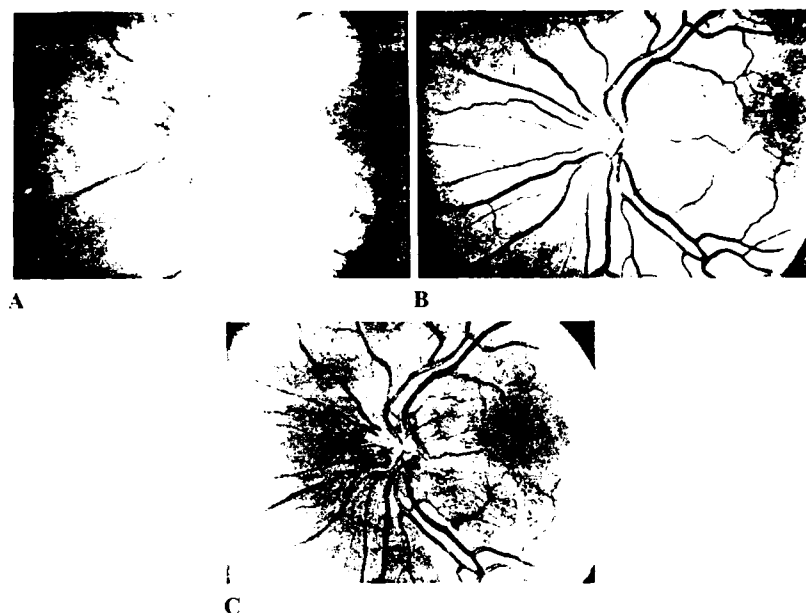


Figure 6-1 Normal fundus as seen in (a) red, (b) green, and (c) blue illumination [6-3].

SUMMARY OF FUNDUS ASPECTS IN THE DIFFERENT SPECTRAL REGIONS\*

Structure	640 nm (deep red)	606 nm (red)	577 nm (yellow-green)	519 nm (green)	504 nm (green-blue)	477 nm (blue)	431 nm (deep blue)
Papilla	Peaky white ← Poor vessel detail		Darkening begins, better vessel detail	Darkening, increasing vessel detail	Darkening, clear vessel detail	Dark	Darker than ad- jacent retina
Circumpapillary area	Patches of choroidal pigment						Excellent vessel detail
Macula	Invisible	Starts to appear	Uniform appearance ← Vessels appear as in other retinal areas		Dark spot Three zone pattern		Start to disappear
Vascular area	Choroidal pigment pattern visible at least to some degree		Striation may no longer be present				
Vessels							
1. Major vessels	Artery invisible veins visible	Artery starts to appear, veins visible and clearer than artery	Rather uniform ← Artery dark but not quite as dark as veins	Striations due to neurofiber layer		Arteries and veins equally dark	
2. Smaller vessels	Invisible	Artery visible some larger arteries start to appear					
3. Smallest vessels	Invisible	Invisible	Start to appear				
							Best visibility of most groups
							Interference from vitreous floaters or adjacent tissue reflections

Table 6-1 Summary of fundus aspects in the different spectral regions [6-2].

One potentially important area is the use of near infrared light (650-900 nm) to view the fundus. Dallow showed that this band of light could penetrate retinal and vitreous opacities in diabetic retinopathy [6-7]. Thus, even though the human eye can not see through the opacities (because the human observer's cones are not sensitive to infrared), video cameras can see the retina in the infrared (because this energy does pass through the anterior part of the eye and some video cameras are sensitive to infrared energy).

#### **6.4 The Detection and Treatment of Retinal Disorders**

This section will discuss the prospects of using computer vision in the automatic detection and treatment of retinal disorders. Yamamoto and Yokouchi recognized this concept in their paper titled, "Automatic Recognition of Color Fundus Photographs" [6-31]. They stated that "(with) the increasing occurrence of geriatric disorders, the quantity of work could well exceed the capacity of the physicians available". They developed a simple recognition algorithm for semi-automatic reading and diagnosis of fundus photographs. Their algorithm is shown in Figure 6-2. They did not develop the software package for the algorithm.

The term streak pattern and spot pattern refers to the general appearance of the feature being detected, either as a streak of information or a spot of information. They stated that the crossing phenomenon is the most difficult to detect, and the remainder of the paper examined the detection of the crossing phenomenon (crossing of a vein and artery).

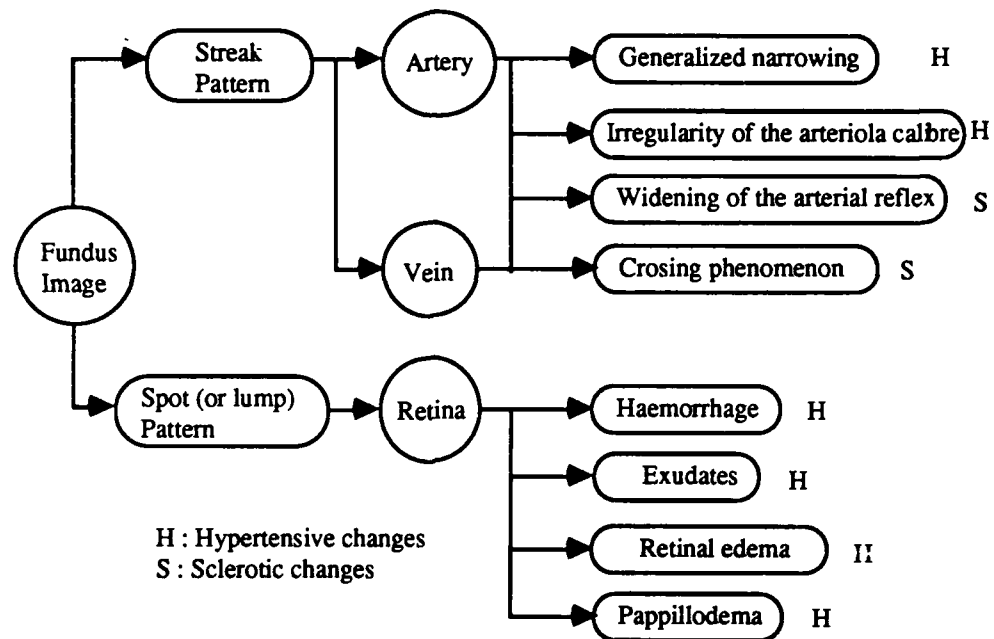


Figure 6-2 Technical classification of fundus changes [6-31].

This algorithm only detects symptoms of a disease. It does not deduce or suggest the disease, nor does it make any therapeutic suggestions. The following case study will illustrate the magnitude of this latter task.

### 6.5 Diabetic Retinopathy - A Case Study

To fully grasp the magnitude of the artificial intelligence task to achieve the goal stated earlier, the diagnosis and treatment for diabetic retinopathy will be discussed. An algorithm will be presented that detects blood vessels in a retinal image, and then lesions will be overlaid onto the filtered image.

### 6.5.1 Diagnosis and Treatment of Diabetic Retinopathy

Diabetic retinopathy is a complication of diabetes. In the USA, about 5% of the population has diabetes [6-10], and diabetic retinopathy is the leading cause of adult blindness in the more "developed" countries [6-24]. Diabetic retinopathy was not a problem until 1921 when Banting and Best discovered insulin. Before that time, diabetics died before developing diabetic retinopathy. Now that diabetes is controlled, its complications must also be controlled.

The onset of this disease always starts with a diabetic, progresses to retinopathy (any noninflammatory disease of the retina), then to preproliferative retinopathy, and finally to proliferative retinopathy. Diabetic patients without retinopathy are recommended to have yearly examinations. If any manifestations of retinopathy develop, then more frequent examinations are recommended. This stage is detected by a moderate number of microaneurysms or intraretinal hemorrhages. The signs of the next stage, preproliferative retinopathy, are retinal ischemia, which includes cotton-wool spots, beaded retinal veins, and/or intraretinal microvascular abnormalities. These individuals should have their eyes checked every four months. In the last stage, proliferative retinopathy, fluorescein angiograms will show both profuse leakage of fluorescein dye from the neovascularization and also wide-spread areas of retinal capillary non-perfusion. The blood from these individuals will show an increased level of hemoglobin A<sub>1C</sub> [6-24].

Photocoagulation is recommended if an eye shows at least three of the following risk factors: (1) vitreous or preretinal hemorrhage, (2) any retinal neovascularization, (3) optic nervehead neovascularization, and (4) moderate or severe retinal neovascularization [6-24]. These eyes have an extremely high risk of progressing to

severe visual loss. The treatment guidelines for this disease have been somewhat established [6-26]. As discussed in Chapter 2, the treatment is to place 1200-1600 lesions in all areas of the retina except the fovea, optic disk, and blood vessels.

This discussion illustrates the complexity of properly diagnosing proliferative diabetic retinopathy. Computer algorithms will have to be quite sophisticated to perform this single task, and even more sophisticated to diagnose all retinal diseases. The following two subsections will show how a computer can identify blood vessels and then select the lesion locations for this disease.

#### **6.5.2 Detection of Retinal Blood Vessel**

Assuming that a digitized image already exists in the computer's memory (which is discussed in Chapter 7), the next step is to identify the fovea, the optic disk, and blood vessels. These areas must not be irradiated. From previous discussions, it was shown that the computer can locate the optic disk and blood vessels. The fovea appears as a small subtle dark disk (1500  $\mu\text{m}$  diameter) about 3000  $\mu\text{m}$  temporal to the optic disk between the superior and inferior arcades. Locating the fovea strictly by contrast is difficult if not impossible. Its position must be fixed by locating the optic disk along with the blood vessels comprising the superior and inferior arcades. A safe alternative is to allow the ophthalmologist to locate the fovea using a computer mouse.

Once these features are identified, the computer can fill all other locations with lesions. Often, these lesions will be 200  $\mu\text{m}$  in diameter and placed 100 to 200  $\mu\text{m}$  apart, but the ophthalmologist will make the final decision. The blood vessel



detection algorithm used here is slightly different than the those reported in the literature. This routine will now be discussed, followed by the lesion insertion algorithm.

### 6.5.3 Detection of Retinal Blood Vessel

The picture shown in Figure 6-3 is a digitized video image of a retinal photograph, printed on a Versatek printer. The spatial size of this image is 512 x 512 pixels. To reduce computation time, the image was reduced to a size of 256 x 256 pixels.

Since the blood vessels appear darker against the background, it would seem that a simple thresholding would be appropriate. A plot of a single row in the image is shown in Figure 6-4. The horizontal line is the row being plotted, and the insert on the top of the figure is identical to the superimposed plot. Notice the downward spikes when the horizontal line crosses a blood vessel. This plot was also used to measure the width of a blood vessel in pixels. The thickest blood vessels 13 pixels wide, which corresponds to 14  $\mu\text{m}$  per pixel if the blood vessel is 180  $\mu\text{m}$  wide. Notice that the background DC level is not constant over the entire picture and a lot of high frequency noise (or unwanted data) is also present in the data. Simple thresholding will not work unless the DC content is removed from the picture.

Since both high and low frequencies must be removed, the Laplacian of the Gaussian seems ideal. The filter is called the  $\nabla^2\text{G}$  operator. The equation for this global operator in two dimensions is [6-16]:

$$\nabla^2\text{G}(\mathbf{r}) = -\frac{(1-r^2/2\sigma^2)}{\pi\sigma^4} \exp\left(-\frac{r^2}{2\sigma^2}\right) \quad (6-1)$$



Figure 6-3 Picture (512 x 512 pixels) of the digitized retina using the Versatek printer.

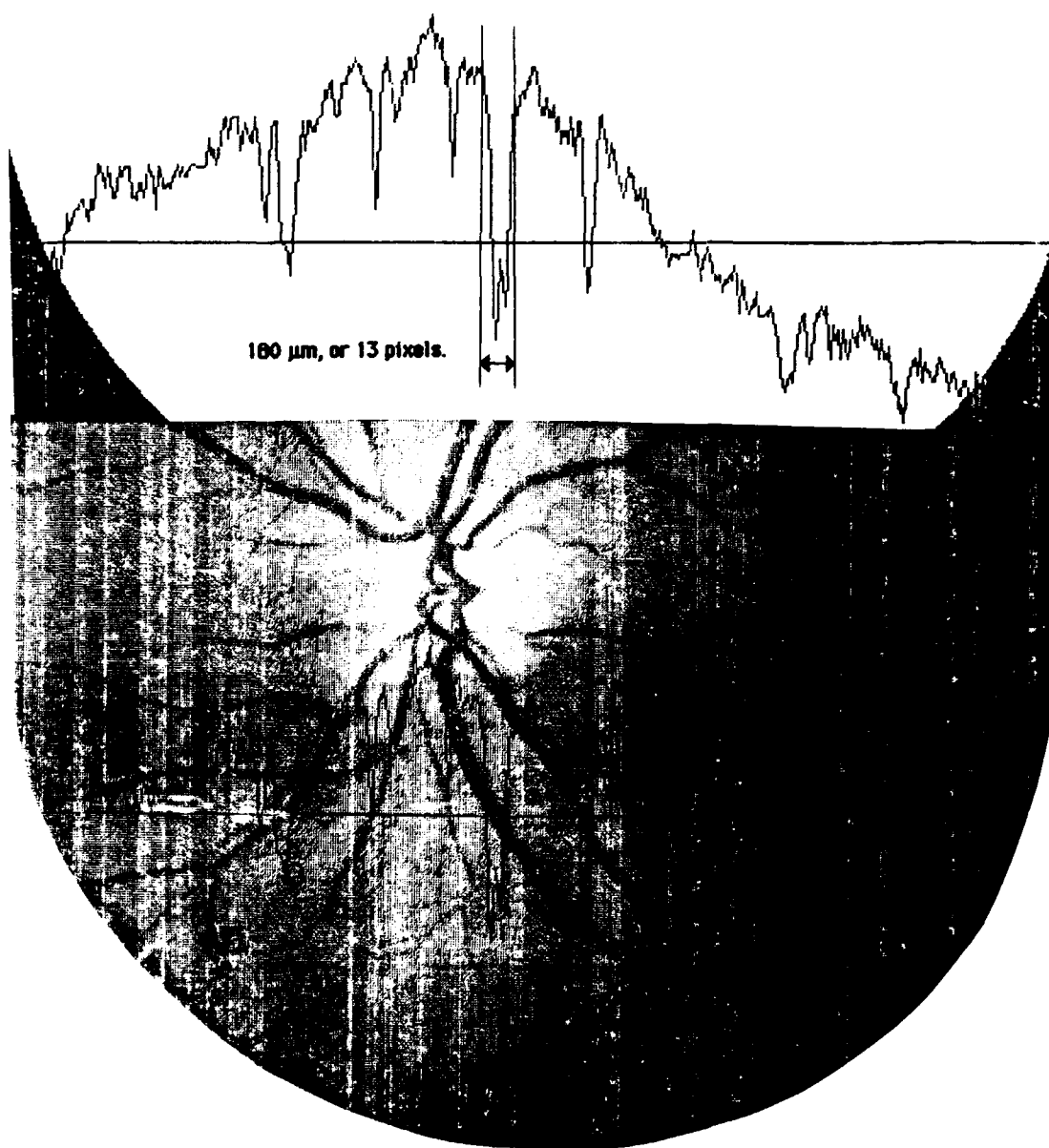


Figure 6-4 Plot of one row of the image. The insert on top is identical to the superimposed plot. The horizontal line is the row being plotted. Notice the downward spikes when the horizontal line crosses a blood vessel. This plot was also used to measure the width of a blood vessel in pixels. For the thickest blood vessel, the count was 13 pixels, which corresponds to  $14\text{ }\mu\text{m}$  per pixel if the blood vessel is  $180\text{ }\mu\text{m}$  wide.

This filter in one dimension is shown in Figure 6-5 [6-16]. The  $\nabla^2 G$  operator is optimum for several reasons. It's isotropic, which is required because the blood vessels are not restricted to any particular directions. It has a unique distribution in that it is simultaneously smooth and localized in both the space and the frequency domains. (Remember that the Gaussian is its own Fourier transform, a property particular only to the Gaussian function.) Its most powerful feature is its ability to perform line detection. As the operator passes over a line, it outputs negative values outside the line boundaries, positive values inside the line boundaries, and the necessary zero crossings at the edges of the line. This operator is most effective on lines that are as wide as the width of the operator ( $2\sqrt{2}\sigma$  in Figure 6-5 (a)). Thus the operator can be fine tuned to detect the right lines. For the remainder of this chapter  $\sigma$  in pixels will refer to the width of the  $\nabla^2 G$  operator (do not confuse  $\sigma$  in this chapter for the scattering coefficient defined in Chapter 2, "Anatomy and Light Interactions of the Eye"). As a side note, there is evidence that this operator closely matches the operator that the human eye uses for its line detection [6-16].

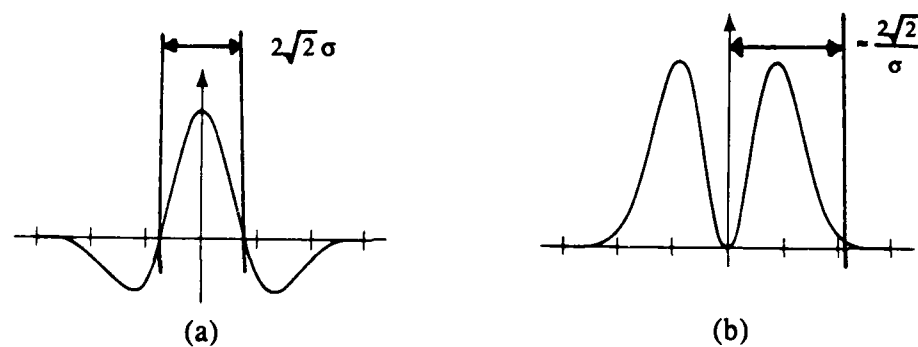


Figure 6-5 The Laplacian of the Gaussian filter ( $\nabla^2 G$ ). (a) This graph shows a one dimensional view. (b) This graph shows the corresponding Fourier transforms. Notice that the  $\nabla^2 G$  operator is a band-pass filter with its bandwidth dependent on the choice of  $\sigma$  [6-16].

The image in Figure 6-3 was filtered with four different widths:  $\sigma = 0.75$ ,  $\sigma = 1.00$ ,  $\sigma = 1.50$ , and  $\sigma = 2.0$ . A threshold of zero was then applied to each of these results, such that all pixels with a value above zero were replaced with a value of "1" and all pixels with values below zero were replaced with a "0". These binary images are shown in Figure 6-6. Notice that the  $\nabla^2 G$  with the smallest width (Figure 6-6 (a)) allowed smaller blood vessel and some high frequency noise to pass through the filter while the  $\nabla^2 G$  with the largest width (Figure 6-6(d)) tended to smear the high frequency data but detect the larger blood vessels. Not shown are filter widths up to  $\sigma = 5.0$ , which just smeared the data worse as  $\sigma$  became larger.

The images appeared to be detecting too many lines, and increasing the threshold might eliminate the noisy lines but still detect the larger blood vessels. The four images in Figure 6-7 are the same images in Figure 6-6 except the thresholds were 30 for  $\sigma = 0.75$ , 40 for  $\sigma = 1.00$ , 50 for  $\sigma = 1.50$ , and 120 for  $\sigma = 2.0$ . Many thresholds were attempted for all the  $\sigma$  values and those shown in Figure 6-7 appeared to produce the best blood vessel templates at that value of  $\sigma$ . Of all the  $\sigma$ 's and thresholds that were tested for this picture, the best seemed to be  $\sigma = 1.25$  and a threshold of 40. This binary image is shown in Figure 6-8(a).

Even this image appears to have some unwanted noise. Since the noise seems very spotty, both the average and median filters were tried. The result of the averaging is shown in Figure 6-8(b). The binary image in Figure 6-8(a) was multiplied by 10, and then smoothed by replacing each pixel with the average of its 8 neighbors. A threshold of 6 was then applied to produce the binary image. This was the best of many thresholds and resulted in a good blood vessel template. For the median filter,

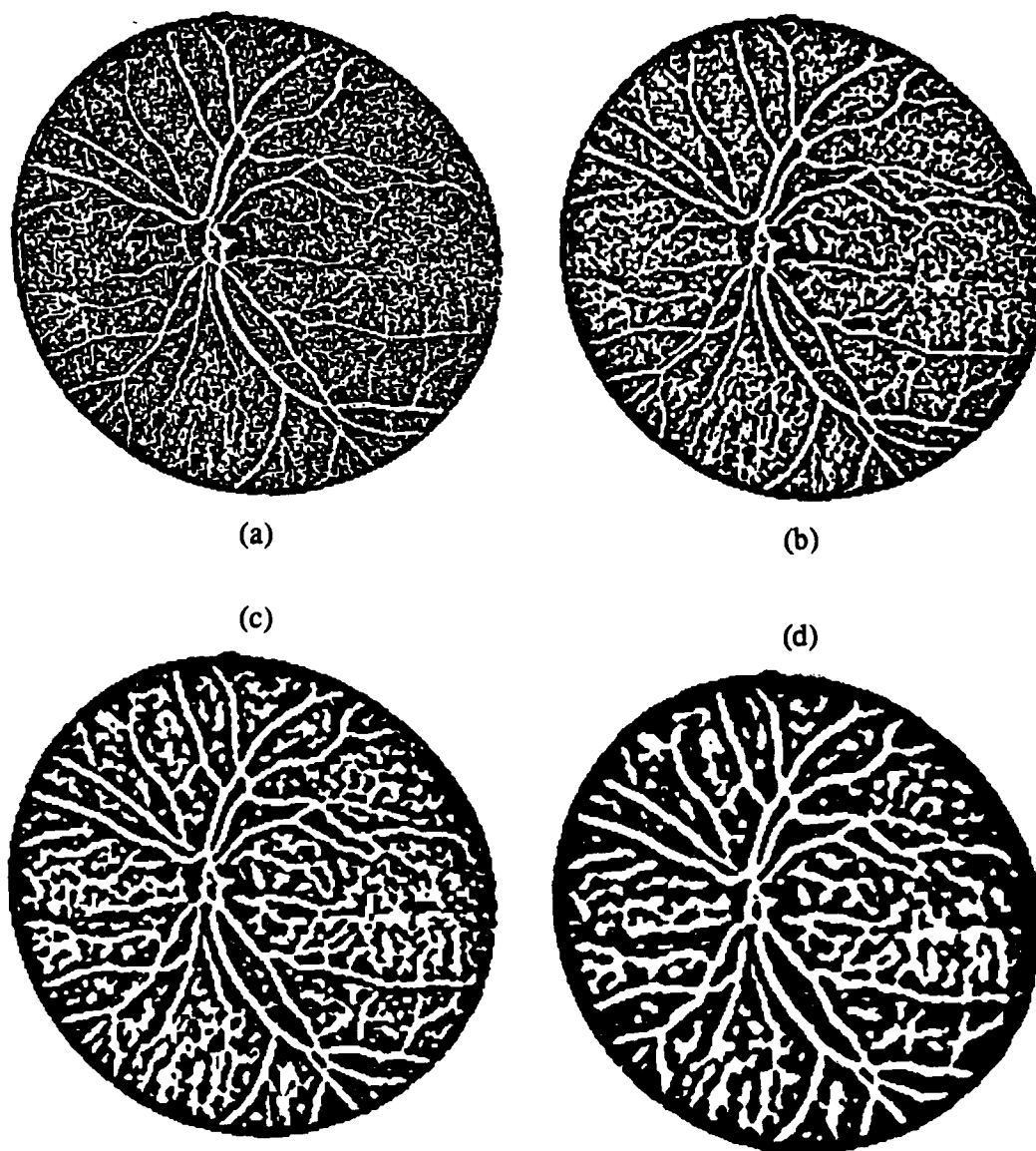


Figure 6-6 The original image was filtered using the  $\nabla^2 G$  operator at four different widths: (a)  $\sigma = 0.75$ , (b)  $\sigma = 1.0$ , (c)  $\sigma = 1.5$ , and (d)  $\sigma = 2.0$ . A threshold of zero was then applied to each of these results, such that all pixels with a value above zero were replaced with a value of "1" and all pixels with values below zero were replaced with a "0".

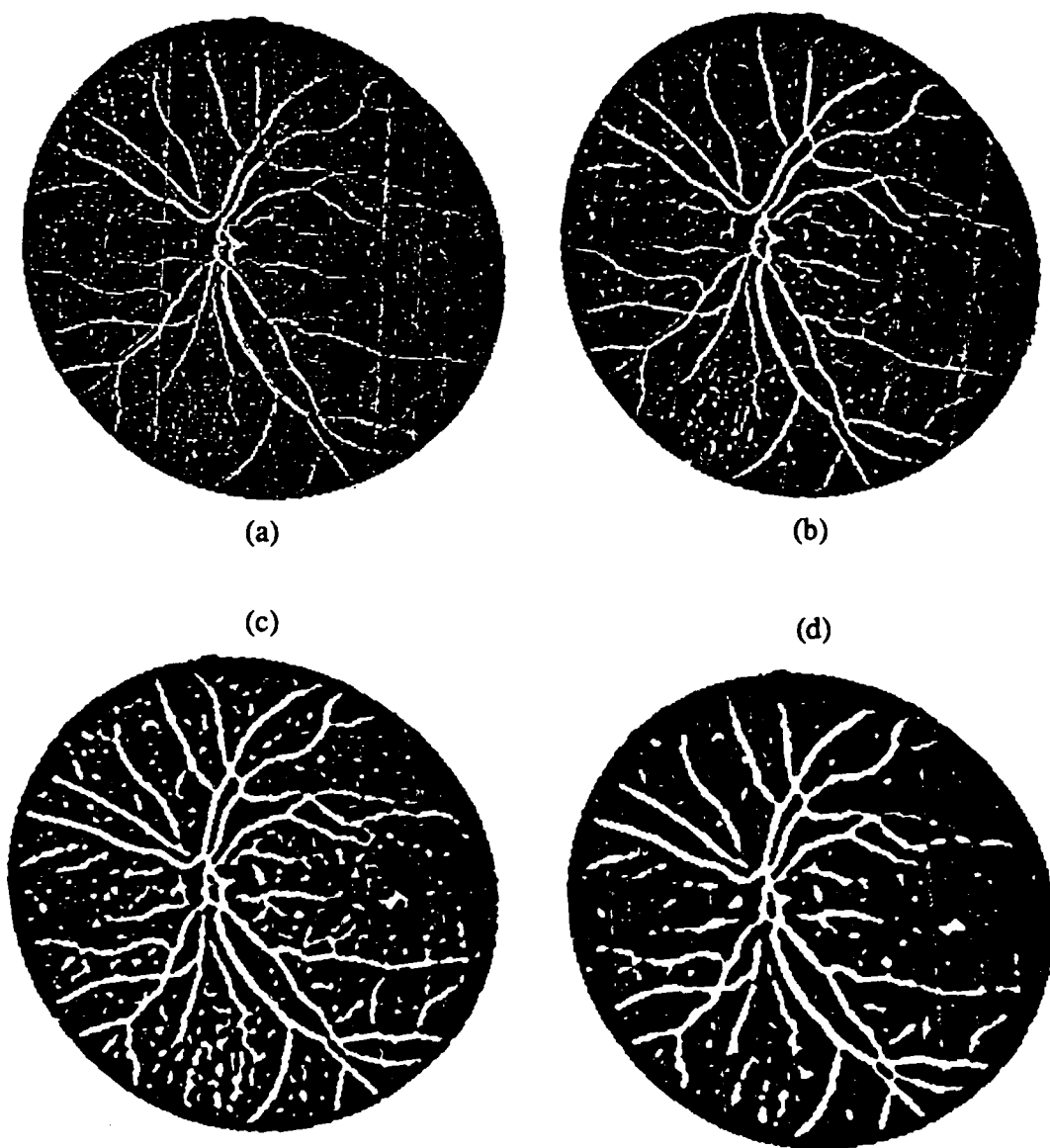


Figure 6-7 The original image was again filtered using the  $\nabla^2 G$  operator at four different widths: (a)  $\sigma = 0.75$ , (b)  $\sigma = 1.0$ , (c)  $\sigma = 1.5$ , and (d)  $\sigma = 2.0$ . Many different threshold were then applied to each of these results, such that all pixels with a value above zero were replaced with a value of "1" and all pixels with values below zero were replaced with a "0". The best results are shown above, which used the following thresholds: (a) 30, (b) 40, (c) 50, (d) 120.

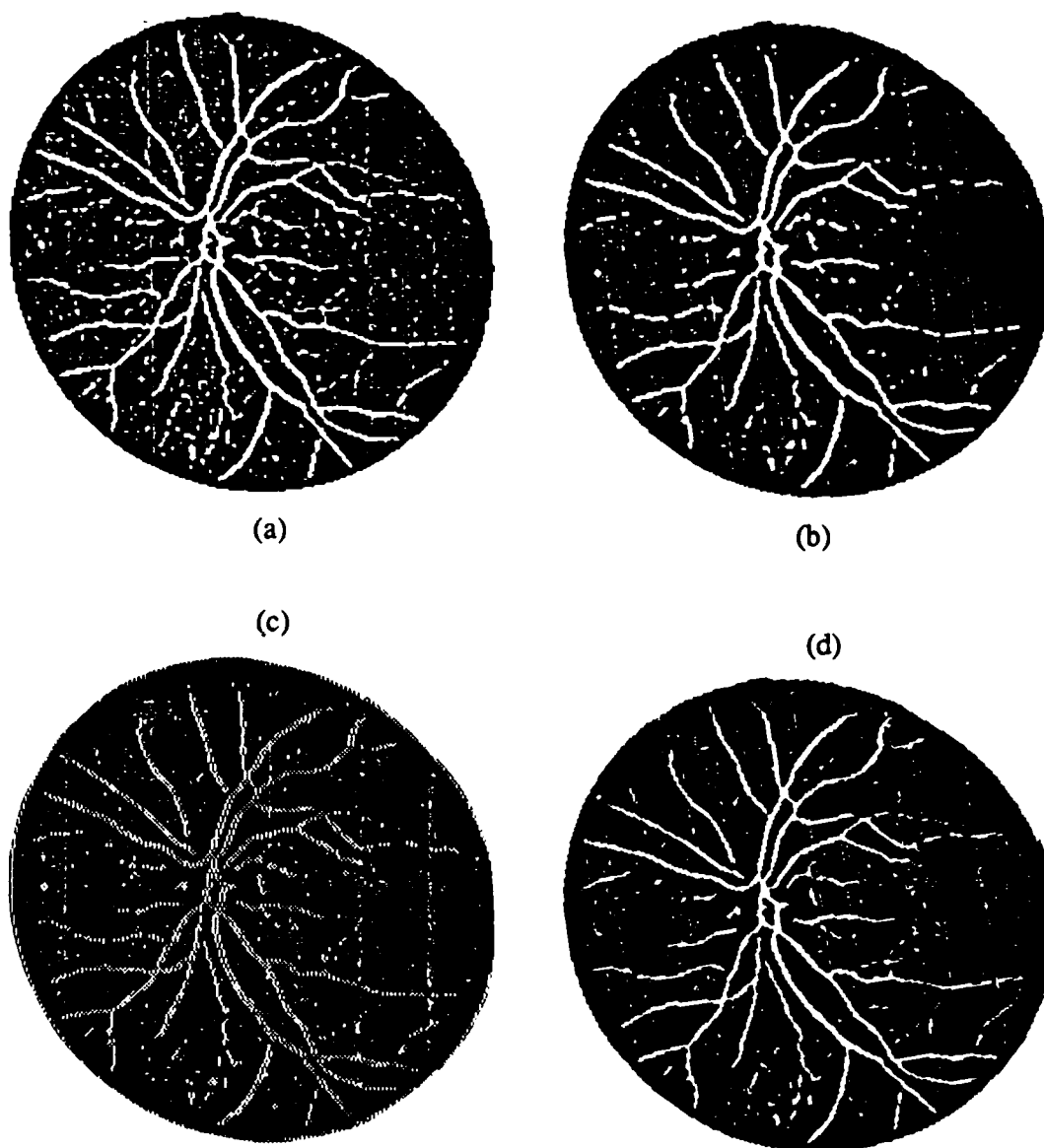


Figure 6-8 (a) The original image was filtered using the  $\nabla^2 G$  operator at  $\sigma \approx 1.25$  and a threshold of 40. (b) The binary image in (a) after averaging and thresholding. (c) The binary image in (a) processed with the median filter. (d) The binary image in (a) processed with a segmentation filter (see text for explanation).



each pixel in the image in Figure 6-8(a) was replaced with the median of its 8 neighbors. The result is shown in Figure 6-8(c), and appeared to chop the image harshly.

The last filter used on Figure 6-8(a) was a segmentation filter shown in Figure 6-9. This is a simple line detector. If a pixel is the center of any one of the four lines shown in Figure 6-9, then that pixel remains a "1", otherwise it was made a "0". The result is shown in Figure 6-8(d). This was the best blood vessel template of all the filtering. This image will be used for the lesion insertion routines.

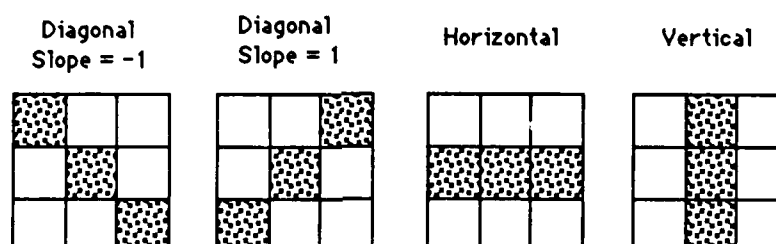


Figure 6-9 The center pixel is the one being examined. If it has at least one of the above neighbors, then the pixel remains a "1", otherwise it is set to a "0".

This final image was good but does not seem to be as good as the work that Akita performed on retinal images [6-1]. Thus, it would seem that even though the  $\nabla^2$  operator is effective, the line following routines used by Akita are better in finding blood vessels in retinal images. Notice also that the segmentation filter could have been more sophisticated [6-5].

#### 6.5.4 Selecting Lesion Locations

The lesions were then superimposed over the final filtered image. A simple mask array of lesions was used to insert lesions into the entire image. The dimensions shown in this mask are adjustable depending on the desires of the ophthalmologist. A hexagonal array is used (Figure 6-10) because it has more lesions per area while still maintaining the required separation. This will produce the most damage to the retina, yet minimize hemorrhaging and patient pain.

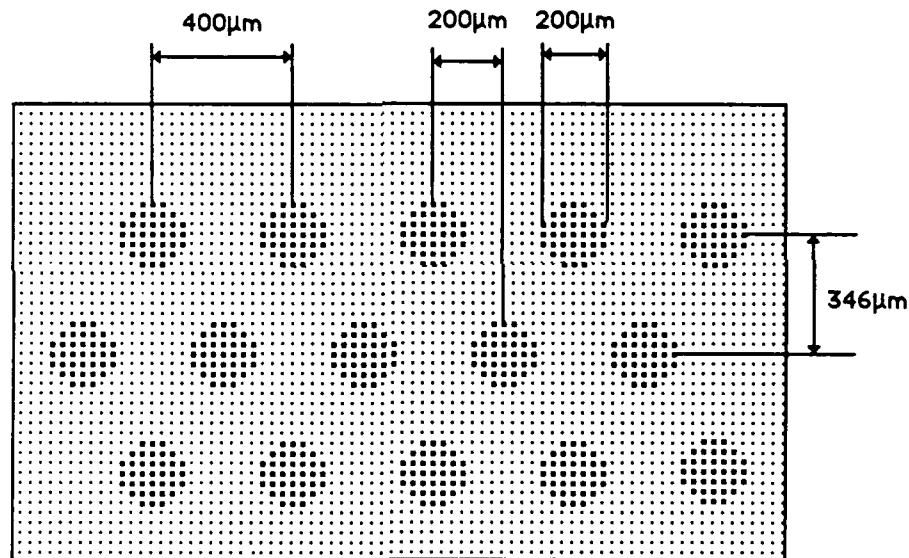
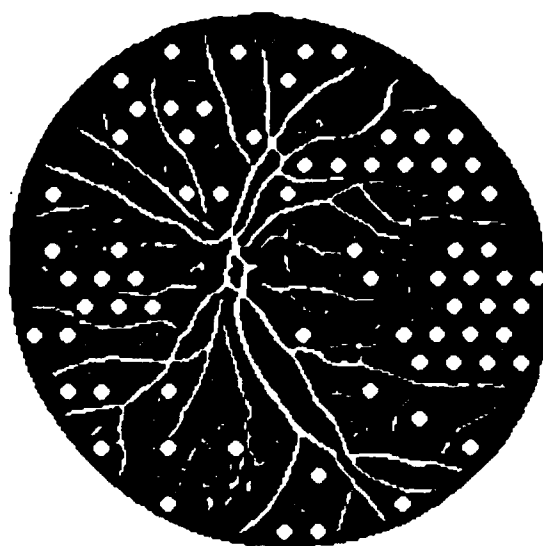
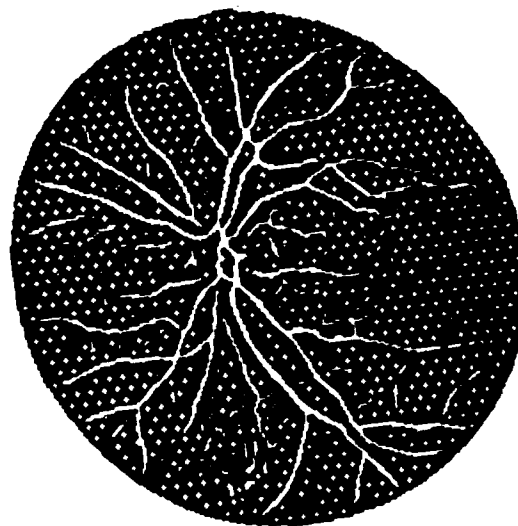


Figure 6-10 Hexagonal array of lesions for widths of  $200\mu\text{m}$  and a separation of  $400\mu\text{m}$ .

A subroutine inserts lesions using the hexagonal pattern into the filtered image of the retina everywhere that blood vessels do not exist. The results are shown in Figures 6-11(a) and 6-11(b). The top image shows lesions inserted every  $400\mu\text{m}$  (center to center) at a width of  $250\mu\text{m}$ , while the bottom image shows lesions in-



(a)



(b)

Figure 6-11 Lesions are inserted into the final image (Figure 6-8 (d)). (a) Lesions widths are about  $250\ \mu\text{m}$  and separated by  $400\ \mu\text{m}$  center to center. (b) Lesions widths are about  $90\ \mu\text{m}$  and separated by  $150\ \mu\text{m}$  center to center.

serted every 150  $\mu\text{m}$  (center to center) at a width of 90  $\mu\text{m}$ . Comparing this to the original image, a satisfactory job has been done at avoiding major blood vessels.

The ophthalmologist should have the capability of selecting areas that are to be irradiated. An algorithm is given in Appendix 1 that can read inputs from the mouse, identify a closed boundary and identify all pixels interior to the closed boundary.

## 6.6 Conclusion

This chapter presented the goal of the retinal image processing system. Video funduscopy was then explained, followed by a review of the spatial, temporal and chromatic studies of retinal image processing. This was followed by a discussion on the prospects of using computer vision in the automatic detection and treatment of retinal disorders, which was found to be an admirable task but exceedingly difficult. Lastly, a simple example demonstrated how the computer can identify retinal blood vessels and then select lesion locations for panretinal photocoagulation.

## Chapter 7 Instrumentation

### 7.1 Introduction and Hardware Overview

This chapter will examine the instrumentation and substantiate the engineering decisions for the proposed design.. An overview of the hardware schematic for the proposed system will be presented first and each subsystem will then be examined. The fundus camera will be discussed in detail. Video camera specifications and their relevance to this project will be reviewed. This will include a discussion on the two video cameras required for this system. A detailed look at the computer hardware and video boards will follow, and then the computer software design will be presented. The laser delivery system and system optics will then be examined. Lastly, the system costs and safety will be given.

An overview of the hardware for the initial system proposed in this dissertation is depicted in Figure 7-1. A fundus camera views the patient's retina. The computer system controls the focussing, field of view, illumination, camera position, point source, and other fundus camera controls. The tracking camera images the same field of view as the fundus camera and provides this image to the computer system. A beam splitter allows the lasers and the lesion camera access to the eye. The two lasers, the surgical and pointing, are maneuvered by the computer system via the servo control mirrors. The computer also controls the laser's spot size, power, and

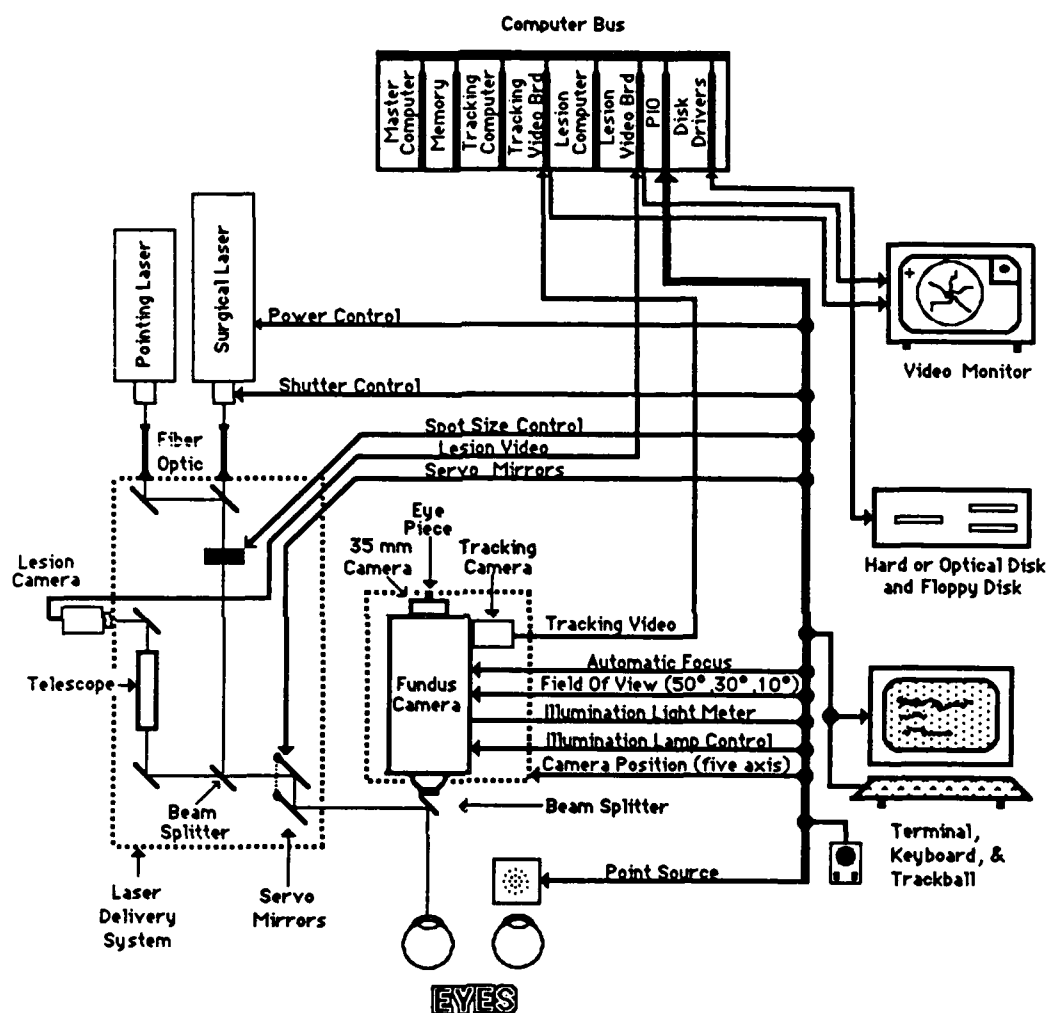


Figure 7-1 Hardware overview of the robotic laser system.

shutter. The lesion camera views the same area that the laser is irradiating. The output of this camera is fed to the computer system.

The computer system is comprised of the master computer, which controls the entire system, the tracking computer, which performs retinal tracking, and the lesion computer, which performs lesion monitoring. The images from the tracking camera and the lesion camera are fed into the tracking video board and lesion video board, respectively. Both images are passed to the video monitor where the retinal image is displayed on the entire monitor and an insert of the lesion image is shown in one corner. The lesion computer has real time access to the digitized data from the lesion camera, and the master and tracker computers have real time access to the digitized data from the tracker camera. The master computer also controls the video terminal, keyboard, trackball, and disk drives.

## **7.2 The Fundus Camera**

This section discusses the fundus camera. An overview will be given first that will review the slitlamp, contact lenses, and the many types of fundus cameras. Imaging with the fundus camera will then be explained followed by a review of the illumination source. This section will conclude with a discussion on the proposed fixating device, video camera pixel separation, autoalignment, stereoscopic fundus cameras, and mosaics.

### **7.2.1 An Overview of Fundus Cameras**

The fundus camera is an optical device that is designed to view and photograph the fundus. A slitlamp microscope (often just called a slitlamp) is a microscope

adapted to view the anterior part of the eye. Presently, laser delivery systems are only interfaced with slitlamps. There are approximately five companies that manufacture ophthalmic laser delivery systems [7-6, 7-11, 7-14, 7-36, 7-41]. Each of these systems use one of three or four slitlamps manufactured by other companies [7-10, 7-26, 7-56]. The fundus camera, as compared to a slitlamp, has the advantages of a superior retinal image and does not require a contact lens to view the retina. The slitlamp is less bulky, less expensive, and has binocular viewing. Because an excellent image of the retina is required for tracking and image processing, the fundus camera is a clear choice.

All laser surgery performed at the present time on the retina uses a contact lens. One reason for this is that all laser delivery systems use a slitlamp, and all slitlamps require a contact lens to view the retina. The advantages of using a contact lens are better coupling of the laser, damping of eye movement, elimination of eye blinks, and a substantial increase in the field of view. Many contact lenses are available for a variety of tasks [7-16], but the panfundoscope contact lens provides a uniform retinal image with a field of view from the posterior pole to the equator (greater than  $130^\circ$ ) [7-5 and 7-37]. The image is inverted and minified with a corresponding reduction in resolution. This contact lens was used with a Zeiss fundus camera and the image quality was found to be very poor. But Nikon [7-43] has introduced an angle magnifying contact lens especially designed for their fundus camera which might provide a better quality image. Nonetheless, since the quality of the image is critical and since automating a device using a contact lens is difficult, the initial design avoids the use of a contact lens.



There are about six companies that manufacture the conventional type of fundus camera [7-10, 7-35, 7-41, 7-43, 7-44, 7-56]. These cameras are called "mydriatic" since pupil dilatation is generally required. Each fundus camera has several operator chosen fields of view. Of all the cameras, the range for the minimum field of view is from  $18^\circ$  to  $20^\circ$  and the range for the maximum field of view is from  $30^\circ$  to  $60^\circ$ . Only the Canon fundus camera reaches the  $60^\circ$  field of view, but it requires a 7 mm pupil dilatation. (It was shown in Chapter 2, "Anatomy and Light Interactions of the Eye", that only 50% of the population can obtain this mydriasis.) All the fundus cameras are manually maneuvered. Most of them allow for 35 mm photography, Polaroid photography, and fluorescein angiography. The cost varies from \$7,000 to \$27,000 [7-33]. Other features not necessarily available on all the cameras are filters, astigmatic correction, nonsimultaneous stereo photography, computerized flash, wide angle contact lens, blink detection, pupil alignment cross hairs, working distance detection, split line focussing and video camera attachments.

There are other types of fundus cameras that are either commercially available or have been discussed in the literature. A non-mydriatic retinal camera [7-9] is used to screen a large number of patients without the inconvenience of pupil dilatation. The camera's capabilities are very limited and it is designed to be operated by individuals with minimal training. Pomerantzeff [7-47] has designed several wide-angle contact and noncontact fundus cameras. His contact camera can image an enormous  $148^\circ$  field of view. This camera has the disadvantages of a limited resolution and camera contact with the patient's cornea. He has also proposed a noncontact fundus camera with a  $90^\circ$  field of view. This design requires the camera's objective to be very close to the eye. He also presented the design for a small-angle contact camera

that was later used by Bronstein *et al.* [7-7] in their Macula-Disk camera. This camera provides a magnified (6.8X) image of the fundus features. A stereoscopic fundus camera will be discussed below in "Stereoscopic Fundus Camera".

The Scanning Laser Ophthalmoscope [7-34, 7-38, 7-59, 7-60] uses a laser to scan the retina as a photomultiplier tube measures the reflected light from the retina. This system has great potential and might be the basis for future fundus cameras. Its advantages are minimal illumination, increased depth of field, versatility, and convenient video camera interface. A noteworthy application for this camera [7-59] is to coalign the surgical laser with the pointing laser and insert lesions at the proper time during the scanning process. On one scan the surgical laser would pulse a small area, and then on the next scan the the lesion size would be checked. The next scan would provide another pulse if the lesion has not reached the required size. This process would continue until the lesion reaches its predetermined size. This camera's disadvantages are its poor resolution and its mechanical, optical, and electrical complexity.

### 7.2.2 Imaging with the Fundus Camera

The quality of an image seen through a fundus camera is excellent. One reason is because only quality optics are used in the camera. The objective is generally an aspheric (to minimize spherical aberrations) and compound (to minimize chromatic aberrations). A second reason for the excellent image quality is the use of the Gullstrand separation principle [7-25] in on all fundus cameras. This principle requires that the area of the cornea where the illumination light enters the eye must be separate from the area of the cornea where the observation light exits the pupil. If this were not the case, a rather significant reflection (called a corneal reflex or first Purk-

inje image) from the cornea overwhelms the reflection from the retina. Many cameras also insure that the Gullstrand principle is followed at the first surface of the crystalline lens (third Purkinje image). Fundus cameras generally create an annulus of illumination light that is focussed onto the cornea. This light is then defocussed as it passes into the eye and uniformly illuminates the fundus. (Unfortunately this illumination light is not completely uniform [7-23].) Only the reflected light from the fundus that passes out of the eye through the center of the annulus is used to create the retinal image.

Imaging the retina creates several interesting problems. Imaging the curved surface of the retina onto a flat photographic plane would normally be considered a substantial problem, but Pomerantzeff [7-46] showed that if the objective lens is properly designed, this problem can be overcome. Another phenomenon that can create blurry photographs in an imaging system is the operator's accommodation. The human operator can focus at different distances, and thus by changing the accommodation of his/her eye, the operator can focus the system at different focus settings. Some equipment will contain a reticule in one eyepiece that aids the operator in establishing a fixed accommodation [7-24]. A video camera and computer (or some other autofocussing device) can often provide better focussing than the human operator.

It would be convenient to superimpose an accurate, absolute graticule onto the retinal image. This graticule could be used to measure the absolute size of features on the retina. Currently, the optic disk is used as the "yard stick" to judge the size of other retinal features. This technique has limited accuracy. The width of the optic disk is variable and the optics of both the eye and fundus camera distort the image.

Behrendt [7-4] took two photographs of the same object but in different positions on the photograph. He found that the size of the object as calculated from the two photographs were different. Measurements must be made so that the size of retinal features can be accurately calculated. Cornsweet and Crane have developed an automated optometer that is accurate to within 0.10 D [7-15]. If the eye's correction (from the optometer) and the axial length of the eye is known, then an accurate retinal image size can be calculated. Szirth [7-54], at the Children Hospital in Los Angeles, is attempting to use a laser range finder to calculate the axial length. (This distance can also be measured using ultrasound, but this technique is quite involved.) It is important to note that just one measurement on an eye is insufficient. The optics, axial length of the eye, and the retinal area per solid angle (see Chapter 2, "Anatomy and Light Interaction of the Eye") change as the radial angle changes. Thus, the eye's correction and axial length must be measured at the point where the retinal image is desired. In addition, oblique astigmatism, which is a rather significant aberration in the periphery of the eye, results in a substantial distortion in the peripheral images [7-8]. Many fundus cameras have astigmatic correction devices that can partially offset this problem.

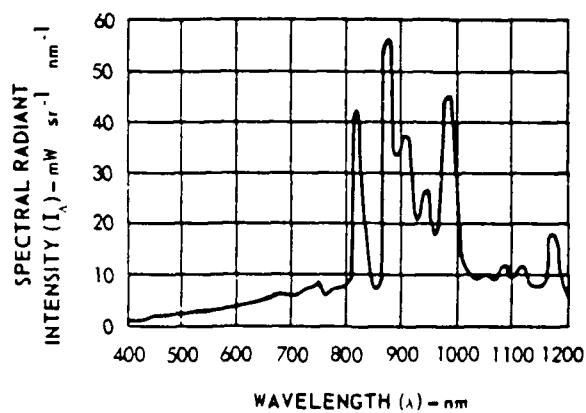
### 7.2.3 Illumination Source

The light directed into the eye that provides the illumination source must be carefully considered. Chapter 2, "Anatomy and Light Interaction with the Eye", discussed the damage that could result from excessive illumination. Manufactures of current day fundus cameras tend not to concerned themselves with light toxicity. A

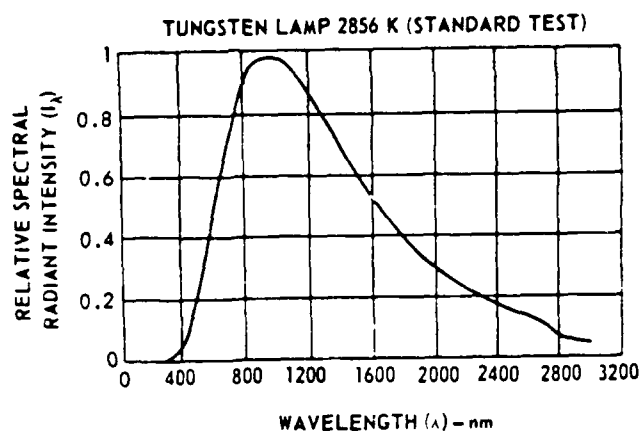
large part of this problem is caused by the lack of any written safety standards for light illuminating sources.

In the applications for the proposed system, two spectral bands must be considered; the visual band and the infrared band. For viewing by the operator and photography, light illumination in the visual band (450 to 650 nm) must be directed into the eye. For 35 mm and Polaroid photography, a xenon flash is used, with the spectral density shown in Figure 7-2(a). Notice the large amounts of unnecessary energy in the infrared region. This excess energy should be filtered. A steady illumination source is required for operator viewing, and the standard light source used is the tungsten-halogen. The spectral output of this lamp is shown in Figure 7-2(b). This lamp also has an excessive amount of energy in the infrared. For applications restricted to fundus viewing by the operator and normal photography, the halogen light should also be filtered to minimize possible damage from light toxicity.

For the applications where a tracker camera needs maximum illumination to view the fundus, the energy in the near infrared band (650 nm to 1000 nm) from the tungsten lamp should not be filtered. This band coincides with the spectral response of CCD detectors (compare Figure 7-2(b) and Figure 7-5). The tungsten lamp energy above 1000 nm should always be filtered. If a human operator needs to view the retina while the tracker camera is also viewing the retina, then only a portion of the visual band (450 - 650 nm) should be delivered to the operator observation port (using a beam splitter). The tracker camera must receive as much illumination as possible while still efficiently using the least amount of illumination. For the proposed systems, the tungsten-halogen lamp is the best illuminating source because it



(a)



(b)

Figure 7-2 (a) Spectral distribution of a 150-watt xenon short arc.  
 (b) Spectral distribution of a 2865 K tungsten lamp [7-49].

provides excellent smooth spectral power at the required wavelengths, and it has an increased life expectancy and increased efficacy over other incandescent lamps.

Two excellent accessories to the fundus camera would be a light meter to measure field illumination and computer control of the illuminating light. Many fundus camera already have a light meter to control the xenon flash for optimum photographic exposure. Since some patients have opacities in the eye which require increased illumination, it would be advantageous if the computer could increase the field illumination in these situations so that an adequate video image could always be acquired. The light meter is required to monitor total light exposure for light toxicity. In this manner, the computer can always maintain a good video image while minimizing the field illumination.

#### 7.2.4 Fixating Device

A fixating device is shown in Figure 7-3. The purpose of this device is to be able to change the field of view of the fundus camera by directing the patient to move his/her eye. It will work only when the fellow eye has reasonable central acuity and the patient is orthophoric. Each dot represents a small lamp and the angles correspond to angles of deviation of the human eye. Only one lamp is on at any given time. This fixating device is positioned a certain distance from the fellow eye. The patient is requested to fixate on the lamp that is lit. When the computer wants to reposition the eye so that a new field is viewed in the fundus camera, a new lamp position is lit and the old lamp position is switched off. The patient fixates on the new position and the fundus camera is realigned. The fixating device is designed so that when a patient views the lamp that is marked  $20^\circ$  and  $30^\circ$  (radial and tangential), the

area of the retina viewed in the center of the fundus camera's field of view is located at a position of  $20^\circ$  and  $30^\circ$  (radial and tangential).

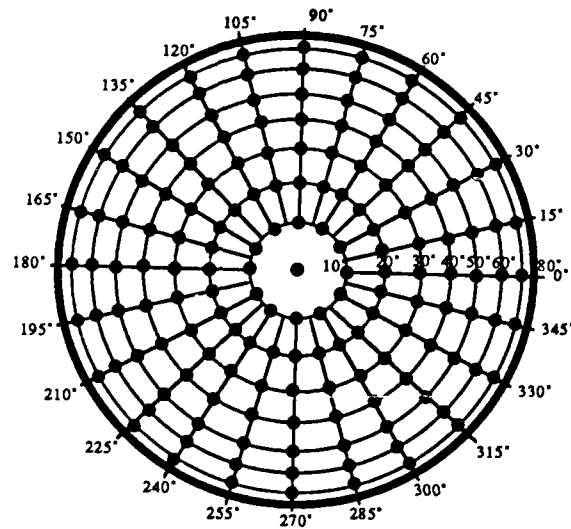


Figure 7-3 Fixating Device.

### 7.2.5 Pixel Separation

Most fundus cameras will permit three levels of viewing magnification, approximately  $10^\circ$ ,  $30^\circ$ , and  $50^\circ$ . Table 1 lists these fields of view along with the image diameter and pixel separation for a 512 by 512 pixel format. The image diameter is the width of the retina seen through the optical system. The pixel separation is the distance between pixels as seen in the image plane (which is the retina). For completeness, the table also includes five other fields of view from  $0.3^\circ$  to  $3^\circ$ , which are used on the lesion camera for monitoring lesion formation.



Field of View	Image Diameter at Retina	Pixel Separation at Retina	Image Format
0.3°	90 $\mu\text{m}$	2.8 $\mu\text{m}$	32 x 32 pixels
0.6°	180 $\mu\text{m}$	5.6 $\mu\text{m}$	32 x 32 pixels
1°	300 $\mu\text{m}$	9.4 $\mu\text{m}$	32 x 32 pixels
2°	600 $\mu\text{m}$	18.8 $\mu\text{m}$	32 x 32 pixels
3°	900 $\mu\text{m}$	28.1 $\mu\text{m}$	32 x 32 pixels
10°	3000 $\mu\text{m}$	5.9 $\mu\text{m}$	512 x 512 pixels
30°	9000 $\mu\text{m}$	17.9 $\mu\text{m}$	512 x 512 pixels
50°	15000 $\mu\text{m}$	29.3 $\mu\text{m}$	512 x 512 pixels

Table 7-1 Pixel separation at the retinal image plane for two cameras at different fields of view.

These pixel separations are close enough for the work required by ophthalmologist during laser surgery [7-51].

### 7.2.6 Fundus Camera Autoalignment

All fundus cameras use manual control to align the patient's eye with the camera. One goal of the system is to fully automate this procedure. Chapter 3, "Overview of the System", discussed the autoalignment procedure at some depth. A few more details will be presented here.

Autofocussing can be done by several methods. Syn-Optics [7-53] markets a camera that monitors the frequency content in the image as the optical system spans its range of focussing ability. The image with the highest frequency content corresponded to the proper focus setting for the camera. Cornsweet and Crane [7-15] have developed a servo-controlled infrared optometer that images two infrared beams onto the retina. When the two beams are coaligned, the retina is in focus. Canon [7-9] has

an autofocus system on their fundus camera which probably uses this method. Olympus [7-44] fundus cameras have a "cats eye" that is superimposed near the bottom of the retinal image (as seen by the operator). When the camera is in focus, the slit in the cats eye appears sharpest. A video camera could monitor this cats eye and adjust the focus of the fundus camera until the camera is in focus.

### 7.2.7 Stereoscopic Fundus Cameras

One disadvantage of the fundus camera is monocular viewing. Binocular viewing provides depth information of retinal features. This can be very useful in diagnosing many diseases, especially the cupping of the optic disk in glaucoma. Some fundus cameras use a flip lens that flips between two slightly offset images of the retina. Donaldson [7-17 and 7-18] has been developing a stereoscopic fundus camera for the past 30 years. His most recent camera is a simultaneous stereoscopic fundus camera that uses only a single optical axis. A video camera attached to his device could alternate its view by imaging one of the stereo pair in one frame and then the other stereo pair in the next frame. The computer could process these images and extract depth information. His camera also has the advantage that a mirror can be placed directly in front of the objective (the retinal images do not pass through the center of the objective lens) so that the laser delivery system can be coaligned with the fundus camera (see "Optics" below). This system has the disadvantage of a smaller field of view because two slightly diverging retinal images must pass through the pupil.

### 7.2.8 Mosaics

The maximum field of view for a fundus camera is about  $50^\circ$  (assuming a high resolution image). Quite often more than just one  $50^\circ$  image from a video camera is required, and several slightly overlapping images are assembled piecewise. This is called a mosaic. This process is shown in Figure 7-4, where the seven circles would correspond to seven slightly overlapping video images of the retina. Unfortunately, the images cannot be easily assembled together. From a previous discussion ("Imaging with a Fundus Camera"), it was shown that the images will not necessarily align near the edges of the images because of aberrations.

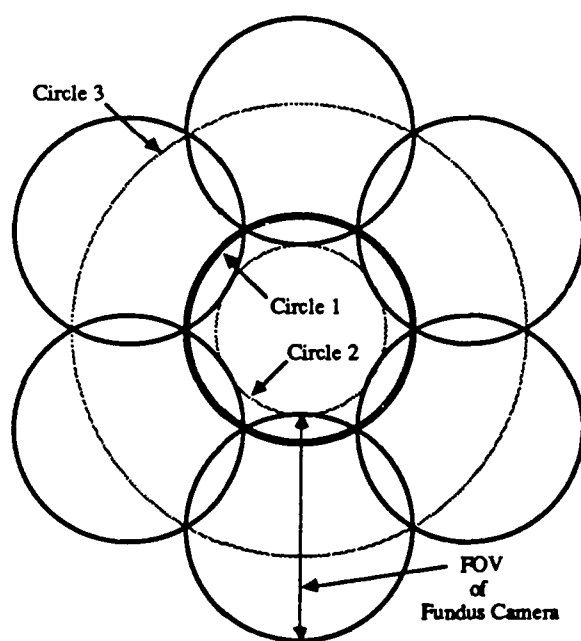


Figure 7-4 The structure of a mosaic for many retinal fields.

Since there exist prominent, slowly changing blood vessels, it is possible for the computer to computationally integrate the images. Tanaka [7-55] provides the algorithm. The total scenario is as follows. The computer acquires seven images of the retina at different views. These images are processed with the Tanaka algorithm. The images are further processed to create an accurate graticule for the entire image (see "Imaging with the Fundus Camera"). The complete image (Circle 3 in Figure 7-4) is finally shown to the ophthalmologist on a video screen. The ophthalmologist uses this image to pinpoint lesion locations (see "Software" below). Notice that the computer must be able to reverse the process. It must maintain a one to one correspondence between the original seven images and the final image.

### 7.3 Video Cameras and Video Cassette Recorders

A revolution has taken place in the past six years in the use of video systems. Before this time, the equipment for video systems were expensive and somewhat specialized depending on the manufacturer. Then came the solid state cameras, the widespread usage of the VCR's, the video digitizing board, and the acceptance of personal computers. With these advancements, a simple video system costs less than \$10,000. It is now possible to store and process information that humans inherently relate to (i.e. vision).

This section will discuss the video camera and the video cassette recorders. Video camera specifications can be divided into general, chromatic, temporal and spatial. As each of these areas are presented, their relevance to the proposed project will be discussed. The specifications for the best camera on the market today for the

tracker camera will be given, followed by a discussion of the lesion camera. Lastly, the capabilities and limitations of the video cassette recorder will be given.

### 7.3.1 General Specifications

There are many good, commercial video cameras on the market [7-12, 7-20, 7-22, 7-27, 7-32, 7-42, 7-45, 7-48, 7-50, 7-52, 7-61]. These video cameras use either vacuum tubes or solid state devices as the detecting mechanism. The vacuum tube cameras are generally either the widely used but simple vidicon, or the intricate but sensitive image orthicon. Both of these use electron beams to scan a light sensitive target. The solid state cameras generally employ either the CCD or the CID solid state devices. These devices use semiconductor electronics to convert the photons to an electrical signal. Generally, intensifiers can be added to most cameras to increase light sensitivity.

The general specifications of the camera include size, weight, reliability, shock resistance, a C mount for optics, and power consumption. Size and weight are important because the video camera must be mounted to a fundus camera. A bulky camera arrangement makes maneuvering difficult. Since the system is used in a clinical environment, reliability and sturdiness are important. The C mount is often required for easy mounting of the video camera to the fundus camera. Power should always be minimized, especially in a medical application.

The RS-170 format is the standard format for monochrome video signal [7-21]. This specification is somewhat detailed and only a portion of it will be reviewed here. Consider an image that consists of 489 horizontal lines. A camera converts the image into an analog electrical signal by scanning each line. The analog

signal varies from 0 to 1 volt (excluding synchronizing signals), where 0 volts is black and 1 volt is white. The image is scanned horizontally from left to right (camera's perspective), starting at the top row and continuing to the bottom row. In the first scan of the image (called the odd field), every other horizontal line is scanned, to include both the first and the last lines. This equates to 245 horizontal lines (this does not include the 17.5 additional lines hidden in the vertical blanking pulse). The entire scan must take exactly 1/60th second. A second scan is performed (called the even field), which scans from the 2nd line down to the 488th line. This equates to 244 lines (with 18.5 more lines hidden in the vertical blanking pulse). This scan must also take exactly 1/60th second. The two fields comprise a frame of 489 horizontal lines (or 525 lines if the lines during vertical blanking are included). Notice that the resolution in the vertical direction is 489 lines, while the resolution in the horizontal direction is dependent on the camera and the corresponding analog signal. The video format can be expressed as either: 1) one frame occurring every 1/30th second with 489 (525) horizontal lines, or 2) as a field occurring every 1/60th second with either 245 or 244 lines, where the odd and even fields are positionally slightly offset.

Two points need to be made concerning the number of rows in an image. First, the "standard" size of an image has become 512 x 512 pixels. This is a convenient size for the binary computers. This size is in contrast to the 489 rows in the RS-170 format. Generally, if the 512 x 512 images are the result of an RS-170 signal, several rows at the top and bottom of the image are not used. Second, the RS-170 specification allows the duration of the vertical blanking pulse to vary slightly. The pulse can actually extend to hide three more horizontal lines per field. If this were the case, the number of usable lines decreases to 242 lines for the odd field and 241 lines

for the even field. (Notice that the odd field is defined as the field containing the extra line, not the field containing the odd number of lines.) This format has proven to be advantageous over the years because most video manufactures follow the specification; making cameras, video monitors, VCR's, and digitizing boards compatible.

It is very important that equipment follow this specification exactly. The Matrox video board used by this researcher accepts strict RS-170 inputs. The Hamamatsu solid state camera used by this researcher produces excellent images on the video monitor, but this camera is incompatible with Matrox digitizing board because its output is not RS-170. A second camera system used by this researcher is an EG&G solid state camera that is specified as a "non-interlaced RS-170" camera. There is no such thing. The camera has never interfaced perfectly with the Matrox board. A camera must conform to all the specifications to be compatible with the RS-170 standard.

### 7.3.2 Chromatic Specifications

The chromatic specifications deal with spectral response, or the relative sensitivity of the camera to different wavelengths of light. The typical spectral response of a CID camera is shown in Figure 7-5. Most solid state cameras tend to be sensitive in the red and infrared regions. The sensitivity of other cameras vary considerably, but most are responsive to the visible band. Color cameras must be sensitive to three colors. The light must be filtered into three bands of light and then sensed. This implies that the camera must either be composed of three detecting mechanisms or one mechanism with time multiplexing.

In the applications for the proposed design, the camera should be able to detect the many bands of light required for the chromatic image processing discussed in Chapter 6, "Retinal Image Processing".

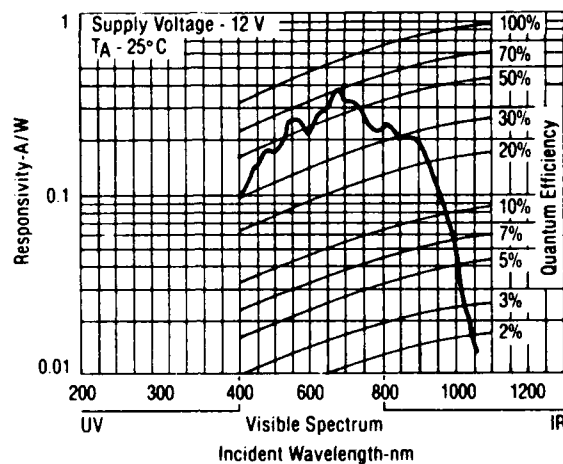


Figure 7-5 Detector sensitivity of a Cohu [7-12] solid state camera.

### 7.3.3 Temporal Specifications

The temporal specifications deal with the sampling of the image in time, or its dynamic response. One point of interest is that the Nyquist criteria dictates that the signal should be temporally filtered to avoid aliasing. Since it is exceedingly difficult to accomplish this task, aliasing will be present in the data if the intensity at a point changes faster than 1/15th of a second. The effects of aliasing can be difficult to assess unless a very specific application is given.

Dynamic resolution is associated with aliasing but deals more with the time integration of the detectors. This problem accounts for the smearing of an image be-



cause an object moves rapidly across the field of view of the camera. Dynamic resolution can be improved by the use of a shuttering system, which integrates the image for only a fraction of the field time (maybe 1 ms of the total 16.6 ms). Dynamic resolution is very similar to lag, which is universally defined as the amount of signal still present in a detector  $3/60$ th of a second (three scans later) after the stimulus is turned off. Lag is often called image retention. Both lag and dynamic resolution will result in a comet tail effect. Tube cameras typically have more lag than solid state cameras.

The Cohu camera that was used in the imaging of the eye for the tracking routines (SIT camera model number 5152-5000) had poor dynamic resolution but satisfactory lag. During movements of the eye, the optic disk showed a considerable comet tail from poor dynamic resolution. During fast saccades, the comet tail extended across the entire image. This problem was significant during the calculations for the blood vessel template (see Chapter 4, "The Retinal Tracker"). If the image was not stationary when a "freeze frame" was performed (the "freeze frame" is explained in "Video Boards" below), the template was not optimal. Also, during tracking, the edges of the blood vessel were blurred, decreasing the reliability of the tracking.

External synchronization of the camera with other devices may be required in many applications. In this project, there is a strong possibility that the tracking and lesion cameras will need synchronization with the laser shutter (discussed further in "Optics" below).

### 7.3.4 Spatial Specifications

The spatial specifications deal with the sampling of the image in space. Resolution, or spatial sampling, is the capability of the camera to resolve spatial detail. As with temporal sampling, Nyquist also dictates that the spatial frequencies should be filtered to avoid aliasing. This also is rarely done except by the preceding optics, which inherently filters the data because of aberrations. Thus some aliasing will occur, especially around pronounced edges.

The actual specification for resolution is incorporated into the modulation transfer function of the camera as measured in the horizontal direction of the camera. Remember that in the vertical direction the resolution is generally fixed at 485 lines, but in the horizontal direction the analog signal is dependent on the camera's detector and bandwidth.

The modulation transfer function (MTF) is a powerful tool in evaluating the overall performance of any optical system. This includes the human eye, (discussed in Chapter 2, "Anatomy and Light Interaction of the Eye"), video cameras, video monitors, telescopes, and a host of other optical systems. The real power in the MTF is its use to analyze cascaded optical systems because the total MTF of the cascaded system is just the product of the individual MTF.

The modulation transfer function of a video camera is measured as follows. The camera views a picture whose illuminance changes in a sinusoidal variation in the horizontal direction. This is similar to a black and white vertical bar pattern except there is a gradual change in illuminance from the black to the white and vice versa. The lighting, sinusoidal picture, and camera are adjusted so that the maximum black

and white of the sinusoid equate to the maximum black and white of the camera. The definition for the contrast of the picture is:

$$\text{Contrast} = C = \frac{I_{\max} - I_{\min}}{I_{\max} + I_{\min}} \quad (7-1)$$

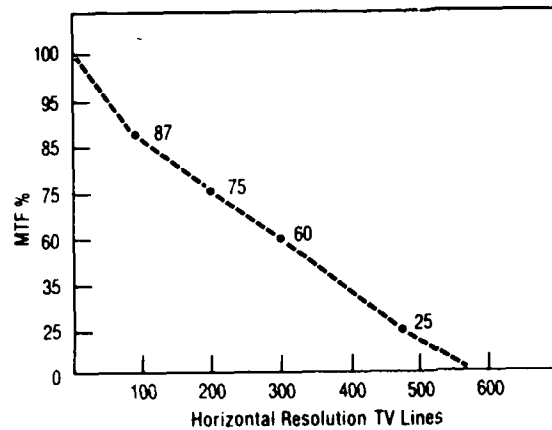
where  $I_{\max}$  and  $I_{\min}$  are the maximum and minimum illuminance in the picture. For a video camera at a very large sinusoidal cycle,  $I_{\max}$  would equate to 1 Volt (maximum white) and  $I_{\min}$  would equate to 0 Volts (maximum black).

The definition for the Modulation Transfer Function at a given spatial frequency is:

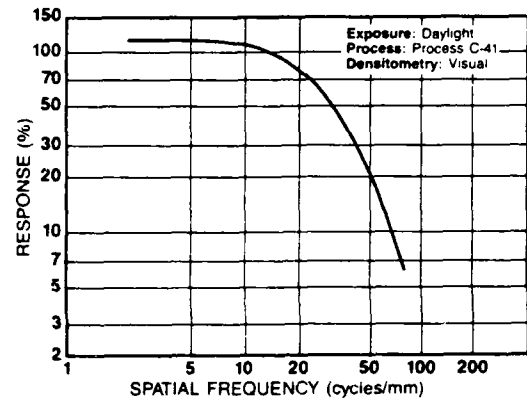
$$\text{Modulation Transfer Function} = \text{MTF} = \frac{C_o}{C_i} * 100 \quad (7-2)$$

where  $C_o$  is the camera output contrast for a given spatial frequency and  $C_i$  is the camera input contrast.

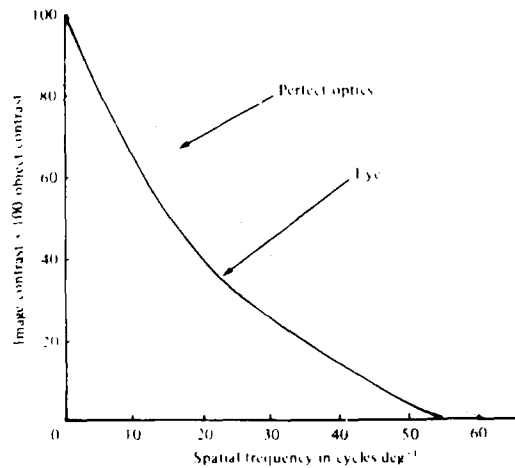
At very long sinusoidal cycle across the picture, the MTF at that spatial frequency will be 100% (this is how  $C_i$  is measured). As the number of sinusoidal cycles increase, the camera will be incapable of sensing the contrast change (and spanning the entire 1 volt) and the MTF will decrease, ultimately to zero. The graph of the MTF verses spatial frequency for a camera is shown in Figure 7-6(a). Notice that the spatial-frequency of the sinusoid is given as the number of sinusoidal cycles in the horizontal direction in a distance equal to the height of the video picture. As a



(a)



(b)



(c)

Figure 7-6 The modulation transfer function for (a) a Cohu solid state camera with a detector size of 754 (W) x 488 (H) pixels [7-12], (b) a photograph using Kodak Vericolor II professional film, type L [7-19], (c) the human eye [7-3]. See text and Appendix 4, "Comparing the MTF's of a Video Camera, a Photograph, and the Eye", for discussion and explanation of horizontal axis.

reference, the MTF of a photograph (Figure 7-6(b)) and the MTF of the eye (Figure 7-6(b)) is also given. Appendix 3 discusses how these three MTF's compare.

Since the ophthalmologist always wants the best picture, using a camera with a good MTF will enhance the image. The knowledge of the MTF of a system will also prevent empty magnification. An image can be magnified just so far before there is no more detailed information that can be resolved with further magnification. If the MTF of the eye, fundus camera, and video camera are known, then the maximum magnification of the retinal image can be calculated.

Many manufacturers will not calculate the MTF of their camera, but will give the resolution specification as the maximum number of vertical black and white lines that the camera can detect (in a horizontal distance equal to the height of the picture). This single number is difficult to relate to the MTF curve, but the threshold for the MTF (MTF = 0%) is probably very close to the resolution specification. (The black and white square wave bar pattern is filtered extensively by the system as the number of bars increase. When the number of bars reaches the camera's threshold, the camera only sees the fundamental frequency. This would thus correspond to the sinusoidal pattern of the MTF at its threshold).

Another specification deals with the light sensitivity of each pixel. Sensitivity is generally given in the SI units of lux. (Lux is a photometric term {brightness as seen by the human eye}, not radiometric {amount of energy in Joules}. One lux is equal to the illuminance resulting from the flux of one lumen falling on the surface area within one steradian at one meter from the source.) The graph in Figure 7-7 shows how the lux compares to other photometric units and atmospheric lighting conditions. If a camera claims to have a  $10^{-4}$  lux full video sensitivity, then its output

would change from 0 Volts to 1 Volt when the camera, starting in the dark, is directed at the clouds in an overcast night sky. This camera's sensitivity is at least as good as the human eye. This specification is often determined with the AGC (automatic gain control) of the camera on, which improves sensitivity but decreases the signal to noise ratio (likewise, signal to noise specifications are generally given with AGC off).

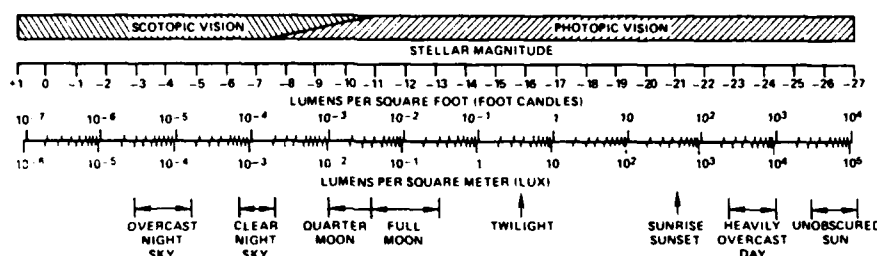


Figure 7-7 Natural scene illuminance [7-50].

The noise specification for a camera is given in dB. It is generally given with AGC off and a gamma of 1 (Gamma is defined below). The signal to noise ratio (SNR) is important in defining the most significant usable bit in a digitizing system. As a rule of thumb, an 8 bit digitizing system requires a SNR of about 60 dB (the ratio of the signal to noise voltage is 1000 to 1). The noise is thus about 1/4 of a quantization level. A SNR of 48 dB correlates to noise that is about one quantization level in an 8 bit digitizing system.

Generally, cameras with high sensitivity have a low SNR. Dennis Makes [7-39] claimed that the retinal images using a very sensitive camera with just field illumination were inadequate for image processing. A flash lamp had to be used to

take a good video image. To avoid taking many flash pictures of the eye, it is important to find a camera that has high sensitivity and a good SNR. Good sensitivity also enables a smaller aperture with the corresponding increase in the depth of field. This allows for a greater error when focussing.

Another specification is geometric distortion, which relates the extent that the actual image is positionally distorted by the camera. When using solid state detectors, the geometric distortion is almost zero. Shading or contrast variation is the variation in amplitude of the electrical signal when a uniform field is imaged. Gamma is the nonlinear gain function. If gamma is less than one, then the sensitivity decreases as the illumination increases. Gamma is related to the dynamic range of the device, which is the range of illuminance the camera can image between its threshold light level and saturation. The AGC of the camera greatly increases the dynamic range. Another similar notion is called intrascene dynamic range, or blooming, which is the ability of the camera to ignore (or deemphasize) a bright spot in the field while still seeing other objects in the image. Good blooming characteristics are important when imaging the retina with a sensitive camera while the bright optic disk is contained in the field (or during laser irradiation).

### 7.3.5 Video Camera for Retinal Observation

The best camera on the market for this system (not considering price) is the Xybion Model ISG-05 gated intensified solid state (CID) video camera. The specifications are as follows:

1. Small physical package (10 cm x 7.6 cm x 8.6 cm).
2. Reliable, shock and vibration resistant (inherent in solid state cameras).

3. Power is 12 volts DC at only 4 watts (even though 110 Volts A.C. would be preferred)
4. Standard "C" mount.
5. Extremely high sensitivity ( $10^{-5}$  lux).
6. Almost uniform response from 400 nm to 900 nm.
7. Virtually no geometric distortion.
8. Minimal blooming (a point source 100 times the intensifier's saturation intensity showed less than a 3.5 pixel width).
9. Shuttered system (Can be externally controlled).
10. Wide dynamic range ( $10^7$  range of light levels).
11. Resolution of 398 lines (the detector size is 775 x 488. The MTF is not available).
12. Noise level of 52 dB without intensifier (noise levels with intensifier is not available).
13. The camera cost over \$18,000.

Development in camera technology is attempting to better most of the specifications listed above. Tektronix [7-29] has build a 2048 x 2048 pixel detector. Many cameras, such as the Xybion, have the capability to increase the video rates. Color cameras are using a single detector with a spinning wheel that contains color filters. In each field, the camera actually gets three images, one for each color. The RCA random access camera C1181 is a tube camera capable of random access to any pixel [7-50]. If a highly sensitive version were to be made available, this camera would be an excellent choice for the proposed system.



### 7.3.6 Video Camera for Lesion Monitoring

This section will discuss the lesion monitoring video camera, to include the system built here at UT Austin, the problems with this system, and specifications for a future system.

The lesion monitoring video camera used in the experiments in Chapter 5, "Control of Lesion Size", is a noncommercial camera that contains an EG&G [7-20] 32 x 32 pixel detector and operates at a speed of 420 frames per second. The 32 x 32 pixel detector and evaluation board is interfaced to the EG&G 128 x 128 pixel camera system. This formats the 32 x 32 pixel detector in the RS-170 format and allows the data to be swept into the video digitizing board in the computer. This provides the computer with real time access to the data, and the data can also be viewed on the video monitor and stored by a VCR. The data appears as 14 interlaced frames on the right side of the video monitor.

Numerous problems were encountered with this camera. Because of the inherent speed, the detector sensitivity is low and a large amount of illumination was required to see the developing lesion. This problem can be partially corrected by developing better optics to collect more of the light (in the camera used for the experiments discussed in Chapter 5, "Control of Lesion Size", a small telescope with only a 20 mm diameter objective was used). For this application, an inexpensive intensifier with a small gain and poor resolution would be beneficial yet economical. Because the detector could only be clocked at 2 MHz, the image on the video monitor is not square. The 32 pixels in one row of the lesion camera can not be inserted into a 32 pixel position in the RS-170 format. The 32 pixels of the lesion camera actually oc-

copy a 128 pixel position. Thus the video board oversamples each detector (four times) and the image is four times wider than it is high.

The lesion monitoring video camera optimally needs about a 50 x 50 detector array and frame speeds at 1000 frames per second. This would allow more spatial accuracy than the 32 x 32, which at times seemed needed. The frame rate of 420 frames per second was quick enough for the experiments in Chapter 5, "Control of Lesion Size", but a faster frame rate is required for 100 ms duration burns in the retina. This may not be the case if a pulsed laser system is used and momentary hesitations between laser bursts can be used for lesion size calculations. The video data should also be formatted into an RS-170 signal, thus the image can be easily interfaced to the computer, recorded on a VCR, and viewed on a standard monitor (the 50 x 50 detector array running at 1000 frames per second can be formatted into a RS-170 format that "appears" to be a normal sequence of images on the monitor).

Illumination was always a problem. For the experiments discussed in Chapter 5, "Control of Lesion Size", a tungsten light source was used (Figure 7-2(b)), which matches the spectral characteristics of these CCD detectors (very similar to Figure 7-5). One suggestion is to use a semiconductor laser for illumination. These devices are small and should produce the required power and spectral output for good illumination [7-13].

### 7.3.7 Video Cassette Recorders

Since the video cassette recorder (VCR) is an integral part of most video systems, it is important to understand its capabilities and limitations. The VCR is a high capacity storage medium. It is easy to operate, inexpensive, and interfaces with

RS-170 signals. The disadvantages are the slow access time and the further decrease of the SNR (signal to noise ratio) of the analog signal. (If the end product of an analog signal is digital data, it is always advantageous to digitize the data before storage to prevent the unavoidable decrease of SNR.)

There are generally three speeds on most VCR's: SP, LP, and SLP. SP will record about 216,000 images on one cassette in 2 hours, LP will record 432,000 images on one cassette in 4 hours, and SLP will record 864,000 images on one cassette in 8 hours. Table 7-2 shows the result of a video camera and VCR noise test. An RCA VCR with 5 recording heads was used, and the VCR's heads were cleaned before the test. The Good Video was the output of the VCR in the stop mode. This signal represents a clean video signal generated from electronic circuitry not originating from any detector. The Solid State Video is the video signal directly from the output of an EG&G CCD camera (the camera's field of view was stationary). The VCR SP Video is the playback of the Solid State Video signal after it was recorded on the tape, recorded and played in the SP speed. The VCR LP Video and VCR SLP Video are similar, always recording and played at the respective speeds. All five signals were input into the video digitizing board of the computer. A random pixel location was chosen in the digitized image and a temporal data set was built for each signal. The standard deviation for each signal is shown in Table 7-2. Part of the noise in the Good Video represents quantization error from the digitizing process. The SNR of the Solid State Video is about 45 dB. The conclusion from this test is to always record in the SP mode.

Video Source	Standard Deviation (Out of 256 Gray Levels)
Good Video	0.45
Solid State Video	1.51
VCR SP Video	2.24
VCR LP Video	3.31
VCR SLP Video	4.10

Table 7-2 Noise associated with different video cassette recorder speeds.

## 7.4 Computer Hardware and Video Boards

This section will discuss computer hardware. The video boards are an integral part of the system and will be reviewed first. The computer will be then be discussed. The remaining portion of this chapter examines the computer's ability to track the retina and methods that will improve this ability. The retinal tracking algorithm presented in Chapter 4, "The Retinal Tracker", provides a meaningful measure of the abilities of a computer system.

### 7.4.1 Video Boards

The block diagram for a video digitizing board is shown in Figure 7-8. The data is input in the standard RS-170 format, digitized with an A/D converter in real time, converted back (via a D/A converter) to the RS-170 format, and then output. The digital data between the A/D and D/A is fed into a 256K dual port memory. The memory is configured as a 512 x 512 image. In the "continuous mode" of this device, the data is in the memory only a short time before the data is overwritten by the next frame. The computer can access this data through the dual port memory, but it only has 33.3 ms to read the data in a particular frame. The board can be asked to perform

a "freeze frame", where the next frame of data is kept in the memory buffer. The A/D is switched off and no further data is accepted from the input channel. The D/A converter outputs the RS-170 signal of the frozen frame. At this point, the computer can read the data (and store the frame at another location) or change the data (such as insert cursors or display the date). When the computer is finished with this frame, the "continuous mode" is started again and new frames are loaded into the memory.

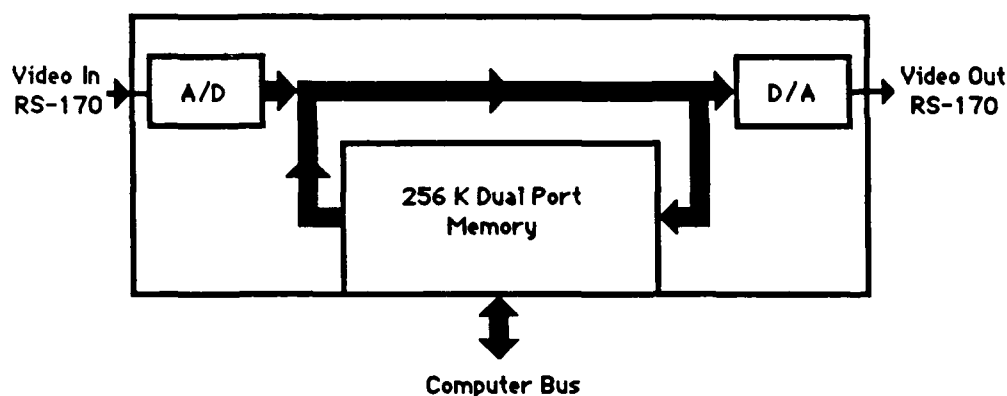


Figure 7-8 Video processing board used routinely for image analysis.

These video systems are not great instrumentation systems. The noise problems for the video camera and VCR's have been discussed above in "Video Cameras and Video Cassette Recorders". One significant problem of all video signals is the loss of low frequency data due to AC coupling. On the particular board that this researcher used (Matrox [7-40]), the video input is filtered with a high-pass filter (AC coupled). The filter's 3 dB cutoff is 192 Hz. This creates a rather significant distortion in some images. For example, the thermal camera was used to image the lesions discussed in Chapter 5, "Control of Lesion Size". The lesion size was approximately

150 x 150 pixels in the 512 x 512 image. The background was about 90 gray levels before the laser shutter was opened. After the laser shutter was opened, the center of the lesion jumped to 230 gray levels. The problem was that the background to the left and right of the lesion (on the same row as the lesion) dropped to 55 gray levels. The background in the top and bottom of the picture (above and below the lesion) was still at 90 gray levels. This implies that the intensities at the lesion were 35 gray levels too low. This type of problem is associated with AC coupled systems, and it's the reason why FM modulation is used in good quality instrumentation magnetic recorders.

There are several methods of minimizing or eliminating the error. Some manufactures of video boards use the voltage of the back porch in the previous horizontal synchronization pulse as a DC reference level. The back porch is the voltage level directly following the negative going horizontal synchronization pulse and corresponds to the baseline of the video data. The manufactures of the Matrox board claims to use this technique, albeit without great success. Another method of reducing the DC shift is to use a small image. Also, when using the thermal camera, insure that the black bodies in the thermal image are always in view and locate them on the same row as the lesion. When processing the data, digitally offset the affected lines to the required levels.

A new video board being developed by Matrox will greatly enhance the proposed system. These new boards store four 512 x 512 images and contain a 68000 microprocessor with 350K of user memory. This one board will become both the tracking computer and video board, or the lesion computer and video board. This system will operate much faster than the Matrox video board because the memory is

not accessed over a computer bus (such as the Multibus). This new video board/computer uses one VME card slot.

#### 7.4.2 The Computer

This section will discuss which computer might be the best for the proposed system. The new IBM Personal System/2 Model 80 would seem to be a good choice. It uses the Intel 80386 microprocessor, which is downward compatible to the 8086 assembly language (the language used for the tracker programs discussed in Chapter 4, "The Retinal Tracker"). This machine will most likely become popular, making the initial training by the ophthalmologist and staff easier. The big disadvantage is that the physical size of the boards that fit into its bus are very small. This makes it difficult to design a video digitizing board with an on-board microprocessor.

The Macintosh II might be a good alternative even though the tracking algorithms would have to be rewritten. The use of this machine should be dependent on its acceptance by the business community. The most likely choice might be a DEC machine that uses the VME bus. The Microvax's are presently expensive but will very likely fall in price. These computers are geared toward the business community, well supported, and have excellent expansion capability.

Several other options should be included with the computer system. A color monitor would provide excellent pseudocolor images. Ample memory (5 MBytes) should be included in the system, along with a large capacity disk drive (80 MBytes). Magnetic tape drives work well as a long term, high density storage media, although optical disks might be advantageous as this technology improves [7-31]. These devices can currently hold about 400 images (512 x 512 pixels) per disk (5 1/4" remov-

able cartridges), and they only take about one second to store and recall an image. These devices are called "write once read many" (WORM) systems, where once they are written to, they cannot be changed.

### 7.4.3 Quickening the Retinal Tracker

This subsection will suggest and examine hardware improvements that enhance the performance of the tracking routine discussed in Chapter 4, "The Retinal Tracker". The quicker the algorithm can execute, the better it can track.

It is first important to understand the bottleneck of system. In other words, "What is the major stumbling block of the tracking algorithm?" The block diagram in Figure 7-9 shows the bottleneck of the tracker, which is the number of bytes per second that must be fetched by the computer from the digitized image in the dual port memory.

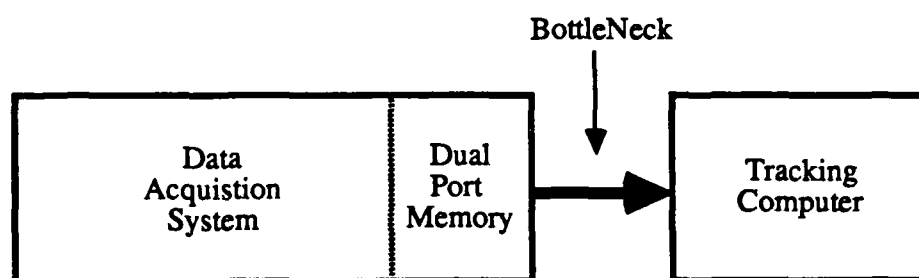


Figure 7-9 The bottleneck of the tracking system.

The following sections will discuss two ways of minimizing the bottleneck (considering just the hardware). First, methods to increase the execution time of the algorithm will be examined. A major factor will be to increase the speed at which the



computer can access the memory. Second, a method to decrease the number of bytes that the computer must fetch from memory will be analyzed. This method hinges on the optimum video rate for tracking. Obviously, the proper algorithm and software coding also minimize the bottleneck. This has been exhaustively discussed in Chapter 4, "The Retinal Tracker".

#### 7.4.4 Decreasing Execution Time

The tracking routine was implemented on the Intel 310 System using an 8086 microprocessor. This algorithm is memory intensive. Every instruction and its operand must be fetched from memory. For the specific tracking routine used in Chapter 4, "The Retinal Tracker", there are 500,000 op codes and operand fetches per second. Of these, 80,000 instructions require additional memory access to the RAM and another 100,000 instructions require memory access to the video board. Obviously, any method of decreasing memory fetches will significantly speed the tracking routine. As a rule of thumb for the tracking system used in Chapter 4, "The Retinal Tracker", an assembly language routine can access about 15,000 pixels in the video memory per second. In other words, the CPU can only access about 0.2% of each video image in real time. It's amazing the tracking routine performed so well under these constraints. The following is a list of improvements that will quicken the tracking routine, mostly by using an 80386 processor instead of the 8086.

1. The 8086 runs at 8 MHz, while the 80386 runs at 16 MHz. This doubles the speed.
2. All memory fetches to the random access memory and the video board were done over the Intel Multibus I. If a video digitizer with on-board microproces-

sor is used, then both the random access memory and the video image memory are local. This will speed the algorithm immensely.

3. The 8086 is a 16 bit processor, and since a memory space of more than  $2^{16}$  (64K) bytes must be addressed, two registers (segmentation and offset) must be manipulated for memory access. This problem is time consuming in the real time tracking routine when the processor must continually update the segmentation register to access different pixels in the video memory (which occupies 256K of memory). The 80386 is a 32 bit processor and eliminates this problem.

4. Both processors have a prefetch unit, but the 80386 also has a predecoding unit which speeds instruction decoding. As an example, an effective address that takes 17 clocks on the 8086 will only take 4 clocks on the 80386.

5. The tracking routines discussed in Chapter 4 were highly structured and heavily laced with testing code. These features can be eliminated once the code is tested and ready for implementation.

#### 7.4.5 The Optimum Video Rate

As will be shown, the video rate has a direct impact on the bottleneck. In many applications, the video rate is fixed on the RS-170 format. But recent advances in video technology, especially solid state cameras, have started to provide programmable frame rates. Even though these are not common, nor are the VCR's and video digitizing boards to go with them, the optimum video rate will be discussed.

The search area was discussed in Chapter 4, "The Retinal Tracker". Even though huge amounts of data are available to the computer in the dual port memory, only a small portion of this data within the search area needs to be addressed. There

are two opposing factors to consider. As the video rate increases, the amount of digitized data per second increases in a linear fashion, but the search window decreases in a square fashion. From a temporal point of view, a quicker video rate means that the computer must perform its tracking algorithm on more images per second. From a spatial point of view, a quicker video rate means the the computer will have a smaller window to search and hence fewer correlations. (Remember from Chapter 4, "The Retinal Tracker", that a correlation was required at each pixel location inside the search area or search window.) It will be intuitive to graph the video rate verses the total number of correlations per second.

Assume that the number of correlations directly relate to the number of bytes that the computer must fetch from memory (i.e. the bottleneck). Assume further that the velocity of the eye is  $600^\circ/\text{sec}$ , the acceleration is  $40,000^\circ/\text{sec}^2$ , the field of view of the camera is  $10^\circ$  and the camera's detector size is  $512 \times 512$ . Using the calculations from Appendix 2, "Correlation Calculations", a graph of the video rate verses the number of correlations per second is shown in Figure 7-10. Notice that as the video rate increases, the number of comparisons decrease. If the images are sampled at 60 images per second, 15 million correlations must be performed per second, while at 120 images per second, only 2 million correlations per second need be done. This is almost getting something for nothing. Even though twice as much data is being gathered by the data acquisition system, one-seventh less data is being accessed. Thus, if the video rate of the tracking camera can be increased by a factor of two, then the bottleneck throughput is decreased by a factor of seven. A corresponding improvement in the trackers performance will be the end result.

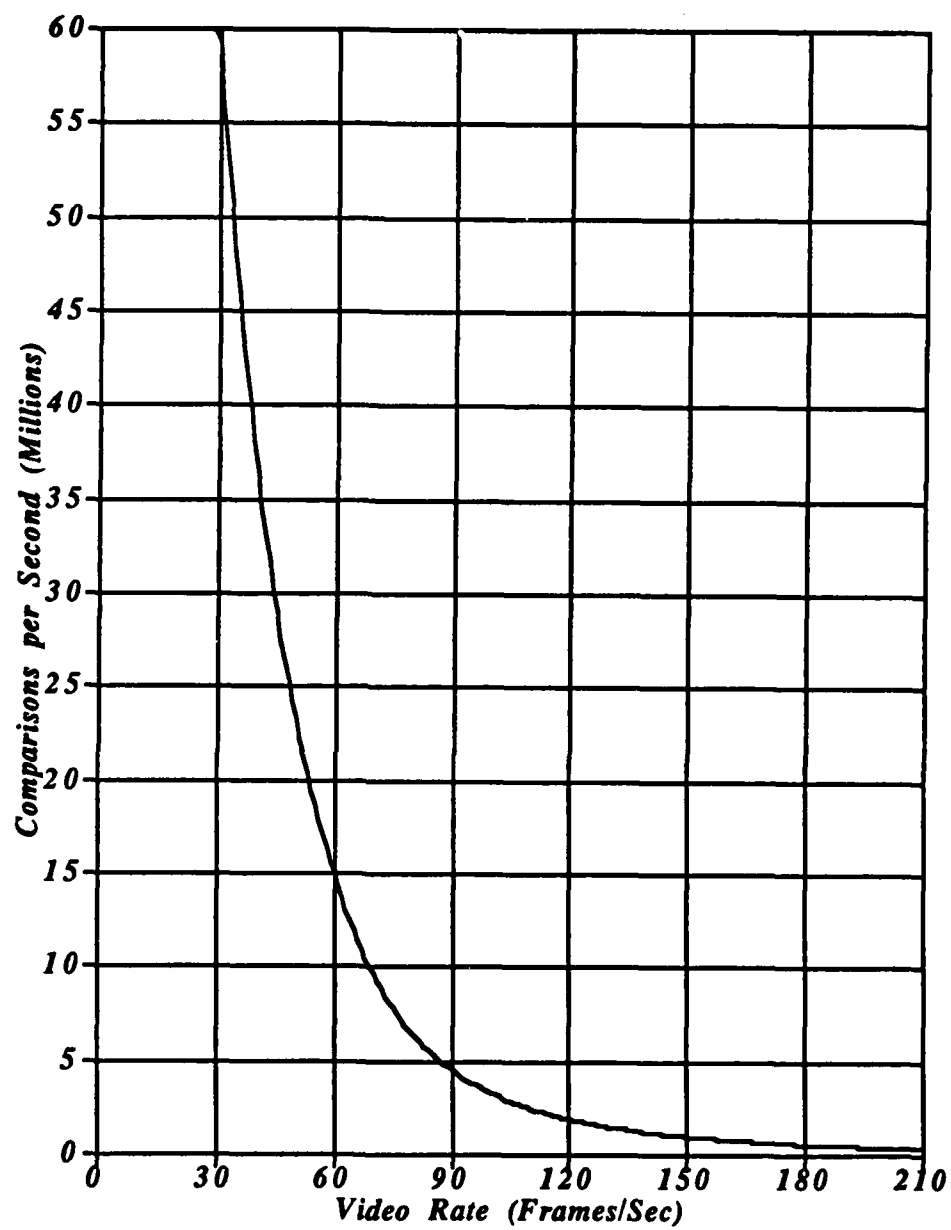


Figure 7-10 Total number of comparisons per second verses video rate.

## 7.5 Computer Software

This section provides the software design for the initial system. The operating system does not have to be a real time or multiuser type. Something as simple as PC DOS would work. It must supply an assortment of drivers (keyboard, terminal, trackball, and disk), an interrupt handler, and file management. The software design for the master computer will be discussed first, then the tracker computer, and finally the lesion computer. Most of this software has not been coded.

### 7.5.1 Master Computer Software Design

This software controls the entire system. Its structured system is shown in Figure 7-11. The initialization subroutine is executed directly after the computer is turned on. The computer then interfaces to the user via the User Interface Software. This routine performs all the imaging processing tasks as discussed in Chapter 6, "Retinal Image Processing". A major requirement of this routine is to detect the prominent points on the blood vessels that are needed by the tracking algorithm. This information is entered into the Image Data Base. An example of this data base is shown in Table 7-3. Because the entire retina cannot be imaged at once, many fields are used. The correct field is viewed by changing the light on the fixating device which results in a corresponding eye movement. Fine adjustments are then made to locate the actual lesion location with respect to local blood vessels.

The center position of each field is given as a radial and tangential angle. The size of the field is also provided as a radial angle. Within this field, the computer must locate the prominent points on the blood vessels for the tracking routine. These

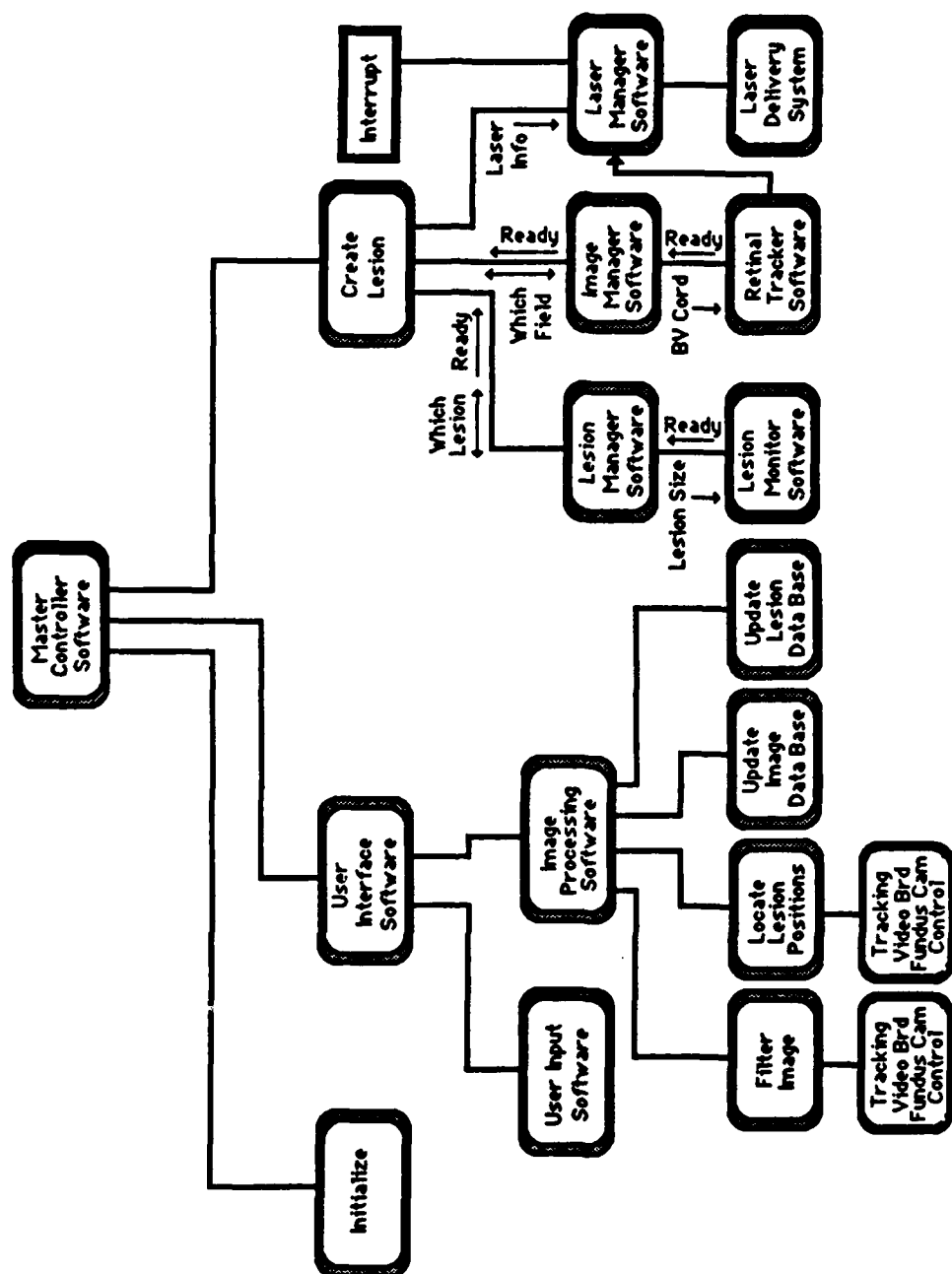


Figure 7-11 Structured design for the master computer software.

are given in rows and columns of the digitized image in the computer's memory. This data base could be significantly extended to include all the retinal features for each field, such as complete blood vessel template.

Field Number	Center Of Field (radial x tangential)	Size Of Field (radial)	Blood Vessel Locations (Rows x Columns)	
			Vertical	Horizontal
1	0° x 0°	50°	1.) 200 x 312	20 x 200
			2.) 120 x 300	170 x 420
2	20° x 30°	50°	1.) 190 x 312	20 x 200
			2.) 290 x 321	170 x 420
3	20° x 90°	50°	1.) 314 x 400	170 x 420
			2.) 234 x 199	170 x 420
4	20° x 150°	50°	1.) 267 x 341	256 x 256
			2.) 430 x 411	170 x 420
5	20° x 210°	50°	1.) 498 x 420	256 x 256
			2.) 156 x 390	170 x 420
6	20° x 270°	50°	1.) 439 x 111	256 x 256
			2.) 120 x 300	170 x 420
7	20° x 330°	50°	1.) 325 x 120	256 x 256
			2.) 103 x 326	170 x 420

Table 7-3 Image Manager Data Base

The User Interface Software must also calculate lesion locations. An example of the Lesion Manager Data Base is shown in Table 7-4. The locations for the lesions must be derived either by computer computation or ophthalmologist interface. Initially, for any disease other than diabetic retinopathy, the ophthalmologist will select the lesion locations using the trackball and video monitor. Selection of the lesion locations for diabetic retinopathy will be performed as discussed in Chapter 6, "Retinal Image Processing". The Lesion Manager Data Base includes the field of the retina where the lesion will be located, the absolute angular position of the lesion, its po-

sition in rows and columns within the digitized image of the field, and the lesion's desired width and depth.

The User Interface Software also performs any other required user interface task. This would include allowing the ophthalmologist the option to view any area of the retina, to update all preselected lesion locations, or to perform image processing on a particular image.

Lesion Number	Lesion Location Radial x Tangential	Field	Lesion Position Row x Column	Lesion Size Width x Depth
1	25° x 320°	7	124 x 312	200 x 300 $\mu\text{m}$
2	15° x 286°	6	20 x 300	200 x 200 $\mu\text{m}$
3	30° x 200°	5	222 x 50	500 x 300 $\mu\text{m}$
4	10° x 10°	1	180 x 100	500 x 300 $\mu\text{m}$
5	5° x 230°	1	200 x 400	500 x 300 $\mu\text{m}$

Table 7-4 Lesion Manager Data Base

After the ophthalmologist is satisfied with the lesion locations, the Create Lesion subroutine is entered. For each lesion, the three subroutines of the Create Lesion subroutine are visited once from left to right. The procedure is repeated for each required burn. The ophthalmologist can interrupt the computer at any time, view the damage, or update the lesion locations. The Lesion Manager Software decides which lesion will be placed next. It communicates with the Lesion Monitor Software (and hence the lesion computer) and sends to the lesion computer the lesion size information. When the lesion computer is ready, a Ready signal is relayed back to the Create Lesion routine.

Next, the lesion coordinates are sent to the Image Manger Software. This subroutine positions the eye in the proper field and informs the Retinal Tracker



Software of the appropriate blood vessel coordinates. Once the tracker has locked onto the retina, a ready signal is relayed to the Create Lesion routine. The Laser Manger Software receives the laser information and then takes control of the lesion burn. The Retinal Tracker Software communicates directly with the Laser Manager to keep the laser properly positioned. The laser shutter is then opened.

The Laser Manager than waits for an interrupt to close the shutter. Five entities can provide an interrupt; the interval timer on the lesion computer, the lesion monitoring routine running on the lesion computer, the retinal tracker running on the tracker computer, the operator, or the power failure detection circuitry. Thus, if the laser burn duration exceeds some maximum, or the lesion reaches the required size, or the tracker loses lock, or the operator senses trouble, or the computer senses a power fault, then an interrupt occurs and the shutter is immediately closed. The exception is then examined and acted upon. Any abnormal exceptions are handled by the operator.

### **7.5.2 Tracking Computer Software Design**

The Retinal Tracker Software design is shown in Figure 7-12. This routine assumes that the proper field is already in view. The blood vessel coordinates are received from the master computer software, and these are passed to the Matching Algorithm. As explained in Chapter 4, "Retinal Tracker", a course match is performed first followed by a fine match.

These new coordinates are passed to a Prediction algorithm. Since the imaging and processing takes time, the computer's calculated position will lag the actual retinal position. The Prediction algorithm predicts the most current position of the

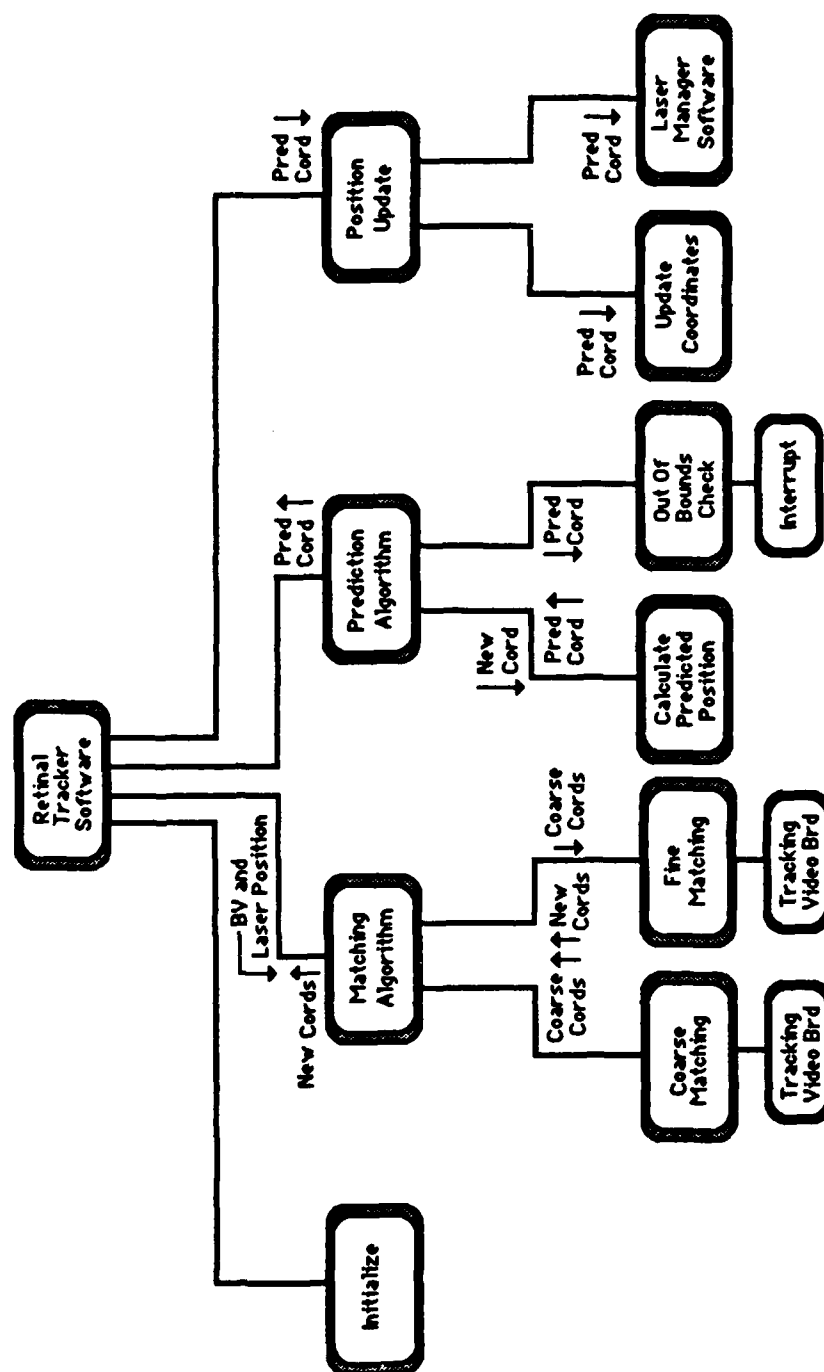


Figure 7-12 Structured design for the tracking computer software.

retina (see "Laser Delivery System" below). An Out of Bounds routine checks for unacceptable eye movement (such as large saccades or movement toward the fovea), which interrupts the computer and closes the shutter. If all is well, the predicted coordinates are passed directly to the Laser Manager Software to update the actual laser position. The sequence is then repeated starting at the Matching Algorithm.

### 7.5.3 Lesion Computer Software Design

The Lesion Monitor Software Design is shown in Figure 7-13. An initialization is performed directly after the computer system is turned on. The Master Interface subroutine then polls the master computer (Lesion Manager Software), waiting for a response. Once communications are established, the lesion information is received by the lesion computer. All initial computations are made for lesion monitoring by the lesion computer and then a Ready is sent to the master computer. The Master Interface routine is exited and the Lesion Burn routine is entered. The lesion computer polls for the start from the master, and upon receipt, starts an interval timer. The interval timer insures that the lesion burn time does not exceed some maximum expected time, thus preventing excessive laser burns. The interval timer will interrupt the lesion computer after a specified time which in turn interrupts the master computer.

After setting the interval timer, the Lesion Burn routine monitors the lesion through its video board and the lesion camera. When the lesion has reached the desired width and depth, an interrupt is furnished to the master computer (Laser Manager Software). The shutter is closed. The criteria that the computer must use to control the lesion size is discussed in Chapter 5, "Lesion Size Control". The routine

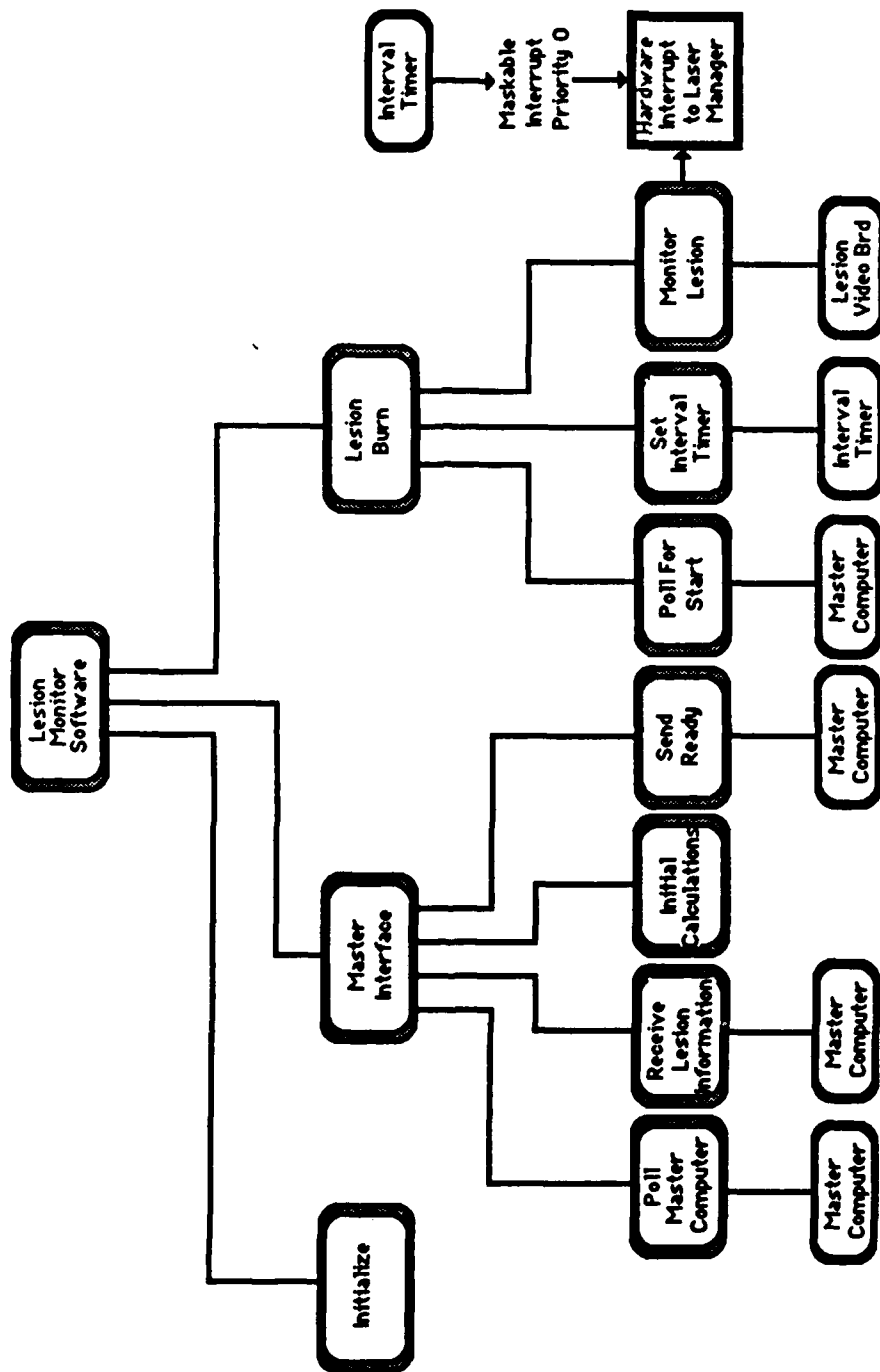


Figure 7-13 Structured design for the lesion computer software.

then returns to the Maser Interface routine and polls the master computer, awaiting for the start of the next lesion.

## 7.6 Laser Delivery System

This section discusses the laser delivery system. A block diagram of the closed loop laser delivery system and retinal tracker is shown in Figure 7-14. The camera is discussed above in "Video Cameras and Video Cassette Recorder" and the feature extraction is discussed in Chapter 4, "The Retinal Tracker". The optics will be discussed in "Optics" below.

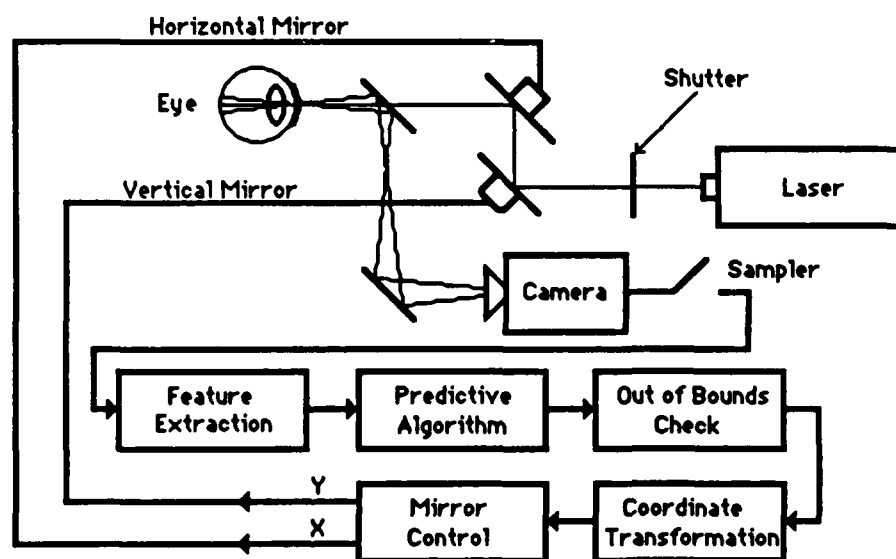


Figure 7-14 Block diagram of the laser delivery system and retinal tracker.

Predictive robotic tracking prevents the laser from lagging the system. Bahill [7-2] studied this problem and derived a simple algorithm to predict the final position of the eye halfway through a saccade. The basic assumption is that the saccadic movements are ballistic (see Chapter 2, "Anatomy and Light Interaction of the Eye"), and once a saccade has reached its maximum velocity, the eye has travelled about half the distance of the saccade. If the tracker knows the initial position of the eye before a saccade and the position of the eye when maximum velocity is attained, then the following equations will predict the final location:

$$\theta_f = (1.4 + 0.05\theta_i)\theta_i \quad \text{for temporal saccades (positive x)} \quad (7-3)$$

$$\theta_f = (1.4 + 0.04\theta_i)\theta_i \quad \text{for nasal saccades (negative x)} \quad (7-4)$$

$$\theta_f = 2.0\theta_i \quad \text{for } \theta_i \text{ greater than } 15^\circ \text{ (1000 Hz)} \quad (7-5)$$

$$\theta_f = 1.2\theta_i \quad \text{for } \theta_i \text{ greater than } 10^\circ \text{ (60 Hz)} \quad (7-6)$$

where

$\theta_f$  = Total angular change from the initial to the final position.

$\theta_i$  = Total angular change from the initial position to the position of maximum velocity.

Equations 7-5 and 7-6 are used for large saccades. The data that Bahill used to derive the first three equations were from eye movements that were sampled at 1000 Hz, but he also analyzed the data for 60 Hz sampling to derive Equation 7-6 (Equations 7-3 and 7-4 were still valid for 60 Hz). He claimed that the above equations predicted actual eye movements with a correlation of 0.961 and 0.927 (his best and worst subject, respectively). For 60 Hz sampling, saccades smaller than  $10^\circ$  could not be predicted because of slow sampling speeds. But other predictions larger

than  $10^\circ$  were made either 0, 17, or 34 ms before the eye came to rest. Vertical saccades showed poorer results, with a correlation of 0.870 and 0.774 for his two subjects. He also claimed that predictions using accelerations were very noisy and required extensive filtering, and that the velocity prediction was more accurate.

One further complication in prediction for the proposed system is the delay of 17 ms that the camera requires to sense the signal and another 17 ms that the computer requires to calculate the current position. The camera delay can be reduced somewhat by using a shuttered camera, but the software tracker calculations will most likely always require at least 17 ms. This supports the evidence shown in the section, "The Optimum Video Rate", that a quicker video rate would significantly enhance the system.

Prediction can also be done using other algorithms. Hunt and Sanderson [7-30] performed vision-based predictive robotic tracking of a moving target using several methods, to include the Kalman filter. They found that most predictions except the most simplest were computationally expensive, where the Kalman Filter took 54 ms for each prediction on a LSI11 computer. Even though the Kalman filter is one of the best predictors, its real time use is limited for personal computers using video cameras that are sampling every 17 ms.

The coordinate transformations adjust the laser's position with new coordinates. In the tracking algorithm in Chapter 4, "The Retinal Tracker", only translation was calculated. If rotation, scaling and translation are calculated, the following equation is used to update the laser's coordinates [7-30]:

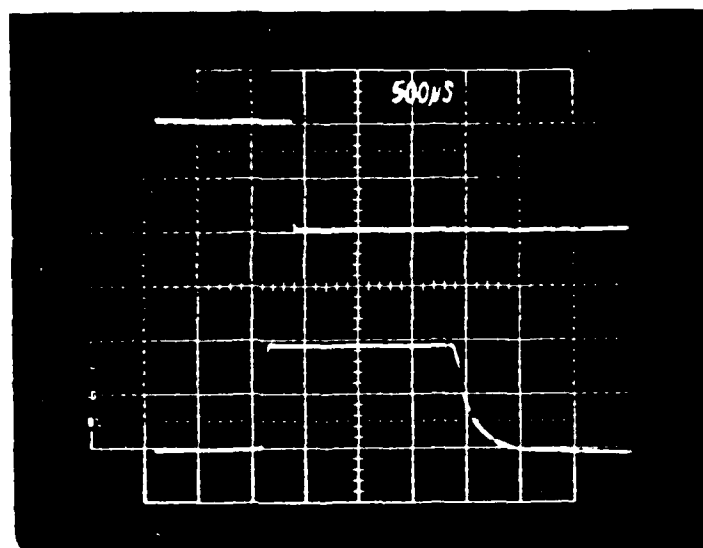
$$\begin{pmatrix} x_r \\ y_r \end{pmatrix} = \begin{pmatrix} \cos(\lambda) & \sin(\lambda) \\ -\sin(\lambda) & \cos(\lambda) \end{pmatrix} \begin{pmatrix} m & 0 \\ 0 & n \end{pmatrix} \begin{pmatrix} x_c + h \\ y_c + k \end{pmatrix} \quad (7-7)$$

where

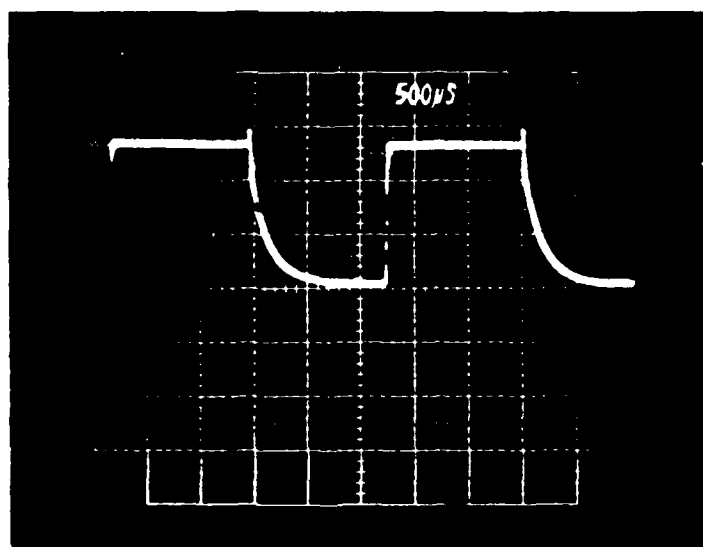
- $x_r, y_r$  = new coordinates.
- $x_c, y_c$  = old coordinates.
- $h, k$  = translational mismatch in the x and y direction, respectively.
- $\lambda$  = rotational mismatch.
- $m, n$  = scaling mismatch in the x and y direction, respectively.

The Out of Bounds Check examines the predicted coordinates and decides if the retinal tracker has lost track. For this situation, and many others as outlined in "Software" above, the laser shutter is closed. Once it has been decided that the laser shutter must be closed, the response time is very quick. The three waveforms shown Figure 7-15 are experimentally measured results of the shutter's response times. The shutter is manufactured by A. W. Vincent Associates [7-57]. The waveform in Figure 7-15(a) is the electrical input to the shutter. The rising edge is not shown but occurs just prior to the start of the waveform. The waveform in Figure 7-15(b) is the output of a photodetector that detects the laser's passage through the shutter. Notice that the delay of the shutter is only 1 ms. The opening of the shutter is very rapid (from the rapid rise time of the second waveform) but the falling edge could not be measured because of the poor detector response. The waveform in Figure 7-15(c) is the photodetector response to a pulsed laser. Notice the time for the falling edge to drop in Figure 7-15(c) corresponds to the time for the falling edge to drop in Figure 7-15(b).





(a)



(b)

Figure 7-15 Laser shutter Response. (a) Input verses output of the shutter. (b) Detector used as the detecting source.

It would seem from the previous discussion that the system will perform quite poorly. But, in deciding how good is good, remember two points. First, when the laser is irradiating a point on the retina and the individual moves his/her eye, the laser will smear across the retina, generally not causing any damage until the eye becomes motionless. Even after it is motionless, the laser does not immediately create a new lesion. Since the laser duration is timed by the interval timer (see "Software" above), there is a low probability that an accidental lesion can be created before the tracker "catches up". Second, the tracker will be successful if its reaction time is faster than a human, since humans now perform the laser surgery. The human reaction time is about 80 ms, at least twice as slow as the tracker.

## 7.7 Optics

This section discusses the design of the optical system. This system is extremely complex and the suggested ideas that follows are only preliminary groundwork. The purpose is to discuss the problems and propose avenues for their solutions.

The optical system interfaces the fundus camera, the laser delivery system, the lesion camera, and the tracker camera. Initially, the design should insure that the fundus camera and laser delivery system remain as commercial products with little, if any, modifications; these optical systems are much too complex to redesign. There are basically three ways of combining the systems: chromatic, spatial, and temporal. Each of these will be discussed. The optics required to focus the laser onto the retina will also be reviewed.

### 7.7.1 Coaligining the Optical Systems

A chromatic arrangement is shown in Figure 7-16. The fundus camera is positioned to the right of the figure. The working distance between the objective of the fundus camera and the surface of the cornea is only 45 mm on most fundus cameras. The laser cannot be delivered through the fundus camera objective because of the severe aberrations caused by the objective when the laser is directed off axis [7-28]. The only recourse is to coalign the fundus camera with the laser and lesion computer within the working distance. The working distance cannot be lengthened without reducing the 50° field of view. To chromatically mix these images, beam splitters are required.

First, the lesion camera and its illuminating laser must be coaligned. The illuminating laser will often double as the pointing laser and will hence be called the pointing laser (This laser might conveniently be an inexpensive HeNe laser {633 nm}). These can be coaligned by using a beam splitter (Beam Splitter 1) that reflects a certain phase orientation of the pointing laser but transmits all other energy. Some of the laser light returning from the eye will be incoherent and will pass through the beam splitter to the lesion camera. (Some of the returning light could be polarized [7-58] and would have to be passed through a prism to allow reverse passage through the beam splitter.)

The next beam splitter (Beam Splitter 2) must coalign the surgical laser with the lesion camera and pointing laser. The surgical laser could be an Argon blue-green (488 nm and 514 nm), Argon green (544 nm), Krypton yellow (568 nm), a tunable dye (590 nm to 630 nm), or Krypton red (647 nm). This covers most of the visible band. A dichroic filter can be manufactured that reflects all wavelengths except the

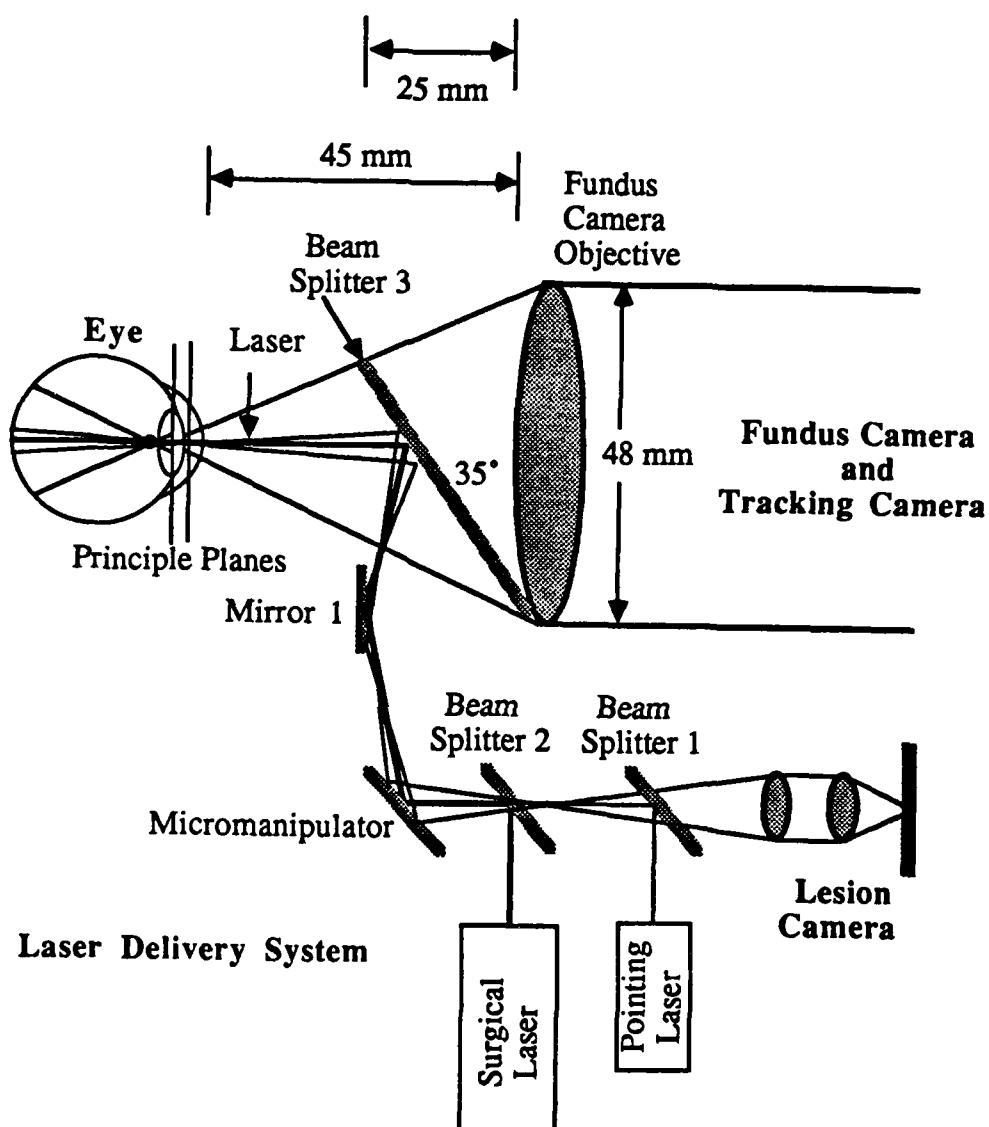


Figure 7-16 Optical schematic for the integration of the laser delivery system with any fundus camera.

HeNe, which it transmits. This filter only cost \$110 [7-1]. All this coalignment is done behind the micromanipulator. Thus, all three systems (pointing laser, surgical laser, and lesion camera) are all maneuvered together and always image the same area of the fundus.

Chromatically combining the mixture just developed with the fundus camera is expensive and difficult. Beam Splitter 3 must reflect the pointing laser into the eye and then reflect the returning light into the lesion monitor. It must also transmit some of this energy because the tracking camera needs to see the laser's position. All the energy from the surgical laser must be reflected to avoid blinding both the operator and tracking camera. Special dichroic filters can be manufactured that reflect 80 % of the HeNe energy and 98 % of the Argon energy (if the surgical laser was an Argon), but pass all other wavelengths. This filter costs \$1900 [7-1].

This design is weakened considerably at Beam Splitter 3. It occupies a considerable portion of the working distance. Because the beam splitter must reflect two separate bands of energy, it's expensive. If another surgical laser other than Argon is used, the beam splitter must be replaced with another expensive beam splitter.

The tracking camera is generally coaligned with the fundus camera using a beam splitter. This alignment was discussed above in "Illumination Source".

Before the two other methods of coaligning images are discussed (spatial and temporal), an explanation of the angle of Beam Splitter 3 will be given. If the edges of the beam splitter are not to be seen in the fundus image, then it must completely cover the viewing cone from the fundus camera. Notice that the proposed integration optics does not simply use an angle at  $45^\circ$ , since this is not the most compact method of inserting the mirror system. It can be shown that the beam splitter can be placed at

an angle of  $35^\circ$  if another mirror is placed nearby (Figure 7-16). This arrangement makes optimum use of the space provided.

Spatial alignment is performed by putting a small mirror in the field of view of the fundus camera. The lasers would reflect from this mirror and enter the eye, coaligning with the fundus camera. If the small mirror is not inserted at a focal plane and if it is substantially smaller than the viewing cone from the fundus camera, the mirror would only reduce the intensity of the fundus image, not the information content (i.e. it should not be seen). Unfortunately, the viewing cone of the fundus camera is actually two cones, one for the field illumination and one for observation, complicating the problem. But, Donaldson [7-17], in his stereoscopic fundus camera, finds room in the viewing cone to add a lens used for initial pupil alignment. This could be substituted with a mirror.

Temporal alignment inserts a mirror in front of the fundus camera for just a short period of time, and then removes it. A rotating wheel similar to the Zybion color wheel in their cameras would work well. The tracking camera views the fundus when the mirror is removed and the lasers irradiate the fundus when the mirror is in place. This design results in a pulsed laser system. Some disadvantages with this design are the mechanical complications of the rotating wheel, the inability of the tracking camera to see the pointing laser, and the use of a pulsed laser when they have not been extensively used for eye surgery.

The optimum arrangement might be the design shown in Figure 7-16 but eliminate Beam Slitter 3 by using a spatial or temporal technique. Notice that in any arrangement, the surgical laser light must be blocked from the view of the operator, tracking camera, and lesion camera.

An alternative to the previously discussed design is to eliminate the pointing laser. Maintaining the alignment of two lasers can be extremely difficult, especially in a clinical environment. This idea also simplifies the optics, decreases the system's cost and size, and allows for easier FDA approval. To implement this alternative, the field illumination of the fundus camera must be capable of providing the illumination source for the lesion camera. A more sensitive lesion camera will have to be used. Also, the tracking camera must still be able to monitor the laser's position during laser irradiation. This can be done by either allowing some of the surgical laser's energy to bleed through the filters, or using a pulsed laser system.

#### 7.7.2 Focussing the Laser

The laser spot size on the retina must be controlled. Slitlamps allow the ophthalmologist to select the spot size of the laser, generally from 50  $\mu\text{m}$  to 1000  $\mu\text{m}$ . Unfortunately, this is the spot size of the laser in air, not on the retina. The optics of the eye obviously modify the size. At the present time, ophthalmologist can only guess the true retinal spot size of the laser. The optical system must also insure that the surgical laser, pointing laser, and slitlamp are all in focus on the same plane. It is thus assumed that when the ophthalmologist focuses onto the retina, the lasers are also at their focal point. (The accommodation of the human operator can add some error to this procedure. See "Imaging with the Fundus Camera" above.)

Generally, the laser is not colinear but is geometrically focussed onto the retina. There are several techniques that are used to control the spot size of the laser. The prevailing method of delivering the laser to the general area of the patient's eye is with a fiber optic [7-24]. The articulated arm, which consist of mirrors connected to-

gether in a flexible tube, is the second method and is only used with lasers that cannot propagate down a fiber optic (such as the CO<sub>2</sub> laser).

The laser is then directed into the eye with mirrors and its spot size is controlled with lenses. The proper laser spot size can be achieved by either focussing the right size beam onto the target (modifying the magnification of the image), or focussing the beam behind the target and insuring the defocussed beam on the target is the right size. The first of these is called parfocal, and the second is called defocussing. To determine the best method, two constraints must be considered. The first is the possibility of an accidental decrease in the spot size from a focussing error. The second is the spot size of the laser on the cornea.

For a 50  $\mu\text{m}$  spot size, the parfocal method must be used because this is the diffraction limited spot size (the laser spot size never gets any smaller). The laser must be focussed onto the retina. For 100  $\mu\text{m}$  spot size, the defocussing method could create a 100  $\mu\text{m}$  spot size on the retina by focussing the laser to a 50  $\mu\text{m}$  spot behind the retina. Goldblatt [7-24] showed (using a standard set of parameters) that if this was done, then a 0.3 mm focussing error caused by patient movement or operator error could decrease the spot size to 50  $\mu\text{m}$  and hence increase the power density by a factor of four. Thus for both 50  $\mu\text{m}$  and 100  $\mu\text{m}$  spot sizes, the parfocal method is used to control the spot size.

For these two situations, the spot size on the cornea is relatively large. But as the spot size on the retina gets larger using the parfocal, the spot size on the cornea get smaller. Using the parfocal method to focus a 500  $\mu\text{m}$  spot on the retina would result in a 0.9 mm spot size on the cornea, while the defocussing method would result in a



1.5 mm corneal spot size. It is thus advantages to use the parfocal method for 50  $\mu\text{m}$  and 100 $\mu\text{m}$ , and then the defocussing method for 200  $\mu\text{m}$  and larger.

### 7.8 System Costs

The estimated costs, excluding engineers, to build the first prototype is given in Table 7-5.

Equipment		Price
1.	Fundus Camera (Olympus)	14K
2.	Laser Delivery System (Coherent LDS-20)	16K
3.	Laser System (Argon, Krypton, and Dye)	70K
4.	Tracking Video Camera (Xybion)	18K
5.	Lesion Video Camera (unknown, 1000 frames/sec at 32 x 32 pixels)	12K
6.	Video Mixer	5K
7.	Video Cassette Recorder	2K
8.	Computer (VME Bus)	15K
9.	Imaging Boards (qty 2)	15K
10.	Color Video Monitor and Trackball	5K
11.	Optics	50K
12.	Mechanical Work	30K
Total		252K

Table 7-5 Equipment Cost in 1987 prices.

If the lesion video camera is not commercially available then it will have to be custom built. The optics work is discussed in "Optics" above, and the mechanical work is to mount the optics and modify the fundus camera with the additional attachments discussed in "Fundus Camera" above.

## 7.9 Safety

Criteria should be established to decide if this system is suitable for actual clinical use. One such criteria could be 100% fail-safe operation. Since this is impossible, the following three questions might lead to a more intuitive and realistic criteria. (An accident is defined as a malfunction or error that unintentionally harms the patient):

1. What are the estimates for the probabilities of different types of accidents?
2. How accurate are these estimates?
3. How small do the probabilities have to be for the system to be clinically safe?

No attempt is made to answer the first two questions since a prototype has not been built. These are not easy questions to answer, but analyzing the probability of failure or error for each subsystem might be a start. The graphs in Figure 4-15 and 4-16 are examples of estimating the probability for false positives in the tracker routine (see Chapter 4, "The Retinal Tracker"). A partial answer to the third question is that the probability of an accident for this new system must be lower than the probability of an accident using present laser surgery techniques. Unfortunately, statistics are not available to quantitatively answer this question. But these questions should be answered before the system is used in a clinical environment.

### 7.10 Conclusion

This chapter presented the instrumentation requirements for the robotic system. The design emphasized the use of commercially available equipment since the system spans a diverse number of engineering fields. Some of the ideas that surfaced in this chapter were to use a stereoscopic fundus camera, increase the video frame rate to 120 frames/sec and use a video digitizing board with an on board microprocessor. Overall, the electrical and mechanical work appears to be straight forward, the optical work will be difficult, and the software will be exceedingly difficult.

## **Chapter 8 Further Research**

This chapter provides a list of further research related to this project. The research is divided into general, light interaction with tissue, retinal tracking, retinal image processing, instrumentation, optics, mechanical, and software. The research items that are considered significant in the development of a prototype are starred.

### **8.1 General**

- \*1. Analyze the difficulty that the system will encounter with imaging and tracking abnormal eyes (eyes with such problems as variable opacities of the lens (cataract), aqueous (hyphema), or vitreous (vitreous hemorrhage)).
2. Investigate how this system could be used on the anterior part of the eye. (see Chapter 3, "Overview of the System - Advanced Features")
3. Analyze the economic implications and marketing of this system. (see Chapter 1, "Introduction - Economic Implications")
4. Analyze the FDA requirements for clinical testing. (see Chapter 8, "Instrumentation - Safety")

## **8.2 Light Interaction with Tissue**

1. Examine the actinic (photo) effects on tissue. (see Chapter 2, "Anatomy and Light Interaction with Tissue - Tissue Optics and Damage", and Chapter 7, "Instrumentation - Illumination Source")
2. Examine the effects of a pulsed laser on tissue. (see Chapter 2, "Anatomy and Light Interaction with Tissue - Tissue Optics and Damage")
- \*3. Overview the present strategy that ophthalmologist use (and researchers propose) for laser surgery. This should include a listing of all diseases that are treated with lasers, the required results from the laser treatment, and the laser parameters that produce these results. (see Chapter 5, "Control of Lesion Size - Lesion Development")
- \*4. Continue the work in relating reflection changes to tissue damage [8-3]. (see Chapter 5, "Control of Lesion Size")

## **8.3 Retinal Tracking**

1. Investigate the use of acousto-optical cells in the image registration problem [8-2]. (see Chapter 4, "The Retinal Tracker ")
- \*2. Modify the initial routine that identifies and delivers the best horizontal and vertical blood vessels to the real time tracking routine to insure that the vessels are indeed horizontal or vertical. (see Chapter 4, "The Retinal Tracker - Building the Template" and Chapter 4, "The Retinal Tracker - Strengths and Weaknesses")
3. Investigate the idea of only using one edge of the blood vessel instead of two in the tracking algorithm. (see Chapter 4, "The Retinal Tracker - Building the Template")

4. Investigate the idea of using bifurcations of blood vessels instead of the edges of blood vessels in the template. (see Chapter 4, "The Retinal Tracker - Building the Template")

\*5. Examine the reason why the tracking program could not identify that it had lost track (i.e. why did the precalculated correlation not agree with the real time correlations?). (see Chapter 4, "The Retinal Tracker - Strengths and Weaknesses")

6. Develop a real time routine that can detect rotation and scaling mismatch in the images. (see Chapter 4, "The Retinal Tracker - Strengths and Weaknesses" and Chapter 7, "Instrumentation - Laser Delivery System" )

\*7. Analyze the quickening of the tracking algorithm. Use the ideas mentioned in Chapter 7. Especially, try executing the program on an 80386, use a video board with an on board microprocessor, and speed the video rate of the video camera. (Chapter 7, "Instrumentation - Decreasing Execution Time" and Chapter 7, "Instrumentation - The Optimum Video Rate")

\*8. Implement the prediction algorithm and test it on data generated from the tracking routine. (Chapter 7, "Instrumentation - Laser Delivery System" )

#### **8.4 Retinal Image Processing**

A general approach to research in this area is:

1. List every feature that is present in a retinal image. Divide these features into normal and abnormal.
2. Create and test a computer algorithm to detect each feature listed in 1. (see Chapter 5, "Retinal Image Processing - Retinal Image Analysis")

3. List the conditions (such as the wavelength of illumination) where the features in 1 would be most visible. (see Chapter 5, "Retinal Image Processing - Retinal Image Analysis")
4. Build an algorithm that suggest the pathological conditions that relate to any abnormal features or combination of features in the retina. (see Chapter 5, "Retinal Image Processing - The Detection and Treatment of Retinal Disorders")
5. Build an algorithm that suggest therapy for the pathological conditions.

Some specific suggestions are as follows.

- \*1. Analyze the methods that other researchers have used to detect blood vessels in retinal images. Derive the "best" algorithm. Canny [8-1] wrote an excellent thesis on finding lines in images. The data structure that defines the blood vessel template must also be developed. Also derive the best algorithm for mosaic calculations. (see Chapter 5, "Retinal Image Processing - Detection of Retinal Blood Vessel" and Chapter 8, "Instrumentation - Mosaics")
2. Develop an algorithm to calculate depth information from stereoscopic images. (see Chapter 8, "Instrumentation - Stereoscopic Fundus Cameras")
- \*3. Improve the lesion insertion algorithm for diabetic retinopathy. The routines in Chapter 5, "Retinal Image Processing", used a simple mask. What's needed is an adjustable mask to optimally fit the lesions around blood vessels. (see Chapter 5, "Retinal Image Processing - Selecting Lesion Locations")

### 8.5 Instrumentation

1. Design the system to accurately measure retinal image sizes. (see Chapter 2, "Anatomy and Light Interaction with Tissue - Optics of the Eye" and Chapter 7, "Instrumentation - Imaging with the Fundus Camera")
- \*2. Design the autofocussing system. (see Chapter 7, "Instrumentation - Fundus Camera Autoalignment")
3. Design the system to control the illumination source. (see Chapter 7, "Instrumentation - Illumination Source")
4. Investigate the feasibility of using the Scanning Laser Ophthalmoscope in lieu of the fundus camera for this system. (see Chapter 7, "Instrumentation - An Overview of Fundus Cameras")
- \*5. Build the fixating device. (see Chapter 7, "Instrumentation - Fixating Device")
6. Analyze how an advanced video camera (one with a video rate greater than 30 frames per second or detector sizes larger than 512 x 512 pixels) can interface to a computer for real time access. (see Chapter 7, "Instrumentation - Video Camera for Retinal Observation")
- \*7. Design and build the lesion camera. (see Chapter 7, "Instrumentation - Video Camera for Lesion Monitoring")
- \*8. Investigate the use of semiconductor lasers as the illumination source for the lesion camera. (see Chapter 7, "Instrumentation - Video Camera for Lesion Monitoring")
9. Quantify and identify all errors (both DC and AC) associated with the data acquisition system (especially the VCR and video digitizing boards). (see Chapter 7,



"Instrumentation - Video Cassette Recorders" and Chapter 7, "Instrumentation - Video Boards")

10. Derive the equation or software algorithm that relates the SNR of a video signal to the probability that the least significant bit of a digitizing system is in error. Chapter 7, "Instrumentation - Spatial Specifications"

### **8.6 Optics**

1. Examine the issue of whether a contact lens should be used with the fundus camera. (see Chapter 7, "Instrumentation - An Overview of Fundus Cameras")

2. Investigate the off-axis image quality in the human eye. (see Chapter 2, "Anatomy and Light Interaction with Tissue - Optics of the Eye")

3. Calculate the MTF of a fundus camera. (see Chapter 7, "Instrumentation - Spatial Specifications")

\*4. Design the integration optics for the system. (see Chapter 7, "Instrumentation - Coaligining the Optical System")

\*5. Research the use of a stereoscopic fundus camera in the proposed system. (see Chapter 7, "Instrumentation - Stereoscopic Fundus Camera")

### **8.7 Mechanical**

\*1. Build the servo controlled system to allow the computer to maneuver the fundus camera. (see Chapter 3, "Overview of the System - Advanced Features" and Chapter 7, "Instrumentation - Fundus Camera Autoalignment")

## **8.8 Software**

- \*1. Develop the software to autoalign the fundus camera with the patient. (see "Chapter 3, "Overview of the System - Advanced Features" and Chapter 7, "Instrumentation - Fundus Camera Autoalignment")**
- \*2. Develop the software for the system. (see Chapter 7, "Instrumentation - Computer Software")**
- \*3. Develop the software and control equations to track and point the laser on the retina.**

## Chapter 9 Summary of Major Accomplishments

The research goals for this dissertation were to analyze, design and demonstrate the feasibility of a second generation laser delivery system used for retinal surgery. The goal of the project is to develop an automated laser delivery and retinal observation system that is capable of placing multiple lesions of predetermined sizes into known locations in the retina. The major accomplishments of this dissertation are as follows.

1. A substantial amount of literature pertaining to this project was collected and documented.
2. A preliminary design for the entire system has been provided.
3. Retinal blood vessels were identified in a retinal photograph, and lesion locations for panretinal photocoagulation were selected.
4. Simple retinal tracking was performed on a moving picture of the retina using a personal computer and a video digitizing board. Small circular motion of approximately 5 Hz was successfully tracked.
5. Lesions were placed in four *in vivo* rabbit livers. Each lesion's width was measured histologically, microscopically, visibly (using a video camera), and thermally (using a thermal camera). Even though the results of this experiment were disappointing, the experimental procedure and equipment has been established.

6. Lesions created in an *in vitro* beef liver were controlled by monitoring (at 420 frames/sec) the growing width of the forming white spot and terminating the laser irradiation at some predetermined diameter. The standard deviation of the resulting widths for 31 lesions was 13%. The average of the resulting widths was only 8% larger than the desired width.

Even though the specific project goal is stated above, a more general goal of the research is the advancement of knowledge that will provide better quality health care to mankind. This researcher is convinced that the research in this field will lead to the development of a system that will do just that.

## **Appendix 1 Algorithm to Identify a Closed Area**

This algorithm identifies a closed boundary as traced by the operator using a mouse or trackball. All pixels inside the closed boundary are then identified. Linked lists are used to conserve memory.

1. Wait until the mouse button is pushed. If the mouse button is released before the completion of step 4, then initialize and start over at step 1.

*The first task is to establish a closed boundary.*

2. Read the mouse position. Insert this position into the linked Boundary List, which is a singularly linked list that connects the last position of the boundary to the next position.
3. The next current position is read from the mouse. All pixel locations that lie on a line between the last position of the mouse and the current position are calculated and entered into both lists. The current position is also entered into the list.
4. Step 3 continues until a Repeated Pixel Location is found. A Repeated Pixel Location is defined as follows: when a pixel location from step 3 is selected to be inserted into the Boundary List, the list must be searched to insure that pixel is not already in the list. The Boundary List is also checked to insure that all neighbors (one

of the eight pixels surrounding the pixel) are also not in the list. If any of these 9 pixel locations are found in the list, then the mouse or trackball has already crossed or has been close to that location and the boundary is closed. This location is called the Repeated Pixel. Notice that when the list is searched for neighbors, the previous entry into the list should not be checked since it will be a neighbor - the boundary is a continuous line.

5. The Boundary List is searched from the starting position to the first occurrence of the Repeated Pixel Location. All these nodes up to the Repeated Pixel Location are deleted from the lists. This removes the initial portion of the line that is not included on the boundary.

*The second task is to determine if a given pixel is interior to the boundary.*

6. From the given pixel, draw four imaginary lines extending up, down, left, and right. These lines extend to the edge of the picture.

7. Traverse the Boundary List. Count the number of times that each of the four lines are crossed. The boundary must fully cross the line, not just touch it.

8. If the number of crossings for each line is greater than 0 and odd, then that pixel is in the interior of the boundary.

*The third task is to quickly identify all pixels interior to the boundary.*

9. Find at least one pixel in the interior of the boundary.

10. Using a breadth first type of search employed in graph theory, look at all neighbors (first generation) of this preliminary pixel location. If these neighbors are not in the Boundary List, then add them to the Interior Pixels List and check their neighbors

(Never check a neighbor of a pixel found on the boundary). Insure the next generation of neighbors are not on the boundary, and then check their neighbors. Continue this process until all neighbors have been examined. The Interior Pixels List now contains all pixel locations that are interior to the enclosed area.

## Appendix 2 Correlation Calculations

This appendix provides the calculations that relate the number of correlations or comparisons to the video frame rate. The computer must perform a correlation at each pixel location in a small window (an assumption for these calculations). This must be done for each window in each image. This window is a circle with radius  $R$ , where  $R$  must be calculated using the actual velocity and acceleration parameters of the eye.

The size of the window can be defined in two ways. In one case, the eye is considered to be motionless during the last image and all subsequent movement is caused by the acceleration from the motionless state to the present velocity. The second case deals with the more general idea of the eye having a velocity component during the previous image. This case can be a significant problem since the eye can move very rapidly. The patient will not be allowed to gaze about the room as the laser surgery takes place. If the eye starts to move rapidly, the laser will be turned off. Thus the following calculations will assume the first case.

From Chapter 2, "Anatomy and Light Interaction of the Eye", the maximum velocity of the eye is  $600^\circ/\text{sec}$ , and the maximum acceleration is  $40,000^\circ/\text{sec}^2$ . The maximum movement that can occur between two successive video frames is when the eye, starting motionless, precedes on a maximum acceleration course until it reaches



maximum velocity, then maintains that velocity. The minimum time to reach maximum velocity is:

$$\text{Minimum Time} = \frac{600^\circ/\text{sec}}{40,000^\circ/\text{sec}^2} = 0.015 \text{ seconds} \quad (\text{A2-1})$$

The distance moved during this first acceleration period (Time < 15 ms) is:

$$\text{Distance (mm)} = \frac{(\text{Acceleration (mm/sec}^2\text{)})(\text{Time})^2}{2} \quad (\text{A2-2})$$

Using the acceleration of  $40,000^\circ/\text{sec}^2$  and knowing that  $1^\circ = 0.3 \text{ mm}$  on the retina then:

$$\text{Distance} = \frac{(40,000^\circ/\text{sec}^2)(0.3 \text{ mm/deg})(\text{Time})^2}{2} \quad (\text{A2-3})$$

At 15 ms (up to this time the eye is accelerating) the total distance is (using A2-1 into A2-3):

$$\text{Distance} = \frac{(40,000^\circ/\text{sec}^2)(0.3 \text{ mm/Deg})(0.015 \text{ sec})^2}{2} = 1.35 \text{ mm} \quad (\text{A2-4})$$

Thus the eye has moved 1.35 mm during this first acceleration period.

Subsequent to 15 ms, the eye is moving at a constant velocity. The total distance moved is equal to the distance moved before 15 ms (which was 1.35 mm) plus the velocity multiplied by the amount of time the eye has had to move after 15 ms, or:

$$\text{Distance (mm)} = 1.35 \text{ mm} + (600^\circ/\text{sec})(0.3 \text{ mm/deg})(\text{Time} - 0.015 \text{ sec}) \quad (\text{A2-5})$$

This represents the total distance as a function of time that the eye has moved from its motionless state.

The sampling period is the time between successive images. The radius of the window is the maximum distances just calculated. Equation A2-3 is used for sampling periods under 15 ms and Equation A2-5 is used for sampling periods over 15 ms. The millimeter must be converted to pixels, which will use the following equation:

$$(512 \text{ pixel}) / (10^\circ)(0.3 \text{ mm/}^\circ) = 170.7 \text{ pixels / mm}$$

If the sampling period is smaller than 15 ms then from Equation A2-3:

Radius (pixels) =

$$(12,000 \text{ mm/sec}^2)(1/2)(\text{sampling period})^2(170.7 \text{ pixels / mm}) \quad (\text{A2-6})$$

If the sampling period is greater than 15 ms then from Equation A2-5:

$$\begin{aligned} \text{Radius (pixels)} = \\ (1.35 \text{ mm} + (180 \text{ mm/sec})(\text{sampling period} - 0.015 \text{ sec})) (170.7 \text{ pixels / mm}) \quad (\text{A2-7}) \end{aligned}$$

Lastly, the curve for the number of correlations per second is the number of frames per second (Video Rate) times the number of pixels in the window ( $p * R^2$ ).

$$\text{Correlations per second} = (\text{Video Rate}) * (p * R^2) \quad (\text{A2-8})$$

The graph in Figure 7-10 plots Equation A2-8.

### **Appendix 3 Comparing the MTF's of a Video Camera, a Photograph, and the Eye**

This appendix will compare the modulation transfer function of a video camera, a photograph, and the human eye. The MTF's of each of these are shown in Figure 7-6. The ultimate goal of the comparison is to calculate the resolution of the device at its imaging plane (at its detector).

The MTF in Figure 7-6(a) is for the Cohu 4800 series solid state (CCD) video camera. The axis labeled *Horizontal Resolution TV Lines* is the number of sinusoidal cycles in the horizontal direction contained in a distance equal to the height of the imaged picture (see Chapter 7, "Instrumentation", for discussion). The size of its detector array is 8.8 mm (width) x 6.6 mm (height). Thus the resolution per distance for this device at a MTF of 60% (see Figure 7-6(a)) at the detector plane is:

$$\text{Resolution} = \frac{300 \text{ horizontal lines}}{6.6 \text{ mm}} = 45 \text{ cycles / mm} \quad (\text{A3-1})$$

The MTF in Figure 7-6(b) is for Kodak Vericolor II professional film, type L. The resolution per distance for this device at a MTF of 60% at the film plane is:

$$\text{Resolution} = 35 \text{ cycles / mm} \quad (\text{A3-2})$$

The MTF in Figure 7-6(c) is for the human eye. One minute of arc is equal to a distance of  $4.9 \mu\text{m}$  on the retina, or  $0.294 \text{ mm/degree}$ . Thus the resolution per distance for the eye at a MTF of 60% on the retina is:

$$\text{Resolution} = \frac{12 \text{ cycles per degree}}{0.294 \text{ mm/degree}} = 41 \text{ cycles / mm} \quad (\text{A3-3})$$

It would appear that all three systems are similar, but several rather significant caveats must be addressed. The detector size in a video camera is always small, such as  $8.8 \times 6.6 \text{ mm}$ . If the still camera had to always enlarge pictures from an  $8.8 \times 6.6 \text{ mm}$  area, then the video camera would indeed be slightly better. But the still camera uses a  $50 \times 35 \text{ mm}$  area. If the video camera and photograph were to image the same object, the still camera will have more detector area to image the object. Thus the still camera's resolution can be increased by  $35 / 6.6$ , or about 5 times. The photograph is thus far superior to the video camera. The second point to make is that the video camera's resolution is measured in the horizontal direction. The vertical resolution of 485 lines (RS-170) is generally less than its horizontal resolution.

The human eye's resolution appears similar to a video camera. But since the eye's central vision detector area (fovea) is only  $0.35 \text{ mm}$  in diameter, it is somewhat inferior to either the video camera or the still camera according to this particular criteria. This could be considered a poor comparison. However, the eye uses a rather elegant positioning system, which makes maximum use of its  $0.35 \text{ mm}$  detector area, and the eye does possess a large, poor resolution detector area (the peripheral vision) that enhances the eye's abilities considerably.

## Bibliography

### Chapter 1 Introduction

- 1-1. T. A. Rice, R. G. Michels and W. J. Stark, *Ophthalmic Surgery*, C. V. Mosby Company, St. Louis, 1984.

### Chapter 2 Anatomy and Light Interactions of the Eye

- 2-1. R. Agah, J. A. Pearce and A. J. Welch, "Quantitative Characterization of Arterial Tissue Thermal Damage", *Proceedings of AAMI 22th Annual Meeting*, pp. 9, May 1987.
- 2-2. H. B. Barlow and J. D. Mollon, *The Senses*, Cambridge University Press, Cambridge, 1982.
- 2-3. G. R. Barnes, "Vestibulo-Ocular Function During Co-ordinated Head and Eye Movement to Acquire Visual Targets", *J. Physiol.*, Vol. 287, pp. 127-147, 1979.
- 2-4. C. C. Barr, "Estimation of the Maximum Number of Argon Laser Burns Possible in Panretinal Photocoagulation", *American Journal of Ophthalmology*, Vol. 97, pp. 697-703, June, 1984.
- 2-5. T. Behrendt and E. Slipakoff, "Spectral Reflectance Photography", in: J. Justice, Jr., Ed., *Ophthalmic Photography*, Little, Brown and Company, Boston, pp. 95-100, Dec. 1982.
- 2-6. R. Birngruber, V. P. Gabel and F. Hillenkamp, "Fundus Reflectometry: A Step Towards Optimization of the Retina Photocoagulation", *Mod. Probl. Ophthalm.*, Vol. 18, pp. 383-390, 1977.
- 2-7. E. A. Boettner and J. R. Wolter, *Investigative Ophthalmology*, Vol. 1, No. 6, pp. 776-783, 1962.
- 2-8. R. A. Braunstein, MD, Morriston, N.J., personal conversation, Sept. 1985.
- 2-9. K. T. Brown, "The Electroretinogram: Its Components and their Origins", *Vision Res.*, Vol. 8, pp. facing page 644, 1968.

- 2-10. B.J. Busse and D. Mittelman, "Use of the Astigmatism Correction Device on the Zeiss Fundus Camera for Peripheral Retinal Photography", in: J. Justice, Jr., Ed., *Ophthalmic Photography*, Little, Brown and Company, Boston, pp. 65-76, 1982.
- 2-11. F. W. Campbell and R. W. Gubisch, "Optical Quality of the Human Eye", *J. Physiol.* 186, pp. 558-578, 1966.
- 2-12. J. A. S. Carruth, "Lasers in Medicine and Surgery", *IEEE Engineering in Medicine and Biology Magazine*, Vol. 5, No. 1, pp 37-40, March 1986.
- 2-13. H. D. Crane, personal conversation, Stanford Research Institute, Menlo Park, CA, July 1987.
- 2-14. F. C. Delori, J. S. Parker and M. A. Mainster, "Light Levels in Fundus Photography and Fluorescein Angiography", *Vision Research*, Vol 20, pp 1099-1104, 1980.
- 2-15. N. Drasdo and C. W. Fowler, "Non-Linear Projection of the Retinal Image in a Wide-Angle Schematic Eye", *Brit. J. Ophthalmol.*, pp.709-714, 58, 1974.
- 2-16. N. Ducrey, O. Pomerantzeff, C. L. Schepens, F. C. Delori, and J. Schneider, "Clinical Trials With The Equator-Plus Camera", *American Journal of Ophthalmology*, Vol. 84, No. 6, pp. 840-846, Dec. 1977.
- 2-17. E. Engelken, personal communications. USAF School of Aerospace Medicine, Brooks AFB, TX 78235.
- 2-18. V. P. Gabel, "Laser in Ophthalmology", in: F. Hillenkamp, Ed., *Lasers in Biology and Medicine*, Plenum Press, pp. 383-396, 1979.
- 2-19. W. J. Geereats, R. C. Williams, G. Chan, W. T. Ham, Jr, and D. Guerry III, "The Loss of Light Energy in Retina and Choroid", *Archives of Ophthalmology*, Vol. 64, pp. 157-167, Oct. 1960.
- 2-20. W. J. Geereats and E. R. Berry, "Ocular Spectral Characteristics as Related to Hazards from Lasers and Other Sources", *American Journal of Ophthalmology*, Vol. 66, No. 1, pp. 15-20, July 1968.
- 2-21. W. T. Ham, Jr., J. J. Ruffolo, Jr., H. A. Mueller and D. Guerry III, "The Nature of Retinal Radiation Damage Dependence on Wavelength, Power Level, and Exposure Time", *Vision Research*, Vol. 20, pp. 1105-1111, 1980.
- 2-22. E. Hecht and A. Zajac, *Optics*, Addison-Wesley Publishing Company, Reading, Mass., pg. 56, 1974.
- 2-23. F. C. Henriques, "Studies of Thermal Injury", *Arch. Pathol.*, Vol. 43, No. 12, pg. 489, 1947.

- 2-24. R. Hurtes, "Evolution of Ophthalmic Photography", in: J. Justice, Jr., Ed., *Ophthalmic Photography*, Little, Brown and Company, Boston, pp. 1-18, 1982.
- 2-25. W. T. Jackman and J. D. Webster, "On Photographing the Retina of the Living Eye", *Phil. Photographer*, Vol. 23, pg. 275, 1886.
- 2-26. J. A. M. Jennings and W. N. Charman, "Off-Axis Image Quality in the Human Eye", *Vision Res.*, Vol. 21, pp. 445-455, 1981.
- 2-27. E. R. Kandel and J. H. Schwartz, *Principles of Neural Science*, Elsevier/North-Holland, New York, pg. 685, 1981.
- 2-28. T. Lawwill, R. S. Crocket, G. Currier and R. B. Rosenberg, "Review of the Macaque Model of Light Damage with Implications for the Use of Ophthalmic Instrumentation", *Vision Research*, Vol. 20, pp. 1113-1115, 1980.
- 2-29. R. S. Longhurst, *Geometrical and Physical Optics*, 3rd Ed., Longman Group Limited, London, pg. 402, 1973.
- 2-30. W. Lotmar, "Theoretical Eye Model With Aspherics", *J. Opt. Soc. Am.*, Vol. 61, No. 11, pp. 1522-1529, Nov. 1971.
- 2-31. M. A. Mainster, D. H. Sliney, D. Becher, III, and S. M. Buzney, "Damage Mechanisms, Instrument Design and Safety", *American Academy of Ophthalmology*, Vol. 90, No. 8, pp. 973-991, August 1983.
- 2-32. M. A. Mainster, "Wavelength Selection in Macular Photocoagulation: Tissue Optics, Thermal Effects and Laser Systems", *Amer. Acad. Of Ophthal.*, Vol. 93, pp. 952-958, July, 1986.
- 2-33. W. B. Marks, W. H. Dobelle and E. F. MacNichol, Jr., "Visual Pigments of Single Primate Cones", *Science*, (Washington D. C.), Vol. 143, pp. 1181-1183, 1964.
- 2-34. D. Marr, *Vision*, W. H. Freeman and Company, New York, pg. 55, 1982.
- 2-35. G. Meyer-Schwickerath, "Development of Photocoagulation", in: Wayne F. March, Ed., *Ophthalmic Lasers: Current Clinical Uses*, (SLACK, 1984), pp. 5-11.
- 2-36. F. W. Newell, *Ophthalmology, Principles and Concepts*, 5th Ed., C. V. Mosby Company, 11830 Westline Industrial Drive, St. Louis 63141, 1982.
- 2-37. K. N. Ogle, *Optics, An Introduction for Ophthalmologist*, Charles C Thomas publisher, Springfield, Ill, 1961.
- 2-38. G. Polhamus, personal Conversation, Aug 1985.



- 2-39. O. Pomerantzeff, "Equator-Plus Camera", *Investigative Ophthalmology*, Vol. 14, No. 5, pp. 401-506, May 1975.
- 2-40. T. A. Rice, R. G. Michels and W. J. Stark, *Ophthalmic Surgery*, C. V. Mosby Company, St. Louis, 1984.
- 2-41. G. H. Robinson, "Dynamics of the Eye and Head During Movement Between Displays: A Qualitative and Quantitative Guide for Designers", *Human Factors* 21, pp. 343-352, June 1979.
- 2-42. H. G. Rylander, III, personal conversation, Biomedical Engineering Program, University of Texas at Austin, Austin, TX.
- 2-43. D. H. Sliney and M. L. Wolbarsht, *Safety With Lasers and Other Optical Sources*, pp. 265-267, 1980.
- 2-44. D. H. Sliney and M. L. Wolbarsht, "Safety Standards and Measurement Techniques for High Intensity Light Sources", *Vision Research*, Vol. 20, pp. 1133-1141, 1980.
- 2-45. T. Stevens, G. Bresnick, M. Davis, S. Chandra and F. Meyers, "An Approach to Laser Management of Diabetic Retinopathy", in: Wayne F. March, Ed., *Ophthalmic Lasers: Current Clinical Uses*, (Slack, 1984), pp. 170-180.
- 2-46. A. N. Takata, L. Zaneveld and W. Richter, "Laser-Induced Thermal Damage of the Skin", Final Tech. Rep. SAM-TR-77-38, USAF School of Aerospace Medicine, Brooks AFB, TX., Dec. 1977.
- 2-47. W. S. Weinberg, R. Birngruber and B. Lorenz, "The Change in Light Reflection of the Retina During Therapeutic Laser-Photocoagulation", *IEEE J. of Quan. Elec.*, Vol. QE-20, No. 12, pp. 1481-1489, Dec. 1984.
- 2-48. A. J. Welch and G. D. Polhamus, "Measurement and Prediction of Thermal Injury in the Retina of the Rhesus Monkey," *IEEE Trans. Biomed Eng.*, Vol. BME-31, No. 10, pp. 633-644, Oct. 1984.
- 2-49. A. J. Welch, "The Thermal Response of Laser Irradiated Tissue", *IEEE Journal of Quantum Electronics*, Vol. QE-20, No. 12, pp. 1471-1481, Dec. 1984.
- 2-50. H. C. Zweng, "Lasers in Ophthalmology", in: M. L. Wolbarsht, Ed., *Lasers Applications in Medicine and Biology*, (Plenum Press, 1971), pp. 239-243.

### Chapter 3 Overview of the System

- 3-1. S. Ghaffari, "2-D Correlation Using 1-D Acousto-optic Cells", A Proposal for Ph. D Research, H. G. Rylander III, supervising professor, University of Texas at Austin, Texas, July 1987.

- 3-2. Laserscope, "Ophthobeam", Laserscope, 3350 Scott Boulevard, Bld. 29, Santa Clara, CA 95054, 1984.

#### Chapter 4 The Retinal Tracker

- 4-1. M. Alpern, *The Eye*, Vol. 3, Edited by H. Davson, Academic Press, New York, 1969.
- 4-2. J. F. Andrus, C. W. Campbell and R. R. Jayroe, "Digital Image Registration Using Boundary Maps", *IEEE Trans. Comput.*, C-24, pp. 935-940, Sept. 1975.
- 4-3. P. E. Anuta, "Spatial Registration of Multispectral and Multi-Temporal Digital Imagery Using Fast Fourier Transform Techniques", *IEEE Trans. Geosci. Electron.*, GE-8, No. 4, pp. 353-368, Oct. 1970.
- 4-4. P. E. Anuta, "Digital Registration of Multispectral Video Imagery", *SPIE Journal*, Vol. 7, pp. 168-175, Sept. 1969.
- 4-5. Applied Science Laboratories, 335 Bear Hill Road, Waltham, MA 02154 1982.
- 4-6. D. I. Barnea and H. F. Silverman, "A Class of Algorithms for Fast Digital Image Registration", *IEEE Trans. Comput.* C-21, No. 2, pp. 179-186, Feb. 1972.
- 4-7. T. N. Cornsweet and H. D. Crane, "Servo-Controlled Infrared Optometer", *Journal of the Optical Society of America*, Vol. 60, No. 4, pp. 548-554, April 1970.
- 4-8. T. N. Cornsweet and H. D. Crane, "Accurate Two-Dimensional Eyetracker Using First and Fourth Purkinje Images", *Journal of the Optical Society of America*, Vol. 63, No. 8, pp. 921-928, Aug. 1973.
- 4-9. H. D. Crane and C. M. Steele, "Accurate Three-Dimensional Eyetracker", *Applied Optics*, Vol. 17, No. 5, pp. 691-705, March 1978.
- 4-10. H. D. Crane, personal conversation, Stanford Research Institute, Menlo Park, CA, 20 Aug., 1986.
- 4-11. L. S. Davis and A. Rosenfeld, "An Application of Relaxation Labelling to Spring-Loaded Template Matching", *Proc. Internat. Joint Conf. Pattern Recognition*, 3rd, pp. 591-597, 1976.
- 4-12. M. A. Fischler and R. A. Elschlager, "The Representation and Matching of Pictorial Structures", *IEEE Trans. Comput.*, C-22, No. 1, pp. 67-92, Jan. 1973.
- 4-13. A. L. Gilbert, M. K. Giles, G. M. Flachs, R. B. Rogers and Y. Hsun U, "A Real-Time Video Tracking System", *IEEE Transaction on Pattern Analysis and Machine Intelligence*, Vol. PAMI-2, No. 1, pp. 47-56, Jan. 1980.

- 4-14. F. Glazer, G. Renolds and P. Anandan, "Scene Matching by Hierarchical Correlation", Proceedings IEEE Computer Soc. Conference on Computer Vision and Pattern Recognition, pp. 432-441, June 1983.
- 4-15. A. Goshtasby, S. H. Gage and, J. G. Bartholic, "A Two-Stage Cross Correlation Approach to Template Matching", *IEEE Trans. Pattern Anal. Machine Intelligence*, Vol. PAMI-6, No. 3, pp. 374-378, May 1984.
- 4-16. Hamamatsu System, Inc., "C1055 X-Y Tracker," Hamamatsu System, Inc., Waltham, Mass., June 1984.
- 4-17. ISCAN, "Eye Movement Monitoring Systems", ISCAN Inc., 755A Concord Ave., Cambridge, MA 02238, 1986.
- 4-18. D. H. Kelly and H. D. Crane, "Research Study of a Fundus Tracker for Experiments in Stabilized Vision", NASA Contractor Report, NASA CR-1121, Sept. 1968.
- 4-19. R. N. Nagel and A. Rosenfeld, "Ordered Search Techniques in Template Matching", *Proc. IEEE* 60, pp. 242-244, Feb. 1972.
- 4-20. H. K. Nishihara, "Practical Real-Time Imaging Stereo Matcher", *Optical Engineering*, Vol. 23, No. 5, pp. 536-545, Sept. / Oct. 1984.
- 4-21. J. L. Riedl, "CCD Sensor Array and Microprocessor Application to Military Missile Tracking", *SPIE*, Vol. 95, Modern Utilization of Infrared Technology II, pp. 148-154, 1976.
- 4-22. A. Rosenfeld, R. A. Hummel, and S.W. Zucker, "Scene Labelling By Relaxation Operations", *IEEE Trans. on Systems Man Cybernet.*, Vol. 6, pp. 420-433, 1976.
- 4-23. A. Rosenfeld and G. J. Vanderbrug, "Coarse-Fine Template Matching", *IEEE Trans. Systems Man Cybernet.*, SMC-7, pp. 104-107, Feb. 1977.
- 4-24. A. Rosenfeld and A. C. Kak, *Digital Picture Processing*, Vol. 1, Academic Press, New York, 1982.
- 4-25. A. Rosenfeld and A. C. Kak, *Digital Picture Processing*, Vol. 2, Academic Press, New York, 1982.
- 4-26. H. G. Rylander, III, personal conversation, Biomedical Engineering Program, University of Texas at Austin, Austin, TX.
- 4-27. J. T. Schwartz and G. R. Williams, "Proceedings of Workshop on Television Ophthalmology", Public Health Service Publication No. 1490, 1965.

- 4-28. S. M. Snodderly, W. P. Leung, G. T. Timberlake and D. P. M. Smith, "Mapping Retinal Features in a Freely Moving Eye with Precise Control of Retinal Stimulus Position",
- 4-29. G. Stockman, S. Kopstein and S. Benett, "Matching Images to Models for Registration and Object Detection Via Clustering", *IEEE Trans. Pattern Anal. Machine Intelligence* Vol. PAMI-4, No.3, pp. 229-240, May 1982.
- 4-30. M. Svedlow, C. D. McGillem and P. E. Anuta, "Experimental Examination of Similarity Measures and Preprocessing Methods Used for Image Registration, "Symp. Machine Processing of Remotely Sensed Data", Purdue, 1976.
- 4-31. G. T. Timberlake and H. D. Crane, "Eyetracker-Stabilized Laser Photocoagulation", *Invest. Ophthalmol. Visual Sci.*, 26S:38, 1985.
- 4-32. G. T. Timberlake, personal conversation, Eye Research Institute of Retina Foundation, Boston, Mass., 10 Oct. 1985.
- 4-33. G. J. Vanderbrug and A. Rosenfeld, "Two-Stage Template Matching", *IEEE Trans. Comput.* C-26, No. 4, pp. 384-393, April 1977.
- 4-34. B. Widrow, "The rubber-mask technique", *Pattern Recognition* , Vol. 5, pp. 175-211, 1973.

#### Chapter 5 Control of Lesion Size

- 5-1. *British Journal of Ophthalmology*, "Editorial: Search for the Ideal Laser", Vol. 63, pp. 655-656, 1979 (no name provided with editorial).
- 5-2. G. Coscas and G. Soubrane, "The Effects of Red Krypton and Green Argon Laser on the Foveal Region", *American Academy of Ophthalmology*, Vol. 90, No. 8, pp. 1013-1022, Aug. 1983.
- 5-3. Z. F. Gourgouliatos, *Behavior of Optical Properties of Tissue as a Function of Temperature*, Master Thesis, University of Texas at Austin, Texas, 1984.
- 5-4. M. A. Mainster, "Wavelength Selection in Macular Photocoagulation: Tissue Optics, Thermal Effects and Laser Systems", *Amer. Acad. Of Ophthal.*, Vol. 93, pp. 952-958, July, 1986.
- 5-5. J. Marshall, G. Clover and S. Rothery, "Some New Findings on Retinal Irradiation by Krypton and Argon Lasers", Ed: R. Birngruber and V-P Gabel, *Laser Treatment and Photocoagulation of the Eye*, Dr. W. Junk Publishers, Boston, 1984.
- 5-6. S. R. Mordon, A. H. Cornil, S. M. Jensen, B. Gosselin and J. M. Brunetaud, "Comparative Study of Pulsed and CW Nd. YAG Laser Coagulation", *IEEE Engineering in Medicine and Biology Society 8th Annual Conference*, Nov. 1986.

- 5-7. O. Pomerantzeff and C. L. Schepens, "Variation of Energy Density in Argon Laser Photocoagulation", *Arch. Ophthalmol*, Vol. 93, pp. 1033-1035, Oct. 1975.
- 5-8. O. Pomerantzeff, G. J. Wang, M. Pankratov and J. Schneider, "A Method to Predetermine the Correct Photocoagulation Dosage", *Arch. Ophthalmol*, Vol. 101, pp. 949-953, June 1983.
- 5-9. O. Pomerantzeff, G. Timberlake, G. J. Wang, M. Pankratov and J. Schneider-Goren, "Automation in Krypton Laser Photocoagulation", *Investigative Ophthalmology and Visual Science*, Vol. 45, No. 6, pp. 711-719, June 1984.
- 5-10. W. S. Weinberg, B. Lorenz, R. Birngruber and V. P. Gabel, "Controlling Retinal Photocoagulation By Light Reflection", *Docum. Ophthal. Proc. Series*, Vol. 36, ed. by R. Birngruber and V. P. Gabel, Dr. W. Junk Publishers, The Hague, pp. 299-311, 1984.
- 5-11. W. S. Weinberg, R. Birngruber and B. Lorenz, "The Change in Light Reflection of the Retina During Therapeutic Laser-Photocoagulation", *IEEE J. of Quan. Elec.*, Vol. QE-20, No. 12, pp. 1481-1489, Dec. 1984.
- 5-12. Y. Yang, "A Computerized Robotic Laser Capable of Inducing Lesions of Predetermined Size for Ophthalmic Treatment", A Proposal for Ph.D Research, A. J. Welch, supervising professor, University of Texas at Austin, Texas, Aug. 1987.
- 5-13. L. A. Yannuzzi, "Krypton Red Laser Photocoagulation", *Ophthalmic Forum*, Vol. 2, No. 1, pp. 26-28, 1984.

#### Chapter 6 Retinal Image Processing

- 6-1. K. Akita and H. Kuda, "A Computer Method of Understanding Ocular Fundus Images", *Pattern Recognition*, Vol. 15, No. 6, pp. 431-443, 1982.
- 6-2. T. Behrendt and L. A. Wilson, "Spectral Reflectance Photography of the Retina", *American Journal of Ophthalmology*, Vol. 59, pp. 1079-1088, 1965.
- 6-3. T. Behrendt and E. Slipakoff, "Spectral Reflectance Photography", in: J. Justice, Jr., Ed., *Ophthalmic Photography*, Little, Brown and Company, Boston, pp. 95-100, 1982.
- 6-4. J. L. Cambier, "Ophthalmic Imaging", *Medical Electronics*, pp. 90-94, Dec. 1986.
- 6-5. A. M. Coutinho, *The Estimation of the Cup-Disc Ratio from Digitized Pictures of the Optic-Disc*, Master Thesis, The University of Texas at Austin, Dec. 1984.

- 6-6. R. L. Dallow, *Television Ophthalmoscopy: Instrumentation and Medical Applications*. Springfield, Ill.: Thomas, 1970.
- 6-7. R. L. Dallow and J. W. Wallace, "Penetration of Retinal and Vitreous Opacities in Diabetic Retinopathy", *Arch. Ophthalmol.*, Vol. 92., pp. 531-534, Dec. 1974.
- 6-8. D. D. Donaldson, R. Prescott, and S. Kennedy, "Simultaneous Stereoscopic Fundus Camera Incorporating a Single Optical Axis", *Invest. Ophthalmol. Vis. Sci.*, Vol. 19, Num. 3, pp. 289-296, Mar. 1980.
- 6-9. M. Drumheller and T. Poggio, "On Parallel Stereo", *IEEE 1986 Conference on Robotics*, pp. 1439-1448, 1986.
- 6-10. W. F. Ganong, *Review of Medical Physiology*, Lange Medical Publications, CA, 1983.
- 6-11. M. Greene and A. L. Thomas, "Quantitative Television Fluorangiography - The Optical Measurement of Dye Concentrations and Estimation of Retinal Blood Flow", *IEEE Transactions on Biomedical Engineering*, Vol. BME-32, No. 6, pp. 402-406, June 1985.
- 6-12. W. M. Haining, "Video Funduscopy and Fluoroscopy", *British Journal of Ophthalmology*, 65, pp 702-706, 1981.
- 6-13. Humphrey Instruments, 3081 Teagarden St., San Leandro, CA 94577.
- 6-14. Kontron Bildanalyse GMBH, "IPS Ophthalmic Image Analysis Systems For Ophthalmology", Breslauer Str. 2, D-8057 Eching/Munich, FRG.
- 6-15. R. S. Manor, N. Schleinn, Y. Yassur, E. Svetlize and I. Ben-Sera, "Narrow-Band (540 nm) Green-Light Stereoscopic Photography of the Surface Details of the Peripapillary Retina", *Amer. Journal of Ophthalmol.*, Vol. 91, No. 6, pp. 774-780, 1981.
- 6-16. D. Marr, *Vision*, W. H. Freeman and Company, New York, pg. 55, 1982.
- 6-17. P. A. Nagin and B. Schwartz, "Approaches to Image Analysis of the Optic Disk", *Proc. of the 5th International Conference on Pattern Recognition*, Vol 2, pp. 948-956, 1980.
- 6-18. Ophthalmic Imaging Systems, Inc, P.O. Box 160266, Sacramento, CA 95816.
- 6-19. PAR Microsystems Corp., PAR Technology Park, New Hartford, NY 13413-1191.
- 6-20. E. Peli, T. R. Hedges and B. Schwartz, "Computerized Enhancement of Retinal Nerve Fiber Layer", *Acta Ophthalmologica*, Vol. 64, pp. 113-122, 1986.

- 6-21. A. M. Potts and M. C. Brown, "A Color Television Ophthalmoscope", *Amer. Acad. Of Ophthal.*, Vol. 62, pp. 136-137, 1958.
- 6-22. J. S. Read, B. H. McCormick and M. F. Goldberg, "The Television Ophthalmoscope Image Processor: Methods and Applications", *IEEE Computers in Ophthalmology*, pp. 123-132, April 1979.
- 6-23. H. Ridley, "Television in Ophthalmology", *International Congress of Ophthalmology*, Vol. 2, Issue 16, 1950.
- 6-24. T. A. Rice, R. G. Michels and W. J. Stark, *Ophthalmic Surgery*, C. V. Mosby Company, St. Louis, 1984.
- 6-25. J. T. Schwartz and G. R. Williams, "Proceedings of Workshop on Television Ophthalmology", Public Health Service Publication No. 1490, 1965.
- 6-26. T. Stevens, G. Bresnick, M. Davis, S. Chandra and F. Meyers, "An Approach to Laser Management of Diabetic Retinopathy", in: Wayne F. March, Ed., *Ophthalmic Lasers: Current Clinical Uses*, (Slack, 1984), pp. 170-180.
- 6-27. S. Tamura, K. Tanaka, M. Hashi, S. Omori, A. Okada, M. Inoue and K. Okasaka, "Analysis of Fluorescence Fundus Angiographies, *National Convention of I. P. S. J.*, pp. 673-674, 1977..
- 6-28. S. S. West, A. M. Potts, and J. R. Shearer, "Television Ophthalmoscopy", *IRE Transactions on Bio-Medical Electronics*, pp. 159-164, 1962.
- 6-29. W. Van Heuven and C. Schaffer, "Advances in Televised Fluorescein Angiography", International Symposium of Fluorescein Angiography, Tokyo. In: *Fluorescein Angiography*. Tokyo: Igaku Shoin, pp. 10-14, 1973.
- 6-30. A. Vogt, "Ophthalmoscopic Investigation on the Macula Lutea in Red-Free Light", *Klin. Monatsbl. Augenh.*, Vol. 66, pp. 321-363, 718-730, 838-859, Jan.-June 1921.
- 6-31. S. Yamamoto and H. Yokouchi, "Automatic Recognition of Color Fundus Photographs", in: K. Preson. Jr. and M. Onoe, Ed., *Digital Processing of Biomedical Images*, Plenum Press, pp. 385-398, 1976.

#### Chapter 7 Instrumentation

- 7-1. Andover Corporation, One Power Street, Lawrence, Mass., 01843.
- 7-2. A. T. Bahill and J. Kallman, "Predicting Final Eye Position Halfway Through a Saccade", *IEEE Transactions on Biomedical Engineering*, Vol. BME-30, No. 12, pp. 781-786, Dec 1983.
- 7-3. H. B. Barlow and J. D. Mollon, *The Senses*, Cambridge University Press, Cambridge, 1982.

- 7-4. T. Behrendt and K. E. Doyle, "Reliability of Image Size Measurements in the New Zeiss Fundus Camera", *American Journal of Ophthalmology*, Vol. 59, pp. 896-899, 1965.
- 7-5. G. W. Blankenship, "Panretinal Laser Photocoagulation with a Wide-Angle Fundus Contact Lens", *Annals of Ophthalmol.*, Vol. 14, No. 4, pp. 362-363, April 1982.
- 7-6. Britt Corporation, 2231 South Barrington Avenue, Los Angeles, CA 90064.
- 7-7. M. A. Bronstein, M. A. Mainster, O. Pomerantzeff, C. L. Trempe, C. L. Schepens, M. P. Avila and J. Schneider, "High Magnification Fundus Photography with the Macula-Disk Camera", *Ophthalmology, Instrument and Book Supplement*, pp. 189-191, Aug. 1982.
- 7-8. B.J. Busse and D. Mittelman, "Use of the Astigmatism Correction Device on the Zeiss Fundus Camera for Peripheral Retinal Photography", Ed: J. Justice, Jr., *Ophthalmic Photography*, Little, Brown and Company, Boston, pp. 65-76, 1982.
- 7-9. Canon U.S.A. Inc., One Canon Plaza, Lake Success, N.Y., 11042.
- 7-10. Carl Zeiss, Inc., One Zeiss Dr., Thornwood, N.Y. 10594.
- 7-11. Coherent Medical, 3270 West Bayshore Road, P.O. Box 10122, Palo Alto, CA 94303.
- 7-12. Cohu Inc., Electronics Division, 5755 Kearny Villa Road, San Diego, CA 92138-5623.
- 7-13. J. J. Coleman and W. T. Tsang, "Semiconductor Lasers: A Choice Structure for Lightwave Communications", *IEEE Potentials*, Vol. 4, No. 2, pp. 16-21, May 1985..
- 7-14. CooperVision/Cavitron, 17601 Fitch, Irvine, CA 92714.
- 7-15. T. N. Cornsweet and H. D. Crane, "Servo-Controlled Infrared Optometer", *Journal of the Optical Society of America*, Vol. 60, No. 4, pp. 548-554, April 1970.
- 7-16. J. P. Dieckert, M. A. Mainster and P. C. Ho, "Contact Lenses for Laser Applications", *Ophthalmology, Instrument and Book Supplement*, pp. 55-62, 1983.
- 7-17. D. D. Donaldson, R. Prescott, and S. Kennedy, "Simultaneous Stereoscopic Fundus Camera Incorporating a Single Optical Axis", *Invest. Ophthalmol. Vis. Sci.*, Vol. 19, Num. 3, pp. 289-296, Mar. 1980.



- 7-18. D. D. Donaldson, "Stereophotographic Systems", Ed: J. Justice, Jr., *Ophthalmic Photography*, Little, Brown and Company, Boston, pp. 107-128, 1982.
- 7-19. Eastman Kodak, "Kodak Color Films and Papers for Professionals", Pub. No. E-77, Eastman Kodak Company, Rochester, NY, 14650, pg. DS-36, 1986.
- 7-20. EG&G, 345 Potrero Avenue, Sunnyvale, CA 94096.
- 7-21. Electronic Industries Association, "Electrical Performance Standards - Monochrome Television Studio Facilities, EIA RS-170", Electronic Industries Association, Engineering Department, 2001 Eye Street, N. W. Washington, D. C., 20006, Nov. 1957.
- 7-22. Fairchild CCD Imaging, 3440 Hillview Ave., Palo Alto, CA 94304.
- 7-23. S. Fonda, A. M. Gatti and D. Vecchi, "Reliability of Photometric Measurements in the Zeiss Fundus Camera", *Acta Ophthalmologica*, 61 pp. 58-66, 1963.
- 7-24. N. Goldblatt, "Technical and Biological Aspects of Ophthalmic Laser Procedures", *Laser Institute of America, ICALEO*, Vol. 32, pp. 56-62, 1982.
- 7-25. A. Gullstrand, *Einführung in die Methoden der Dioptrik des Auges des Menschen*, S. Hirzel, Leipzig, pp. 90, 1911.
- 7-26. Haag-Streit, 6 Industrial Park, Waldwick, N.J., 07465.
- 7-27. Hamamatsu System, Inc., 40 Bear Hill Road, Waltham, Mass. 02254.
- 7-28. D. Hennings, Coherent Medical, 3270 West Bayshore Road, P.O. Box 10122, Palo Alto, CA 94303.
- 7-29. J. Holt, "1985 Trends in Detector Technology", *Laser Focus/Electro-Optics*, pp. 76-94, Dec. 1985.
- 7-30. A. E. Hunt and A. C. Sanderson, "Vision-Based Predictive Robotic Tracking of a Moving Target", CMU-RI-TR-82-15, Office of Naval Research, Arlington, VA 22217, Jan. 1985.
- 7-31. Information Storage Inc., "115MB and 230 MB Optical Storage Products", Information Storage Inc., 2768 Janitell Road, Colorado Springs, CO 80906, Dec. 1986.
- 7-32. Javelin Electronics (Hitachi), 19831 Magelian Drive, Torrance, CA 90502.
- 7-33. J. Justice, Jr., "Comparison of Fundus Camera", *Ophthalmology, Instrument and Book Supplement*, pp. 90-92, Aug. 1982.

- 7-34. B. Katz and J. F. Bille, "Digitized Laser Scanning Funduscopy: Preliminary Results", *Investigative Ophthalmology and Visual Science*, Vol. 25, Supp. 252, pg. 252, 1984.
- 7-35. Kowa Optimed, Inc., 20001 So. Vermont Ave., Torrance, CA 90502.
- 7-36. Lasertek, 1717 Walnut Hill Lane, Irving, TX 75062.
- 7-37. L. A. Lobes, "Panfundoscope Contact Lens for Argon Laser Therapy", *Annals of Ophthalmol.*, Vol. 13, pp. 713-714, June 1981.
- 7-38. M. A. Mainster, G. T. Timberlake, R. H. Webb and G. W. Hughes, "Scanning Laser Ophthalmoscopy", *Ophthalmology*, Vol. 89, No. 7, pp. 852-857, July 1982.
- 7-39. D. Makes, personal conversation, Ophthalmic Imaging Systems, Inc, P.O. Box 160266, Sacramento, CA 95816.
- 7-40. Matrox Electronic Systems, Ltd., "Video Digitizer", Manual No. 222-A50-02/1, 1055 St. Régis Blvd, Dorval, Quebec, H9P2T4, Canada, August 17, 1985.
- 7-41. Medical Instrument Research Associates, 87 Rumford Avenue, Waltham, MA 02154.
- 7-42. NEC America, Inc., Broadcast Equipment Division, 130-Martin Lane, Elk Grove Village, Ill., 60007.
- 7-43. Nikon Inc. Instrument Division, 623 Stewart Ave., Garden City, N.Y., 11530.
- 7-44. Olympus Corporation, 4 Nevada Drive, Lake Success, N.Y. 11042-1179.
- 7-45. Panasonic Video Systems Division, Division of Matsushita Electric Corporation of America, One Panasonic Way, Secaucus, N.J. 07094.
- 7-46. O. Pomerantzeff, "Image Formation in Fundus Cameras", *Invest. Ophthalmol. Visual Sci.*, Vol. 18, No. 6, pp. 630-637, June 1979.
- 7-47. O. Pomerantzeff, "Wide-Angle Noncontact and Small-Angle Contact Cameras", *Invest. Ophthalmol. Vis. Sci.*, Vol. 19, No. 8, pp. 973-979, Aug. 1980.
- 7-48. Pulnix America, Inc., 770-A Lucerne Drive, Sunnyvale, CA. 94086.
- 7-49. RCA Corporation, *Electro-Optics Handbook*, Technical Series EOH-11, Solid State Division/Electro Optics and Devices, Lancaster, PA 17604, 1974.
- 7-50. RCA Corporation, New Holland Ave., Lancaster, PA 17604-3140.

- 7-51. H. G. Rylander, III, personal conversation, Biomedical Engineering Program, University of Texas at Austin, Austin, TX.
- 7-52. Sony Communications Products Company, Sony Drive, Park Ridge, N.J., 07656.
- 7-53. Syn-Optics, Model AFS-3000, Syn-Optics, 1225 Elks Drive, Sunnyvale, CA 94089.
- 7-54. B. Szirth, personal communication, Children Hospital, Division of Ophthalmology, Los Angeles, CA, Dec. 1987.
- 7-55. M. Tanaka and K. Tanaka, "An Automatic Technique for Fundus-Photograph Mosaic and Vascular Net Reconstruction", Ed: Lindberg and Kaihara, *Med-Info 80*, North-Holland Publishing Company, pp. 116-120, 1980.
- 7-56. Topcon Instrument Corporation of America, 65 West Century Road, Paramus, NJ, 07652.
- 7-57. A. W. Vincent Associates, Inc., Advanced Electro-Mechanical Engineering, 1255 University Avenue, Rochester, NY 14607.
- 7-58. R. A. Weale, "Polarized Light and the Human Fundus Oculi", *J. Physiol.*, Vol. 186, pp. 175-186, 1966..
- 7-59. R. H. Webb, G. W. Hughes and O. Pomerantzeff, "Flying Spot TV Ophthalmoscope", *Applied Optics*, Vol. 19, No. 17, pp. 2991-2997, Sept. 1980.
- 7-60. R. H. Webb and G. W. Hughes, "Scanning Laser Ophthalmoscope", *IEEE Trans. Biomed. Eng.*, BME-28, No. 7, 1981.
- 7-61. Xybion Electronics Systems Corp., 7750-A Convoy Court, San Diego, CA 92111.

#### **Chapter 8 Further Research**

- 8-1. J. F. Canny. *Finding Edge and Lines in Images*, Master Thesis, Massachusetts Institute of Technology, June 1983.
- 8-2. S. Ghaffari, "2-D Correlation Using 1-D Acousto-optic Cells", A Proposal for Ph. D Research, H. G. Rylander III, supervising professor, University of Texas at Austin, Texas, July 1987.
- 8-3. Y. Yang, "A Computized Robotic Laser Capable of Inducing Lesions of Pre-determined Size for Ophthalmic Treatment", A Proposal for Ph. D Research, A. J. Welch, supervising professor, University of Texas at Austin, Texas, Aug. 1987.

## VITA

Michael Stephen Markow ~~was born in [redacted] July 12, 1954,~~  
the son of Marilyn Joyce Markow and Nicholas Michael Markow. His wife's name is  
Radiana and he has three children; Abel, Joshua, and Sarah, ~~[redacted]~~ Not  
having finished high school, he entered the United States Air Force Academy in July of  
1974 and graduated in May of 1978 as a Second Lieutenant and an Electrical Engineer.

He worked as a research and development engineer with the Airborne Laser  
Laboratory at the Air Force Weapons Laboratory in Albuquerque, New Mexico. Dur-  
ing these four years he gained practical experience in electrical engineering, emphasiz-  
ing system integration, digital design, and communication. He earned his Master's  
Degree in Electrical Engineering in December of 1981 at the University of New Mex-  
ico.

In July of 1982, he joined the Electrical Engineering Faculty at the United States  
Air Force Academy. During these two years, his teaching focused on courses in digital  
design and microprocessor systems. He became a Professional Engineer registered in  
Colorado in August of 1984 and entered The Graduate School of The University of  
Texas also in August of 1984.

~~[redacted]~~

~~This dissertation was typed by the author~~